Estimating Uncertainties in Future Global Warming using a Simple Climate Model

by

Roger William Bodman

Thesis

Submitted in total fulfillment of the requirements for the degree of

Doctor of Philosophy

Supervisor: Professor David J. Karoly

Co–Supervisor: Professor Ian G. Enting

Co–Supervisor: Professor Peter J. Rayner

School of Earth Sciences

The University of Melbourne

November, 2011

Estimating Uncertainties in Future Global Warming using a Simple Climate Model

Roger William Bodman
rwbodman@unimelb.edu.au
The University of Melbourne, 2011

Supervisor: Professor David J. Karoly

Abstract

This research has investigated the sources of uncertainty that apply to global–mean temperature change projections. Uncertainties in climate system processes have led to a wide range of projections for future temperature changes, which are compounded by the range of possible future greenhouse–gas emissions. For example, the 2007 Intergovernmental Panel on Climate Change Fourth Assessment Report reported that, by 2100, the global–mean temperature increase relative to 1990 is likely to be in the range 1.1°C to 6.4°C, a result that reflects uncertainties in both future emissions and the response of the climate system. However, such a wide range is not particularly helpful for policy and planning purposes, especially in the absence of probabilities. This research has investigated the reasons for this wide range, assessed the sources of uncertainty and developed a method for producing probabilistic temperature change projections.

A simple climate model was selected as the research tool for this investigation, instead of a complex three–dimensional model. The model chosen was the latest version of MAGICC (Model for the Assessment of Greenhouse–gas Induced Climate Change), which represents many of the important processes that determine variations of the Earth's climate, including radiative forcing, heat uptake in the ocean and the carbon cycle, albeit highly simplified and only for temperature changes at the global scale.

One of the features of this research is the development of alternative approaches to constraining the model's primary climate system and carbon cycle parameters. It was found that indices using land minus ocean and Northern Hemisphere minus Southern Hemisphere temperature anomalies are only weakly correlated with global–mean temperatures, and therefore provide additional independent information that can assist in better estimating some model parameters. A ratio of sea–surface temperature to ocean heat content was also found to have a low correlation to the sea–surface temperatures, creating an alternate measure for constraining ocean parameters. This ratio, as well as the vertical ocean temperature change profile, led to revised estimates for the ocean vertical diffusivity parameter, resulting in a new estimate that is nearly a quarter of the previously standard setting used with the Third and Fourth IPCC assessment report versions of MAGICC.

In addition to constraining individual model parameters with targeted observational information, a Bayesian statistical technique, the Monte Carlo Metropolis–Hastings algorithm (MCMH),

was applied to constraining groups of model parameters using historical observations. One advantage of the MCMH technique is that it addresses uncertainty that arises from observations, model structure and climate system response. This resulted in probability distributions for the key model parameters which then allowed the production of probabilistic temperature change projections. The carbon cycle was included in the MCMH process, leading to a successful calibration of MAGICC's key carbon cycle parameters with observations for the first time.

The MCMH technique was applied to a number of emissions scenarios, enabling probabilistic estimates to be made of global–mean temperature changes to the end of this century. These show reduced uncertainty ranges for future warming projections, with higher lower bounds for warming due to business–as–usual emissions as compared to the results reported in the IPCC's Fourth Assessment Report. The upper bound for the likely range is also considerably reduced. For the highest emissions scenario, the SRES A1FI, there is a 50% probability of exceeding 2°C by 2042, with a 73% probability of exceeding 4°C by 2100.

Analysis of stabilisation scenarios shows that limiting further increases in global–mean temperature to 2°C above pre-industrial requires massive reductions in anthropogenic greenhouse–gas emissions, to the extent that almost zero CO_2 emissions are required by the end of this century. Even then, the temperature increase will peak around mid-century, with the upper bound of the likely range temperature change exceeding 2°C, which then entails the risk of irreversible changes to the climate system.

Estimating Uncertainties in Future Global Warming using a Simple Climate Model

Declaration

This is to certify that:

(i) the thesis comprises only my original work towards the PhD,

(ii) due acknowledgment has been made in the text to all other material used,

(iii) the thesis is less than 100,000 words in length, exclusive of tables, maps, bibliographies and appendices.

Signed,

Roger William Bodman
February 27, 2012

Acknowledgments

I would like to express my appreciation and gratitude to my PhD supervisors: Professor David Karoly for his unfailing patient guidance and assistance; Professor Ian Enting for his kind advice and help throughout; and Professor Peter Rayner for invaluable support, arriving at a crucial time to help with the MCMH work. They all contributed to helping my endeavours. Thanks also to Professor Roger Jones for his role as a member of my PhD advisory panel.

A special thanks to David Karoly who, in addition to being all one could ask for in a supervisor, offered me a scholarship without which I would not have been able to take up postgraduate study. Also to Professor Jim Falk, who employed me as a research assistant at the University of Melbourne, involved me in work for the Garnaut Review, which in turn led to working with David. Its been an interesting journey.

Particular thanks also go to Tom Wigley and Malte Meinshausen for providing the MAGICC code and answering questions, and to Jens Kattge for the MCMH code. Also to Susan Wijffels for discussing concerns about CMIP3 ocean temperature trends compared to observations and sharing her ocean temperature data.

Thanks also to Dr Frank Drost for general discussions and assistance with MATLAB problems, to Dr Ailie Gallant, other colleagues and fellow students in the School of Earth Sciences.

I also acknowledge the various groups around the world that collate and make available the observational and model data sets that provided an essential resource for this research work, including the Hadley Centre of the UK Met Office and the Climatic Research Unit of the University of East Anglia, the NASA Goddard Institute for Space Studies, the National Oceanic and Atmospheric Administration and the National Climatic Data Center, the Carbon Dioxide Information Analysis Center, the Global Carbon Project, and the Program for Climate Model Diagnosis and Intercomparison, as well as individual researchers as referenced in the thesis.

Finally, huge thanks go to my partner Paula and my family for their love and support. Returning to full time study entails some sacrifices, which they have shared in. Their encouragement and support has been invaluable and helped me immensely.

Roger William Bodman

The University of Melbourne
November 2011

To Paula

Contents

List of Figures

List of Tables

List of Acronyms

Acronym	Description
AGCM	Atmosphere General Circulation Model
AOGCM	Atmosphere–Ocean General Circulation Model
AR4	Fourth Assessment Report of the IPCC
C4MIP	Coupled Carbon Cycle Climate Model Intercomparison Project
CDIAC	Carbon Dioxide Information Analysis Center
CH_4	Methane
CMIP3	Third Coupled Model Intercomparison Project
CMIP5	Coupled Model Intercomparison Project Phase 5
CO_2	Carbon Dioxide
CSIRO	Commonwealth Scientific and Industrial Organisation
DAI	Dangerous Anthropogenic Interference
DCC	Dangerous Climate Change
EBM	Energy Balance Model
EMIC	Earth systems Model of Intermediate Complexity
EML	Equivalent Mixed Layer
ESM	Earth System Model
FL	Fraction of Land, i.e., the proportion of the Earth's surface that is land
FO	Fraction of Ocean, i.e., the proportion of the Earth's surface that is ocean
GCM	General Circulation Model
GDP	Gross Domestic Product
GHG	Greenhouse–gas
GISS	Goddard Institute for Space Studies
GPP	Gross Primary Productivity
GSAT	Global–mean Surface Air Temperature
GWP	Global Warming Potential
HadCRU	Hadley Centre of the UK Met Office and the Climatic Research Unit (CRU) of the University of East Anglia
HadCRUT3	HadCRU land and sea surface temperature anomaly data set
HadSST2	HadCRU sea surface temperature anomalies
IAM	Integrated Assessment Model
IPCC	Intergovernmental Panel on Climate Change
L−O	Land minus ocean (temperature difference)

Acronym	Description
MAGICC	Model for the Assessment of Greenhouse–gas Induced Climate Change
MLE	Maximum Likelihood Estimate
MLT	Mixed Layer Temperature
MOC	Meridional Overturning Circulation
MSLP	Mean Sea Level Pressure
NASA	National Aeronautics and Space Administration
NCAR	National Center for Atmospheric Research
NCDC	National Climatic Data Center
NH	Northern Hemisphere
NOAA	National Oceanic and Atmospheric Administration
NPP	Net Primary Productivity
N−S	Northern minus Southern (hemispheric temperature difference)
OHC	Ocean Heat Content
PCMDI	Program for Climate Model Diagnosis and Intercomparison
PDF	Probability Density Function
RCP	Representative Concentration Pathway
RF	Radiative Forcing
RMSE	Root Mean Square Error
SAR	Second Assessment Report of the IPCC
SCENGEN	Scenario Generator (add-on pattern scaling routine to MAGICC)
SCM	Simple Climate Model
SH	Southern Hemisphere
SRES	Special Report on Emissions Scenarios
SST	Sea–surface temperature
TAR	Third Assessment Report of the IPCC
TIM	Total Irradiance Monitor
THC	Thermohaline circulation
TSI	Total Solar Irradiance
UCAR	University Corporation for Atmospheric Research
UD	Upwelling Diffusion
UNFCCC	United Nations Framework Convention on Climate Change
WG1	Working Group 1 of the IPCC
WG2	Working Group 2 of the IPCC
WG3	Working Group 3 of the IPCC
wrt	with respect to

List of Notation

α Scaling factor used to convert mixed layer temperature to near surface air temperature

α_{e} Earth's albedo

α_T Ocean carbon cycle temperature feedback

β Down dwelling water temperature to mixed layer temperature fraction.

β_m CO_2 fertilisation method

β_s CO_2 fertilisation factor

Γ $(dK_z top/dT)$ Dependence of vertical diffusivity on ocean warming gradient

$\Delta T_{2\mathrm{x}}$ Climate sensitivity (temperature for doubled CO_2 concentration)

Δw change in w

κ_{lo} Heat exchange coefficient land ocean

κ_{ns} Heat exchange coefficient North South

λ_G Global mean climate sensitivity $(\Delta T_{2\times}/\Delta Q_{2\times})$

λ_O Temperature feedback over ocean

λ_L Temperature feedback over land

μ Asymmetry coefficient for heat transfer between land and ocean

ϕ Land sea adjustment factor (used with *Wigley and Raper*, 1990, energy balance equation)

ρ Density of sea water

$\theta(z)$ Ocean temperature at depth z

θ_{BW} Bottom water temperature

θ_{ML} Mixed layer temperature

σ_{B} Stefan–Boltzman constant

σ_{NPP} Temperature feedback factor, NPP

σ_{Q} Temperature feedback factor, detritus

σ_{R} Temperature feedback factor, respiration

σ_{U} Temperature feedback factor, soil

Φ_{H} Carbon flux partition, detritus to soil

ζ_O Ocean heat capacity $= \rho ch$ per unit area

ζ_L Land heat capacity, taken as zero. Hence the land temperatures are diagnostic variables

ξ Dependence of feedback factors on forcing (sensitivity factor)

AF_{tot} Aerosol forcing parameter, total

AF_{soxi} Direct sulfate fossil fuel aerosol forcing parameter

c Ocean heat capacity

D Depth of ocean

$f_{\mathrm{land}}, f_{\mathrm{l}}$ Land area fraction

f_{no} Fraction of hemisphere in Northern ocean

$f_{\mathrm{ocean}}, f_{\mathrm{o}}$ Ocean area fraction

f_{so} Fraction of hemisphere in Southern ocean

g_{H} Carbon flux partition, NPP to detritus

g_{P} Carbon flux partition, NPP to plant

h Mixed layer depth

H_0 Initial detritus pool

k Ocean carbon cycle gas exchange scale factor

K Ocean effective diffusion coefficient

LF Likelihood Function

N_0 Initial NPP flux

O_{r} Ocean carbon cycle impulse response scale factor

P_0 Initial plant pool

Q Radiative forcing. ΔQ is change

q_{H} Carbon flux partition, plant to detritus

r Correlation coefficient

R Radius of Earth

$R_{(\mathrm{P},0)}$ Initial respiration flux

R_{lo} Land ocean warming ratio (used to derive λ_O, λ_L)

S Solar radiation, Wm^{-2}

S_0 Initial soil pool

t Time (in years)

T Surface temperature (global–mean) — ΔT is change

T_{e} Effective temperature

T_{global} Global surface temperature

T_{land} Land surface temperature

T_{moc} Upwelling temperature threshold for collapse of meridional overturning circulation

T_{ocean} Ocean surface temperature

w Upwelling velocity

w_0 Initial upwelling velocity

w_{var} Variable fraction of w

z Depth below mixed layer

Chapter 1

Introduction

1.1 Background

This research investigates the sources of uncertainty associated with global–mean temperature change projections using a simple climate model. A feature of this research is the development and application of new approaches to constraining the model parameters using independent constraints based on historical observations. In addition, a Bayesian Monte Carlo approach is applied to estimating the climate system parameters, the carbon cycle parameters and then the combined climate–carbon cycle parameters. This is the first time that the chosen simple climate model has had its carbon cycle parameters estimated in this way. A method of producing probabilistic temperature results is also demonstrated and then applied to a number of emissions scenarios with a focus on 'committed climate change', avoiding 'dangerous climate change', and stabilisation of greenhouse–gas concentrations in the atmosphere.

One motivation for this research stems from the 2007 Intergovernmental Panel on Climate Change (IPCC) Fourth Assessment Report (AR4) which concluded that 'warming of the climate system is unequivocal', with a total temperature increase from 1850–1899 to 2001–2005 of 0.76°C (0.57°C to 0.95°C) and that, by 2100, the global-mean temperature increase relative to 1990 is likely to be in the range 1.1°C to 6.4°C, where 'likely' means a greater than 66% probability and 'likely range' is a 67% confidence interval (*IPCC*, 2007a). This result reflects uncertainties in both future emissions and the response of the climate system. The temperature range is derived from simulations using complex Atmosphere–Ocean General Circulation Models (AOGCMs), Earth System Models of Intermediate Complexity (EMICs) and Simple Climate Models (SCMs). However, this very wide range is not particularly helpful for policy and planning purposes, especially in the absence of probabilities. This research examines the reasons for this range, considers the sources of uncertainty and quantifies the probabilities of future temperature changes associated with different sources of uncertainty. A simple climate model provides an appropriate, versatile and economical tool for this task, rather than a complex and costly AOGCM. Some specific climate system problems concerning global–mean temperature change projections form part of the investigation.

Another reason for examining a simple climate model is the continuing role such models have in the climate change policy processes at national and international levels. This is demonstrated by work such the IPCC assessment reports, the Stern Review (*Stern*, 2007), the Garnaut Review

(*Garnaut*, 2008), and the UK Climate Projections project (*Murphy et al.*, 2009). Evaluation of emissions scenarios and trajectories towards stabilisation will continue as a role for simple climate models. In addition, a number of Integrated Assessment Models (IAMs) and regional impact studies rely on a simplified climate model to provide an accessible and computationally efficient tool that is appropriate for their purpose. Parameter estimates within IAMs are important since they can impact on economic and impact assessments that feed into policy making (*van Vuuren et al.*, 2011). Accordingly, maintaining and refining simple climate models remains an important task.

A summary of the research questions and their significance is presented next, followed by a discussion concerning the role of simple climate models, their basic features and relationship to more complex models. The selected simple climate model, MAGICC (Model for the Assessment of Greenhouse–gas Induced Climate Change) is introduced. The evolution of MAGICC is reviewed in Chapter 2, together with some of the ways in which the model has been applied. A description of the model is included along with the basic energy–balance equations and forcing components.

The model parameter settings and the tuning of MAGICC using observations as parameter constraints are investigated in Chapter 3. As the primary source of uncertainty, the climate sensitivity parameter is examined including consideration of its time–dependent and state–dependent nature. Chapter 3 also focusses on specific issues concerning the ocean's response to heating, including a review of the relevant model parameters that control the rate and distribution of heat uptake, and how observations can be utilised to constrain the key ocean parameters independently of the global–mean temperature. This work on the climate system parameters is continued into Chapter 4, which investigates the relative contribution that the uncertainty in these parameters makes towards global–mean temperature change projections, and then applies a Monte Carlo Markov Chain with Metropolis–Hastings algorithm (MCMH) to estimate posterior joint probability density functions for the key climate parameters.

The carbon cycle, another important source of model uncertainty, is examined in Chapter 5, where the MCMH algorithm was successfully applied to estimating selected carbon cycle parameters using historical observations, something that has not been previously attempted for MAGICC. The climate system and carbon cycle parameters are then brought together to investigate them jointly in Chapter 6. Uncertainty concerning future emissions and projections of global–mean temperatures is addressed in Chapter 7, with a discussion of climate commitment, temperature targets and stabilising greenhouse–gas concentrations. The results and conclusions of the thesis are summarised in Chapter 8.

1.2 Research Themes

1.2.1 Uncertainty in temperature projections

This research investigates selected aspects of changes in the Earth's climate system caused by anthropogenic greenhouse–gases, with a focus on global–scale temperature changes, since changes in surface air temperatures are a primary indicator of climate change. A particularly useful tool for this purpose is a simple climate model (SCM) of the type described by *Harvey et al.* (1997). This

investigation examines projected changes in global–mean temperatures over the twenty–first century and demonstrates how the range of uncertainty in these temperature changes can be quantified using such a model.

Sensitivity analysis and testing of twentieth–century model results against historical observations has been used to identify key model parameters and constrain their uncertainties. This has included using the land−ocean and hemispheric temperature differences as constraints. The use of these temperature differences as additional independent variables, in conjunction with the global–mean temperature, is a new approach to constraining parameters in MAGICC (hemispheric differences were used in *Andronova and Schlesinger* (2001) and *Harvey and Kaufmann* (2002), but the land−ocean difference does not appear to have been applied in this context previously). Furthermore, it is important that the land−ocean temperature contrast is modelled correctly since the significant difference between the mean land and ocean temperatures has important implications for assessing impacts on people, water and agriculture etc, as well as for mitigation and adaptation policies.

A Monte Carlo Markov Chain with Metropolis–Hastings algorithm has also been used to investigate prior and posterior probability density functions for the climate system and carbon cycle parameters using twentieth–century observations to help constrain the model parameters. This method provides another perspective on the sources of uncertainty and enables the generation of probabilistic temperature change projections.

1.2.2 Ocean heating

A problem that emerges from reviewing some of the recent research on climate change is the question of whether coupled climate models are over–estimating the mixing of heat from the upper lower layers of the ocean into the deep ocean. Recent observations show more upper layer warming than expected from the Third Coupled Model Intercomparison Project model results (CMIP3; *Meehl et al.*, 2007a) for the twentieth century (*Wijffels*, 2009). Modelling this correctly is important for projecting temperature changes. The warming of the upper–ocean layers has the potential to slow down or even collapse the thermohaline circulation with significant repercussions. This is also important for Arctic ice formation, and influences seasonal climate variations and climate modes such as El Niño. This problem has been investigated with a simple climate model in order to determine its significance for future global–mean temperature change projections and the land−ocean temperature contrast. As part of this process, it was discovered that the model's ocean temperature parameters needed revising and a re-formulation of the ocean heat calculation was required. In addition, a modified constraint for setting the ocean vertical diffusivity was developed based on a ratio between sea–surface temperatures and ocean heat content.

1.2.3 Carbon cycle uncertainties

The carbon cycle is an important element of the overall uncertainty connected with global–mean temperature change projections for the twenty–first century and needs to be taken into account when making such projections. Indeed, one of the limitations of many climate models, including complex models, has been the fact that they do not include a carbon cycle and related temperature

feedbacks. It is important to consider the carbon cycle since there are a number of temperature–dependent processes that can lead to positive feedbacks in the terrestrial biosphere and the ocean carbon cycle.

Uncertainties in modelling the carbon cycle arise for a number of reasons, including the lack of relevant observations, ambiguities in paleo–records and model limitations. The performance of a simple climate model has been tested against twentieth–century observations and the Coupled Carbon Cycle Climate Model Intercomparison Project (C4MIP; *Friedlingstein et al.*, 2006) results to determine the range of uncertainty associated with the carbon cycle, along with its relative contribution to changes in the atmosphere's composition and the global–mean temperature.

1.2.4 Stabilising emissions

The previous research themes have addressed scientific uncertainty combined with some important issues in climate modelling. However, there are other aspects of uncertainty that need to be considered when projecting global–mean temperature changes, in particular the magnitude of future anthropogenic greenhouse–gas emissions. The focus here is the continuing trend in emissions and the mitigation targets agreed to at Copenhagen 2009 as compared to SRES (Special Report on Emissions Scenarios, (*Nakicenovic and Swart*, 2000)) scenarios, RCPs (Representative Concentration Pathways) and stabilisation pathways. Given the concern over dangerous climate change, what emission reductions will be required to keep atmospheric concentrations below a target such as 450ppm CO_2 equivalent or a nominated temperature increase, such as 2°C above pre-industrial temperatures by 2050? What are the associated uncertainties and risks? These are important issues for national and international mitigation policies.

1.3 Climate Models

Computer–based climate models are an important tool for assessing the likelihood and extent of human activities impacting on the Earth's climate system. These models range from a single point representation of the Earth's climate through to high resolution three–dimensional coupled Atmosphere–Ocean General Circulation Models (AOGCMs) and Earth System Models (ESMs). *McGuffie and Henderson-Sellers* (2001) provide a useful historical overview of the main types of numerical climate models and their development. Each of the different types of model has a role for investigating potential climate change, which can be broadly categorised into three model classifications, simple, intermediate and general:

1. Simple Climate Models (SCMs). A valuable discussion of simple climate models is provided by *Harvey et al.* (1997).

2. Earth Models of Intermediate Complexity (EMICs). See, for example, *Claussen et al.* (2002), *Claussen* (2005) and *IPCC* (2007b) for further details.

3. General Circulation Models (GCMs), which can be Ocean (OGCM), Atmosphere (AGCM) or combined Atmosphere–Ocean (AOGCM).

Simple Climate Models (SCMs) have been discussed and utilised in the IPCC Assessment Reports, where they were used to investigate implications for temperature and sea–level rise changes

arising from a range of emissions scenarios. Simple climate models can only represent the primary processes in a highly approximated way, with the main climate elements described by a small number of paramaterised equations. In contrast, complex models are able to identify most of the atmospheric, terrestrial and marine processes in detail by using a much more complete set of equations that describe the physical and biogeochemical interactions. The more advanced SCMs are able to calculate the concentrations of greenhouse–gases, the resultant radiative forcing and then the global–mean surface temperature response and global–mean sea–level rise due to ocean thermal expansion combined with glacier and ice sheet melting. The most recent IPCC Fourth Assessment Report includes a review of climate models, although the majority of the analysis is devoted to AOGCMs, with some consideration of Earth System Models of Intermediate Complexity (EMICs) and only a short section on SCMs (*IPCC*, 2007b).

1.3.1 The role of Simple Climate Models

While there may be a tendency to think that more complex climate models are 'better' than simple ones, the different models all have their place:

> 'SCMs are ideal for exploring the global scale consequences of alternative emission scenarios and for investigating the interactive effect of specific assumptions concerning the behaviour of individual subsystem components' (*Harvey et al.*, 1997).

Complex models are better at representing a wider range of climate phenomena at regional scales, but they are not as suitable for looking at multiple scenarios or for sensitivity studies of large–scale system components. Each has their role, as is evident from the way the models are utilised in the IPCC assessment reports. For climate research over long time–scales, both past and future, SCMs are still a very useful tool, although care is needed in their application and interpretation of results due to their inherent limitations (*Stocker and Knutti*, 2003).

The latest IPCC report explains:

> 'Their role is to perform comprehensive analyses of the interactions between global variables, based on prior estimates of uncertainty in their controlling parameters obtained from observations, expert judgement and from tuning to complex models' (*IPCC*, 2007b).

SCMs provide only a limited range of results, such as the global temperature anomaly and sea–level rise. They are not generally able to resolve regional results or provide precipitation amounts. However, some additional results, such as precipitation and surface pressure, can be derived from pattern scaling (*Santer et al.*, 1990; *Mitchell*, 2003).

Advantages of SCMs include:

- They are faster and more economical to run than AOGCMs and hence can be applied more readily to a range of emissions scenarios over a longer time frame. The computational costs associated with complex models tend to limit the number of experiments that they can be used to investigate.

- Uncertainties can be concatenated, which allows temperature and sea level results to be expressed as probabilities (*IPCC*, 2007b). The ability of simplified models to calculate uncertainties and use observational constraints is one of their advantages (*Stocker and Knutti*, 2003).
- They can be more easily used in economic modelling, for example within Integrated Assessment Models (IAMs).
- They can assist in developing new strategies and policies to deal with future climate change.
- SCMs are useful for testing hypotheses and parameter sensitivity, which can then lead to further testing with more complex models.
- They can provide a useful crosscheck for consistency with more complex models.
- Pattern scaling offers the potential to provide regional results from a SCM.

Meinshausen et al. (2011a) identified four roles for simple climate models:

1. Emulation of AOGCMs. Complex models are generally too computationally expensive for investigating multiple emissions scenarios and perturbed physics experiments. MAGICC is capable of emulating the large–scale AOGCM results and hence a wide range of emission scenarios;
2. Structural uncertainties. A simple climate model can capture the range of structural uncertainties across a set of complex models. For example, the climate sensitivity diagnosed from AOGCMs summarises the feedback processes represented within the AOGCMs; differences in this value provide an indication of the structural uncertainty;
3. Factor separation analysis. A simple climate model can assist in separating different aspects of the climate system, such as climate or carbon cycle responses from forcing uncertainties, which helps to clarify differences in forcing assumptions used in AOGCMs. This is particularly useful for trying to deal with varying model forcing set–ups;
4. Joint response and feedback analysis. Estimates of the coupled response of more complex models can be derived using a suitably tuned simple model, where the more complex model lacks an interactive carbon cycle with climate feedbacks.

Simple climate models may need to be tuned to AOGCMs in order to establish some parameter values, since there are limitations in the number and types of historical observations that can be used for this purpose. The tuning process for MAGICC is discussed, for example, by *Cubasch and Meehl* (2001), *Raper et al.* (2001) and more recently by *Meinshausen et al.* (2009) and *Meinshausen et al.* (2011a).

Unlike simple climate models, AOGCMs are able to directly model many of the climate processes to simulate temperature and other variables such as rainfall, evaporation, soil moisture, cloudiness and winds, over relatively small regions, according to the model resolution. Since many physical processes are directly simulated, a short time–step is required, but this then provides for various cycles, such as diurnal and seasonal changes, features that cannot be resolved

in a simple climate model. Hence, complex models also have the potential to simulate changes in important modes of inter–annual variability (e.g., the El Niño Southern Oscillation) as well as mean values. AOGCMs can also simulate major changes in the ocean's circulation, although the predicted timing and nature of such changes may not yet be particularly reliable. Simple climate models can only represent the most basic features of the ocean circulation such as vertical diffusion and advection only, with no horizontal transport. Simple climate models typically have no or only very limited treatment of natural variability. They are also unable to replace the more detailed modelling and sophisticated analysis possible with AOGCMs, but they can extend their key characteristics to a larger range of scenarios.

Intermediate complexity climate models lie between SCMs and AOGCMS as their name implies; they are less complex, low-resolution models with simplified physical equations as compared to AOGCMs, and yet typically have a carbon cycle. They more closely represent the climate system than do SCMs, having more physical processes such as precipitation and may have more realistic ocean circulation. Although computationally less costly than a full AOGCM, EMICs nevertheless do not lend themselves to the large number of runs needed for Monte Carlo type calibration as envisaged for this research project.

1.3.2 Selecting a Simple Climate Model

A simple climate model is an appropriate tool for the purposes of this research programme. It was decided that an existing SCM would be used rather than developing a new model since this would save considerable time and, rather than re-inventing the wheel, build upon an existing body of tested expertise. Using a pre–existing and proven model allows effort to be directed towards investigating the research questions. This section briefly discusses some candidate models and then looks at the selected model, MAGICC (Model for the Assessment of Greenhouse–gas Induced Climate Change).

There are a number of examples of working SCMs in the literature, although only a few appear to have been maintained and made available to other researchers. A review of simple climate models is provided by *Harvey et al.* (1997), *An Introduction to Simple Climate Models used in the IPCC Second Assessment Report* (IPCC Technical Paper II). In the IPCC Second Assessment Report (SAR; *IPCC*, 1996) three simple models were referred to: *Jain et al.* (1995), *Siegenthaler and Joos* (1992), and *Wigley and Raper* (1992). The latter is MAGICC version 2.4, while the former two models do not appear in later research literature and seem not to have been maintained and used for the IPCC Third Assessment Report (TAR; *IPCC*, 2001). The tuning of MAGICC and its performance relative to AOGCMs at that time are discussed in the SAR (*IPCC*, 1996). The TAR used a number of AOGCMs and MAGICC version 4.2, tuned to emulate the AOGCMs, was used for modelling all 40 SRES scenarios, since time and cost restricted the wider use of AOGCMs (*IPCC*, 2001).

For the most recent Fourth Assessment Report (AR4; *IPCC*, 2007b), AOGCMs, probabilistic methods, EMICs and tuned SCMs were used for global climate projections. The SRES (Special

Report on Emissions Scenarios; *Nakicenovic and Swart*, 2000) multi–model (CMIP3) mean surface air temperatures were reported for six illustrative scenarios (A1FI, A1B, A1T, A2, B1, B2)[1]. Unlike the TAR, carbon cycle uncertainties were included in the range of results. MAGICC was again used as the SCM.

Searching through the literature identified some other simple climate models that are discussed in the following paragraphs. It was also found that a number of models make use of MAGICC as the basis for their work, such as SIMCAP (*Meinshausen*, 2005), OzClim (http://www.csiro.au/), IMAGE (*Schaeffer and Stehfets*, 2010), ESCAPE (*Hulme et al.*, 1995) and MiniCAM (*Smith and Wigley*, 2006). These models utilise MAGICC as their core climate module.

COSMIC is an energy balance climate, upwelling diffusion ocean model that was developed by Larry Williams and Michael Schlesinger. Some information on this is available from http://my.epri.com. It appears to be similar in concept to MAGICC and also has a pattern scaling capability. However, emails to EPRI and the nominated contact, L. Williams, have not been replied to. A reply from M. Schlesinger only confirmed that inquiries should be directed to the former. This model does not appear to have been used as extensively as MAGICC.

JCM, the Java Climate Model, is a web–based implementation of a simple climate model by Ben Matthews. It can be downloaded for local installation and the source code is available. The web site is http://www.astr.ucl.ac.be/users/matthews/jcm/jcm5/. The documentation indicates that the model is based on the Bern model for the carbon–cycle/chemistry, and the Wigley–Raper model is used for temperature and sea level changes. This suggests that JCM is based on the same climate model as MAGICC, but with a different carbon cycle model to versions of MAGICC prior to version 6. This model was not selected since it does not appear to have been widely used and it is coded in Java, which would have necessitated additional research time in gaining familiarity with a new programming environment without benefit to the aims of this research program.

References to other simple climate models also exist in the literature (for example, *Frame et al.*, 2005; *Andrews and Allen*, 2008). There is also a Hadley Met Office simple climate model, HadSCCCM1 (*Allen et al.*, 2009), which is a development of earlier work by *Jones et al.* (2006).

It is possible to find some other simple climate models, but these are generally of limited utility. An example of this type is one by Atul Jain at the University of Illinois. This allows selection of one of the old IPCC IS92 scenarios and displays results for emissions, concentrations and temperature (http://forecast.uchicago.edu/Projects/isam.html). Typically, such models are out–of–date and unsupported, with minimal documentation and limited assurance of their validity for correctly modelling global–mean temperature changes.

1.3.3 The selected model: MAGICC

The outcome of the search for a simple climate model was the choice to use MAGICC (Model for the Assessment of Greenhouse-Gas Induced Climate Change). This particular model has played an important role in the IPCC process, especially the Second and Third Assessment Reports. It is the only simple climate model to have been used consistently throughout the IPCC process, having been developed and maintained over time. Tom Wigley provided the version 5.3 source

[1] AOGCM results were produced for A1B, A2 and B1; the other AOGCM estimates were scaled from MAGICC results

code for use in the early stages of this research program. Subsequently, a new revision by Malte Meinshausen (*Meinshausen et al.*, 2008) was made available.[2]

The next chapter, Chapter 2, provides more details on the evolution of MAGICC, relevant literature and applications. In addition, it addresses the basic scientific principles on which the model is built, its structure and operation. The primary parameters involved in the climate system, their settings, relative importance (parameter sensitivity) and how they can be estimated from historical observations and constrained by constructing indices based on, for example, temperature differences, are examined in greater detail in Chapter 3.

[2]Note that the model code was provided by Malte Meinshausen for the purposes of this project and is subject to a licensing arrangement with him.

Chapter 2

MAGICC

This chapter provides an introduction to the development of MAGICC (Model for the Assessment of Greenhouse–gas Induced Climate Change), with a discussion of the model's primary literature, the history of the model and a review covering some examples of the various ways in which MAGICC has been applied.

The climate model on which MAGICC is built is then discussed in order to explain the overall structure of the model and the significant parameters that occur in the energy–balance equations. Essentially, MAGICC is a perturbed energy–balance model; the climate (temperature) responds as a consequence of changes in the radiative forcing components of the model since 1750 (i.e., prior to the industrial revolution), at which time the climate system is assumed to have been in a state of balance. There are a number of different forcings that have since perturbed this balance over the twentieth–century, both natural and man–made. Anthropogenic forcings are expected to increase the present energy imbalance unless steps are taken to change current trends.

A review of the solar and volcanic forcings used by MAGICC is also included in this chapter. The next chapter then looks in more detail at the climate system parameters and investigates some alternative approaches to estimating these parameters based on observational constraints.

2.1 General Description of MAGICC

MAGICC is a simplified Earth system model that represents the movement of energy through the atmosphere, land, ocean mixed–layer and deep ocean due to changes in greenhouse–gas concentrations and radiative forcing. An overall schematic, Figure 2.1, indicates the way that emissions from selected scenarios are processed though gas–cycle models to arrive at annual changes in atmospheric concentrations. A set of simplified expressions converts these concentrations into radiative forcings, which are summed to estimate the total change in forcing (for details see *IPCC* (2001) Table 6.2 and 6.7, and *IPCC* (1997) Appendix 2, as well as the most recent implementations given in *Meinshausen et al.* (2011a)). This forcing is then applied to the energy–balance equations to determine the resulting annual temperature changes across each of the four model regions, the land and ocean areas for each hemisphere. The user can change the default parameter settings used in these steps.

MAGICC is essentially a coupled gas–cycle/climate model, with two principal components:

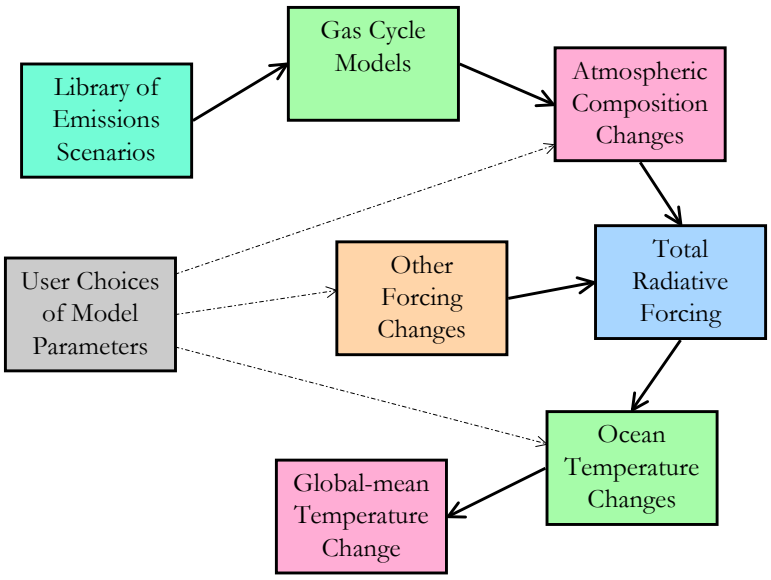

Figure 2.1: Schematic of MAGICC.

- The climate model: an Upwelling–Diffusion (UD) Energy–Balance Model (EBM) divided into four boxes for the Northern Hemisphere (NH) and Southern Hemisphere (SH), land and ocean;
- The carbon cycle model: a terrestrial biosphere model, represented by a simple four–box model of the atmosphere, living plants, detritus and soil, and an impulse response function to represent the oceanic carbon cycle.

A number of parameters are used in MAGICC's representation of the climate system, since it models the main processes as a small number of global–scale parameterised energy–balance equations with a set of gas–cycle models, and parameterised carbon exchange equations for the carbon cycle. These parameters are derived from a combination of observations, model testing and tuning to more complex models. There are essentially three primary tuned parameters whose values are most important for correctly representing the response of the climate system to a perturbation:

1. The equilibrium climate sensitivity, $\Delta T_{2\mathrm{x}}$;
2. The ocean effective vertical diffusivity, K;
3. The equilibrium land ocean warming ratio, R_{lo}.

Other important climate parameters include the:

- Land ocean heat exchange coefficient, κ_{lo};
- Inter-hemispheric heat exchange coefficient, κ_{ns};
- Warming to collapse the thermohaline circulation, T_{moc};

- Ratio between the near–surface air temperature and the ocean's mixed–layer temperature, α;
- Initial upwelling velocity w_0 and the variable upwelling fraction, w_{var}.

A number of others are also required, for example, for gas lifetimes, initial forcing values, factors for aerosol direct and indirect effects, uncertainty range specifications, ice melt factors and exchange coefficients. There are default values provided for all of them. The most recent work of *Meinshausen et al.* (2011a), together with *Meinshausen et al.* (2009), provide reasonably good coverage of the equations and parameters for version 6.3, although there remain a few shortcomings, with some parameters having been neglected, as discussed in Section 3.1.

MAGICC allows for a number of feedback processes, including feedback between the climate and the carbon cycle (*Wigley*, 2008). It does not provide directly for water vapour, lapse rate, surface albedo, cloud and cryosphere feedbacks since these are included through the climate sensitivity parameter. There is also some feedback interaction through atmospheric chemistry, such as the relationship between methane and tropospheric ozone.

2.2 The Development of MAGICC

2.2.1 Background papers

The primary references that provide the scientific basis for MAGICC are introduced in this section along with an outline of the origins and development of the model. There is no single piece of documentation for understanding MAGICC and its scientific foundations; it is necessary to combine information from various sources. Some of the different versions of MAGICC have had manuals that provide background information and explanations of how to run the model (see, for example, *Wigley et al.*, 2000; *Wigley*, 2004; 2008). *Wigley and Raper* (1987) provides the basis for the climate system model and *Wigley* (1993) describes the carbon cycle model, although these have been updated in the latest version of the model. One of the most useful recent references is *Meinshausen et al.* (2011a), which provides a relatively comprehensive coverage of the equations on which MAGICC is based. Many of these equations are reproduced here in Appendix A for accessibility. Further references are required for more specific details, such as the basis for some of the parameter settings, while some details have to be ascertained by reference to the actual Fortran code.

Wigley and Raper (1992) provide a discussion of the then new IPCC emission scenarios IS92a-f and the resultant projections for radiative forcing, global–mean temperature and sea–level changes (this paper relates to the SAR version of MAGICC). The carbon cycle model was explained as being based on a convolution integral representation for the ocean uptake and a box model for the terrestrial uptake. Background references are *Harvey* (1989) and *Wigley* (1991a); the ocean carbon cycle model was based on the ocean general circulation model of *Maier-Reimer and Hasselmann* (1987), and the terrestrial component is detailed in *Wigley* (1993).

The model was initialised with an inverse mode run from 1765 to 1990 to establish emissions consistent with observed concentrations. That led to the problem of the 'missing sink', which was addressed by including a 'fertilisation factor'. This CO_2 fertilisation factor is, to some extent,

a balancing term to achieve consistency between observed historical atmospheric concentrations and estimates for sources of CO_2 (*Enting*, 2011). For the future projections, the model input was based on selecting emissions scenario data for 1990 onward, i.e., the six IS92 scenarios.

Radiative Forcing (RF) was calculated using the equation:

$$\Delta Q = 6.3\ln(C/C_0) \tag{2.1}$$

This formula was based on *Shine et al.* (1990), where ΔQ is the change in radiative forcing, $\mathrm{W\,m^{-2}}$; C is the CO_2 concentration; and C_0 is the initial concentration. Note that this formula was revised in the TAR where the constant 6.3 changed to 5.35 (*IPCC*, 2001).

Methane was approached using a parameterised mass balance model with empirically determined constants (refer *Osborn and Wigley*, 1994; *Prather*, 1996); similarly for nitrous oxide and halocarbons.

Only sulfate aerosols were allowed for at that time, with three effects, a direct effect that reduces incoming solar radiation, and two indirect effects, an increase in cloud reflectivity and a possible increase in cloud lifetimes. These are negative radiative forcings that cool the climate, but with considerable uncertainty as to their magnitude. The direct forcing effect was taken to be proportional to sulfate emissions due to their short lifetime. For this earlier version of MAGICC, the direct effect was partitioned between the Northern Hemisphere (NH) and Southern Hemisphere (SH) at 90% to 10% respectively, while the indirect effect was assumed equal to 20% of the direct effect. The conclusions of the *Wigley and Raper* (1992) paper noted the importance of aerosols and the need to reduce uncertainty in their treatment.

Temperature changes were calculated from the upwelling–diffusion energy–balance climate model of *Wigley and Raper* (1987), which is discussed later in this section. Important parameters for this version of the model are noted as being:

- Climate sensitivity (the most important), with a range of 1.5–4.5°C and a best guess value 2.5°C from IPCC First Assessment Report (FAR, *IPCC*, 1990). The conclusion reinforces the significance of this value for this type of model;
- Mixed–layer depth h (which was fixed inside the model at 90m);
- Oceanic vertical diffusivity, K = 1 $\mathrm{cm^2\ s^{-1}}$;
- Upwelling rate, w = 4 m $\mathrm{yr^{-1}}$ (this was treated as a constant although revised in later versions to have a variable component);
- Temperature change ratio of high–latitude sinking water to global mean, β = 0.2.

Raper et al. (1996) updated the model from that described by *Wigley and Raper* (1992), with the inclusion of stabilisation levels for CO_2 and a discussion of warming commitment. They also considered observed changes in sea–level and global–mean temperature. They used an upwelling–diffusion, energy–balance climate model and provided references to earlier box models. Modifications made to the model since the 1992 version were:

- Land/ocean contrast and evidence for different land/ocean climate sensitivities, referring to *Raper and Cubasch* (1996) and *Murphy* (1995), addressed by using an additional parameter

R_{lo}, the ratio of the equilibrium temperature changes over land versus ocean, with R_{lo} set to 1.3;

- The need for a variable upwelling rate to allow for a reduction in the thermohaline circulation as warming increases.

This older version of MAGICC was concerned with anthropogenic forcings and did not take into account any potential changes to natural forcings. As such, it could not attempt to reproduce the historical record unless volcanoes and solar insolation changes were allowed for.

An older paper, *Wigley and Raper* (1987), provides additional information on the origins of MAGICC. The model used was described as an advective upwelling balanced by high–latitude (polar) down–welling in an upwelling–diffusion model, as compared to a pure diffusion model. It was constucted for the purposes of investigating ocean expansion in response to increased concentration of greenhouse–gases. Their revised model draws on the pure diffusion model of *Wigley and Schlesinger* (1985), but has differentiated land and ocean in the Northern Hemisphere and Southern Hemisphere, using land ocean and NH SH heat exchange coefficients, similar to the model of *Harvey and Schneider* (1985a). Parameters were provided for the ocean mixing processes (mixed–layer depth, diffusivity and upwelling velocity) and climate sensitivity. Ocean feedback processes were not considered. Oceanic thermal expansion was computed using an expansion coefficient from *Leyendekkers* (1976). Vertical variations in the expansion coefficient were explicitly included in the model, latitudinal variations were based on polar, mid-latitude and tropical zones, with the equilibrium mixed–layer results of *Manabe and Stouffer* (1980).

Harvey and Schneider (1985b;a) discussed the ocean's physical processes that have a substantial influence on transient climate response and their sensitivity to changes in external forcing together with model parameter sensitivity. In Part 1, the authors looked at two model arrangements to explore the sensitivity of transient global average surface temperatures to ocean mixing parameters, a multi–box ocean model and a box–advection–diffusion model. In Part 2, the authors extended the box advective–diffusion model to have land sea and Northern Hemisphere Southern Hemisphere resolution, which is the basic concept for MAGICC. Using their model, Harvey and Schneider investigated seasonal temperature variations as well as the decadal transient response. They also looked at the response to a CO_2 increase and short–term volcanic perturbations.

The paper by *Raper et al.* (2001) is referred to as the basis for the climate model used in the Java Climate Model of Ben Matthews (http://www.astr.ucl.ac.be/users/matthews/jcm/). It described an upwelling–diffusion energy–balance climate model (UD/EBM) of the type used in *Harvey and Schneider* (1985b). It was effectively an update of *Wigley and Raper* (1987) and *Wigley and Raper* (1992), modified by *Raper et al.* (1996), but tuned to AOGCM results from the HadCM2 AOGCM. However, the overall model equations were not supplied and none of these three references does so directly. The *Wigley and Raper* (1992) paper focussed on carbon cycle aspects, and referred to the temperature projections being based on *Wigley and Raper* (1987). The latter in turn referred to *Wigley and Schlesinger* (1985) and *Harvey and Schneider* (1985b) . Examination of the references from these two papers suggests that *Hoffert et al.* (1980) was a primary source for the equations underlying the MAGICC UD/EBM, although the detailed implementation differs.

2.3 Applied MAGICC

This section outlines some examples of the diverse ways MAGICC has been applied to investigate a wide range of climate change issues in various arenas, including science, economics and policy.

2.3.1 Temperature changes and sea–level rise

One of the main research topics that MAGICC was developed to investigate was sea–level rise due to thermal expansion of the oceans and the melting of ice. The early work of *Wigley and Raper* (1987) was directed towards using their ocean model to estimate the contribution of thermal expansion and the melting of small glaciers to past and future sea–level changes due to changes in the global-mean temperature resulting from increases in greenhouse–gas concentrations. In a later paper, *Wigley and Raper* (1992) used the IPCC IS92a–f emissions scenarios to determine future changes in greenhouse–gas concentrations, radiative forcing and hence project changes in the global–mean temperature and sea–level.

Wigley and Raper (1993) was effectively a follow up to the previous paper but, being longer, provides some more useful explanations of the model, its tuning and their approach to the melting of small glaciers and ice sheets. In addition, they discuss expansion commitment, the consequences of oceanic thermal inertia and the sensitivity of the ocean model parameters. *Wigley* (1995) looked at projections for global–mean temperature and sea–level changes in the context of stabilising greenhouse–gas concentrations using MAGICC. It is interesting that in his conclusion, Wigley stated that the most damaging consequences of anthropogenic climate change may well accrue through changes in sea level. Although stabilising carbon dioxide concentrations can lead to relatively rapid stabilisation of the global–mean temperature, the stabilisation of the sea–level will take many centuries.

Raper et al. (1996) provide a useful study of global sea–level rise. They reviewed the evidence for past sea–level change and the historical temperature record before applying MAGICC to project future temperature and sea–level changes based on the IPCC IS95 emissions scenarios, as well as five carbon dioxide stabilisation scenarios.

Although sea–level rise results remained throughout the development of MAGICC, including version 5.3, sea–level rise in version 6 of MAGICC is no longer functional. Sea–level rise was not considered in this study, which has concentrated on temperature change.

2.3.2 Emulation and intercomparison of AOGCMs

A simple climate model can be used to emulate the results of coupled atmosphere ocean general circulation models (AOGCMs). A number of studies have reported on approaches to emulation and the results achieved. For example, *Raper and Cubasch* (1996) proposed a general methodology for this purpose and applied it to results from the Hamburg model (ECHAM/LSG). By comparing results and tuning parameters in MAGICC, they were able to obtain reasonably similar global–mean temperature change profiles, although there are discrepancies and limitations that the authors discuss.

In a later paper, *Raper et al.* (2001) compare MAGICC and the HadCM2 AOGCM. In their study, the authors tuned the parameters of MAGICC to reproduce the HadCM2 results. The earlier

version of MAGICC (i.e., *Wigley and Raper*, 1987; *Raper et al.*, 1996) was modified to include a parameter to scale the ocean mixed–layer temperature change to a near–surface ocean temperature change. MAGICC was found to be able to fit the anthropogenically forced surface temperature change and thermal expansion results over the period 1860 to 2100. In order to improve the agreement with the ocean temperature profile of HadCM2 the upwelling–diffusion model was modified to include a depth–dependent ocean area and variable vertical diffusivity.

Osborn et al. (2006) used MAGICC in a different way, as a tool to investigate the atypical behaviour of the ECHO–G AOGCM. In an intercomparison of eight climate simulations, the ECHO–G model showed noticeably different temperature trends. The authors investigated the reasons for these differences and demonstrated how MAGICC could be tuned to reproduce the ECHO–G results for the last 1,000 years.

The latest version of MAGICC has a number of configuration files that provide parameter settings that enable it to emulate most of the individual CMIP3 AOGCMs reasonably well. The SRES A1B and B1 scenarios were used in the calibration process. The A2 scenario, which was not used for calibration, was used as a test case for the skill of the emulations (*Meinshausen et al.*, 2011a). RMSE comparison between the CMIP3 ensemble mean temperature change and MAGICC is small, averaging less than 0.2°C, as shown in Figure 2.2. This indicates that MAGICC is able to represent the complex climate processes affecting the climate sensitivity, ocean heat uptake and global temperature response quite well for a range of emission scenarios.

2.3.3 Emissions, stabilisation and climate commitment

One of MAGICC's main roles is the evaluation of emission scenarios and projected global–mean temperature changes. Related to this are stabilisation pathways in which greenhouse–gas concentrations are brought to a fixed level in order to stabilise the Earth's temperature, as well as consideration of the climate changes that will occur as a result of past emissions, irrespective of further emissions. A helpful introduction to the concepts and the underlying mathematical principles is provided by *Wigley* (2000a).

Much of the early work concerning stabilisation scenarios focussed on emissions and concentrations of carbon dioxide. *Meinshausen et al.* (2006) distinguished between the terms 'scenarios'and 'emissions pathways', along with the difference between 'emission scenarios' and 'concentration profiles'. They discussed some approaches to dealing with non–CO_2 gases, and identified four different approaches that have been used. The authors presented another method, referred to as the Equal Quantile Walk (EQW) approach. Based on this technique, an emissions pathway was obtained which was then processed through MAGICC to determine the corresponding global–mean temperature change profile.

Meinshausen et al. (2006) looked at multi–gas emissions pathways in the context of a 2°C global–mean temperature change target. Accepting this as a policy target, the paper then sought to estimate the probability that greenhouse–gas concentration levels were consistent with this temperature. The approach adopted used a Probability Density Function (PDF) for climate sensitivity, based on a set of published climate sensitivity PDFs. Using these PDFs, transient probabilistic temperatures were calculated using MAGICC. Note that other forms of uncertainty were not explicitly modelled, with other key climate system parameters assigned values based on maximum

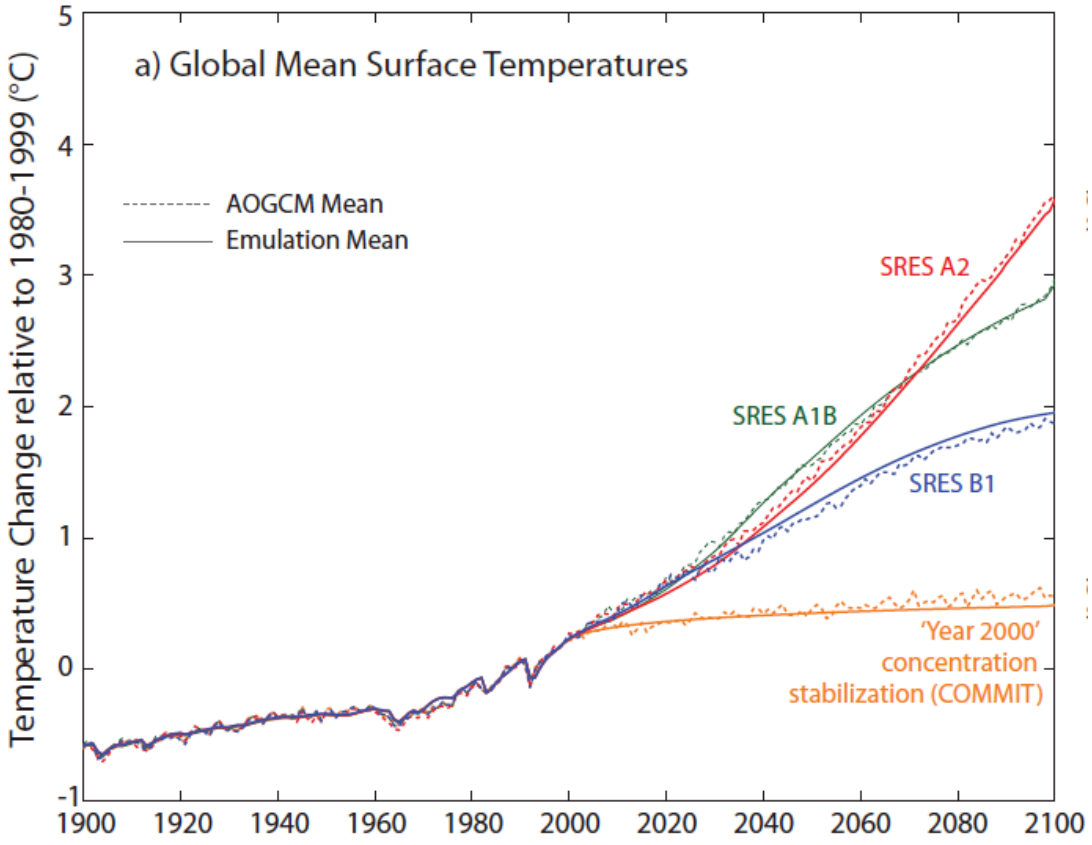

Figure 2.2: Comparison of mean surface temperatures as diagnosed from CMIP3 AOGCMs (dashed lines) and the emulations with MAGICC v6 (solid lines) (from Figure 4, *Meinshausen et al.*, 2011a).

likelihood estimates derived from historical constraints. Using this approach, the probability of exceeding 2°C for selected multi–gas emissions pathways was then determined.

In another study of multi–gas stabilisation pathways, *Wigley et al.* (2007) revised their earlier work (i.e. the 'WRE' profiles from *Wigley et al.*, 1996) and also considered 'overshoot' pathways in which CO_2 concentrations overshoot the stabilisation target before declining. The authors developed some new multi–gas emissions pathways and utilised MAGICC to project the resulting changes in global–mean temperature and sea–level changes. They suggested that an overshoot pathway might occur due to either initially adopting too high a concentration target or as a deliberate strategy. However, it may also result from continued delays in effectively implementing proposed emissions mitigation policies. For example, a 450ppm CO_2-equivalent target has already been exceeded, since current concentrations are higher than this level. In their study, a larger absolute warming and a larger maximum warming rate occur in the overshoot pathway. Hence, there is a greater risk of adverse climate impacts and increased risk for a non–linear climate response. For that investigation, the authors did not apply probabilistic methods.

MAGICC has also been used to investigate the concept of climate commitment. This is the idea that some degree of climate change is inevitable due to human activity up to the present. The aim is to convey a measure of what we have already set in train and point out that further global

warming will result even if we could halt what we are doing now. This topic is addressed in greater detail in Chapter 7.

2.3.4 The Garnaut and Stern Reviews

Some of the climate modelling and impact studies undertaken for *Garnaut* (2008) were based on MAGICC and the related SiMCaP (Simple Model for Climate Policy assessment) program. While the main focus of the Garnaut Review was the economic issues of climate change, the Review used climate modelling to develop projections for greenhouse–gas concentrations for a no–mitigation or business–as–usual scenario, and for two stabilisation scenarios, 450 and 550 ppm CO_2-equivalent concentrations. Temperature projections were then made using MAGICC (refer Figures 4.5 and 4.7 of the Review). Further details of the climate modelling are given in the Garnaut Climate Change Review (2008) Technical Paper 2, including the use of SiMCaP to produce multi-gas emissions pathways for a given set of criteria, which in turn incorporated MAGICC version 4.1 to calculate temperature outcomes. There is also a background technical paper which details the modelling work conducted by CSIRO, who made use of MAGICC as a tool for generating CO_2 concentrations from emissions as the input to an AOGCM (*Harman et al.*, 2008).

The climate modelling information was then used as the basis for assessing climate impacts and some of the economic costs of climate change. This led into developing an argument that it is better to take action now rather than later, that is, accept a small reduction in GDP now rather than take the risk of larger reductions in the future.

The Garnaut Review illustrates the contribution that a simple climate model can make towards significant government policy making. It also demonstrates some of the problems that arise, with the different levels of uncertainty that occur. These range from the underlying science of the climate model and the response of the climate system, through uncertainty over future emissions pathways, to the changes in policy and the timing and extent of effective approaches to mitigation.

The Stern Review (*Stern*, 2007) referred to the papers *Wigley and Raper* (2001), *Meinshausen* (2006) and *Meinshausen* (2005), which relate to MAGICC and SiMCaP. The temperature results and emissions pathways from MAGICC and SiMCaP, along with other sources, were used as a basis for projecting future climate change, impacts and economic costs. The Stern Review was a predecessor to the Garnaut Review; it had a significant impact on government and industry attitudes towards the problem of climate change, notably in the United Kingdom where significant efforts are being directed towards mitigation.

2.4 The Climate System Model

An outline of the structure of MAGICC, its development history and documentation has been provided in the previous sections of this chapter, together with some examples of its application. The underlying scientific principles of the method are reviewed next, including the energy–balance principles and the basic concepts of the upwelling–diffusive ocean model.

As mentioned previously, MAGICC is a simplified Earth System Model (ESM) that tracks the movement of energy through the atmosphere, land, ocean mixed–layer and deep ocean due to

changes in greenhouse–gas concentrations and radiative forcing. Four boxes are used for land and ocean in the Northern and Southern Hemispheres. An upwelling–diffusion model represents the ocean, while the land is assumed to have zero heat storage capacity.

A reduced form of the basic energy–balance equation and the ocean mixing equation is presented here, based on *Wigley and Raper* (1990), in order to emphasise the significance of the climate sensitivity and ocean heat uptake parameters in this type of simple climate model. The equations in current use are given in *Meinshausen et al.* (2011a), with most of the details reproduced here in Appendix A for ease of reference.

The temperature change, ΔT, due to a perturbation in thermal forcing ΔQ, together with atmospheric feedback $\lambda \Delta T$, results in energy transfer from the mixed–layer to the deep ocean of ΔF, where diffusion occurs. The expression for the mixed–layer heating rate is:

$$\phi \rho c h \frac{\Delta T}{dt} + \lambda \Delta T = \Delta Q - \Delta F \tag{2.2}$$

where λ is the climate feedback parameter, ϕ is a factor accounting for land ocean differences in heat capacity, ρ is ocean density, c is the ocean heat capacity and h is the mixed–layer depth.

Note that climate sensitivity is not the same as the climate feedback parameter. In general terms, climate sensitivity is the change in climate that results from a specified forcing of the global climate (*Hansen et al.*, 1993). More specifically, climate sensitivity is defined as the equilibrium global–mean temperature response to a sustained doubling of atmospheric CO_2 (*Senior and Mitchell*, 2000).

The temperature, ΔT_{2x}, which is, by definition, the climate sensitivity, is given by:

$$\Delta T_{2\mathrm{x}} = \Delta Q_{2\mathrm{x}} \lambda^{-1} \tag{2.3}$$

Hence, the climate sensitivity parameter λ^{-1}, is directly proportional to the climate sensitivity. This leads to λ^{-1} being referred to as the climate sensitivity parameter, with the symbol λ, that is the inverse of the usage given in equation 2.3 (see also *Cubasch and Cess*, 1990).

The AR4 estimate for equilibrium climate sensitivity is 2 to 4.5°C, with a best estimate of 3°C (*IPCC*, 2007b). It has been estimated by evaluating the results for a doubling of atmospheric CO_2 concentration in atmosphere general circulation models (AGCMs) coupled to a slab ocean. In AOGCMs, the Transient Climate Response (TCR) is the global average surface air temperature over a 20–year period centred at the time of doubling CO_2 in a 1% per year increase experiment (*Cubasch and Meehl*, 2001; *IPCC*, 2007b). Effective climate sensitivity is evaluated from model output for evolving non–equilibrium conditions (AR4 Annex I glossary; see *IPCC*, 2001; *Murphy*, 1995). For additional discussion on climate sensitivity see, for example, *Wigley and Raper* (1991), *Gregory et al.* (2002), *Andronova et al.* (2007), and *IPCC* (2007b). Climate sensitivity is also discussed further in Chapter 3 in the context of the relative significance of the climate sensitivity parameter and how its likely range of values can be constrained by twentieth–century observations.

The ocean heat uptake and thermohaline circulation are modelled in MAGICC by vertical diffusion and advection (Figure 2.3). Heat, due to a change in radiative forcing, crosses through the top mixed–layer and diffuses down through the deep ocean. A small column of down–welling

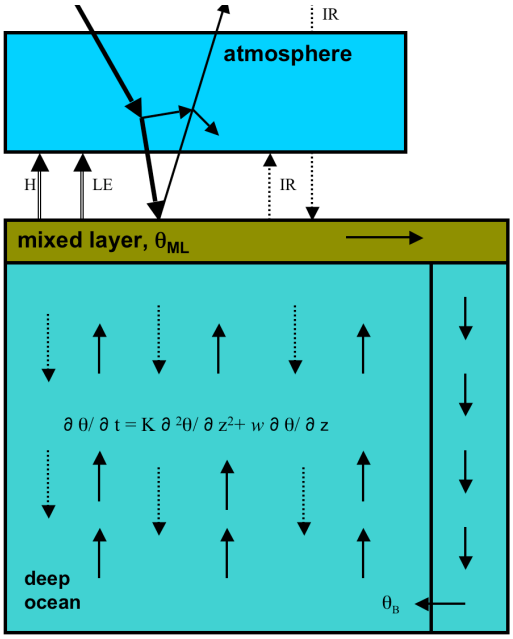

Figure 2.3: Ocean circulation in MAGICC.

cold polar water descends to the ocean floor and then spreads vertically upwards. The ocean temperature θ is described by the mixing equation:

$$\frac{\partial}{\partial t}\Delta\theta = K\frac{\partial^2\Delta\theta}{\partial z^2} - w\frac{\partial}{\partial z}\Delta\theta \qquad \text{For } 0 < z < D\ . \tag{2.4}$$

with boundary conditions:

$$\theta(z = h) = \theta_{ML}$$

$$\theta(z = D) = \theta_B$$

where θ is the deep ocean temperature, θ_{ML} is the mixed–layer temperature, θ_B is the bottom water temperature, h is the mixed–layer depth, z is the depth below the mixed–layer and D is the bottom ocean depth (refer *Hoffert et al.*, 1980; *Harvey and Schneider*, 1985a; *Morantine and Watts*, 1990). The steady state solution is:

$$\theta(z) = \theta_B + (\theta_{ML} - \theta_B)\exp^{-(z-h)w/K} \tag{2.5}$$

The strength of mixing depends on the mixed–layer depth h, diffusivity K and upwelling velocity w. For this solution, $K$and w are assumed constant. Over the course of developing MAGICC this simple upwelling–diffusion model has been modified in order to improve its ocean heat characteristics relative to AOGCMs. For example, AOGCM results show a reduction in the upwelling rate as global warming increases and, consequently, MAGICC has provided alternate ways of representing this relationship (refer *Raper et al.*, 1996; *Wigley and Raper*, 2002).

In its current form, MAGICC version 6.3 continues to use a depth–dependent ocean with entrainment and a variable upwelling rate. It uses a standard depth–dependent ocean area profile

based on HadCM2 (see *Raper et al.*, 2001), with the option for a warming–dependent vertical diffusivity gradient (*Meinshausen et al.*, 2011a).

2.5 Model Forcing Components

This section discusses the natural forcings that have been added to MAGICC since the previous version that enable it to better represent the twentieth–century global–mean surface temperature changes. Some aspects of other forcing components are also addressed, although many of the details are described elsewhere, notably in *Meinshausen et al.* (2011a) (the equations for calculating radiative forcing are reproduced in Appendix B for ease of reference).

2.5.1 Solar forcing

The Sun is the primary source of energy that maintains the warmth of our planet. The energy balance is maintained, on average, by the Earth radiating the same energy back to space, but as long–wave rather than short–wave radiation. A proportion of the long–wave radiation emitted from the land and ocean is absorbed by the mix of atmospheric greenhouse–gases, some of which is then re-radiated back to Earth. This is commonly known, somewhat erroneously, as the greenhouse effect, since the Earth's surface is thereby kept warmer than would otherwise be the case.

The Sun's energy intensity, as it arrives at the top of the Earth's atmosphere, changes on long time scales due to orbital variations and on shorter time scales due to solar activity. The solar forcing contribution to global warming is small, of the order of 10% over the past 100 years (*Lean and Rind*, 2008) and is not expected to have very much impact on future warming, particularly relative to the much greater warming that is projected from current trends in greenhouse–gas emissions (*Feulner and Rahmstorf*, 2010).

Considering the Earth as a simple black body, the total energy received from the Sun per unit time is $\pi R^2 S$, where R is the radius of the Earth and S is the solar radiation. The area of the Earth is $4\pi R^2$, so that the time–averaged energy arriving at the Earth is $S/4$. Hence:

$$\frac{(1-\alpha_{\rm e})S}{4} = \sigma_{\rm B} T_{\rm e}^4 \tag{2.6}$$

where $\alpha_{\rm e}$ is the Earth's albedo, S is the solar constant, $\sigma_{\rm B}$ is the Stefan–Boltzmann constant, and $T_{\rm e}$ is the effective temperature (*McGuffie and Henderson-Sellers*, 2005).

For MAGICC, variations to the solar constant are scaled down by a quarter (the area effect) and by the average surface albedo, which is taken as being 0.3. The incoming solar radiative forcing is therefore multiplied by 1/4 $\times$ (1 - 0.3) = 0.175.

There are recommended solar forcing files for the CMIP5 (Coupled Model Intercomparison Project Phase 5) project website, available from http://cmip-pcmdi.llnl.gov/cmip5/forcing.html. The relevant file for MAGICC is TSI_WLS_ann_1610_2008.txt (data from J. Lean), with the recommendation to use the TSI (Total Solar Irradiance) time series with varying background scaled by 0.9965 to TIM (Total Irradiance Monitor) scale (refer *Kopp and Lean*, 2011, and website for further explanations).

This CMIP5 solar history is the basis for the solar forcing file provided with MAGICC version 6.3, converted into radiative forcing by dividing by 4 (area effect) and multiplying by 0.7 (albedo

effect). In addition, the data is normalised to have an average zero around 1750 (22 years around 1750). Figure 2.4 shows the resulting MAGICC historical solar forcing for the period 1880–2010; the roughly 11–year solar cycle is evident, with a magnitude of approximately 0.2 Wm^{-2} but with a negligible trend over the past 50 years.

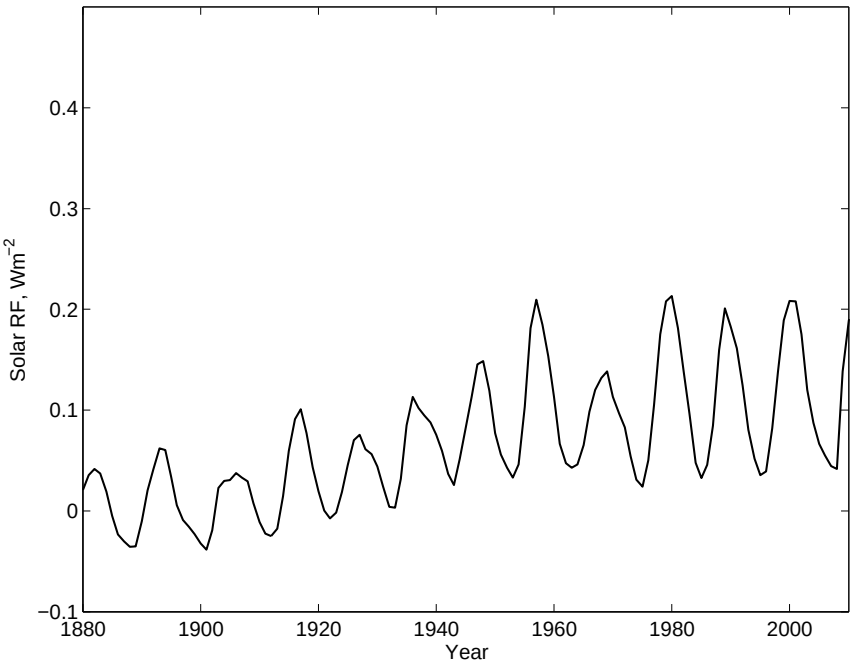

Figure 2.4: MAGICC solar forcing for 1880–2008.

2.5.2 Volcanoes

Historical volcanic forcings were not included in MAGICC as part of the standard or default model configuration prior to version 6.0. Earlier versions required the user to provide an auxiliary input file for this purpose, expressed as annual radiative forcing perturbations. The new version of MAGICC utilises a different internal processing time step, changing from 0.1 to 1/12, i.e. monthly, in order to make use of a monthly volcanic radiative forcing time series. This new input file is based on the NASA GISS stratospheric aerosol optical depth index (refer *Sato et al.*, 1993a, and updates on the NASA GISS website, http://data.giss.nasa.gov/modelforce/strataer/).

Volcanic forcings used in climate models are generally derived from an optical depth index which is a measurement of stratospheric aerosols (*Lacis et al.*, 1992), of which a number have been constructed (e.g., *Sato et al.*, 1993b; *Ammann et al.*, 2003). MAGICC has an historical volcanic forcing file derived from the updated *Sato et al.* (1993b) index. There are some issues concerning this volcanic forcing file:

1. It is based on only one data source — there are others, e.g., *Ammann et al.* (2003) and *Robock and Free* (1996), with different forcing values;

2. The radiative forcing is derived from an optical depth index using a conversion factor. However, there is uncertainty concerning what the correct value for this should be. NASA GISS lists different values for the relation between the optical thickness and the forcings as:

   - Instantaneous forcing Fi ($\mathrm{W\,m^{-2}}$) = -27 τ
   - Adjusted forcing Fa ($\mathrm{W\,m^{-2}}$) = -25 τ
   - SST-fixed forcing Fs ($\mathrm{W\,m^{-2}}$) = -26 τ
   - Effective forcing Fe ($\mathrm{W\,m^{-2}}$) = -23 τ

   Here, τ is the optical depth index. It would appear that the factor to use would be -25, where adjusted forcing allows for the stratospheric temperature to adjust. According to *Meinshausen et al.* (2011a, Supplementary Material Table 1), the conversion factor is -25 $\mathrm{W\,m^{-2}}$ and, by default, the historical volcanic forcing is adjusted to a mean zero. In addition, there is a further scaling factor of 0.7 applied to this forcing specified in the configuration file for each model run. This setting stems from a calibration process (*Meinshausen et al.*, 2009, Table 1) that explains this is the default setting to 'approximately match the net volcanic forcing magnitude applied to the majority of CMIP3 AOGCMs, which include volcanic forcings';

3. The optical thickness for older volcanoes, i.e., for those prior to recent astronomical and satellite measurements, can only be estimates and is therefore subject to a large degree of uncertainty (this will also be true for any alternative data set). *Hansen et al.* (2002) gives a subjective uncertainty estimate for the stratospheric aerosol forcing as 15% for Mt Pinatubo, 20% for El Chichon, 30% for Mt Agung and 50% for large volcanoes prior to 1915.

It is not entirely evident that this forcing should be applied in full within MAGICC. Considering the solar beam, the full amount of the Sun's incoming radiation is reduced by a quarter since

the Earth both presents itself as a disc to this radiation, rather than as a sphere, and is further reduced by the Earth's albedo. Volcanic aerosols reflect incoming solar radiation back out, as well as reflect some outgoing longwave radiation down towards the Earth's surface. The question is whether the volcanic radiative forcing derived from the optical depth index can be regarded analogously with the solar beam or not. In other words, is the volcanic radiative forcing used in full or is only a quarter applied as the perturbation to MAGICCs energy–balance equations?

Previous studies, such as *Wigley et al.* (2005) and *Thompson et al.* (2009), provide useful background material concerning volcanic forcing. *Wigley et al.* (2005) sought to estimate climate sensitivity from the climate system's response to volcanic forcing and in the process discusses some of the issues that arise. For example, there are variations in different forcing estimates from even recent volcanoes; the poor signal–to–noise ratio, that is, the relatively short lived volcanic response can be swamped by natural variability; and the fact that the response may also depend on the nature of the forcing and its spatial distribution (see *Joshi et al.*, 2003). This issue was investigated further by *Hansen et al.* (2005), which showed that the same radiative forcing can lead to different degrees of global–mean temperature change depending on the location of the forcing. As a consequence, the forcing from individual volcanic events needs to be dealt with carefully and the conversion of optical depth to radiative forcing by a single conversion factor may require some further adjustment.

Wigley et al. (2005) used the NCAR PCM AOGCM with a forcing history developed by Ammann to create an ensemble average which reduces noise about the volcanic response signal. Control runs gave an estimate for the amount of interannual variability (0.171°C) superimposed on the volcanically induced temperature signal. They were able to improve the definition of the volcanic signal, with four events being clear (Santa Maria, Agung, El Chichon and Mt Pinatubo), although these were still not regarded as being well defined. They used an upwelling–diffusion energy–balance model, i.e., MAGICC, tuned to emulate the PCM AOGCM. They note the problem of the conversion from optical depth to RF at the top of the troposphere, with various conversion factors having been suggested, ranging from 30 to 21 $\mathrm{W\,m^{-2}}$. *Wigley et al.* (2005) used 20 $\mathrm{W\,m^{-2}}$ to match PCM results, although the AOGCM/MAGICC match is said to be not all that sensitive to the value selected. Their paper demonstrates the use of full volcanic forcing; there is no quarter issue, only that the conversion factor from optical depth to RF is uncertain.

Thompson et al. (2009) also looked at volcanic forcing in their study, similarly deriving forcing estimates from the NASA GISS optical thickness data, but using a conversion factor of 24 $\mathrm{W\,m^{-2}}$. They calculated a global–mean peak forcing of around -3 $\mathrm{W\,m^{-2}}$ just after the eruption of Mount Pinatubo. This is consistent with using 'full' volcanic forcing.

MAGICC temperature results do not include internal natural variability. ENSO is a dominant mode of natural variability — there is simply no mechanism within the model structure that can generate such effects. ENSO and volcanoes impact on the temperature record; the interaction of ENSO with volcanic events can increase or decrease the temperature response that follows from an eruption. Hence, comparing MAGICC temperature results to the observed temperature record over short time scales is, to some extent, not a valid comparison (although the volcanic forcing is set to a mean zero, so that over the 1750–2005 period the overall impact is evened out, and the natural variability tends to oscillate around a climatic mean). In order to test the RMSE fit

to the twentieth–century observations, with either 'full' or 'quarter' volcanic RF, the results were evaluated with the ENSO signal statistically removed from the observations.

Removing the ENSO signal has been done previously with different approaches, for example, *Fawcett* (2007), *Cai and Whetton* (2001), *Wigley* (2000b), *Privalsky and Jensen* (1995), *Jones* (1994). There are some variations in the methods adopted in these studies concerning whether or not data is smoothed, and, if so, the techniques applied, and whether or not the data is detrended. The method applied here involved taking the mean of three observed global–mean surface temperature records, then using the mean of three temperature time series, HadCRUT3, NCDC and GISS. A Southern Oscillation Index (SOI) was used as a proxy for the temperature variability caused by ENSO, based on an index from the Australian Bureau of Meteorology (http://www.bom.gov.au/climate/glossary/soi.shtml). Additional smoothing was not applied to the temperature timeseries since the annual temperatures have already smoothed out the monthly temperature variations. This timeseries was also not detrended, so that it remains as is; the aim is just to remove the ENSO signal for comparison to the MAGICC temperature results.

The temperature effect due to ENSO is preceded by the change in ENSO, so that the annualised SOI is based on a different 12-month period to that of the January to December calendar year. The appropriate lag can be determined by maximising the correlation between the HadCRU temperatures and a 12-month averaged SOI, where the 12 months is offset by a number of months (refer also *Fawcett*, 2007)). Testing the correlation in this way yields a maximum at 5-months over the chosen interval here of 1880-2008 (Fawcett used 1910-2006).

After aligning the SOI to the annual temperatures, both data sets (lagged annual SOI and annual mean temperature anomalies) were adjusted to a common base period of 1880-2008. A linear regression was then applied to scale the SOI and derive an ENSO-adjusted temperature series.

The next step was to test the goodness-of-fit between the ENSO adjusted temperatures and the MAGICC temperatures with full and quarter volcanoes. Figure 2.5 shows the ENSO–adjusted mean observed temperatures compared to MAGICC results for 'full', 'qtr' and 'no' volcanoes. The 'full' volcanic forcing uses the optical depth index τ scaled by -23.5 Wm^{-2} times the volcanic scaling factor 0.7, the 'qtr' volcanic forcing uses the optical depth index τ scaled by -23.5 Wm^{-2} times 0.25 times the volcanic scaling factor 0.7, and, for 'no' volcanic forcing, the volcanic forcing file is removed as an input to the model.[1] The RMSE for these cases are included in Table 2.1. According to this result, for the whole of the period 1880–2008, the 'qtr' volcanoes RF provides the best fit to the ENSO adjusted mean temperatures, although only by a very small margin. However, looking at Figure 2.5, this result is not very convincing. The temperatures around some of the individual events such as Mt Pinatubo and Mt Agung appear to be better represented with 'full' volcanic RF, whilst a large temperature dip after Krakatau is not evident, which suggests that there is a problem with the data for that period, with one or more of the temperature, SOI and optical depth index records being incorrect.

A closer examination of four of the 20th–century's major volcanic eruptions that produced sufficient stratospheric aerosols to have an observed impact on global–mean surface temperatures

[1]The actual conversion factor used with the 'as-supplied' volcanic history file is -23.5 Wm^{-2}, rather than 25 indicated above; the reason for this discrepancy is not known (personal communication with M. Meinshausen, October 2011).

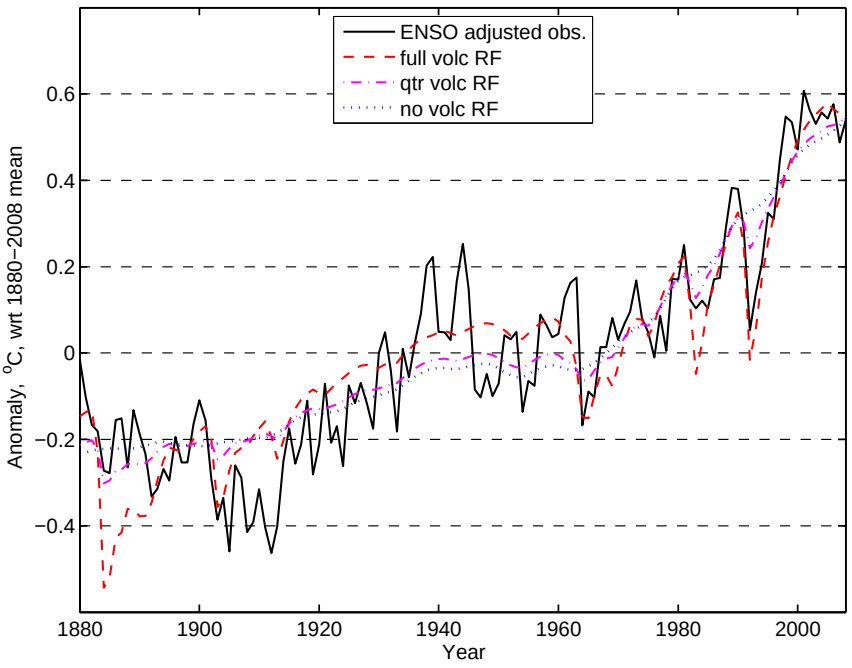

Figure 2.5: ENSO adjusted mean and MAGICC temperatures for 'full', 'qtr' and 'no' volcanoes.

Table 2.1: RMSE between ENSO adjusted time series and MAGICC's temperature results for 1880–2008.

Volcanic RF	RMSE
'full' volcanoes	0.0960
'qtr' volcanoes	0.0859
'no' volcanoes	0.0954

was undertaken (Santa Maria (1902), Mt Agung (1963), El Chichon (1982), and Mt Pinatubo (1991)). The three–year average temperature upto a volcanic event was calculated for each temperature timeseries (event year and two prior years), from which the annual temperature in the following year (event year plus one) was subtracted to measure the temperature change due to that event. The temperature change results for three of the four events found that the modelled temperature change that was closest to the ENSO adjusted observations was best achieved using the full volcanic forcing rather than the quarter–scale volcanic forcing.

The *Sato et al.* (1993b) derived forcings seem to be correct on the basis of this investigation. Accordingly, the volcanic forcing used for subsequent modelling work was the 'as-supplied' historical volcanic forcing file, with the optical depth index τ scaled by -23.5 Wm^{-2} times the volcanic scaling factor 0.7. The spikiness in the 20th–century temperature record is a feature of climate models in general, and not just a problem in MAGICC. The lack of an ENSO signal and other forms of natural variability contribute to the discrepancies between observed temperatures and model results. Removing this ENSO signal from the temperature time series helps clarify the

volcanic response. However, there remains a degree of uncertainty in the historical volcanic forcings, both in the magnitude of the conversion factor to use and uncertainty in the volcanic aerosol optical depths, particularly prior to the era of satellite measurements.

2.5.3 Aerosol forcings

In addition to the volcanic stratospheric aerosols discussed above, there are a variety of other natural and anthropogenic aerosols that occur in the troposphere that impact the Earth's climate system. Collectively, these have a significant effect on the net radiation balance (or imbalance) but have a large degree of uncertainty associated with them (*Bellouin et al.*, 2005; *Yu et al.*, 2006). They can be classified into two groups, direct and indirect, where the direct aerosol effects result from reflecting the incoming solar radiation, and the indirect effects result from other changes that aerosols bring about, such as changes in cloud albedo and cloud lifetime.

Changes to aerosol forcings in MAGICC rely on an estimate for the aerosol forcing values in 2005, where they are specified as parameter values (e.g., for sulfates, nitrates, black carbon, organic carbon and mineral dust). These forcings are then scaled backwards in time to represent their historical values, while the future perturbations are calculated appropriately based on the emission scenario for the related sources. Aerosol radiative forcing is determined by their emissions since they have a very short atmospheric lifetime, unlike greenhouse–gases. In addition, the spatial distribution is based on optical thickness estimates which are provided as historical data files using NASA GISS data (refer *Meinshausen et al.*, 2011a, for full details).

The significance of aerosols is apparent from their size relative to CO_2 forcing. Total aerosol forcing is estimated to be -1.2 W m^{-2} (-2.7 to -0.4) as compared to a CO_2 forcing estimate of 1.66 W m^{-2} in 2005 (1.49 to 1.83W m^{-2}) (*IPCC*, 2007b). Hence, the aerosol forcing settings are an important source of uncertainty for the model results. This problem is discussed further in Section 4.2.3.

2.5.4 Greenhouse gases and other agents

Forcings from greenhouse–gases are calculated from their atmospheric concentrations using a series of relatively simple relationships. These were set out in Appendix 2 of *IPCC* (1997) as the equations used in the SAR (*IPCC*, 1996; *IPCC*, 1997). Some of these have since been updated, in particular the carbon dioxide forcing, which is now taken to be:

$$\Delta Q = 5.35 \ln(C(t)/C_0) \tag{2.7}$$

where $C(t)$ refers to concentrations at time t, while C_0 is the pre-industrial concentration. Further details, the gases covered and all other forcing agents that are provided for in MAGICC (such as stratospheric ozone, tropospheric ozone, land–use albedo changes, and aviation induce water–vapour forcing, contrails and induced cirrus) are all covered in the MAGICC documentation (most recently *Meinshausen et al.*, 2011a); details of the methods for working out non–CO_2 concentrations from emissions and the formulas for calculating radiative forcing are also outlined in Appendices B and C (CO_2 concentrations are covered in the context of the carbon cycle, Chapter 5). For the historical period (generally 1765 to 2005), gas concentrations and other forcings are

provided in a series of history files; thereafter MAGICC determines concentrations based on an emissions file.

2.6 Chapter Summary

This chapter has provided background for the simple climate model selected for this research project. An outline of the model, MAGICC, has been presented, covering its historical origins and evolution along with some examples of how the model has been applied to a range of scientific and policy problems. The basic upwelling–diffusion energy–balance principles on which the model is based have also been presented. It uses a series of simplified, semi–empirical equations to track changes in the Earth's energy balance due to changes in atmospheric greenhouse–gas concentrations. These expressions necessitate the use of a number of parameters whose values have to be estimated for the model to work. The next chapter identifies and describes the parameters involved in the climate system, and investigates some approaches to re-evaluating the previously standard or default model settings using historical observations to assist in estimating their values. This work is continued in Chapter 4. The carbon cycle parameters are then addressed in Chapter 5.

Chapter 3

Constraining the Climate System Parameters

Some new methods of constraining the settings for MAGICC's climate system parameters using historical observations are investigated in this chapter. The climate system parameters are firstly identified and then the significance of each of these parameters in relation to the global–mean temperature results is assessed by individually varying each parameter in turn and examining the impact this has on the global–mean temperature results. This work confirms the importance of the climate sensitivity and ocean vertical diffusivity parameters, which is consistent with previous studies (for example *Wigley and Raper*, 1993; 2001). However, the temperature results are also sensitive to some other parameters that have been largely neglected in the literature concerning MAGICC. In particular, the ratio of land to ocean warming R_{lo} and the ratio of sea–surface to mixed–layer temperature α, are parameters that have not received much discussion, yet the modelled surface temperatures are sensitive to these settings. Identifying which parameters most affect the model's results provides a basis for prioritising which parameters to constrain.

Methods of constraining the parameter values using historical observations are then investigated. Previous approaches, such as *Meinshausen et al.* (2009), have relied on observed surface temperatures and ocean heat content. However, these observations are highly correlated (at least for ocean heat content down to 700m), which leads to problems in dealing with the interaction of the parameters, cross–correlations and weighting of constraints. This research examines an alternative approach that seeks to isolate some of the key model parameters using land−ocean and hemispheric temperature differences as potentially independent pieces of information, a method that does not appear to have been previously applied to a simple climate model, although used in climate change detection studies. For example, the work of *Karoly and Braganza* (2001) reported that these temperature differences are independent of the global–mean temperature for natural unforced climate variations. Weak correlations between these temperature differences and the global–mean surface temperature are demonstrated here. This then suggests that these temperature differences could be used as additional independent information to help set some of the model parameters. Testing of the land−ocean temperature difference finds that this provides a means of setting the land/ocean warming ratio R_{lo} and the land to ocean heat exchange coefficient κ_{lo}. The Northern−Southern Hemisphere temperature difference was expected to help set the North−South heat exchange coefficient κ_{ns} but was found not to be that useful in practice.

Ocean temperature and heat content changes are also carefully examined as further pieces of information that can be used to help constrain the ocean parameters. Methods of constraining some of these parameters have been investigated using differences and ratios of heat between ocean layers. A ratio of sea–surface temperatures to ocean heat content was found to have only a weak correlation with the sea–surface temperatures. Taking this ratio as a (largely) independent piece of information allows it to be used as an alternative constraint for setting the vertical diffusivity parameter K. The observed ocean temperature change profile also provides a constraint for estimates of K as well as providing a check on the initial upwelling velocity w_0 and the upwelling variable fraction w_{var}.

This ocean parameter research was also prompted by a mismatch between the observed ocean temperature change profile and model results, both for MAGICC and CMIP3 AOGCMs (Third Coupled Model Intercomparison Project, *Meehl et al.*, 2007a). Ocean temperature observations and model results are compared in the context of this evaluation of MAGICC's ocean settings. This research examines the changes needed to MAGICC's parameters so that an improved fit to the observed ocean temperature change profile is obtained and then considers what implications the revised parameter settings have for future surface temperatures, including the implications that these modified ocean parameters have for the best estimate of the climate sensitivity parameter.

The outcome of testing and applying the constraints, as discussed in this chapter, is a revised set of climate system parameters for MAGICC which differs from the model's previously standard settings. The most significant changes were found to be a reduction in the ocean diffusivity K, a change to the variable ocean upwelling fraction w_{var}, and an increase in the land ocean warming ratio R_{lo}. Decreasing the ocean diffusivity also leads to a reduced value for the climate sensitivity parameter in conjunction with twentieth–century observed global–mean temperatures as a constraint. The combined impact of these revised parameter settings does not change projected global–mean temperatures by very much. However, there are noticeable differences in the land and ocean temperatures, with potentially much more warming over land. This could have significant implications for the future of the planet, with a range of effects such as accelerated melting of glaciers and permafrost.

The model's parameters remain one of the main sources of uncertainty for projecting temperatures; their settings can have a significant impact on the results as demonstrated later in this chapter. The following chapter continues the investigation of the climate system parameters by looking at the relative contribution each parameter makes to the overall uncertainty in the global–mean temperature change results through the impact of fractional changes to the individual parameters. Then, the joint climate system parameter space is studied using a Bayesian Monte Carlo Markov Chain Metropolis–Hastings algorithm. Chapter 5 then moves to examine another important component of the model, the carbon cycle and its associated parameters. The propagation of parameter uncertainty through to the model results due to the combined climate and carbon cycle parameters combined is investigated in Chapter 6.

3.1 Model Parameters

The most recent MAGICC version 6.3 has a comprehensive set of tuned parameters based on CMIP3 AOGCM results for the climate system and C4MIP (Coupled Carbon Cycle Climate Model Intercomparison Project; *Friedlingstein et al.*, 2006) models for the carbon cycle, as developed by *Meinshausen et al.* (2011a). However, tuning to the CMIP3 AOGCMs only means that MAGICC has a capacity to emulate these more complex models; it will only produce similar temperature change projections, which may or may not be reliable. For example, there is some evidence that the CMIP3 models do not reproduce the recently observed ocean temperature profile changes all that well, as discussed in Section 3.4. A different set of ocean parameters is required for MAGICC to achieve a better representation of this observed change. This has implications for both the climate sensitivity parameter and simulated future surface temperatures.

The new version of MAGICC has also had many of its climate system parameters reviewed during a historical constraining exercise, as described by *Meinshausen et al.* (2009). Nevertheless, some issues arise related to these results that concern the cross–correlation of constraints and missing parameters. Although historical surface temperatures for land and ocean, for the Northern and Southern Hemisphere, and trends in ocean heat content, were used to constrain the likely range of possible parameter values, these observations are highly correlated with each other. Some of the important ocean parameters were missed in this analysis, as discussed later in this section, and observations were not used for constraining the carbon cycle.

There were 82 parameters used in the MAGICC parameter space referred to by *Meinshausen et al.* (2009), which can be divided into three groups: nine parameters that are 'crucial for the simple energy–balance upwelling–diffusion–entrainment model in MAGICC 6.0' (Table 3.1); 33 parameters that are connected with the different gas–cycle models and estimates of forcing values in 2005 for different forcing components; and forty scaling factors for apportioning forcing agents across the four regions of the model (ten sets of four).

Note that:

- The carbon cycle parameters are not included in this parameter space;
- The parameter μ is used for asymmetric land ocean heat exchange, but its standard value is one, i.e., it has no effect. It is a new parameter introduced in version 6 for fine tuning MAGICC to emulate AOGCMs and does not seem to be 'crucial', or even particularly important, to the model;
- Two of the parameters, the feedback sensitivity factor ξ and the ocean warming gradient Γ, are also new in version 6, and are not essential to the model;
- There are no sea–level rise parameters included in the calibration; this is not currently a working feature of MAGICC version 6, although it was in previous versions.

However, some important parameters are missing from the 82 member parameter space: the ratio of surface temperature to mixed–layer temperature α; the mixed–layer depth h; the initial upwelling velocity w_0; and the variable upwelling velocity fraction w_{var}. The significance of these will be made clearer in the following sections of this chapter.

Table 3.1: MAGICC's nine 'crucial' parameters (adapted from *Meinshausen et al.*, 2009, Table S1).

No.	Parameter	Description
1	$\Delta T_{2\mathrm{x}}$	Climate sensitivity
2	K	Ocean vertical diffusivity
3	μ	Amplification factor for ocean to land heat transport
4	ξ	Dependence of feedback factors on forcing
5	κ_{lo}	Heat exchange coefficient land ocean
6	κ_{ns}	Heat exchange coefficient north south
7	R_{lo}	Ratio land ocean warming
8	T_{moc}	Upwelling temperature threshold
9	Γ $(dK_z top/dT)$	Dependence of vertical diffusivity on ocean warming gradient

3.1.1 Climate sensitivity

Climate sensitivity is the single most important parameter in MAGICC; results are very sensitive to this setting, as demonstrated in Section 3.2. Its role was introduced in Chapter 2 in the context of the energy–balance equation on which MAGICC is based. However, despite many different studies, the value of this parameter remains uncertain. The IPCC AR4 suggests that the likely range for equilibrium climate sensitivity is 2–4.5°C, based on investigations using observationally based methods and results from AOGCMs (*IPCC*, 2007b). It is most unlikely (5% lower confidence limit in a normal distribution) to be less than 1.5, but the 95% upper confidence limit is not given, since different studies indicate values from 5 to 10°C; there is no formal way to combine the different probability distributions to obtain this upper value. Part of the uncertainty surrounding climate sensitivity arises from differences between models, particularly from different cloud feedbacks (*Forster and Gregory*, 2006). In addition, *Roe and Baker* (2007) propose that the broad shape of probability distributions for climate sensitivity is a feature of the climate system, and that decreases in uncertainties associated with underlying climate processes is unlikely to reduce the spread of this distribution.

A useful discussion on the history of the climate sensitivity concept is provided by *Andronova et al.* (2007). Climate sensitivity is defined relative to fast–feedback processes, such as water vapour amount and changes to clouds or sea ice, and based on adjusted forcing estimates within one year in complex models, that is, including stratospheric temperature adjustment, but not slow–feedback processes, such as a reduction in the area of continental ice sheets, dissolution of carbonate sediments in the ocean and enhanced chemical weathering on land, processes that involve timescales of hundreds to thousands of years (*Harvey et al.*, 1997). However, some of the cloud response can be considered as a change in forcing and not feedback (*Gregory and Webb*, 2008). *Hansen et al.* (2007) argues that the standard fast–feedback climate sensitivity underestimates the equilibrium climate response, which should be larger on long timescales due to changes in land cover and ice sheets.

With AOGCMs, the climate sensitivity is diagnosed from the state of the model; it is a property of the simulated climate system. In contrast, MAGICC requires a specified climate sensitivity

value for the model to work. Furthermore, this value is notionally for equilibrium, which is a somewhat theoretical construct since it can only be reached many years after greenhouse–gas concentrations have stabilised. Until equilibrium is reached, AOGCM results indicate that climate sensitivity changes. This is a consequence of variations in the strength of different feedbacks, which vary with climate forcing (*Colman and McAvaney*, 2009).

The issue of a non–constant climate sensitivity was looked at by *Senior and Mitchell* (2000) using the HadCM2 AOGCM. They found that, for the doubled CO_2 experiment, the climate sensitivity changed from around 2.7°C after 70 years (doubled CO_2) to 3.8°C after another 830 years. They concluded that using a fixed climate sensitivity in a simple climate model may lead to error. If the climate sensitivity chosen is the equilibrium value it will overestimate the warming in the early period, but, if an effective climate sensitivity is selected it will underestimate the long–term equilibrium warming. *Raper et al.* (2001) noted this problem in tuning MAGICC to the HadCM2 model, and pointed out that the change in effective climate sensitivity resembles that of the global–mean temperature.

Boer et al. (2005) suggested that, with the NCAR model and their experimental conditions, climate sensitivity increases linearly with temperature, that is, climate sensitivity is state–dependent (not time–dependent). However, *Williams et al.* (2008) proposed that the centennial scale variation in climate sensitivity is a product of using forcings that only allow for instantaneous effects and stratospheric adjustment. They argued that, if forcings are adjusted on shorter time scales there is then little long–term change to effective climate sensitivity.

On the other hand, from the calibration of MAGICC against the CMIP3 AOGCMs, *Meinshausen et al.* (2011a) stated that many of these models have variable effective climate sensitivities. In order to improve the emulation of models, a state–dependent climate sensitivity was investigated and two new features introduced into MAGICC version 6 to allow the effective climate sensitivity to increase. One modifies the land ocean heat exchange using an additional parameter that varies the standard land ocean heat exchange coefficient to provide for an asymmetric heat exchange. The second feature models a forcing dependency on the sensitivity, so that the land and ocean feedback parameters are scaled in proportion to the change in forcing, using a sensitivity factor as the parameter for this relationship (refer appendices A4.2 and A4.3 in *Meinshausen et al.*, 2011a, for full details).

This discussion then raises an issue concerning the interpretation of the climate sensitivity parameter in MAGICC; in selecting a value for this parameter, a choice has to be made as to whether it is the long–term equilibrium value or a value for the effective climate sensitivity. In addition, any value derived from fitting to historical observations, as per the later work in this chapter and again in Chapters 4 and 6, is an estimate for an observed climate sensitivity, which may well be less than a future effective climate sensitivity or equilibrium climate sensitivity.

3.1.2 Land ocean warming ratio

The land ocean warming ratio R_{lo} is another important parameter in MAGICC, where it is used to separate the climate sensitivity parameter into land and ocean feedback terms. It is the ratio of annual–mean temperature change averaged over land to that averaged over ocean at equilibrium in response to a change in forcing ΔQ. Since the ocean heat uptake is zero when the Earth's radiative

energy balance is zero, the global energy balance equation, Equation 2.2, can be arranged into land and ocean components:

$$\Delta Q = \lambda \Delta T = f_{\mathrm{l}} \lambda_{\mathrm{l}} \Delta T_{\mathrm{l}} + f_{\mathrm{o}} \lambda_{\mathrm{o}} \Delta T_{\mathrm{o}} \tag{3.1}$$

where ΔQ, λ and ΔT are the global–mean forcing, climate feedback and global–mean temperature change respectively. The right–hand terms use the land and ocean area fractions, f_{l} and f_{o}, the separate land and ocean feedbacks, λ_{l} and λ_{o}, together with the matching mean temperature changes for the land ΔT_{l} and for the ocean ΔT_{o}. λ_{l} and λ_{o} are calculated from a set of non-linear equations for a given land ocean warming ratio R_{lo} (= $\Delta T_{\mathrm{l}}/\Delta T_{\mathrm{o}}$) (refer Appendix A.2 and *Meinshausen et al.*, 2011a, for details).

The standard model setting for R_{lo} is 1.3, which was assessed from long–term AOGCM results for equilibrium conditions. The equilibrium R_{lo} value depends on the difference in evaporation and other surface properties of land and ocean, whereas the transient R_{lo} also depends on the different heat capacities of land and ocean. *Lambert et al.* (2011) confirmed that this ratio is a robust feature of both observed and modelled climate change and found that the coupling between land and ocean surface temperature change is largely due to heat transport between the land and ocean surfaces. This value is re-assessed in Section 3.3.2 in the context of applying the land−ocean temperature difference as an observational constraint, and again in the Monte Carlo Metropolis–Hastings investigations (Sections 4.3 and 6.2).

3.1.3 Surface to ocean temperature ratio

A ratio of ocean near–surface to ocean mixed–layer temperature change α is used within MAGICC to calculate the ocean near–surface air temperature changes from the ocean mixed–layer temperature changes (i.e., determines the sea–surface temperature anomaly, SST). MAGICC's only prognostic variables are the hemispheric ocean layer temperature changes: ocean–surface and land–surface temperature changes are then diagnosed from the ocean mixed–layer temperature changes.

This parameter was introduced into version 4.1 as part of a number of changes to improve the model's performance relative to AOGCM global–mean temperature change results. A value of 1.2 was originally used, based on HadCM2 experiments (*Raper et al.*, 2001), which changed to 1.25 for the IPCC Third Assessment Report experiments. Model results are sensitive to this setting, yet this parameter has received very little discussion in the MAGICC literature. It does not appear as one of the calibrated parameters used in the comprehensive historical calibration exercise by *Meinshausen et al.* (2009) or in the CMIP3 work by *Meinshausen et al.* (2011a).

This ratio appears to be a genuine feature of the climate system, and not just a 'fudge factor' required to improve the model's performance. *Raper et al.* (2001) suggests that there is a physical basis for α: as sea–ice cover is reduced the air temperature will warm more as the cold ice temperature felt by the atmosphere is replaced by warmer surface water temperatures. This difference was previously noted in *Raper and Cubasch* (1996). However, the suggestion that this is a constant ratio for this reason is something of a puzzle. If the rate of warming due to greenhouse–gases was slower or very much faster, the sea–ice melt rate would be different, and hence this ratio would change. Further, if all the sea–ice melted this ratio would presumably no longer apply. It might

be useful to check if α is a stable feature in AOGCMs, particularly for future temperatures. This could be checked by examining the CMIP3 (or forthcoming CMIP5) projections. This has been left for other researchers to investigate further.

The SST to ocean mixed–layer temperature ratio α was first tested by considering 30–year linear trends in the SSTs and MLTs (mixed–layer temperatures); α is then the ratio of the line gradients (this smoothes out the annual variability). Historical annual–mean sea–surface temperatures anomalies from the Hadley Met Office (HadSST2) (1850 to the present) and the National Climatic Data Center (NCDC) (1880 to the present) were used. The MLT was based on *Levitus et al.* (2009) ocean–layer temperature anomalies from the World Ocean Atlas on-line database for 0 to 700m depths, 1955 to 2009, depth–weight averaged over 60m (henceforth L09).

The SSTs and MLTs (mixed layer temperatures) were also tested as a linear fit based on the expression:

$$SST' = a(MLT') + b \tag{3.2}$$

where a is the slope, which is an estimate for α, and b is the approximation error. The results for both methods (trends and linear fits) are given in Table 3.2, with six intervals starting in 1955 and incrementing by five years. The 30–year linear fits produce smaller values for α than the trend lines. The 30–year trends and fits are also quite variable. The HadCRU SSTs yield larger α values than the NCDC SSTs.

For comparison, results for the 55 years 1955–2009 are summarised in Table 3.3. The average of the 55–year trend results is 1.23, close to the MAGICC standard setting of 1.25. A longer trend period is precluded due to the starting year of the ocean temperature observations.

A comparison of SSTs and an equivalent mixed layer temperature derived from the L09 ocean temperature data indicates that there is a linear relationship between the time series. The average of the two values determined from straight line fits to HadCRU and NCDC observed SSTs and the L09 equivalent MLTs is 1.23, which is very close to the standard MAGICC setting of 1.25. Differences between these historical data sets mean that there is some uncertainty as to what the value for the SST to mixed layer temperature ratio is. Alternative ocean temperature data could also be tested.

Table 3.2: Results for trends and linear fits between observed SSTs and MLTs.

		30 year trend		30 year fit linear fit	
start	end	HadCRU	NCDC	HadCRU	NCDC
1955	1984	1.353	1.223	0.982	0.875
1960	1989	1.019	1.009	0.898	0.841
1965	1994	0.867	0.845	0.832	0.796
1970	1999	1.023	0.957	0.954	0.887
1975	2004	1.607	1.375	1.318	1.143
1980	2009	1.629	1.376	1.288	1.111
	mean	1.250	1.131	1.045	0.942
	std dev	0.327	0.226	0.206	0.147

Table 3.3: Summary of α estimates for 55 year interval, 1955–2009.

SST/L09	55–year trend	55–year linear fit
NCDC	1.147	1.062
HadCRU	1.309	1.200
Average	1.228	1.131

3.1.4 Forcing parameter ΔQ_{2x}

There is another parameter included in the CMIP3 configuration files that has not been included in the list of climate parameters for investigation here. This is the parameter ΔQ_{2x}, the amount of forcing that occurs at the time of doubled CO_2 in, for example, a 1% per annum CO_2 growth experiment. This is the forcing corresponding to the climate sensitivity diagnosed from an AOGCM. It is tied to ΔT_{2x}, since the ratio of ΔQ_{2x} over ΔT_{2x} sets the overall climate feedback amount λ. Reference to it is included here for the sake of completeness. It was left at its standard value of 3.71 (5.35 ln 2) W m^{-2} for the purposes of this work .

3.1.5 The ocean parameters

MAGICC uses a series of simplified parameterised equations to determine the response of the model's climate system to a perturbation, as discussed previously in Chapter 2. The ocean parameters in these equations control the rate at which heat is moved downwards into the ocean, which affects the evolution of the mixed–layer temperature and consequently the surface temperature because of the way they are interlinked within the model. Of the ocean parameters listed in Table 3.4, *Raper et al.* (2001) indicates the important settings are the effective ocean vertical diffusivity K, the vertical mixing speed w, land ocean heat transfer coefficient $\kappa_{\rm lo}$, the temperature to collapse thermohaline circulation $T_{\rm moc}$, and the temperature dependence of w. These are all set based on observations and AOGCM results. In addition, there is the depth of the mixed–layer h, and the ratio of polar sink water to mixed–layer temperature β.

There has now been over 40 years of research into estimating the world ocean's vertical diffusivity and advection velocity based on various approaches including theoretical consideration, model studies and physical observations. Theoretical considerations set bounds on K and w: $0.1<K<10$ cm^{2}s^{-1} and $0.3<w<30$ m yr^{-1} (*Craig*, 1969; *Garrett*, 1979). Ocean profiles of measured quantities such as temperature, salinity, dissolved oxygen, total dissolved inorganic carbon, and tracers such as carbon-14 and tritium, have produced various estimates for K, typically between 0.5 and 2.0. *Veronis* (1975) provides a useful summary of early tracer work. *Wigley and Raper* (1987) adopted the range 0.5 to 2.0 cm^{2}s^{-1} for uncertainty in K based on these types of results. The values used for modelling results with the early version of MAGICC, reported in the IPCC First Assessment Report (FAR; *IPCC*, 1990), were for K = 0.62 and 1.27 cm^{2}s^{-1}. A change to K = 2.3 cm^{2}s^{-1} occurred around the time of the IPCC Third Assessment Report (TAR; *IPCC*, 2001) as a result of tuning to CMIP2 models (Second Coupled Model Intercomparison Project; *Meehl et al.*, 2000). The more recent tuning to 19 CMIP3 models (Third Coupled Model Intercomparison Project; *Meehl et al.*, 2007a), as reported in *Meinshausen et al.* (2009), results

Table 3.4: MAGICC's ocean parameters.

Abbreviation	Description	Units
K	ocean vertical diffusivity	$\mathrm{cm^2 s^{-1}}$
κ_{lo}	heat exchange coefficient land ocean	$\mathrm{W\,m^{-2}\,{}^\circ C^{-1}}$
κ_{ns}	heat exchange coefficient north south	$\mathrm{W\,m^{-2}\,{}^\circ C^{-1}}$
T_{moc}	variable upwelling temperature threshold	$^\circ$C
h	mixed–layer depth	m
w	upwelling velocity	$\mathrm{m\,yr^{-1}}$
w_0	initial upwelling velocity	$\mathrm{m\,yr^{-1}}$
w_{var}	variable upwelling velocity fraction	
β	ratio of polar sink water to mixed–layer temperature	

in a span of K values from 0.43 to 2.6 $\mathrm{cm^2 s^{-1}}$, with an average value of 1.30 $\mathrm{cm^2 s^{-1}}$, while the value for the aggregate CMIP3 temperature response is 1.1 $\mathrm{cm^2 s^{-1}}$.

However, it is important to keep in mind that the ocean circulation in MAGICC is only a representation of the real processes. In MAGICC, the ocean is modelled by narrow sinking polewards cool limbs balanced by broadscale uniform upwelling in the rest of the ocean. The upper–ocean vertical temperature gradient is maintained by uniform vertical mixing, scaled by the effective ocean diffusivity parameter K. In the real ocean, the vertical temperature gradient in the upper 1000m is largely maintained by wind–driven ocean subduction of the meridional temperature gradient (*Luyten et al.*, 1983) and interior ocean mixing actually plays little role in setting the vertical scale of this gradient. Consequently, the upwelling–diffusion balance in MAGICC should only be regarded as a proxy for the ocean subduction process.

The temperature dependence of w has been addressed in different ways, based on an initial upwelling velocity w_0 and a variable component. The parameter T_{moc} is closely tied into this relationship, which complicates their calibration. This is discussed further in Section 3.4.1.

Three new parameters were introduced into MAGICC version 6.3, as noted previously: an amplification factor to allow for asymmetric ocean to land heat transport μ; a parameter that allows for a dependence of feedback factors on forcing ξ, which provides for a variable climate sensitivity; and a dependence of the ocean vertical diffusivity on the ocean warming gradient Γ. These have been added as refinements that enable additional tuning options to better emulate AOGCMs. However, the first two are not important in setting MAGICC's ocean temperature profile. The third parameter is discussed further in Section 3.4, which investigates the ocean parameters in the context of improving the fit between the observed and modelled ocean temperature change profile.

Note that there is no direct relationship between the ocean parameters and the carbon uptake, since the latter is modeled by an impulse response function that is not connected to ocean parameters such as K and w. There is some linkage from the temperature change effects that can alter K and w, and the temperature feedback term in the ocean carbon cycle. This is a limitation of this type of model (this was also pointed out by *Urban and Keller*, 2010).

3.2 Parameter Sensitivity

MAGICC's climate system parameters are examined in this section to assess and quantify the relative sensitivity of MAGICC's temperature projections to changes in parameter values as a basis for

subsequent research using historical observations to constrain the model's parameters. Included in this investigation are sub–sections that look at parameter sensitivity for global–mean temperatures, land−ocean and Northern−Southern Hemisphere temperature differences. The relative sensitivity of the parameters helps in prioritising efforts to constrain the parameter values to best estimate the climate system response.

Pulse response testing was used for the sensitivity study in this chapter. A specified radiative forcing pulse was applied to the model and its response determined for different parameter settings. The difference in the peak temperature response and the overall change over time provide a measure of the individual parameter sensitivity. Previous studies have reported on the importance of climate sensitivity, ocean heat uptake parameters, and the land ocean equilibrium–warming ratio (e.g., *Wigley and Raper*, 2001; 2002). The latter is important for obtaining the correct land ocean temperature contrasts, as well as having significant implications for climate change impacts. This study confirms these findings, but also demonstrates the relative sensitivity of the model to some of the other parameters.

3.2.1 Global–mean temperature case

The parameter sensitivity in relation to global–mean temperatures is considered here (parameter sensitivity in relation to the ocean temperature profile is examined in Section 3.4). A 'Standard Run' was established using historical concentrations and radiative forcings up to 1999 followed by constant concentrations and radiative forcing for the period 2000–2100, with standard parameter settings. A 'Perturbed Run' used the 'Standard Run' but with an added radiative forcing pulse of 1.0 W m^{-2} for five years, 2010–2014. Sets of model results were created for each climate model parameter, varying one parameter at a time over a range of values, with all the others left at the standard settings.

The difference between the peak temperature response and the corresponding standard temperature is an indication of the parameter sensitivity. These differences are recorded in Table 3.5 for the lowest and highest parameter settings, sorted by the peak temperature difference, where the peak difference refers to the maximum difference between the 'Perturbed Run' and the 'Standard Run' for each parameter. In addition, the area–under–the–curve for the time integral temperature response for the period 2000 to 2100 was determined (Table 3.6), which provides an alternate sensitivity measure that takes into account the model's adjustment time to the perturbation. The tabled 'Area diff' is the difference between the areas for the lowest and highest parameter settings. It is evident that MAGICC is more responsive to some parameter changes than others, with rapid rises and falls in temperature, while others have longer–term effects. These response differences essentially depend on how each parameter relates to the ocean's thermal inertia.

Selected results for some of the parameters are illustrated in Figures 3.1 to 3.3 for climate sensitivity $\Delta T_{2\mathrm{x}}$, ocean vertical diffusivity K, and the land ocean warming ratio R_{lo}. Table 3.5 and Table 3.6 present the climate parameters in descending order of sensitivity, sorted by the peak temperature difference in Table 3.5, and by the area–under–the–curve in Table 3.6.

It is clear that climate sensitivity $\Delta T_{2\mathrm{x}}$, followed by ocean diffusivity K, are the two most important parameters for MAGICC's global–mean temperature change projections. This is consistent with previous studies and, accordingly, these two are going to take priority when seeking to

constrain MAGICC's parameters using historical observations. However, the next two parameters in Table 3.5, R_{lo} and α, are an unexpected result, in that these parameters are relatively significant but have received little attention in the MAGICC related literature. Over the longer–term, T_{moc}, β, and w_0 become more significant than R_{lo} and α to a short–term perturbation. The ocean mixed–layer depth, h, has only a limited influence on the global–mean temperature change results. Changes in both κ_{lo} and κ_{ns} have little effect on the results.

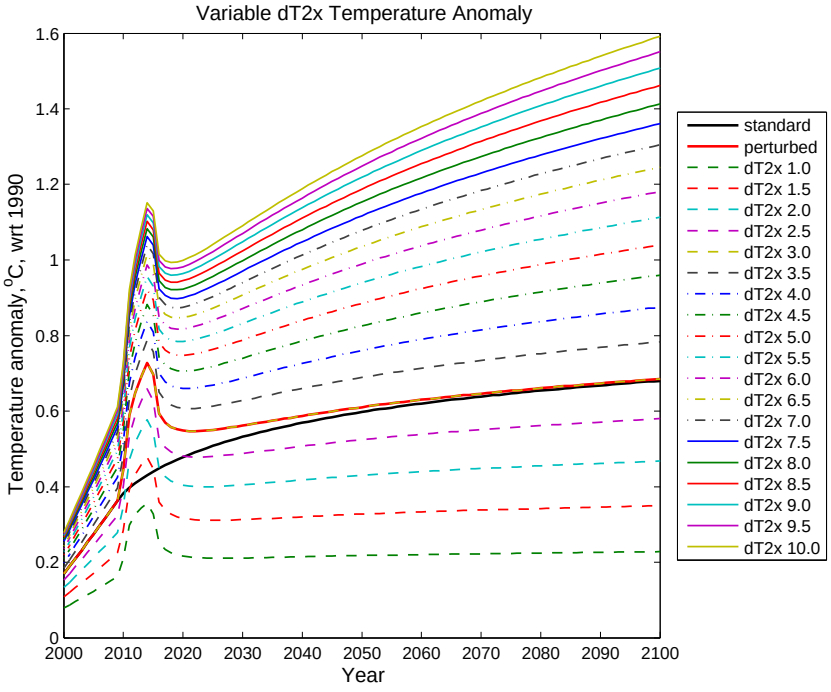

Figure 3.1: Varying the climate sensitivity parameter, $\Delta T_{2\mathrm{x}}$.

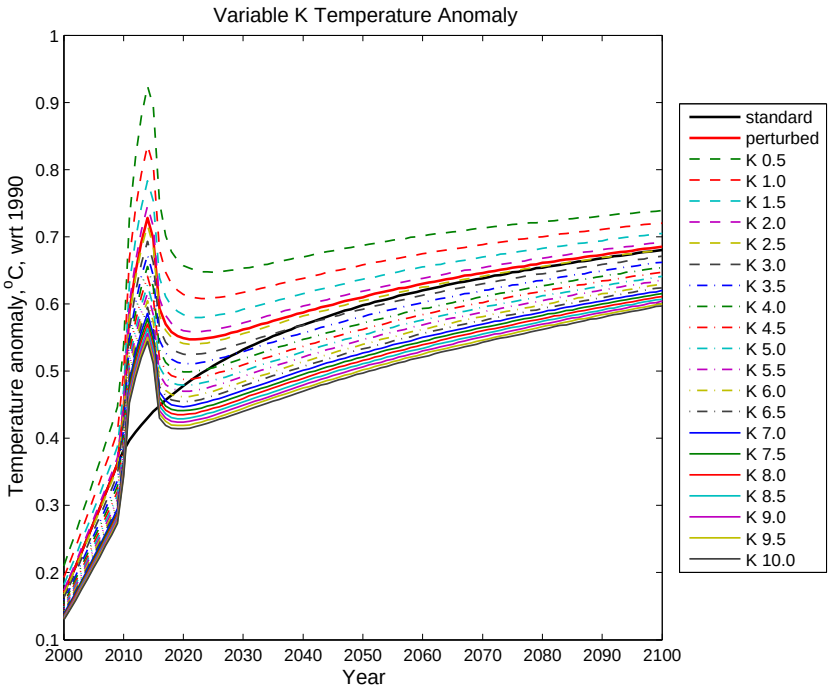

Figure 3.2: Varying the ocean diffusivity parameter, K.

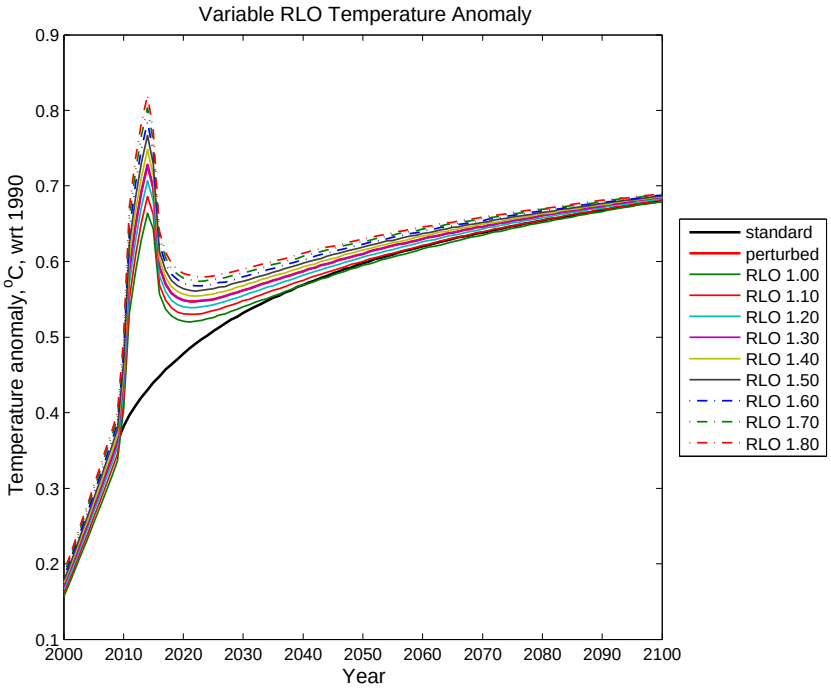

Figure 3.3: Varying the land/ocean warming ratio parameter, R_{lo}.

Table 3.5: Sensitivity results sorted in descending order of peak temperature range for a 1 Wm^{-2} forcing pulse.

Parameter	standard	low	high	Peak temp. diff.	Area diff.
vary $\Delta T_{2\mathrm{x}}$	3.0	1.0	10.0	0.795	99.67
vary K	2.3	0.5	10.0	0.380	18.92
vary R_{lo}	1.3	1.0	1.8	0.156	4.088
vary α	1.25	1.00	1.50	0.113	3.800
vary T_{moc}	8.0	4.0	26.0	0.068	7.600
vary w_0	4.0	3.0	5.0	0.059	5.957
vary h	60.0	30.0	120.0	0.057	1.331
vary β	0.2	0.0	1.0	0.048	7.185
vary κ_{lo}	1.0	0.4	1.2	0.040	0.458
vary κ_{ns}	1.0	0.4	1.2	0.001	0.036

temp. = temperature; diff. = difference.

Table 3.6: Sensitivity results sorted in descending order of area–under–the–curve range for a 1 Wm^{-2} forcing pulse.

Parameter	standard	low	high	Peak temp. diff.	Area diff.
vary $\Delta T_{2\mathrm{x}}$	3.0	1.0	10.0	0.795	99.67
vary K	2.3	0.5	10.0	0.380	18.92
vary T_{moc}	8.0	4.0	26.0	0.068	7.600
vary β	0.2	0.0	1.0	0.048	7.185
vary w_0	4.0	3.0	5.0	0.059	5.957
vary R_{lo}	1.3	1.0	1.8	0.156	4.088
vary α	1.25	1.00	1.50	0.113	3.800
vary h	60.0	30.0	120.0	0.057	1.331
vary κ_{lo}	1.0	0.4	1.2	0.040	0.458
vary κ_{ns}	1.0	0.4	1.2	0.001	0.036

temp. = temperature; diff. = difference.

3.2.2 Land minus Ocean temperatures

The method adopted for the land minus ocean temperature case is similar to that for the global–mean temperature sensitivity testing, except the time series is for the land minus ocean temperature difference. The results are summarised in Table 3.7 and Table 3.8. These tables present the parameters in descending order of sensitivity, sorted by the peak temperature difference in Table 3.7, and by the area–under–the–curve in Table 3.8, where the peak difference again refers to the maximum difference between the 'Perturbed Run' and the 'Standard Run' for each parameter, and similarly for the area–under–the–curve.

Table 3.7: L−O sensitivity results sorted in descending order of peak temperature range for a 1 Wm^{-2} forcing pulse.

Parameter	low	high	Peak temp. diff.	Area diff.
vary $\Delta T_{2\mathrm{x}}$	1.00	10.00	0.608	43.82
vary R_{lo}	1.00	1.80	0.496	39.19
vary κ_{lo}	0.40	1.20	0.293	0.201
vary K	0.50	10.00	0.026	2.117
vary α	1.00	1.50	0.008	0.417
vary h	30.00	120.0	0.006	0.133
vary T_{moc}	4.00	26.00	0.006	0.976
vary w	3.00	5.00	0.005	0.774
vary β	0.00	1.00	0.003	0.824
vary κ_{ns}	0.40	1.20	0.002	0.201
temp. = temperature; diff. = difference.				

Table 3.8: L−O sensitivity results sorted in descending order of area–under–the–curve range for a 1 Wm^{-2} forcing pulse.

Parameter	low	high	Peak temp. diff.	Area diff.
vary $\Delta T_{2\mathrm{x}}$	1.00	10.00	0.608	43.82
vary R_{lo}	1.00	1.80	0.496	39.18
vary K	0.50	10.00	0.026	2.117
vary T_{moc}	4.00	26.00	0.006	0.976
vary β	0.00	1.00	0.003	0.824
vary w	3.00	5.00	0.005	0.774
vary α	1.00	1.50	0.008	0.417
vary κ_{lo}	0.40	1.20	0.293	0.201
vary κ_{ns}	0.40	1.20	0.002	0.201
vary h	30.00	120.0	0.006	0.133
temp. = temperature; diff. = difference.				

These results demonstrate that climate sensitivity remains the parameter with the most impact on both the peak temperature change and the longer–term area–under–the–curve change. However, the significance of the other parameters changes noticeably. Not surprisingly, the R_{lo} parameter is important, now ranking second in both tables. This land ocean warming ratio's impact stems from

its role in determining the land and ocean temperature feedbacks terms, and hence the land and ocean temperatures.

$\kappa_{\rm lo}$ takes on more significance for the perturbed temperature change, but has little effect on the land−ocean temperature difference in the long–term, as indicated by the very small change in the area–under–the–curve. The ocean vertical diffusivity K is now much less important than for the global–mean temperature change case. This is because, in MAGICC, the land temperature is calculated from the ocean temperature, so that while all the other parameters are held fixed, changes to $\kappa_{\rm lo}$ and K have only a small influence on the land−ocean temperature differential.

3.2.3 Northern−Southern Hemisphere difference

The method adopted for the Northern−Southern Hemisphere temperature difference is as before for the global–mean temperature case, except the time series is for the hemispheric temperature difference. The 'as received' MAGICC version 6.3 does not output Northern and Southern Hemisphere ocean–layer temperatures. However, the hemispheric information exists within the program code and so the program was modified to output these values.

The sensitivity results are summarised in Table 3.9 and Table 3.10 for the Northern−Southern Hemisphere temperature differences. These tables present the parameters in descending order of sensitivity, sorted by the peak temperature difference between the 'Perturbed Run' and the 'Standard Run' in Table 3.9, and by the 'area–under–the–curve' in Table 3.10.

Table 3.9: N−S sensitivity results sorted in descending order of peak temperature range for a 1 Wm $^{-2}$ forcing pulse.

Parameter	low	high	Peak temp. diff.	Area diff.
vary $\Delta T_{2\rm x}$	1.00	10.00	0.419	34.78
vary $R_{\rm lo}$	1.00	1.80	0.310	25.22
vary $\kappa_{\rm lo}$	0.40	1.20	0.061	2.852
vary K	0.50	10.00	0.027	0.315
vary $\kappa_{\rm ns}$	0.40	1.20	0.026	2.852
vary α	1.00	1.50	0.005	0.113
vary w	3.00	5.00	0.004	0.473
vary $T_{\rm moc}$	4.00	26.00	0.004	0.543
vary β	0.00	1.00	0.002	0.032
vary h	30.00	120.0	0.001	0.208

temp. = temperature; diff. = difference.

The climate sensitivity parameter has the most impact on both the peak temperature change and the longer–term area–under–the–curve change. The land ocean warming ratio $R_{\rm lo}$ is also important, with the other parameters having very little relative impact. $R_{\rm lo}$ is significant, as it was for the land−ocean temperature difference, because of its close association with $\Delta T_{2\rm x}$. These feedback terms have the effect of multiplying the radiative warming pulse used in these parameter sensitivity tests, whereas the other parameters are more related to the distribution of the temperature change between the four regions and the rate of energy transfer into the deeper ocean. This is also evident from the increased significance of the heat exchange coefficients $\kappa_{\rm lo}$ and $\kappa_{\rm ns}$, which have more impact on the Northern−Southern Hemisphere temperature difference than for

Table 3.10: N−S sensitivity results sorted in descending order of area–under–the–curve range for a 1 Wm^{-2} forcing pulse.

Parameter	low	high	Peak temp. diff.	Area diff.
vary $\Delta T_{2\mathrm{x}}$	1.00	10.00	0.419	34.78
vary R_{lo}	1.00	1.80	0.310	25.22
vary κ_{lo}	0.40	1.20	0.061	2.852
vary κ_{ns}	0.40	1.20	0.026	2.852
vary T_{moc}	4.00	26.00	0.004	0.543
vary w	3.00	5.00	0.004	0.473
vary K	0.50	10.00	0.027	0.315
vary h	30.00	120.0	0.001	0.208
vary α	1.00	1.50	0.005	0.113
vary β	0.00	1.00	0.002	0.032
temp. = temperature; diff. = difference.				

the global–mean temperature.

3.2.4 Sensitivity summary

It is clear that climate sensitivity $\Delta T_{2\mathrm{x}}$ is the most important parameter for MAGICC's global–mean surface temperature projections, followed by the ocean vertical diffusivity K. $\Delta T_{2\mathrm{x}}$ effectively multiplies a perturbation to the energy balance of the climate system. It follows that it is also the most important parameter for the land−ocean and North−South temperature differences. For these temperature differences, the land ocean warming ratio R_{lo} is then the next most significant parameter, since it is connected to the climate sensitivity parameter. This suggests that if R_{lo} can be constrained from historical observations (perhaps also confirmed over the longer term from AOGCM projections), then the L−O and N−S temperature differences may help to constrain some of the other model parameters, depending on the correlations between the different sets of temperatures. This is investigated further in the next section. The model results are much less sensitive to the settings of the remaining parameters, although some of the ocean parameters affect the model's response on longer time scales. The ocean parameters are examined in the context of the ocean's vertical temperature profile in Section 3.4, and then in relation to ocean heat content in Section 3.5.

3.3 Using Observations to Constrain Parameters

3.3.1 Observations as constraints

The previous sections of this chapter have identified the climate system parameters used in MAGICC and investigated one approach to assessing their relative importance for determining global–mean temperature changes, land−ocean temperature differences and Northern−Southern Hemisphere temperature differences. This section investigates how these sensitivity results can assist in estimating values for these key parameters.

Historical temperature observations can be used as a constraint on the possible range of values that any one set of model parameters can adopt. Sources for historical surface temperature used in this study were:

1. HadCRU. The Hadley/Climatic Research Unit temperatures are available as both gridded data and large–scale area means for land, ocean and each hemisphere. Downloads are available from http://www.cru.uea.ac.uk/cru/data/temperature/. The principal reference is *Brohan et al.* (2006);

2. NCDC. The National Climatic Data Center supplies gridded data with monthly and annual global anomalies (http://www.ncdc.noaa.gov/cmb-faq/anomalies.html). A number of references are included on their website, and a recent study of the NCDC approach is provided by *Smith et al.* (2008), which also includes some useful discussion of differences to HadCRU methods;

3. GISS. The NASA Goddard Institute for Space Studies (http://data.giss.nasa.gov/gistemp/), with a range of references included (http://data.giss.nasa.gov/gistemp/references.html). Gridded data sets as well as monthly and annual global and hemispheric temperature anomalies are available. For further discussion refer *Hansen et al.* (2010), which includes a comparison to NCDC and HadCRU analyses.

To illustrate fitting to observations, a plot of 1880 to 2008 global–mean temperatures for the three data sets, to represent the observational uncertainty in estimating the variations of global–mean temperature, is shown in Figure 3.4(a), together with MAGICC temperature changes calculated using different values for the climate sensitivity parameter.

It is not immediately clear from Figure 3.4(a) which value of ΔT_{2x} provides the best fit. Accordingly, a test for goodness–of–fit using Root Mean Square Errors (RMSE) was performed, with the result shown in Figure 3.4(b). This suggests that the climate sensitivity parameter lies in the range of 3 to 6°C, perhaps up to 8 or 10°C. The Hadley and GISS data sets produce similar results, but the NCDC result shows a more defined minimum. However, this is the result for a single parameter only; there are other important parameters that need to be accounted for, such as ocean diffusivity, as discussed in previous sections of this chapter. Further, the model parameters are not necessarily independent. Different combinations of parameters can give equally valid fits to particular sets of observations. For example, *Meinshausen* (2006) demonstrated how MAGICC temperature results for both a low climate sensitivity and a low sulphate aerosol forcing value, or a high climate sensitivity and a high sulphate aerosol forcing, can equally fit the twentieth–century observed global–mean surface temperature record.

Additional information is required to constrain multiple parameters. There are a restricted number of possibilities, since MAGICC is limited by its four regions of hemispheric land and ocean temperatures, as well as ocean–layer temperatures and heat content. Temperature differences are potentially additional sources of information that can be used to constrain the model's parameters. The next two subsections examine the large–scale surface temperature correlations and test temperature differences as a way of constraining some of MAGICC's parameters.

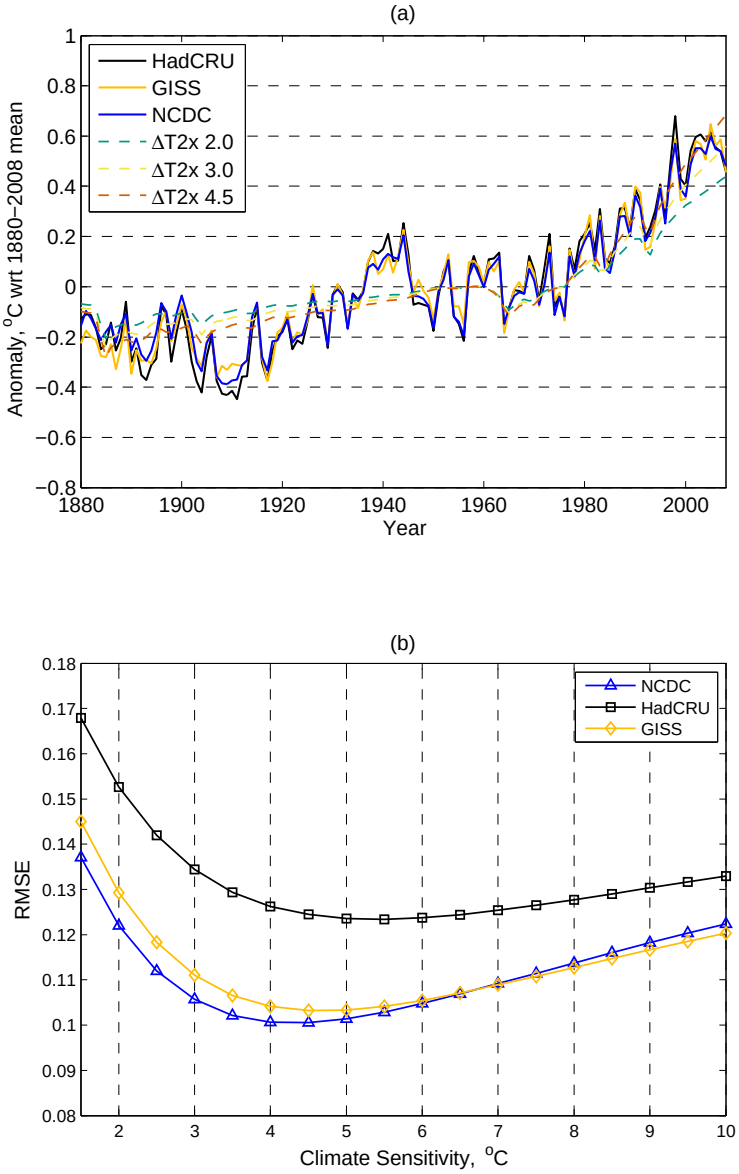

Figure 3.4: (a) Observed 1880–2008 global–mean temperature anomalies compared to MAGICC. Model parameters are the standard settings, with climate sensitivity ΔT_{2x} varied as shown. Natural variations due to solar and volcanic forcings have been included for the MAGICC results. (b) RMSE plot for goodness-of-fit between observations and MAGICC global–mean 20th century temperatures for different ΔT_{2x} settings.

3.3.2 Investigating the L−O constraint

The correlations between land, ocean and land−ocean (L−O) temperature differences and a representative set of historical global–mean temperature anomalies (HadCRUT3) are presented in Table 3.11. The correlations between the global–mean temperature and the separate land and ocean temperatures are very high. However, for the land−ocean difference the correlation coefficient is only about 0.2 for the de–trended data. De-trending removes the forced response, leaving a larger contribution from unforced internal variability.

The land−ocean temperature difference is therefore approximately independent of the global–mean temperature itself, for unforced variations, and so it offers the possibility of being used as an additional observational constraint for determining parameter values. This L−O temperature difference suggests itself as a potential constraint for the land ocean warming ratio R_{lo} and the land ocean heat exchange coefficient κ_{lo} parameters.

Table 3.11: Land−Ocean correlations with HadCRUT3 1880–2008 observations.

correlation	observations	detrended
global to land	0.962	0.877
global to ocean	0.987	0.962
global to L−O	0.523	0.214

The land−ocean temperature difference observations, taking the mean of three historical data sets (HadCRUT3, NCDC and GISS), compared to MAGICC results with different settings for the parameter R_{lo}, are shown in Figure 3.5(a). Varying this parameter over the range 1.0 to 1.8 and testing the goodness–of–fit finds a minimum in the RMSE between the model results and the mean of the three historical sets of observations between 1.5 and 1.6, as shown in Figure 3.5(b). This demonstrates that this land−ocean temperature difference can assist in estimating the value of parameter R_{lo}.

Sutton et al. (2007) determined that this ratio should be around 1.5 for present day non–equilibrium conditions, based on AOGCM results and recent observations for the period 1980–2004. Analysis of the mean temperature anomaly for the last 30 years of observations (1979–2008) from three sets of global–mean temperature anomalies found an observed mean R_{lo} of 1.58.

An alternate way to check this result was also investigated, taking the average of 30–year temperature anomaly time series beginning in 1955 and stepping forward five years at a time for land and ocean, and then R_{lo} as the ratio of these two averages. Each time series (HadCRU, NCDC and GISS) was arranged for matching time intervals for 1880–2009 and adjusted to a common mean period of 1880–2009. The results are presented in Table 3.12. The R_{lo} values calculated in this way exhibit generally higher values and more variability than anticipated. A revised estimate for R_{lo} of 1.6, although considerably greater than the standard (equilibrium) value of 1.3, appears to be a conservative selection.

Although the R_{lo} in MAGICC was intended to be the equilibrium value, this comparison using observations and model results is for transient land and ocean temperatures. Using the equilibrium value will underestimate the land ocean temperature contrast whilst the Earth's energy budget is

Table 3.12: Results for 30-year trends between observed SSTs and land temperatures used for assessing R_{lo}. GISS SSTs courtesy Karl Braganza (personal communication, 2010).

start	end	HadCRU	NCDC	GISS	Mean
1955	1984	1.204	1.316	1.716	1.382
1960	1989	1.721	1.630	1.607	1.652
1965	1994	1.834	2.057	2.000	1.962
1970	1999	1.773	2.135	1.793	1.898
1975	2004	1.519	2.084	1.763	1.774
1980	2009	1.603	2.483	1.849	1.949
	mean	1.608	1.951	1.788	1.769
	std dev	0.229	0.413	0.132	0.224
	variance	0.053	0.170	0.018	0.050

out of balance. The standard equilibrium value for R_{lo} does not match the recently observed land−ocean temperature difference, as seen in Figure 3.5.

The land ocean heat exchange coefficient κ_{lo} was also investigated using these land−ocean temperature difference observations, again comparing the historical data to MAGICC results with different settings for the parameter κ_{lo}, as shown in Figure 3.6(a). Varying this parameter over the range 0 to 6.0 and testing the goodness–of–fit between the model results and the mean of the three historical sets of observations found a minimum at 1.25 $\mathrm{cm^2 s^{-1}}$ for the mean of the three historical temperature sets (Figure 3.6(b)). The standard setting for this parameter is 1.0 $\mathrm{cm^2 s^{-1}}$. Note that the curves flatten out considerably, indicating the relative insensitivity of the MAGICC land−ocean temperature difference to changes in this parameter (to two decimal places the RMSE values are the same between 0.75 and 6.00 $\mathrm{cm^2 s^{-1}}$ for the mean temperature case). The results also indicate some disparities between the NCDC and GISS RMSE values compared to the HadCRUT3 values.

It is important to point out that, although this temperature difference constraint is independent to the global–mean temperatures, these RMSE results are not independent of the other model parameters. These results help to constrain the range of values that the model parameters can take; they do not uniquely determine them.

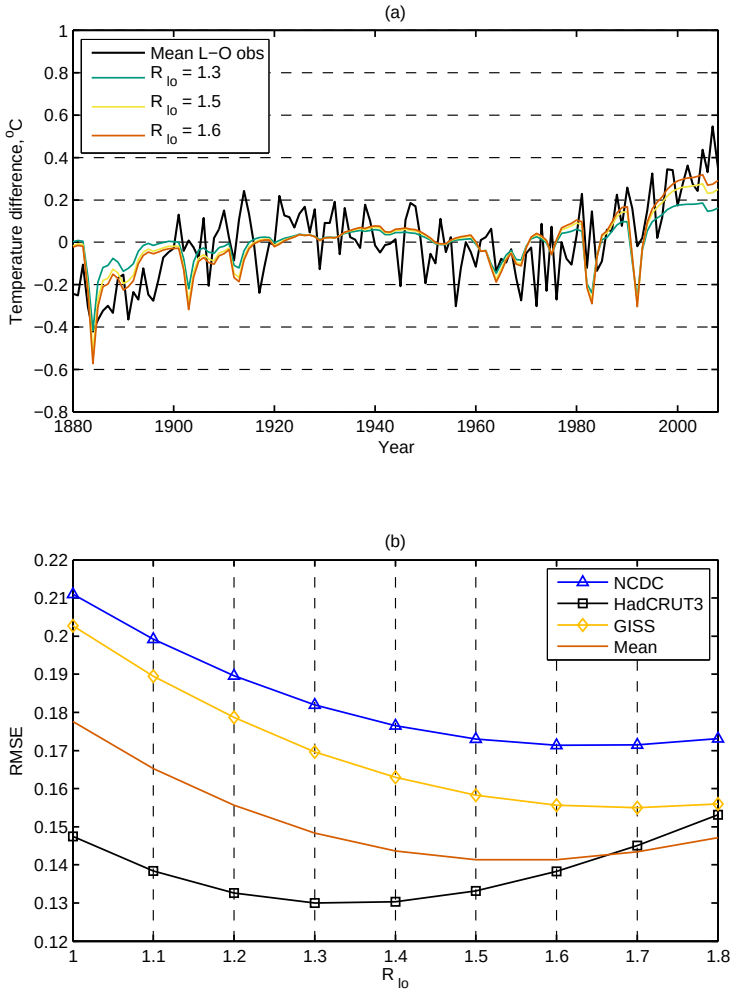

Figure 3.5: (a) The land−ocean temperature difference observations compared to MAGICC results with different settings for the parameter R_{lo}, and (b) corresponding RMSE results.

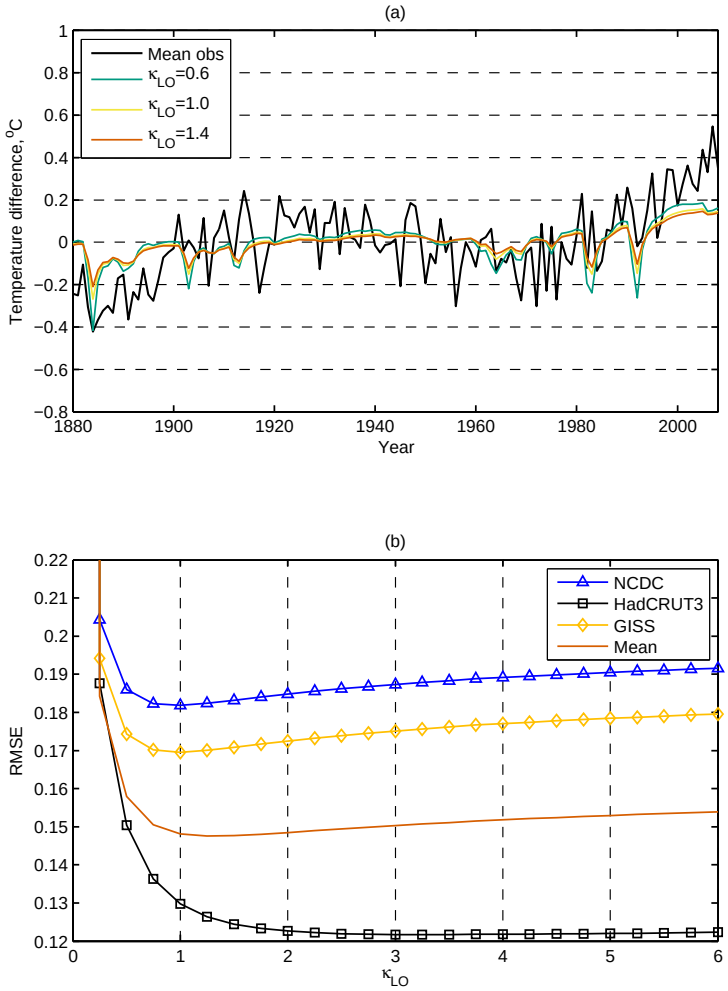

Figure 3.6: (a) The land−ocean temperature difference mean observations compared to MAGICC results with different settings for the parameter κ_{lo}, and (b) corresponding RMSE plot.

3.3.3 Testing the N−S constraint

The Northern Hemisphere (NH), Southern Hemisphere (SH) and NH−SH temperature difference correlations for a representative set of historical global temperature observations (HadCRUT3) are presented in Table 3.13. The correlation between the global–mean temperatures and the NH−SH temperature differences were checked for the 1880 to 2008 historical observations, and for the same time series with the warming trend removed. The correlation coefficient between the global–mean temperature and the separate hemispheric and ocean temperatures is very high. However, for the hemispheric difference the correlation coefficient is less than 0.2 for the de-trended data.

The NH−SH temperature difference is close to being independent of the global–mean temperature itself, and is therefore another possible observational constraint for determining parameter values. This temperature difference suggests itself as a potential constraint for the North South heat exchange coefficient $\kappa_{\rm ns}$ parameter.

The NH−SH temperature difference observations, taking the mean of three historical data sets (HadCRU, NCDC and GISS), compared to MAGICC results with different settings for the parameter $\kappa_{\rm ns}$, are shown in Figure 3.7(a). Varying this parameter over the range 0.2 to 2.0 and testing the goodness-of-fit finds no clear minimum in the RMSE between the model results and the mean of the three historical sets of observations (Figure 3.7(b)). The curves flatten out considerably, indicating the relative insensitivity of the MAGICC North−South Hemispheric temperature difference to changes in this parameter. The standard setting for this parameter is 1.0, which remains a satisfactory estimate of $\kappa_{\rm ns}$ according to this test.

Table 3.13: NH−SH correlations with HadCRUT3 1880–2008 observations.

correlation	observations	detrended
global to NH	0.975	0.925
global to SH	0.969	0.905
global to NH−SH	0.222	0.157

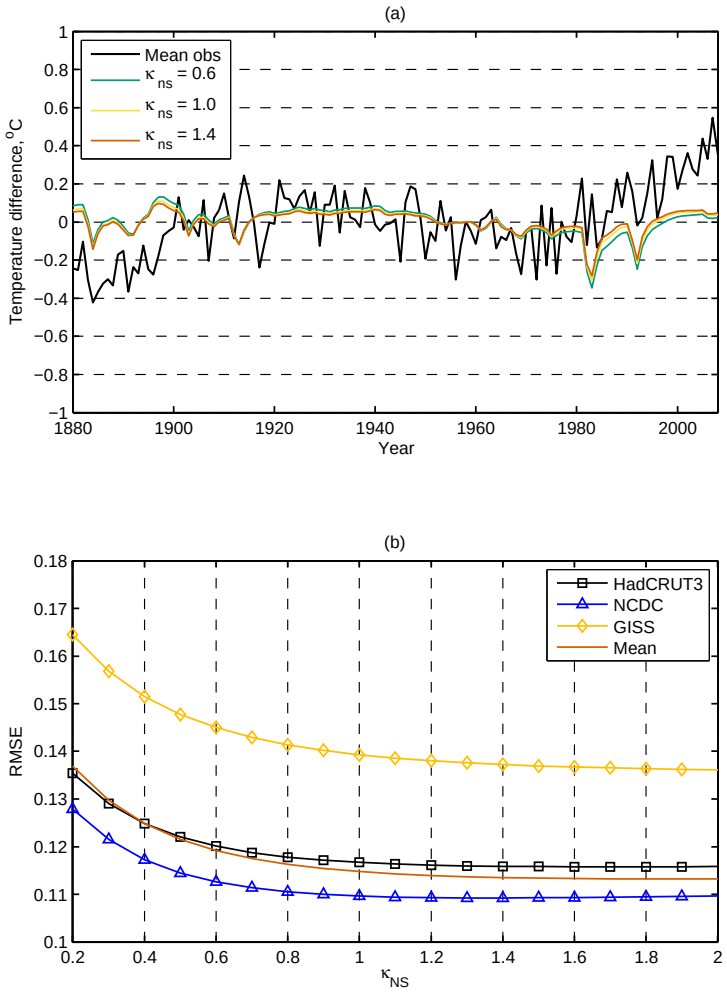

Figure 3.7: (a) The NH−SH temperature difference mean observations compared to MAGICC results with different settings for the parameter $\kappa_{\rm ns}$, and (b) corresponding RMSE results.

3.4 Ocean Temperature Profile Constraint

The investigation of MAGICC's parameters continues in this section with a study of the ocean parameters. The observations used for this work were:

1. The WOA09 (World Ocean Atlas 2009) 1° gridded annual data (*Levitus et al.*, 2009, henceforth L09). These temperatures are provided as annual anomalies from 1955 to 2009 for 16 ocean levels, 0 to 700m, each level containing 360 × 180 temperature points. This annual gridded data set was converted into annual mean temperature anomalies for the world and hemispheric oceans.

2. A 1960–2008 observed ocean temperature change, based on data provided by S. E. Wijffels, personal communication, 2010 (henceforth SW10).

There are other data sets that could be used for the ocean temperature change, which have different treatments for bias corrections and spatial distribution/infilling. However, these concerns are outside the scope of this research work; a decision was made that these two data sets were sufficient (refer to, for example, *Wijffels et al.*, 2008; *Barker et al.*, 2011, for discussion of these issues).

The mixed–layer in MAGICC is 60m (current default value), so the observations were combined to create an equivalent mixed–layer for this comparison. After calculating this, weighting the temperatures in proportion to the depth covered, a new time series was obtained. A plot comparing the LO9 observed and modelled mixed and 100m layers is shown in Figure 3.8. While the model is similar to the observations, there is noticeably more impact from volcanoes in the model results. Otherwise, MAGICC appears to be tracking these observations reasonably well.

The ocean temperature change through the ocean down to 700m for the period 1960–2008 is compared in Figure 3.9, which plots the SW10 ocean temperature change data, the L09 derived data and a series of MAGICC profiles for different values of ocean vertical diffusivity K. The two sets of observations converge below about 400m, but show some difference in the upper layers, especially around about 50m deep. Also noticeable is a temperature change difference of 0.1°C at the zero layer between the two sets of observations. This result was produced with some revised parameter settings, with R_{lo} = 1.6 and κ_{lo} = 2.0 based on Section 3.3.2, and w_{var} changed from 0.7 to 0.2 as a result of the subsequent analysis in Section 3.4.1 (which is the reason for the contrast between the plots in Figures 3.9 and 3.10).

There are time series of SST (sea–surface temperature) anomalies that can provide a useful crosscheck on these two sets of ocean temperature changes. Hadley/CRU SST data are available as annual global–mean temperature anomalies. The temperature change for 1960–2008 works out to be 0.476°C, taking the temperature difference from a linear fit to the time series.

The 1960–2008 temperature change at 0m from SW10 is 0.491°C, while the corresponding temperature change at 0m from the L09 temperatures is 0.391°C. The similarity between the HadCRU SST change and the the SW10 zero layer change suggest that the SW10 ocean temperature change is a robust data set. On the other hand, different SST observations might produce a different result (this was not tested).

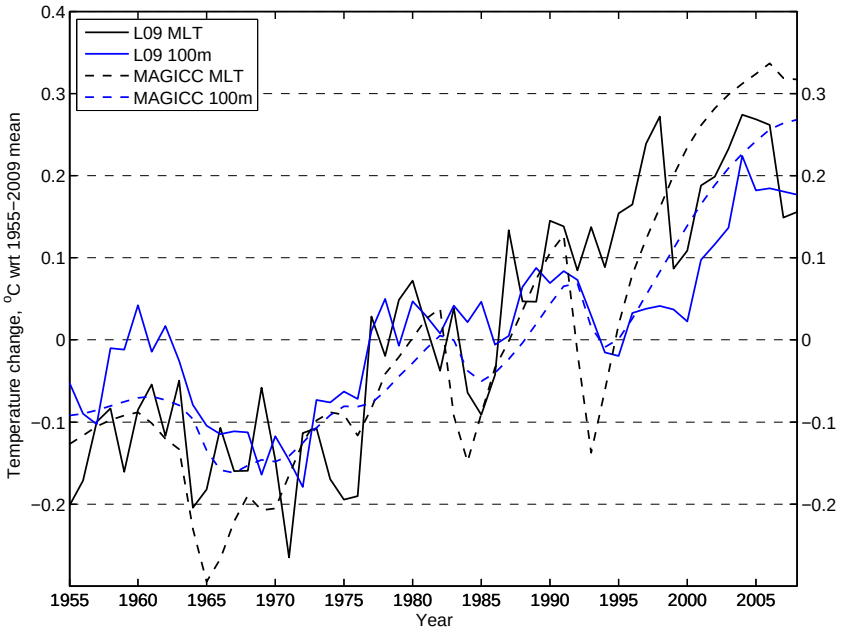

Figure 3.8: L09 ocean temperature anomalies and MAGICC ocean temperature changes compared (MLT is mixed–layer temperature); source: http://www.nodc.noaa.gov/OC5/3M_HEAT_CONTENT/anomaly_data.html.

In comparing the fit between the model results and the observed ocean temperature change, a scheme that weights the layers differently might also be tested in order to create a greater differentiation in the comparisons for different ocean parameter settings, especially for testing the ocean vertical diffusivity K, although this was not addressed here.

3.4.1 Ocean parameter sensitivity

The sensitivity of the ocean parameters in relation to the ocean temperature change profile is considered next before investigating approaches to using the ocean observations to assist in constraining the ocean parameters. For this work, the climate sensitivity ΔT_{2x} was provisionally accepted as 3.0°C. This is the standard MAGICC setting and is in agreement with the AR4 best estimate and likely range of 2–4.5°C (i.e, with greater than 66% probability; most unlikely less than 1.5, but upper 95% not settled, with different studies ranging between 5 and 10°C; *IPCC*, 2007b).

Beginning with the effective ocean vertical diffusivity parameter K, and running the model with the standard parameter settings except for varying the K parameter, the results shown in Figure 3.10 were obtained (R_{lo} = 1.3, κ_{lo} = 1.0 and w_{var} = 0.7; refer Table 3.16) . It is apparent that, for the standard configuration of MAGICC, the model results are relatively insensitive to

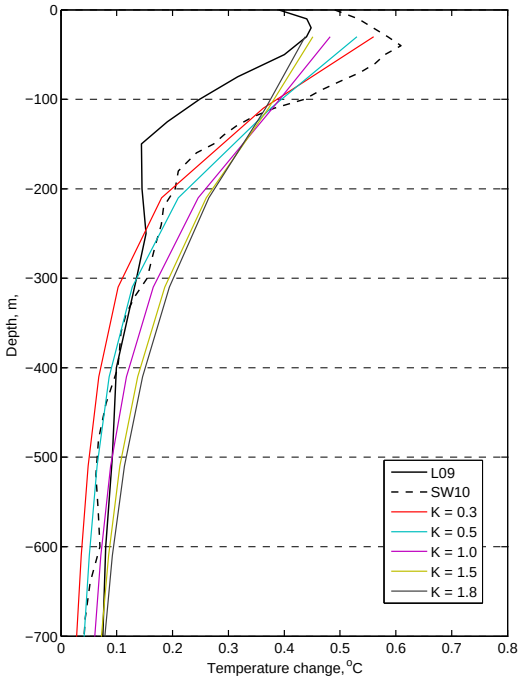

Figure 3.9: Ocean temperature profile changes 1960–2008, comparing L09 (solid black line) and SW10 (dashed black line) observations to MAGICC for selected values of K (with non-standard settings for R_{lo} = 1.6, κ_{lo} = 2.0, w_{var} = 0.2.)

the value of K, which was an unexpected and surprising outcome. This result also reveals a comparatively poor fit between the observed temperature change and the modelled temperature change, with the model sinking too much heat into the deeper ocean.

Varying the initial upwelling rate w_0 also found that the model is relatively insensitive to this setting. These results for K and w are problematic, since they are the two essential parameters that set the shape of MAGICC's ocean temperature change profile; there is clearly a problem here which needs to be resolved.

MAGICC uses an initial ocean temperature profile, which is then modified over time as heat moves through the ocean layers in response to changes in atmospheric radiative forcing. In order to understand how this profile is affected by its parameter settings, the ocean temperature/depth profile equation (from Equation 2.5 in Chapter 2) was plotted, with results for two pairs of parameter settings, included here in Figure 3.11. Note that the boundary conditions for the initial mixed–layer temperature and ocean bottom water temperature are values set within the program code and are not treated as parameters that can be set through the configuration files used for each model run. It is immediately apparent from this figure that varying the two parameters K and w can substantially change the ocean temperature profile. This differs from the sensitivity results just presented and prompts the question of why this occurs since, otherwise, MAGICC's ocean temperature change profile cannot be modified by the primary ocean parameters to more closely resemble the observed ocean temperature change profile. The following discussion found that this inconsistency is connected with the variable proportion of the upwelling velocity w.

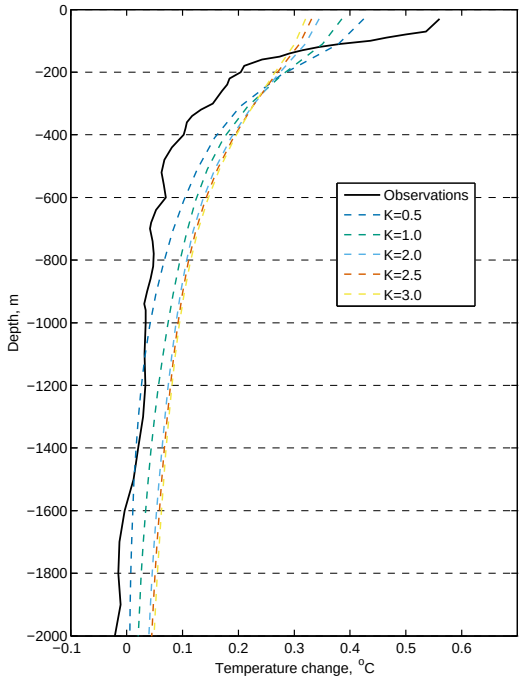

Figure 3.10: The SW10 1960–2008 observed ocean temperature change at depths down to 2,000m (solid black line). Results from MAGICC (dashed lines) are for the standard configuration, except with different values for the ocean vertical diffusivity parameter K, as indicated. The observed ocean temperature change have been converted to an equivalent mixed–layer depth for comparison to the model results. (R_{lo} = 1.3, κ_{lo} = 1.0, w_{var} = 0.7)

The model was tested without the variable upwelling rate (w_{var} set to zero) in order to check that the ocean temperature profile behaves more like the exponential equation, Equation 2.5, initially using a fixed value for w = 8.0 and variable K. The result is shown in Figure 3.12(a), which shows parameter settings that straddle the observations and have a wider range of curves than previously found for varying K (illustrated in Figure 3.10) and w_0.

Testing with K at 1.0 for different values of w_0, again with the w_{var} set to zero, led to the outcome presented in Figure 3.12(b). The result is less sensitive to w_0 values than is the case for K, but points towards higher values providing a better fit. In order to perform a goodness-of-fit test, a spline was fitted to the observations and the RMSE calculated. This suggested a value for w of 7.0 when K is 1.0. This particular combination, derived from fitting the model to the observed ocean temperature change, suggests that a lower ocean vertical diffusivity (1.0 instead of 2.3) and a higher upwelling rate (7.0 rather than 4.0) are required when w_{var} is set to zero. These two results, using revised values for K and w_0 as shown in Figures 3.12(a) and 3.12(b), in which the variable upwelling component w_{var} is set to zero, suggests that MAGICC ocean temperature change profile can be set closer using just K and w_0. However this would lose the variable, temperature–dependent, upwelling component.

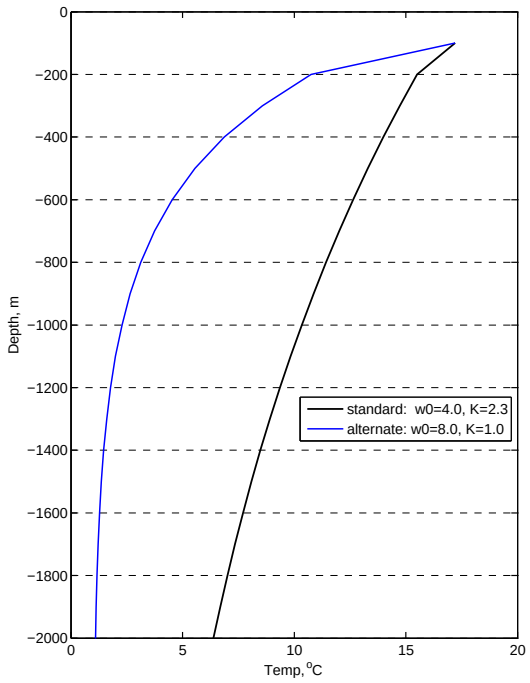

Figure 3.11: Initial ocean temperature profile with two pairs of parameter settings.

The variable upwelling component was introduced into MAGICC to modify the initial upwelling rate w_0 as the ocean warms. Most AOGCM simulations have a reduction in deep water formation with increased warming due to a weakening of the thermohaline circulation (*Raper et al.*, 2001). A variable fraction of the initial upwelling velocity was introduced into MAGICC to represent this feature. In the latest version of MAGICC the formula for the variable upwelling rate is given by:

$$w(t) = w0(1 - w_{\mathrm{var}} T_{\mathrm{g}}/T_{\mathrm{moc}}) \tag{3.3}$$

where w_{var} is a fraction of w_0 (standard value 0.7) and T_{g} is the global temperature anomaly at time t, and T_{moc} is the temperature threshold at which minimum meridional overturning is reached.

In earlier versions of MAGICC, this was represented by applying a variable upwelling rate, $w(t)$, according to the expression;

$$w(t) = w0(1 - \Delta T_{\mathrm{ml}}/T_{\mathrm{moc}}) \tag{3.4}$$

where $w(t) \geq 0$ and T_{moc} is a tuneable parameter representing the magnitude of warming that would result in zero upwelling. w_0 is the initial upwelling rate and ΔT_{ml} is the mixed–layer temperature change. This changeover occurred from the IPCC SAR to the TAR version of MAGICC. *Wigley and Raper* (2002) also explain this division into two parts: this revised method was implemented to better match the ocean heat flux and sea–level rise in AOGCMs. This may be satisfactory if MAGICC is being applied to emulating AOGCMs but, if the aim is to match the model to observations as a basis for making temperature projections, then the current method of using a variable upwelling rate requires a different value for w_{var}.

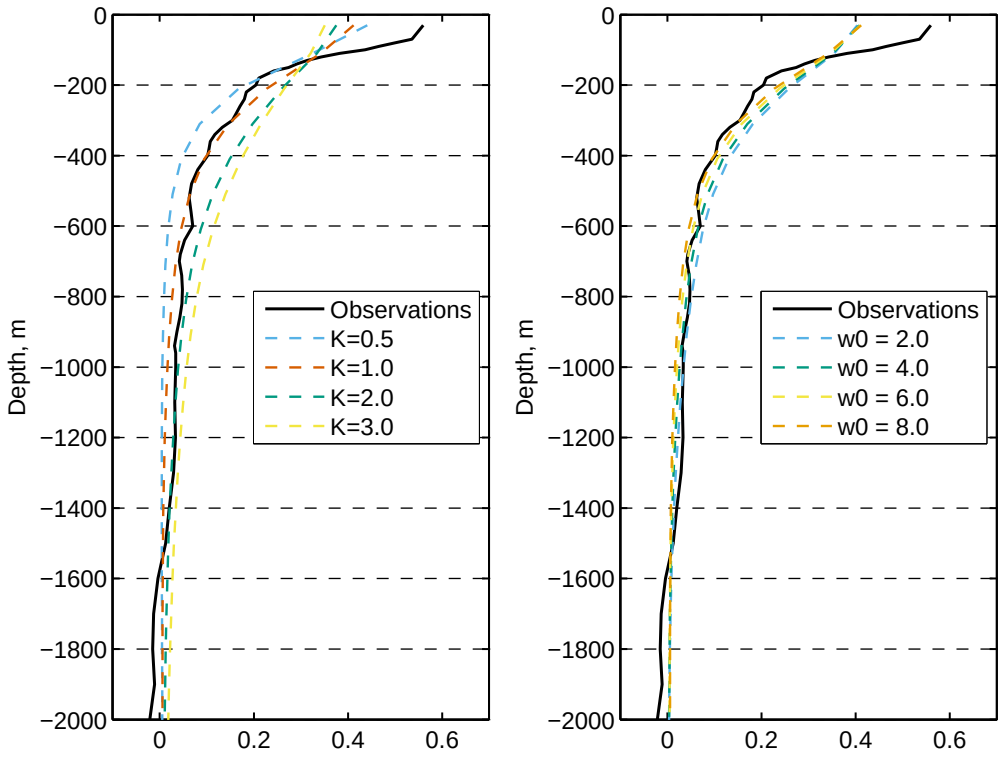

Figure 3.12: Revised model results with (a) fixed upwelling rate, w_0 = 8.0, and variable ocean vertical diffusivity K and, (b) results with K = 1.0 and variable w_0. w_{var} set to zero in both cases (SW10 observations).

The TAR version of MAGICC used equation 3.4. *Raper et al.* (2001) explained that:

> 'In the TAR, the climate model's vertical circulation was divided into a climate–dependent THC component (30%) and a second component that parameterized all heat flux processes other than those captured by the models vertical diffusivity term.'

However, the standard value in version 6.3, with w_{var} = 0.7, appears to be too large. Testing the model if w_{var} is varied showed that a lower value between 0.1–0.3 resulted in an improved fit between the observed and modeled ocean temperature change (refer Figure 3.13).

From this testing process, it was concluded that, for the variable upwelling component of MAGICC version 6.3, a reduced value for the upwelling fraction w_{var} is required, dropping from a standard value of 0.7 to around 0.2 if the model is to achieve a closer fit to the 1960–2008 observed ocean temperature change.

The sensitivity of the other ocean parameters listed in Table 3.4 , that is, Γ, β, T_{moc} and h, were investigated as follows in order to ascertain their role and affect on the ocean vertical temperature change profile.

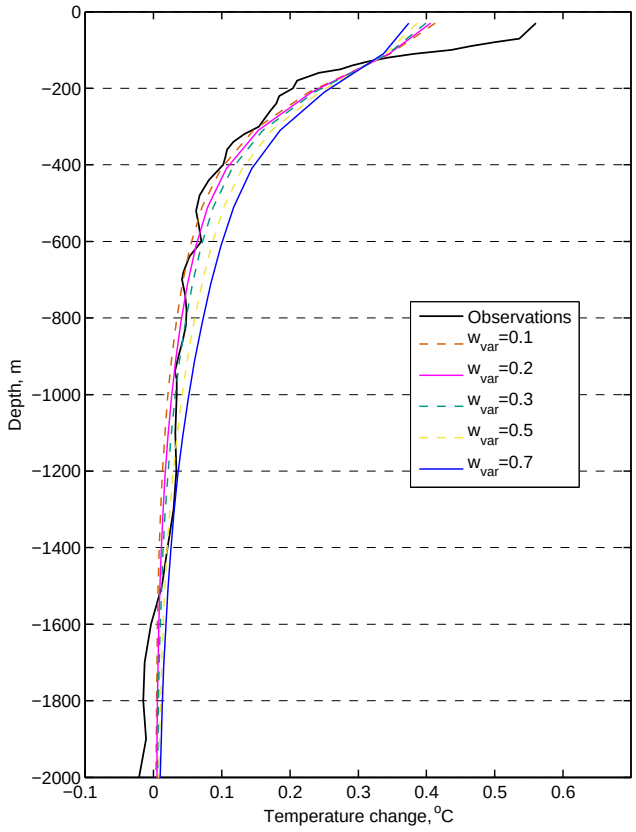

Figure 3.13: 1960-2008 ocean temperature change profiles for different settings of w_{var} with K held at 1.0 and w_0 = 4.0.

Warming-dependent vertical diffusivity gradient, Γ

A new feature in MAGICC version 6 is the introduction of a warming–dependent vertical diffusivity gradient Γ, as explained in *Meinshausen et al.* (2011a). The sensitivity of this parameter setting was examined in the context of the ocean's vertical temperature change profile. This parameter was varied over a range of possible values with all of the other parameters held fixed. The result, (not shown here), found that the model's ocean temperature change profile is relatively insensitive to the value for Γ. This feature is a model refinement that may assist in fine tuning MAGICC to AOGCM results but is not as important for obtaining a better match between the model and observed ocean temperature change. However, subsequent work concerning parameter uncertainty (in Chapter 4) found that Γ, if used, is important for global–mean surface temperature change results because of its relationship to K.

Ratio of polar sinking water temperature change to mixed–layer temperature change, β

Testing of the parameter β, the ratio of polar sinking water temperature change (i.e. the small column of down-dwelling polar cold water) to the mixed–layer temperature change determined that the change in ocean temperature profile is very insensitive to the value of this parameter.

THC temperature threshold, T_{moc}

T_{moc} specifies the temperature threshold for the Northern and Southern Hemispheres at which minimum thermohaline circulation is reached relative to the change in global–mean temperature. Typically, the same value is used for both hemispheres, although there is an option to apply individual values. The results for varying this parameter alone are presented in Figure 3.14. Of interest here, high values shift the model curve so that the upper layer temperature change moves nearer to the observed value, and in the deeper ocean the temperature change is reduced, again moving closer to the observed change. This fits with theoretical considerations, since high upper–ocean temperatures are required for collapse of the oceans thermohaline circulation. Also note that the results are relatively sensitive to this parameter, comparable to that shown by K. However, such high values are physically unrealistic.

It is not clear how this parameter can be estimated from observations. It is only used as part of the formula to calculate the time–dependent upwelling velocity $w(t)$; this also involves w_{var}, so that they are related parameters. As a consequence, the standard value of 8°C has been left unchanged in this study.

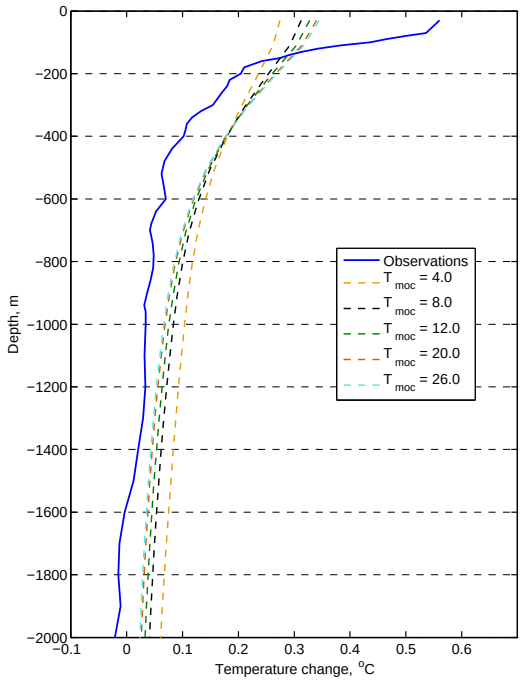

Figure 3.14: Results for varying T_{moc} (SW10 observations).

Mixed–layer depth, h

The sensitivity of the ocean temperature change profile to the mixed–layer depth h was also checked. This parameter was found to have almost no impact on the ocean temperature change profile; accordingly its standard value of 60m was retained.

3.4.2 Applying the ocean temperature profile constraint

The sensitivity of the ocean temperature change profile to parameter changes, as discussed above, found that the shape of MAGICC's ocean temperature profile is largely dependent on the ocean diffusivity setting K, followed by the upwelling velocity. The latter is set by the combination of three parameters: the initial upwelling velocity w_0, the variable fraction w_{var}, and the thermohaline circulation temperature parameter T_{moc}.

The match between the observed change in ocean temperature down through the ocean as compared to MAGICC provides a basis for estimating K. With w_{var} set to 0.2, the ocean diffusivity parameter K was varied to estimate what value provides the best model fit to the observed 1960–2008 world ocean temperature change profile, using L09 data derived from the World Ocean Atlas WOA09 (*Levitus et al.*, 2009) and a second set provided by S. E. Wijffels (SW10). Testing for the goodness–of–fit, the minimum RMSE (Root Mean Square Error) occurs at K = 0.9 cm^{2}s^{-1} for the L09 data and K = 0.6 cm^{2}s^{-1} for SW10 data (Figure 3.15). This is substantially smaller than the model's standard setting of 2.3 cm^{2}s^{-1}, and in better agreement with previous estimates from tracer studies and early model results, as well as the the CMIP3 evaluation of *Meinshausen et al.* (2009).

The next section considers ocean heat content as an alternative approach to using ocean temperatures as a parameter constraint.

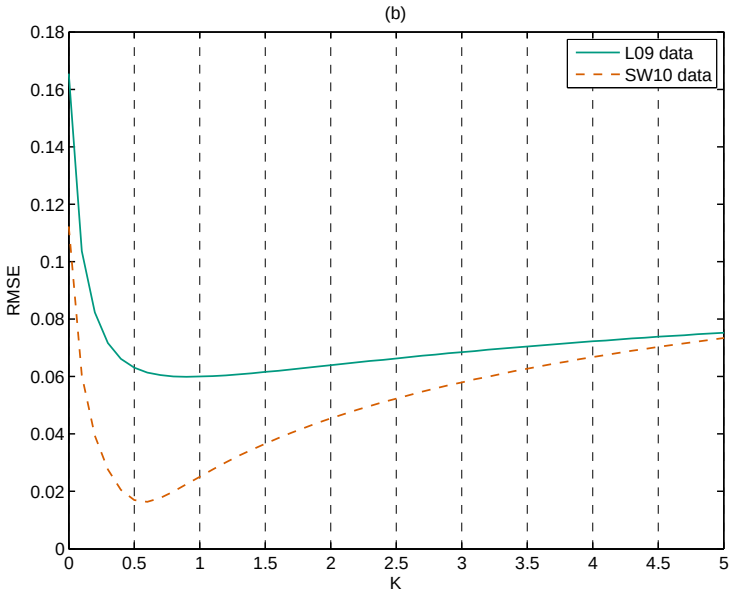

Figure 3.15: RMSE results between two sets of observed ocean temperature change profiles (L09 and SW10) and MAGICC with variable K.

3.5 Ocean Heat Content Constraint

This section considers the change in ocean temperature from a different perspective, that of the ocean heat content (OHC). Although ocean heat content is directly related to ocean temperatures (along with changes in salinity), it has been studied as a separate quantity by a number of researchers, such as *Levitus et al.* (2005), *Gouretski and Koltermann* (2007) and *Domingues et al.* (2008). It provides a measure of the time–integrated evolution of the ocean's temperature changes due to changes in external forcing factors and provides an alternate set of data to assist in estimating the ocean parameter values. In particular, this research investigated some ocean heat content differences and ratios to determine if an independent constraint could be found that would provide a different method of estimating the vertical diffusivity parameter K.

Differences and ratios of OHC were found not to be useful constraints, but a ratio of sea–surface temperature to ocean heat content was assessed as being independent of the sea–surface temperatures. This new ratio was then used to estimate K, which indicated K is less than 1.0 cm^2s^{-1}, a result similar to that determined in the previous section. Differences between alternate sets of observations contribute to the uncertainty in these values.

3.5.1 Observed and modelled OHC

Initial comparisons between MAGICC's OHC results and observation showed noticeable discrepancies, particularly for the 0–100m layer, leading to a detailed check as to whether the OHC representation in MAGICC version 6.3 was correct. The OHC results were therefore investigated further by calculating the heat content from first principles in order to try to resolve this issue. It was concluded that the mixed–layer OHC was being calculated incorrectly within MAGICC, an error that had proportionately less impact at deeper layers. The code was therefore revised using a slightly different procedure.[1] Figure 3.16 shows a comparison between the revised OHC model code and observations. The 0–100 model results are significantly improved over the original version.

Errors in the OHC calculation do not impact on MAGICC's results, since this is a diagnostic variable only, not a prognostic one. However, it does have implications for previous calibration work that utilised this information.

Having investigated the ocean heat calculation process in MAGICC, revised the model code and verified that the model is able to match the observed OHC changes reasonably well, it was then possible to research some approaches to constraining the model's parameters using ocean heat content with greater confidence.

[1] MAGICC has since been updated by Malte Meinshausen in response to this issue.

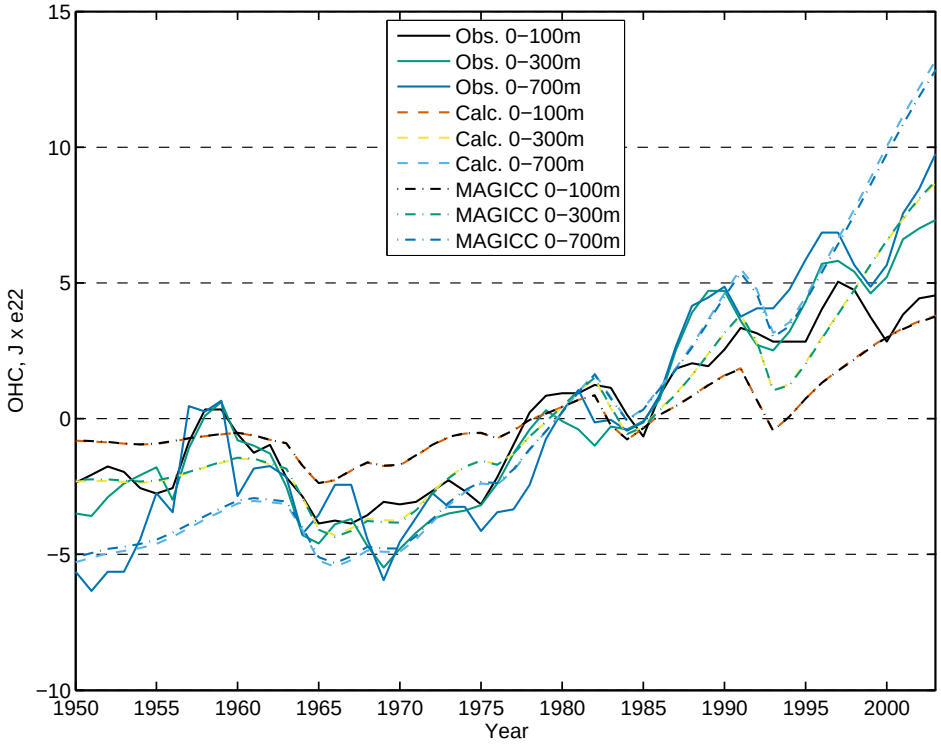

Figure 3.16: MAGICC calculated (Calc.) and D08 observed (Obs.) OHC. The calculated results overlap the MAGICC results. All results set to 1950–2003 mean (Model parameters: ΔT_{2x} = 3.0, K = 1.0, R_{lo} = 1.6, w_0 = 4.0, w_{var} = 0.2).

3.5.2 OHC differences and ratio constraints

Changes in ocean heat content (OHC) over time are an integrated measure of changes in ocean temperature. Such changes must reflect the transport of heat into the layers of the ocean, aggregated into a single vertical transport model in MAGICC with the primary mixing parameters K and w, as discussed in earlier sections of this chapter. Accordingly, it was expected that observed changes in OHC could be used to assist in setting the model's ocean parameters. However, the OHC is itself correlated with the global–mean surface air temperature, and therefore does not provide independent information for constraining any of the ocean parameters. This section tests some approaches to finding an independent OHC constraint, in a similar way to the temperature difference constraints used in Sections 3.3.2 and 3.3.2.

The correlation between the HadCRU global–mean surface temperatures and the D08 OHC is shown in Table 3.14, with values indicating a high correlation between the surface temperature and each of the 100m, 300m and 700m ocean heat content layers. The OHC data was calculated as anomalies with respect to (wrt) 1961, and the HadCRU observations were adjusted to align to this using a 1957–1966 mean. Correlations were calculated over the period of 1960–2003, the time span of the observational data set being used. A strong correlation was found between the surface temperatures and each OHC layer.

Table 3.14: Correlations between observed HadCRU global–mean temperatures and D08 observed OHC for differences and ratios.

correlation between	coefficient
HadCRU to 100m OHC	0.882
HadCRU to 300m OHC	0.863
HadCRU to 700m OHC	0.865
HadCRU to 700-300m diff.	0.462
HadCRU to 700-100m diff.	0.656
HadCRU to 300-100m diff.	0.590
HadCRU to 100-700m ratio	-0.130
HadCRU to 100-300m ratio	-0.433
HadCRU to 300-700m ratio	0.600

As an alternative metric, differences in OHC for different layer pairs were calculated and correlated to global–mean temperature. These have a moderate degree of correlation and therefore do not appear to provide a useful constraint.

Correlations with OHC ratios were also examined. These were calculated over a reduced time span, from 1984 to 2003 to avoid a divide–by–zero problem that otherwise distorts the ratio results. The 100/700 OHC ratio showed a very low correlation, with moderate correlation figures for the 100/300 and 300/700 OHC ratios. These correlation results suggested that these ratios could be useful constraints for estimating the ocean parameters.

Differences and ratios were also calculated for the model results. Model results were set to a 1957–1966 mean so as to align with the OHC observations. Correlations between the model surface temperatures observations and MAGICC OHC were then determined over the same time span, 1950–2003. These revealed very similar correlations to those between HadCRU and D08

observed OHC. Then, the correlations for the layer differences were determined using the same 1950–2003 period. The correlations for this set of differences were high, higher than for the observations to observations case. This is likely due to the lack of natural variability in the model results. OHC ratios were also calculated for the model, again with relatively high correlations. The OHC differences and OHC ratios for MAGICC have correlations to the modelled surface temperatures that were too high to be regarded as independent.

A ratio between sea–surface temperature (SST) changes and OHC changes for the layer to 700m was investigated next. This was subsequently found to be similar to the effective heat capacity or OHC to global–surface temperature ratio used by *Frame et al.* (2005) and *Andrews and Allen* (2008), except inverted, and with SSTs rather than global–surface temperature changes since MAGICC reports separate land–surface and sea–surface temperatures, which enables this somewhat different ratio to be used. The SST/OHC was preferred because it minimised problems with dividing by very small SST values, although testing found little difference in the resulting correlations.

The ratio of SST to 700m OHC changes was found to have almost no correlation with SST changes for two different observed SST data sets, HadSST2 (*Rayner et al.*, 2006) and NCDC ERSST3b (*Smith et al.*, 2008) and 700m OHC (L09 and D08) observations (Table 3.15). The MAGICC results exhibit a similar pattern of weak correlations, although the SST to SST/OHC ratio correlation is not as low as in the observations, due to the lack of natural variability in the model results. The modelled correlations vary a little depending on the setting used for K, hence only approximate values are indicated for the modelled SST to OHC correlation, and a range for the modelled SST to SST/OHC ratio.

Table 3.15: Correlations between observed and modelled SST/OHC ratios for HadSST2 and NCDC ocean–surface temperature anomalies with L09 and D08 observed OHC changes.

Correlation	HadSST2		NCDC SSTs	
	L09	D08	L09	D08
observed:				
SST to OHC	0.789	0.815	0.783	0.845
SST to ratio	-0.030	0.008	-0.077	-0.144
modelled:				
SST to OHC	0.9 approx.	0.9 approx.	0.9 approx.	0.9 approx.
SST to ratio	0.25 to 0.45	0.25 to 0.45	0.25 to 0.45	0.25 to 0.45
RMSE min. K	0.25	0.5	0.25	0.75

The low correlation values indicate that this SST/OHC ratio is almost independent of the SSTs, and hence provides an observational constraint that can be used to estimate K by comparing the observed SST/OHC ratio to modelled SST/OHC ratio. The results point towards low values for the K parameter, between 0.3 and 0.8 cm^2s^{-1}, as seen in Figure 3.17. However, while there is a minimum exhibited in the RMSE results, the range of difference from K = 0.2 to K = 5.0 is very small.

Both the ocean temperature change profile and the SST/OHC ratio provide constraints for estimating K that indicate a range of between 0.2 and 2.0 cm^2s^{-1}, values lower than that used as the default setting in the versions of MAGICC used since the TAR, although values outside this range cannot be entirely ruled out.

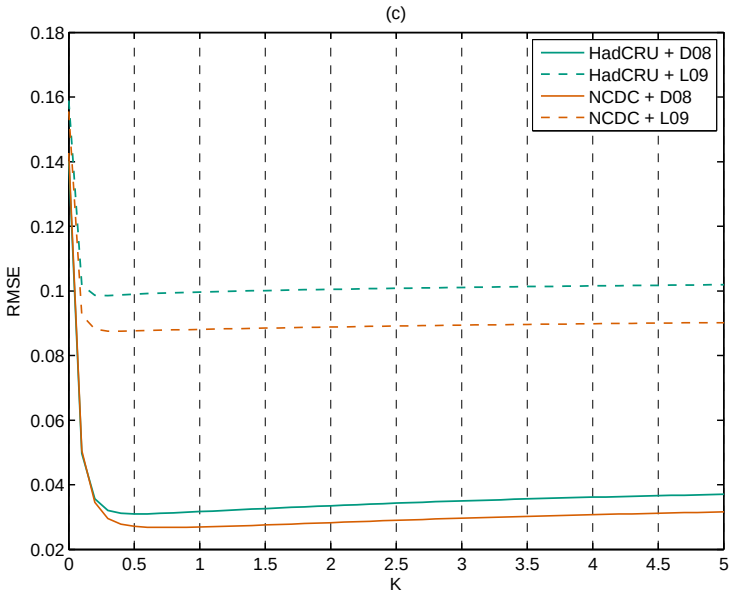

Figure 3.17: RMSE results for SST/OHC ratio using observed SSTs, HadSST2 (*Rayner et al.*, 2006) and NCDC (*Smith et al.*, 2008), observed OHC (L09 and D08), and MAGICC with variable K.

3.6 Review of Results and Implications

3.6.1 Revised parameter settings

This chapter has investigated aspects of the climate system parameters in MAGICC, including identifying the key parameters. A parameter sensitivity study was undertaken to provide a basis for prioritising efforts to constrain the parameters. The climate sensitivity ΔT_{2x} and effective ocean vertical diffusivity K are the most significant climate system parameters for determining the global–mean temperature. The land ocean warming ratio R_{lo} and, to a lesser extent, the land ocean heat exchange coefficient κ_{lo} become important for the land ocean temperature contrast (this is a similar group of parameters to the ones used for tuning in the TAR, *IPCC*, 2001, WG1 Ch9 Appendix 9.1: Tuning of a Simple Climate Model to AOGCM Results). However, because MAGICC's transient response is largely determined by heat transfer into the ocean, the ocean parameters other than K also have a role.

A number of observational constraints were investigated as potentially independent pieces of information to help estimate the climate system parameters. The land−ocean temperature and North−South temperature differences were found to be largely independent of the global–mean temperature. The land−ocean temperature was found to be useful in estimating values for the land ocean warming ratio R_{lo} and the land ocean heat exchange coefficient κ_{lo}. The North South heat exchange coefficient κ_{ns} was checked using the North−South temperature difference. As expected from the sensitivity testing, the RMSE results were essentially flat; the standard value was left unchanged.

To help estimate K, ocean temperature and heat content changes were investigated to see how they might be applied. Both the ocean temperature change profile and a SST/OHC ratio were found to be helpful in estimating K; they suggest a range of between 0.5 and 1.0, significantly lower than the value used in the TAR and AR4 versions of the model, although not dissimilar to the mean values from the CMIP3 calibration (*Meinshausen et al.*, 2009). Higher values are possible, while very small values seem unlikely.

Having reviewed MAGICC's key climate system parameters based on independent pieces of information (summarised in Table 3.16), the climate sensitivity parameter ΔT_{2x} remained to be assessed. This was estimated from the goodness–of–fit between the model's global–mean surface temperature and 20th–century observations. Temperatures and RMSE results are shown in Figure 3.18(a) and (b) for values of K = 0.5, 1.0 and 2.0 cm^2s^{-1}, which give a best fit to the average of three observational data sets for ΔT_{2x} of 2.2, 2.4 and 2.9°C respectively. These values are somewhat less than the standard setting of 3.0°C, but within the generally accepted range for ΔT_{2x}. The pairs of parameter values for ΔT_{2x} and K of (2.2, 0.5), (2.4, 1.0) and (2.9, 2.0) provide estimates for these two parameters that best fit the observed 20th–century global–mean temperature changes for 1880 to 2009.

3.6.2 Implications for future temperatures

Revised parameter values, derived as explained in the previous sections, have been used to estimate future global–mean surface temperature changes for the SRES A1FI emission scenario (*Nakicenovic and Swart*, 2000) and a 450 ppm CO_2 equivalent stabilisation scenario. Projections for

Table 3.16: MAGICC's climate system parameters in descending order of sensitivity for global–mean surface temperature[a].

Abbreviation	Description	Units	Standard	Revised
ΔT_{2x}	Climate sensitivity	°C	3.0	2.2
K	Ocean effective vertical diffusivity	cm^2s^{-1}	2.3	0.6
R_{lo}	Land ocean warming ratio		1.3	1.6
α	Ratio of air temperature to mixed–layer temperature[b]		1.25	1.25
κ_{lo}	Heat exchange coefficient land−ocean	$Wm^{-2}\,°C^{-1}$	1.0	2.0
h	Mixed–layer depth[b]	m	60	60
T_{moc}	Temperature change threshold at which minimum meridional overturning is reached	°C	8.0	8.0
w_0	Initial upwelling velocity[b]	$m\,yr^{-1}$	4.0	4.0
β	Ratio of polar sinking water to mixed–layer temperature[b]		0.2	0.2
κ_{ns}	Heat exchange coefficient North South	$Wm^{-2}\,°C^{-1}$	1.0	1.0
w_{var}	Variable upwelling fraction[a,b]		0.7	0.2

[a] Except w_{var} was not included in our parameter sensitivity study.
[b] Not included in calibration process by *Meinshausen et al.* (2009).

standard parameter and revised settings are shown in Figure 3.19 for paired sets of ΔT_{2x} and K. For the A1FI scenario, the change in 2100 is nearly 0.5°C greater warming than for the standard parameter values when ΔT_{2x} = 2.9°C and K = 2.0 cm^2s^{-1}, with smaller changes for the other cases. The reduced ocean diffusivity leads to greater mixed–layer warming over time, resulting in increased surface warming; this is amplified by the larger R_{lo} value and is despite a lower climate sensitivity.

The impact of the revised parameters is small for the 450 ppm stabilisation scenario, around 0.1°C as indicated in Figure 3.19. Improved climate system parameter estimates are less critical for projecting global–mean temperatures for scenarios that have small changes in radiative forcing, but these become more significant for high emissions scenarios that result in large radiative forcing. Parameter estimates can also have large impacts on the economic assessment of mitigation policies from integrated assessment models that are built on simple climate models, such as MAGICC (*van Vuuren et al.*, 2011).

This revised set of climate system parameters for MAGICC has been determined based on a sequence of systematic testing taking into account parameter sensitivity, observational constraints and RMSE comparisons between observations and model results. An improved fit between MAGICC's ocean temperature change profile and observations has been achieved using revised ocean parameters, including a greatly reduced ocean vertical diffusivity setting (K = 0.5 – 1.0 rather than 2.3 cm^2s^{-1}) and a much smaller variable upwelling component (w_{var} = 0.2 rather than 0.7). However, these results only have a limited treatment for the range of uncertainty. Uncertainty in the carbon cycle parameters, aerosol forcing and observational uncertainty have not been addressed in this Chapter. In addition, no probabilities can be assigned to projected temperatures. These topics are addressed in the following chapters, with further work on the climate system parameters in Chapter 4 and then the carbon cycle in Chapter 5.

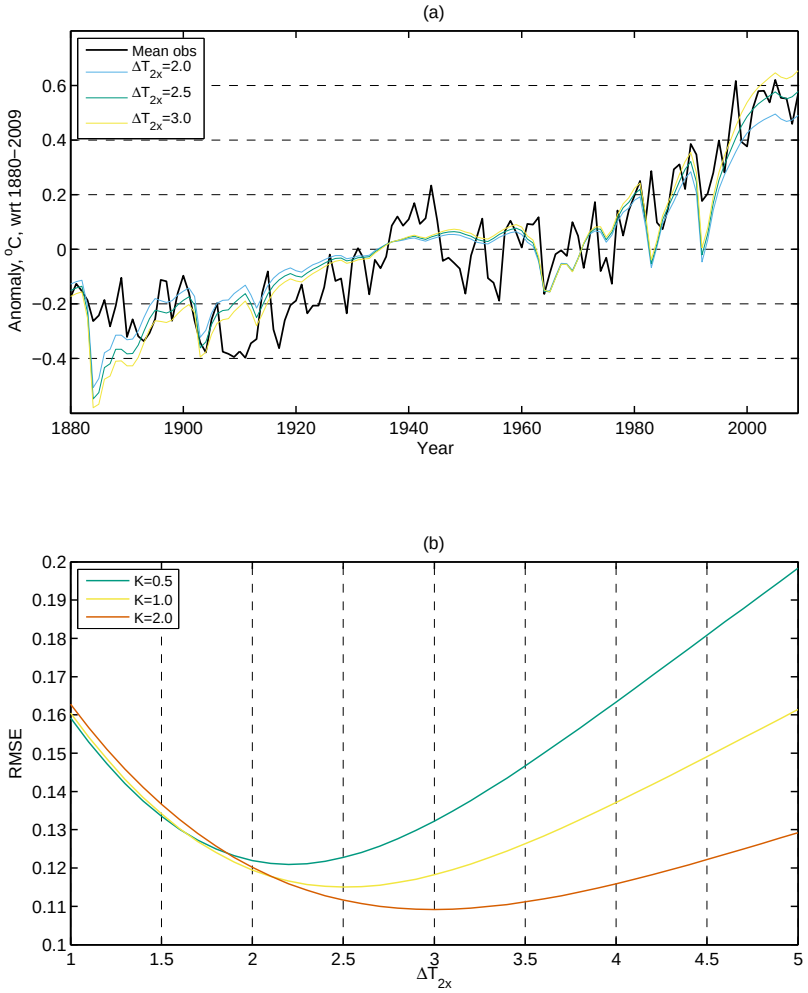

Figure 3.18: (a) Mean of CRU, NCDC and GISS observed 1880–2009 global–mean temperatures with MAGICC results for selected ΔT_{2x} values. (b) RMSE for variable ΔT_{2x} from fitting global–mean surface temperatures with K = 0.5, 1.0 and 2.0.

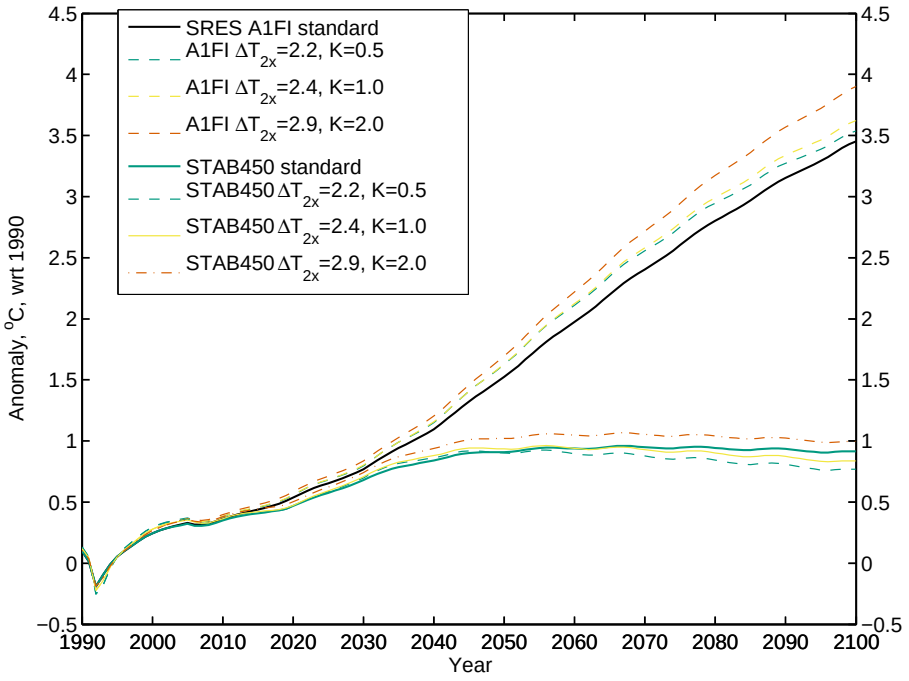

Figure 3.19: MAGICC projected temperature changes for SRES A1FI and 450 ppm CO_2 equivalent stabilisation scenarios with standard and revised parameter sets for 1990–2100, with respect to 1980–1999 mean.

Chapter 4

Climate Parameters and Uncertainty

The previous chapter investigated the climate system from the perspective of assessing the sensitivity of global–mean temperature change results to the settings of individual parameter values in a simple climate model. A process of systematically estimating the key parameters was undertaken using different forms of observational constraints aimed at isolating individual parameters. In particular, the ocean parameters were carefully investigated since the model's transient climate response is largely determined by the heat uptake characteristics of the ocean. However, whilst these methods were able to deliver revised estimates for the key climate system parameters, as well as insights into the important processes involved and model limitations, the potential correlation between parameters was not investigated. In addition, there was no estimate provided for the uncertainty in the results.

The investigation of the climate system is continued here by looking at two further approaches. Firstly, the relative contribution each of the climate system parameters makes to uncertainty in the global–mean temperature change projections is assessed, and, secondly, a Bayesian Monte Carlo Markov Chain with Metropolis-Hastings algorithm (MCMH) method is applied, which looks at joint probability distributions for the model parameters.

A general introduction to uncertainty, in the context of climate models, is presented in the first section, together with a survey of some of the research that addresses this topic. These various forms of uncertainty need to be considered and allowed for in presenting results from a simple climate model. Furthermore, the range of uncertainties should, ideally, have some level of probability associated with them. This becomes particularly important for decision making and climate change policy (*Jones*, 2000; *Webster et al.*, 2003).

The key uncertainties for MAGICC are the climate sensitivity, the rate of ocean heat uptake, aerosol forcing and the response of the carbon cycle. Climate sensitivity determines the magnitude of the temperature response to a change in radiative forcing, while the ocean's thermal inertia influences the transient response. Aerosol forcing uncertainty affects the magnitude of the net radiative forcing, and the carbon cycle is important for determining the proportion of CO_2 that remains in the atmosphere from emissions. Climate sensitivity and ocean heat uptake are set by model parameters which are tuned to either match observations or emulate AOGCMs, as discussed previously in Chapter 3 and then further in this chapter. The uncertainties associated with aerosol forcing are addressed in Section 4.2.3. Issues concerning the carbon cycle are taken up in Chapter

5 and then the combined uncertainty of the climate system and carbon cycle is addressed in Chapter 6.

The contribution that each of MAGICC's climate system parameters makes to the overall uncertainty in the temperature change results is assessed in Section 4.2. The method used, which involves making small changes to individual parameters as a proportion of their estimated range of probable values, provides a systematic way of representing uncertainty by combining different sources of uncertainty, that is, the uncertainty associated with particular model parameters, to achieve an overall uncertainty estimate. The results from this approach confirmed the dominant role of the climate sensitivity parameter, with the ocean vertical diffusivity taking a distant second place, while the remaining climate system parameters make only a small contribution to the model's temperature change uncertainty.

A Monte Carlo Metropolis-Hastings algorithm (MCMH) is introduced next and applied to estimating the climate system parameters. This was successful in constraining the primary climate system parameters using historical observation. Final conclusions are, however, left pending the investigation of the carbon cycle (Chapter 5) and the combined climate and carbon cycle (Chapter 6).

4.1 Uncertainty

The temperature change results from climate models have a degree of uncertainty associated with them, as well as explicit and implicit assumptions that need to be made clear. Early model projections were not provided with any systematic uncertainty estimates, and did not necessarily cover the full range of known climate system processes (*Allen et al.*, 2000). General issues, such as uncertainty in historical temperature data are discussed by *Pollack* (2005), with more specific details in, for example *Folland et al.* (2001) and *Brohan et al.* (2006). Other issues concerning forcing scenarios, model response and missing or misrepresented physics are discussed in the IPCC reports (*IPCC*, 2001; 2007b). A useful review of uncertainties in global temperature projections, in the context of a range of model types, is presented by *Knutti et al.* (2008), including comments concerning differences between MAGICC and Coupled Model Intercomparison Project (CMIP3) AOGCMs.

It is important that model assumptions and limitations are explicit and, for decision making purposes, it makes the projected temperature change results more meaningful if they have probabilities associated with them (*Jones*, 2000; *Webster et al.*, 2003). However, it is debatable whether or not to apply probabilities to emissions scenarios (see, e.g., *Grubler and Nakicenovic*, 2001; *Pittock et al.*, 2001), although this is perhaps really a question of what is possible over what is needed (personal communication, Ian Enting, 2011).

The sources of uncertainty for temperature projections include:

- Observations and measurement uncertainty for historical temperature data against which a climate model is tested for its ability to model the historical record. Natural variability due to changes in climate modes, such as El Niño and the North Atlantic Oscillation, is also present in the observations, although not represented in a model such as MAGICC. There

is also uncertainty in separating out solar, volcanic and anthropogenic forcing components over the historical period.

- Structural model uncertainty may result from errors in the design and implementation of a numerical model, which can be difficult to diagnose once the model has been constructed.

- Carbon cycle/vegetation/oceanic response uncertainties and feedbacks (see, for example, *Wigley*, 1994; 2000a; *O'Neill and Melnikov*, 2008).

- Uncertainties concerning atmospheric chemistry, the evolution of reactive gases and aerosols. Aerosol forcing uncertainties are important because of the large negative forcing effect that is spatially heterogeneous compared to CO_2 (*Wigley*, 1997; *Yu et al.*, 2006). Similarly for tropospheric and stratospheric ozone.

- The conversion of concentrations into radiative forcing and the global temperature response within a simple climate model is represented by a simple parameterised equation, which can only approximate the actual response of the climate system to changes in atmospheric greenhouse–gas concentrations. Global–mean radiative forcing is a useful means of estimating the global–mean temperature response and a linear forcing response continues to be a reasonable assumption (*Forster and Gregory*, 2006).[1]

- Model response and parameterisation. Despite past research efforts, there is still considerable uncertainty concerning the values of important model parameters.

- Future emissions and the choice of emissions scenario associated with the absence of probabilities and the ambiguity assigned to the SRES scenarios, as noted in *Webster et al.* (2003). There is uncertainty concerning future emissions (*Webster et al.*, 2002) and uncertainties in population growth (*O'Neill and Sanderson*, 2008). However, this is more about future choices and policies, which is a different kind of uncertainty from the scientific uncertainty associated with observations, the response of the climate system and model design.

- There is really no provision in a simple climate model for future natural variability and volcanoes, although it is possible to introduce some degree of internal variability into a simple model, as shown for example by *Wigley and Raper* (2001). Solar cycles, such as the 11–year solar cycle, can be provided for, as well as changes due to the Earth's orbit if very long time periods are being investigated. Volcanoes are normally regarded as completely stochastic, that is, there is no realistic way of providing for any such future events. The climate system also recovers from the cooling effect of eruptions over 2 to 7 years (*Thompson et al.*, 2009), meaning that they can be assumed to have no net long term effect.

- Feedback mechanisms, such as carbon–climate feedbacks, ice sheet melting, permafrost, thermohaline circulation, water vapour feedbacks and cloud formation, are all areas of uncertainty, including the potential for non–linear responses and sudden threshold changes. As yet, long–term changes in vegetation and the effect this has on the surface albedo are generally not well represented in climate models.

[1] Such as, $\Delta Q = \alpha_{\mathrm{CO}_2} \ln(C/C_0)$ and $\Delta T = \lambda \Delta Q$.

In order to project likely future temperatures, a number of researchers have used methods involving Probability Density Functions (PDFs) to capture the range of uncertainty for either a single parameter or joint probabilities for two or more parameters. Early work of this type focussed on climate sensitivity as this is the most uncertain parameter for a simple climate model. *Andronova and Schlesinger* (2001) used a simple climate model (COSMIC, *Schlesinger and Williams*, 1997) to perform Monte Carlo simulations comparing the observed and simulated temperature record to arrive at a probability density function for climate sensitivity. *Wigley and Raper* (2001) introduced the use of a PDF with MAGICC, using a log–normal distribution for climate sensitiivty.

New and Hulme (2000) also used a Bayesian Monte Carlo approach to quantify uncertainties within a probabilistic framework. They utilised four SRES marker scenarios, A1, A2, B1 and B2, as being representative of most of the range of future emissions, with the assumption that each emissions pathway is equally likely. Emissions were then converted into global–mean temperature change projections using MAGICC. The authors indicated that the strength of the carbon cycle and ocean heat uptake are two of the models key parameters along with climate sensitivity. It is interesting to note that the carbon cycle was included but the aerosol component was not, although it was acknowledged as a factor. It was not included due to difficulties in modelling the aerosol effects (this was perhaps more of an issue for the older version of MAGICC then in use) as well as a view that aerosol forcing would likely be a less significant forcing than greenhouse–gas forcing by the end of this century. For climate sensitivity, *New and Hulme* (2000) adopted a triangular PDF, based on the IPCC range of 1.5 to 4.5°C.

A useful review of the role of probabilities for arriving at temperature projections and the probability of exceeding a threshold temperature is provided by *Dessai and Hulme* (2003). They traced some of the then recent relevant papers and important discussions for this topic before addressing the question of the whether or not estimates of the likelihood of climate change are needed. They concluded that the answer depends to some extent on the goals of the analysis along with the difficulties of assessing human reflexivity.

Hare and Meinshausen (2006) provides an additional 6 examples of climate sensitivity PDFs whilst pointing out that a joint PDF would be better than focussing on this single parameter since it does not take into account other uncertainties. That paper used MAGICC to investigate different concepts of warming commitment with temperature results expressed in probabilistic terms.

Meinshausen (2006) addressed the idea of a temperature target as a threshold for dangerous climate change. Using a policy target, such as a 2°C increase above pre–industrial as a limit for the global mean temperature, that analysis sought to estimate the probability of exceeding the target temperature. 11 PDFs were used for the climate sensitivity. Two other important parameters, ocean heat uptake and sulfate aerosol forcing, were adapted based on the climate sensitivity using maximum likelihood estimates derived from a simple historical constraint test. Meinshausen's work thus focused on climate sensitivity as the primary uncertainty, and did not attempt to derive a joint PDF.

Forest et al. (2002) derived joint probability distributions for climate sensitivity, ocean heat uptake and aerosol forcing using what they term as an optimal fingerprinting approach. They used the MIT 2D statistical–dynamical model to represent the climate from 1860 to 1995, varying these three parameters to assess the fit to the historical record. They were then able to derive a joint

PDF, which was then used to investigate the likelihood of the climate system response to forcing scenarios. This work has been developed further in *Forest et al.* (2008) and *Libardoni and Forest* (2011).

However, as indicated in subsequent work by *Webster et al.* (2003), it is also important to consider the likely future emissions pathway. That study built on the joint PDF approach of *Forest et al.* (2002) to use probabilities for future emissions projections and to estimate uncertainty for both a policy constraint and a no policy case. *Forest et al.* (2004) point out that, while research into reducing uncertainty should continue, there will continue to be some level of irreducible uncertainty. Accordingly, techniques that allow for the different uncertainties to be incorporated through the climate modelling process need to be utilised and improved upon, which is one of the goals of this research.

4.2 Climate System Parameter Uncertainty

This section investigates a method for assessing the contribution the climate system parameters make to MAGICC's global–mean temperature change results. The model was run using an initial set of parameter values to establish a standard temperature change result, then re–run for each parameter in turn, with the parameter value changed by 1% of its nominal standard deviation for its estimated range. An initial range of values for each parameter and its standard deviation was determined from the CMIP3 calibrated values, the research work of Chapter 3 and previous results, as discussed below. The difference in the model results then provides a measure of the sensitivity of the model outputs to the input parameters (the Jacobian of the model), following a similar method to *Rayner et al.* (2011). The variance of each parameter provides the content for the covariance matrix $\mathbf{C}(v)$ and the calculated sensitivities assume a linear error propagation from the input parameters to the model results.

For a random vector v with multivariate normal distribution described by the covariance matrix $\mathbf{C}(v)$, where $\mathbf{J}$ is any linear mapping, then $\mathbf{U}$ is also a multivariate normal which provides an uncertainty estimate for the parameters according to the equation:

$$\mathbf{U} = \mathbf{J}\mathbf{C}(v)\mathbf{J}^{\mathbf{T}} \tag{4.1}$$

where the superscript represents the transpose of the matrix $\mathbf{J}$.

4.2.1 Specifying the climate parameters

A set of seventeen climate system parameters were identified, based on the CMIP3 tuning files and model documentation, as listed in Table 4.1. These 17 parameters comprise the 11 calibrated parameters used in the CMIP3 configuration files (i.e., the results of the calibration process described in *Meinshausen et al.*, 2009; 2011a) plus six more based on the work in Chapter 3. Of the 11 calibrated parameters listed first in Table 4.1, three are new to version 6.0, introduced for fine tuning MAGICC to emulate the CMIP3 models. The remaining six parameters also need to be considered, as discussed previously in Chapter 3.

The two land area fractions, f_{nl} and f_{sl} are not really climate parameters but model structure settings. They are treated here as constants with no variance and no contribution to MAGICC's

climate response uncertainty. ΔQ_{2x} was discussed in Chapter 3 (Section 3.1.4). It can be left at its default value of 3.71 W m^{-2}, since this is the radiative forcing for a doubling of CO_2.

Values for the variance σ^2 of each parameter are required for the uncertainty assessment. The 19 sets of CMIP3 values provided a basis for setting σ^2 for the 11 calibrated parameters. Table 4.2 lists these parameters with their mean, standard deviation σ, skewness and kurtosis.

The asymmetric heat exchange factor μ has a very small variance and can be treated as a fixed parameter. It is not essential to the operation of MAGICC, rather it helps to fine tune it for emulating the CMIP3 models. The ocean diffusivity temperature gradient parameter Γ could either be left at its default setting of 0, or included as one of the parameters that contributes to the climate system uncertainty.

Table 4.1: List of MAGICC's 17 climate system parameters.

No.	Parameter	Description	Units
1	μ	amplification factor for ocean to land heat transport[a]	
2	ΔT_{2x}	climate sensitivity	°C
3	ΔQ_{2x}	forcing for doubled CO_2	W m^{-2}
4	ξ	dependence of feedback factors on forcing[a]	°Cm^{2}W^{-1}
5	$\kappa_{\rm lo}$	heat exchange coefficient land ocean	W m^{-2} °C^{-1}
6	$\kappa_{\rm ns}$	heat exchange coefficient north south	W m^{-2} °C^{-1}
7	$f_{\rm nl}$	hemispheric fraction of Northern land area	
8	$f_{\rm sl}$	hemispheric fraction of Southern land area	
9	$R_{\rm lo}$	ratio land ocean warming	
10	Γ	dependence of vertical diffusivity on ocean warming gradient[a]	cm^{2}s^{-1} °C^{-1}
11	K	ocean vertical diffusivity	cm^{2}s^{-1}
12	w_0	initial upwelling velocity	m yr^{-1}
13	$w_{\rm var}$	variable upwelling velocity fraction	
14	h	mixed–layer depth	m
15	β	ratio of polar sink water to mixed–layer temperature	
16	$T_{\rm moc}$	upwelling temperature threshold	°C
17	α	SST to mixed–layer temperature ratio	

[a] Three new parameters for fine tuning MAGICC to emulate the CMIP3 models.

The distributions for the 11 parameters listed in Table 4.2 were checked, testing for normal or log normal distributions by plotting the 19 sets of CMIP3 tuned values. In addition, restrictions on the range of physically feasible values were noted.

The remaining six parameters (w_0, $w_{\rm var}$, h, β, $T_{\rm moc}$ and α) also needed a distribution and standard deviation. One way to do this was to assign a PDF (Probability Density Function) to each of these based on the investigations in Chapter 3. Previous studies also provided a guide. For example, *Wigley and Raper* (2001) used a 90% confidence interval 1.5° to 4.5° for climate sensitivity ΔT_{2x} with either uniform or lognormal distributions, and for ocean vertical diffusivity K used a lognormal PDF with 5, 50 and 95% values of 1.3, 2.3 and 4.1 cm^{2}s^{-1}.

For the purposes of this uncertainty evaluation, the climate sensitivity parameter ΔT_{2x} was assigned a lognormal distribution with a 5% to 95% confidence interval of 1.5 and 4.5. The lognormal distribution has the added benefit that it cannot go below zero (this also applies to some of the other model parameters).

Table 4.2: MAGICC's 11 CMIP3 tuned parameters

No.	Parameter	Mean	σ	Skewness	Kurtosis	Notes
1	μ	1.16	0.14	0.12	1.63	$>= 1$ or fixed
2	ΔT_{2x}	2.88	0.92	1.78	6.00	$>= 0$
3	ΔQ_{2x}	3.63	0.29	-0.16	2.30	fixed at 3.71
4	ξ	0.03	0.03	0.64	1.52	$>= 0$ or fixed
5	κ_{lo}	1.49	0.79	-0.88	1.87	$>= 0$
6	κ_{ns}	0.63	0.66	1.31	3.11	$>= 0$
7	f_{nl}	0.50	0.05	0.22	1.73	fixed value
8	f_{sl}	0.25	0.03	0.29	1.73	fixed value
9	R_{lo}	1.37	0.15	0.09	2.38	$>= 1$
10	Γ	-0.32	0.39	-1.03	2.445	$<= 0$ or fixed
11	K	1.30	0.71	0.63	2.01	$>= 0$

The general expression for two values of a normal distribution can be written as:

$$\hat{\mu} + a_1\hat{\sigma} = b_1$$

$$\hat{\mu} + a_2\hat{\sigma} = b_2$$

where $\hat{\mu}$ and $\hat{\sigma}$ are the mean and standard deviation of the normal distribution. b_1 and b_2 are the required confidence values at a_1 and a_2. For a normal distribution the 5% to 95% boundaries are $1.64\hat{\sigma}$ either side of the mean. To change to a lognormal distribution it is only necessary to take the logs of b_1 and b_2. Hence:

$$\hat{\mu} - 1.64\hat{\sigma} = \ln(1.5)$$

$$\hat{\mu} + 1.64\hat{\sigma} = \ln(4.5)$$

This pair of simultaneous equations are easily solved to obtain $\hat{\mu}$ = 0.955 and $\hat{\sigma}$ = 0.335. The variance $\hat{\sigma^2}$ is then 0.112.

In matrix form, where A*X = B, then

$$A = \begin{bmatrix} 1 & -1.64 \\ 1 & 1.64 \end{bmatrix}$$

$$X = \begin{bmatrix} \hat{\mu} \\ \hat{\sigma} \end{bmatrix}$$

$$B = \begin{bmatrix} \ln(1.5) \\ \ln(4.5) \end{bmatrix}$$

This provides a general solution for lognormal distributions with a 90% confidence interval; only the values in B need to be changed to find the mean and standard deviation.

The other climate system parameters were similarly assigned distributions and standard deviations σ, guided by the CMIP3 calibrated values and the knowledge gained in Chapter 3, as listed in Table 4.3, although these are not the only possible choices that could have been made; they are 'best estimate' or 'expert' priors based on the available information and experience gained from working with the model. These prior distributions are reviewed later in the light of joint distribution fitting to observations using the Monte Carlo method in Section 4.3.

Table 4.3: Distribution characteristics for MAGICC's 17 climate system parameters.

No.	Parameter	Distribution	σ
1	μ	fixed at default value, 1.0	0
2	ΔT_{2x}	lognormal, 5% to 95% confidence interval of 1.5 and 4.5	0.33
3	ΔQ_{2x}	fixed setting, 3.71	0
4	ξ	fixed at default value, 0	0
5	$\kappa_{\rm lo}$	lognormal, 5% to 95% confidence interval of 0.1 and 5.0	0.70
6	$\kappa_{\rm ns}$	lognormal, 5% to 95% confidence interval of 0.1 and 2.0	0.91
7	$f_{\rm nl}$	fixed setting	0
8	$f_{\rm sl}$	fixed setting	0
9	$R_{\rm lo}$	normal, mean 1.60	(a)
10	Γ	normal, mean -0.32 or default setting	0.39 or 0
11	K	lognormal, 5% to 95% confidence interval of 0.5 and 2.5	0.49
12	w_0	lognormal, 5% to 95% confidence interval of 2.5 and 8.0	0.35
13	$w_{\rm var}$	lognormal, 5% to 95% confidence interval of 0.1 and 0.8	0.20
14	h	normal, mean 60	18
15	β	lognormal, 5% to 95% confidence interval of 0.1 and 0.8	0.20
16	$T_{\rm moc}$	normal, mean 8.0 or or fixed setting	2.44 or 0
17	α	normal, mean 1.25	(b)

(a) Initially, a standard deviation for $R_{\rm lo}$ of 0.14 was used, based on the CMIP3 values.
(b) α was assigned a standard deviation of 0.05 to start with.

4.2.2 Climate system uncertainty results

After establishing standard deviations σ for the climate parameters based on the selected distributions, estimated as discussed in the previous section, the model was run to determine the effect that small alterations in the parameter values make to the resultant global–mean temperature change in 2100. Each parameter was varied by 1% of its standard deviation. The first set of results is presented in Table 4.4. The standard deviation of 1.29°C gives a 5% to 95% confidence interval of $\pm$ 2.12°C for the temperature change in 2100 (assuming a normal distribution).

The top three parameters account for 99% of the overall uncertainty for the temperature results. Climate sensitivity ΔT_{2x} is almost 88% of the total, re-iterating the significance of this parameter. The next two main contributors are ocean parameters, the temperature gradient component Γ and the ocean vertical diffusivity K. This also confirms the importance of the ocean diffusivity parameters, although they are a surprisingly small part of the total uncertainty according to this analysis; the remaining parameters are all of relatively minor importance.

The diffusivity gradient parameter Γ shows up here as being more significant than anticipated, given the sensitivity result in Section 3.4.1. In addition, the parameters $R_{\rm lo}$ and α contributions to

Table 4.4: Climate system parameter uncertainty for temperature in 2100 with the A1FI emission scenario.

Parameter name	σ	uncertainty contribution %
climate sensitivity $\Delta T_{2\mathrm{x}}$	0.33	87.70%
ocean diffusivity warming gradient Γ	0.39	8.82%
ocean vertical diffusivity K	0.49	2.50%
land ocean heat coefficient κ_{lo}	0.70	0.34%
upwelling temperature threshold T_{moc}	2.44	0.27%
variable upwelling velocity fraction w_{var}	0.20	0.13%
north south heat coefficient κ_{ns}	0.91	0.10%
SST to mixed–layer temperature ratio α	0.05	0.06%
land ocean warming ratio R_{lo}	0.14	0.06%
polar sink water to mixed–layer temperature ratio β	0.20	0.02%
mixed–layer depth h	18.3	0.01%
initial upwelling velocity w_0	0.35	0.00%

the overall uncertainty are smaller than expected. As an alternative, the uncertainty results with Γ not included (i.e., set to a fixed default value with zero variance), are presented in Table 4.5. In this case, the $\Delta T_{2\mathrm{x}}$ dominates, with a 96% contribution to the total uncertainty, K is nearly 3%, leaving just 1% for all the remaining parameters.

The standard distributions used for the R_{lo} and α parameters in Tables 4.4 and 4.5 were based on the CMIP3 calibrated ranges. However, if larger values are used, based on the observational fitting discussed in Sections 3.1.2 and 3.1.3, then the results change, with α and R_{lo} moving higher in the order. If the parameter T_{moc} is treated as fixed, for the reasons discussed in Section 3.4.1, then the modified uncertainty results show very small changes to $\Delta T_{2\mathrm{x}}$ and K, with all the other parameter contributions remaining almost the same.

An additional step was to also fix the SST to mixed–layer temperature ratio α, for which case the results are given in Table 4.6. The reason for considering excluding this parameter is that it has normally been treated as a constant in previous calibration exercises, and so this was an option selected to reduce the number of climate system parameters for the MCMH work in Section 4.3. Testing this setting confirmed the acceptability of its default value (as discussed previously in Section 3.1.3). Removing α shifts most of the uncertainty contribution into the climate sensitivity $\Delta T_{2\mathrm{x}}$ proportion. Before discussing these results further, uncertainty due to aerosol forcing is introduced into the mix.

4.2.3 Aerosol uncertainty

Aerosol forcing uncertainty is concerned with setting a forcing amount for the different aerosol components at a point in time. It is an offset to the radiative energy balance of the climate system; observed warming over the past 50–60 years due to increases in atmospheric greenhouse–gas concentrations is offset by cooling from anthropogenic sulfate aerosols (*Stott et al.*, 2001). As such, aerosol forcing uncertainty is a different type of uncertainty to the uncertainty in the temperature response of the climate system to a perturbation in the radiative forcing energy balance.

Table 4.5: Climate system parameter uncertainty for temperature in 2100 with the A1FI emission scenario — without Γ.

Parameter name	σ	uncertainty contribution %
climate sensitivity $\Delta T_{2\mathrm{x}}$	0.33	96.17%
ocean vertical diffusivity K	0.49	2.74%
land ocean heat coefficient κ_{lo}	0.70	0.38%
upwelling temperature threshold T_{moc}	2.44	0.30%
variable upwelling velocity fraction w_{var}	0.20	0.14%
north south heat coefficient κ_{ns}	0.91	0.10%
land ocean warming ratio R_{lo}	0.14	0.07%
SST to mixed–layer temperature ratio α	0.05	0.06%
polar sink water to mixed–layer temperature ratio β	0.20	0.02%
mixed–layer depth h	18.3	0.01%
initial upwelling velocity w_0	0.35	0.00%

Table 4.6: Climate system parameter uncertainty for temperature in 2100 with the A1FI emission scenario — with larger standard deviation for R_{lo} and fixed values for α and T_{moc}.

Parameter name	σ	uncertainty contribution %
climate sensitivity $\Delta T_{2\mathrm{x}}$	0.33	96.40%
ocean vertical diffusivity K	0.49	2.75%
land ocean heat coefficient κ_{lo}	0.70	0.38%
land ocean warming ratio R_{lo}	0.23	0.19%
variable upwelling velocity fraction w_{var}	0.20	0.14%
north south heat coefficient κ_{ns}	0.91	0.10%
polar sink water to mixed–layer temperature ratio β	0.20	0.02%
mixed–layer depth h	18.3	0.01%
initial upwelling velocity w_0	0.35	0.00%

The net radiative forcing due to all the different aerosol components remains one of the largest sources of uncertainty in climate modelling. This is due to the multiplicity of different sources of aerosols, their heterogeneous distribution, and difficulties in measuring and estimating the forcing contribution of each type of aerosol. Estimates of 20th–century climate sensitivity are compromised by this uncertainty because of the complementary role of aerosols, that is, there is a negative correlation between estimated aerosol forcing and climate sensitivity (*Meinshausen*, 2006); higher climate sensitivities are associated with lower net aerosol forcing and vice versa.

In order to represent the uncertainty and prior distribution for total aerosol forcing AF_{tot}, one parameter for direct fossil fuel sulfate aerosol forcing in 2005, AF_{soxi}, was chosen to allow for uncertainty in all the direct aerosol forcing components, based on the AR4 estimate for total direct aerosol in 2005 of -0.5 W m^{-2}, with an uncertainty range of $\pm$ 0.4 W m^{-2} (*IPCC*, 2007b). This includes organic carbon, black carbon, sulfate and NO_x aerosols from fossil fuels and biomass burning. The total indirect aerosol forcing was scaled as linearly proportional to the direct forcing,

Table 4.7: Climate system parameter uncertainty for temperature in 2100 with the A1FI emission scenario — with aerosol forcing added.

Parameter name	σ	uncertainty contribution %
climate sensitivity ΔT_{2x}	0.33	70.44%
aerosol forcing AF_{soxi}	0.40	26.75%
ocean vertical diffusivity K	0.49	1.97%
land ocean heat coefficient κ_{lo}	0.70	0.43%
land ocean warming ratio R_{lo}	0.23	0.18%
north south heat coefficient κ_{ns}	0.91	0.12%
variable upwelling velocity fraction w_{var}	0.20	0.09%
polar sink water to mixed–layer temperature ratio β	0.20	0.01%
mixed–layer depth h	18.3	0.01%
initial upwelling velocity w_0	0.35	0.00%

according to the historical aerosol forcing results produced by MAGICC. The ratio of total indirect to total direct aerosol forcing for each year 1900 to 2005 was first established, and then the average of the annual values was calculated, which was found to be 2.38. Accordingly, the indirect forcing component of the total model radiative forcing was then replaced by 2.38 times the direct forcing. The AR4 best estimate for indirect forcing in 2005 is -0.7 W m^{-2}, with an uncertainty range of -0.3 to -1.8 W m^{-2}; the total range of aerosol forcing uncertainty is covered by the sum of the direct plus scaled indirect effect as a prior estimate.

The results for the uncertainty analysis with AF_{soxi} included are set out in Table 4.7. The aerosol forcing AF_{soxi} contribution to the total uncertainty is close to 27%, while the climate sensitivity ΔT_{2x} proportion has dropped to about 70%. This demonstrates the relative significance of the aerosol forcing parameter and its close relationship to ΔT_{2x}.

4.2.4 Summary

The uncertainty analysis presented above provides one way of estimating the uncertainty in the global–mean temperature change results produced by MAGICC for the primary climate system parameters that determine the model's temperature response to changes in greenhouse–gas concentrations. In addition, the relative contribution of individual parameters to the overall uncertainty can be separated out with this technique.

Climate sensitivity ΔT_{2x} is the dominant contributor to the uncertainty in global–mean temperature results produced by MAGICC. This again raises the question of what is the 'correct' value to use for this parameter, a fixed quantity based on its equilibrium setting or effective value, a 20th-century value derived from fitting to observations, or one which is allowed to vary over time that reflects some state–dependency. The answer lies, in part, on the issue under investigation and the purpose to which MAGICC's results will be applied, taking into account the time horizon for projections.

If uncertainty in aerosol forcing AF_{soxi} is included, then it is the second most important contributor to the uncertainty in the climate system response for a given set of emissions. Aerosols

affect temperature by their direct physical mechanism, but make it harder to infer the climate sensitivity from historical observations, since it is difficult to isolate and then estimate the aerosol forcing. The aerosol forcing uncertainty contribution is followed by the ocean vertical diffusivity settings K and Γ. The remaining parameters are relatively minor contributors, although their significance might change if the uncertainty in land, ocean and hemispheric temperature changes were to be considered, as was done in the sensitivity analysis of Chapter 3. This has not been explored further here.

The prior distribution and corresponding standard deviation specified for each parameter can affect the relative importance of particular parameters, although this applies principally to the 'minor placings'. The CMIP3 derived distributions can suggest standard deviations that may be too small, as seems to be the case for the R_{lo} parameter as compared to historical temperature observations. In addition, the CMIP3 calibration excluded some of parameters, such as α, that should perhaps have been included. On the other hand, the introduction of Γ may warrant more attention than has been given in this research, particularly in relation to the shape of the ocean temperature change profile.

Another approach to checking the parameter distributions using historical observations to constrain the prior distributions is investigated in the next section using a Bayesian Monte Carlo method.

4.3 MCMH and the Climate System

4.3.1 The Monte Carlo Metropolis–Hastings algorithm

The next approach to considering the climate system parameters and their uncertainty is based on Bayesian statistics, in which prior Probability Density Functions (PDFs) of the parameters are refined using historical observations to obtain posterior PDFs, which can then form the basis for model projections. Model parameters were first assigned initial or expert prior PDFs and then a Monte Carlo Markov Chain with Metropolis–Hastings algorithm (MCMH) program was executed, sampling the prior PDFs to generate random parameter sets. The parameter sets were then used in turn to run MAGICC and produce 20th–century temperature change results. The MCMH program then compared the model results against corresponding 20th–century historical observations, testing the parameter sets based on the likelihood that the modelled values fit the observations. The outcome was a series of accepted parameter sets that form the basis for new posterior PDFs.

The posterior distributions can then be used, together with an emission scenario, to project global–mean temperature and CO_2 concentration changes. This leads to a probability distribution for these future changes (which can then be used as a basis for policy making and for risk assessments).

The MCMH program used for this work is based on a program by Jens Kattge (refer *Knorr and Kattge*, 2005), which was adapted to work with MAGICC. The theory behind it is presented in *Mosegaard and Tarantola* (1995) and *Mosegaard and Sambridge* (2002), and is briefly outlined below, following *Tomassini et al.* (2007). The latter pointed out that this type of Bayesian statistical approach provides a consistent statistical framework in which assumptions can be clearly stated.

It also allows sensitivity and robustness studies to be performed. They also noted the importance of addressing uncertainties associated with observational error and natural climate variability.

The general form of the Bayesian method takes a vector of parameters θ = (θ_1, θ_2, ..., θ_p) and a vector of observations y = (y_1, y_2, ..., y_m), from which the multivariate posterior probability density of parameters is calculated according to Bayes' theorem (*Tomassini et al.*, 2007):

$$p(\theta|y) \propto l(y,\theta)p(\theta), \tag{4.2}$$

where $l(y,\theta)$ is the likelihood function (the conditional probability density of the observations y given the parameters θ) and $p(\theta)$ is the prior probability density for the vector of parameters. The likelihood function is:

$$l(y,\theta) = p_\epsilon[y - y_M(\theta)] \tag{4.3}$$

where $y_M(\theta)$ is the results from the deterministic climate model (in this case, MAGICC), and p_ϵ is the probability density function of a random variable ϵ with E[ϵ] = 0.

Uncertainties in the observations are taken into account using the information provided with the respective data sets. In addition, the observations are assumed to be independent and, in this study, normally distributed from each other. This is a reasonable assumption if the observational errors are large and the process noise, i.e., climate variability, is independently distributed. In practice some of these stipulations breakdown, with certain observations having noticeable correlations. Indeed, one of the reasons for using land−ocean and Northern−Southern Hemisphere temperatures was to minimise these correlations.

Assuming independent and identically distributed observations, then the likelihood function is:

$$l(y|\theta) = \prod_{i=1}^{n} \frac{1}{\sqrt{2\pi\sigma_i^2}} \exp\left(-\frac{1}{2}\left\{\frac{f(\theta,t_i) - y_i}{\sigma_i}\right\}^2\right) \tag{4.4}$$

where $f(\theta,t_i)$ is the model output of observation y_i given the set of parameters θ. The likelihood of a set of n independent observations is the product over the likelihoods of individual observations y_i at times t_i. Here, it is assumed that each observation is sampled independently from a normal distribution with a mean x_i and standard deviation σ_i. This standard deviation allows for the uncertainty in the observations and internal natural variability that is not captured by the model. The work of *Drost et al.* (2011) suggests that the standard deviation of indices such as the global–mean, land−ocean and Northern−Southern Hemisphere temperature anomalies for detrended observations and AOGCM control runs on decadal time scales are quite small (generally less than 0.1).

Further consideration of the climate variability component may however still be needed, although this is taken as being stationary in the long run. If there are significant correlations between the observations and natural variability then a different likelihood function would be required.

It is difficult to separate natural variability from the underlying trend over the relatively short time periods covered by the available data, especially for the carbon cycle. One way around this is to consider a control run from a complex model to represent climate variability, as was done in *Tomassini et al.* (2007). However, the carbon cycle would also need to be addressed. For

the purposes of this study it was decided not to further complicate matters; future investigations could usefully investigate this issue, although it is not expected to impact very much on the results achieved here.

Bayesian Monte Carlo methods have also been applied in other related studies, for calibrating both simple and intermediate complexity Earth system models; the run–times and costs preclude this technique being applied to complex coupled models such as AOGCMs.

Urban and Keller (2010) combined two simple models, an energy balance model, similar in concept to MAGICC called DOECLIM (Kriegler, 2005, PhD thesis), and a box model that represents the overturning circulation of the Atlantic ocean to investigate the risk of an anthropogenic collapse of the Atlantic Meridional Overturning Circulation (AMOC). They applied an MCMH algorithm to estimate the model parameters from observational data that included atmospheric CO_2 concentrations, ocean carbon fluxes, HadCRU surface temperatures, ocean heat uptake and AMOC strength estimates. A slightly more complex likelihood function was used with, in addition to a standard deviation, a statistical parameter for a first–order autoregressive process to better account for autocorrelation. This was also intended to deal with both measurement uncertainty and natural variability.

An MCMH algorithm was also utilised by *Ricciuto et al.* (2008) for their carbon cycle model calibration. They used a modified likelihood function similar to *Urban and Keller* (2010), although the *Ricciuto et al.* (2008) function assumes that all the observations have the same standard deviation of total error. This would appear to be problematic in a different setting, such as an investigation of the combined climate and carbon cycle system where the magnitude of the uncertainties differ significantly across the range of observations. Their results found that autocorrelation was important and ignoring it biased the parameter estimates. However, it is expected that this is less of a problem in the MCMH–MAGICC set-up used here, since it employs decadal averages for the observations rather than annual amounts.

Sansó and Forest (2009) used a variant of the MIT EMIC, running the model using 426 different combinations of 3 parameters drawn from a non–uniform grid. This appears to be a form of Latin Hypercube sampling. As such, it does not select parameters randomly from a prior distribution and is restricted in scope, with only three climate parameters (although these probably account for perhaps 70-80% of the uncertainty) and no carbon cycle. Only observed and modelled surface temperature data were used. The output from the model was then used to create a set of model observations for further analysis with a statistical model involving MCMC, in effect creating a statistical emulator of the EMIC. This study looked at the covariance matrix involved in their probability distribution to address the issue of natural variability, estimating this matrix from GCM control runs. They found that their results were impacted by the choice of values in the covariance matrix. However, they were using only surface temperature change observations organised as a temperature difference between means and decadal means across zonal bands, observations which may well be correlated, in which case a covariance matrix is required. It is less clear that this is required for the globally averaged observations used in the MCMH–MAGICC algorithm, although it would be good to test this at a later date. However, control runs from an Earth system model would be required in the case of calibrating the combined climate–carbon cycle system that is the goal of this research. As a first step, the investigation of the climate system alone could be tackled

to gauge the significance of the cross correlations and natural variability, although the *Ricciuto et al.* (2008) results suggest that the correlations between the carbon cycle observations, natural variability and the parameter estimates would need to be considered as well.

4.3.2 Applying the MCMH algorithm

Four climate system parameters were selected for use with the MCMH program, ΔT_{2x}, K, κ_{lo} and R_{lo} based on the uncertainty analysis of the previous section and earlier work (aerosol uncertainty is considered later, in Section 4.4). These account for some 99.7% of the uncertainty in global–mean temperature changes out of the nine climate parameters in Table 4.6. Each parameter was assigned a prior mean and standard deviation as per Table 4.8, informed by previous studies and the research work discussed so far in this thesis. The distributions for ΔT_{2x} and K are wider than the CMIP3 calibrated values alone would suggest, since these models do not cover the full range of uncertainty for climate sensitivity and ocean heat uptake (*Sokolov et al.*, 2010). These 'well-informed' priors mean that the MCMH program is not expected to explore the full model parameter space, but rather only a reduced region of feasible parameter values. The distributions were assumed to be normal PDFs, but truncated to prevent values of zero or less occurring, which would be physically unrealistic and lead to errors in the climate model. Prior normal distributions were used for simplicity, leaving the MCMH algorithm to determine the form of the posterior distribution.

Three sets of observations were chosen as the historical constraints:

1. The historical 1911 to 2010 HadCRUT3 global–mean surface temperature change, arranged into 10 decadal average temperatures;

2. The 1911 to 2010 HadCRUT3 derived land−ocean temperature difference, also arranged into decadal averages;

3. Ten ocean layer temperature changes for 1960–2008 for different layers over the depths 0–700m (SW10).

Observational uncertainty was allowed for in the HadCRU observations based on the stated temperature uncertainties, appropriately combined for the decadal means and decadal mean differences. The surface temperature observations have relatively small uncertainties. It is difficult to assign an overall estimate for the ocean layer temperature change since the ocean temperatures have large uncertainties in time and space. Standard deviations based on the uncertainties provided by *Levitus et al.* (2009) were used for this purpose.

The posterior results for a run with 5,000 iterations are presented in Table 4.8 and the probability density for each of the parameters is shown in Figure 4.1. In order to achieve this result, the observational standard deviations where scaled so as to obtain roughly equal average contributions to the cost function used in the Metropolis–Hastings likelihood acceptance rule, and to ensure the modelled decadal temperature change distributions lie within the observed decadal temperature change distributions. If the observational uncertainty is too small, the climate model decadal results can lie outside the decadal observational range.

These results were not found to be all that sensitive to the number of iterations once a reasonable number of iterations is reached. This is demonstrated here with this same MCMH set-up repeated with 25,000 iterations, with the posterior results shown in Table 4.9 and Figure 4.2. The differences are generally quite small, mostly around the second decimal place, although the means for K and $\kappa_{\rm lo}$ show more differences. There are also some changes in the shape of the distributions evident between the two sets of histograms (Figures 4.1 and 4.2). After having run the MCMH program a number of times, it appears that 10,000 iterations is about the minimum needed to obtain reproducible results. Longer runs refine the posterior results at the cost of more computer time.

The MCMH program, in conjunction with the selected historical observations has successfully refined the prior PDFs. The outcome is a set of revised means and useful reductions in standard deviations, for example, nearly 50% smaller for $\Delta T_{2\rm x}$, about 20% smaller for K and $R_{\rm lo}$, which are very worthwhile reductions for the uncertainty in these key parameters. However, these results do not take into account aerosol forcing uncertainty, which is addressed later (Section 4.4), or uncertainties in the carbon cycle (see Chapter 5).

The correlations between the parameters are considered next, followed by a look at the information gained from the observations by the MCMH analysis.

Table 4.8: Prior distributions and posterior results for key MAGICC climate parameters (5,000 iterations).

parameter name	prior mean	prior σ	post mean	post σ
climate sensitivity $\Delta T_{2\rm x}$	3.00	1.50	3.21	0.76
ocean vertical diffusivity K	1.00	0.50	1.26	0.40
land ocean heat exchange $\kappa_{\rm lo}$	1.50	0.80	1.79	0.69
land/ocean warming ratio $R_{\rm lo}$	1.60	0.20	1.58	0.16

Table 4.9: Prior distributions and posterior results for key MAGICC climate parameters (25,000 iterations).

parameter name	prior mean	prior σ	post mean	post σ
climate sensitivity $\Delta T_{2\rm x}$	3.00	1.50	3.18	0.77
ocean vertical diffusivity K	1.00	0.50	1.11	0.41
land ocean heat exchange $\kappa_{\rm lo}$	1.50	0.80	1.56	0.71
land/ocean warming ratio $R_{\rm lo}$	1.60	0.20	1.54	0.17

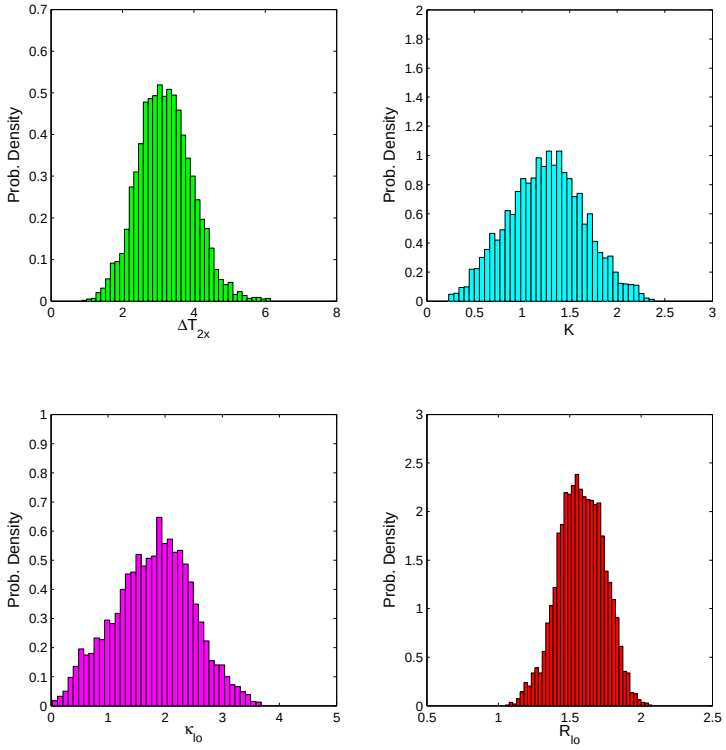

Figure 4.1: Parameter probability distributions associated with Table 4.8.

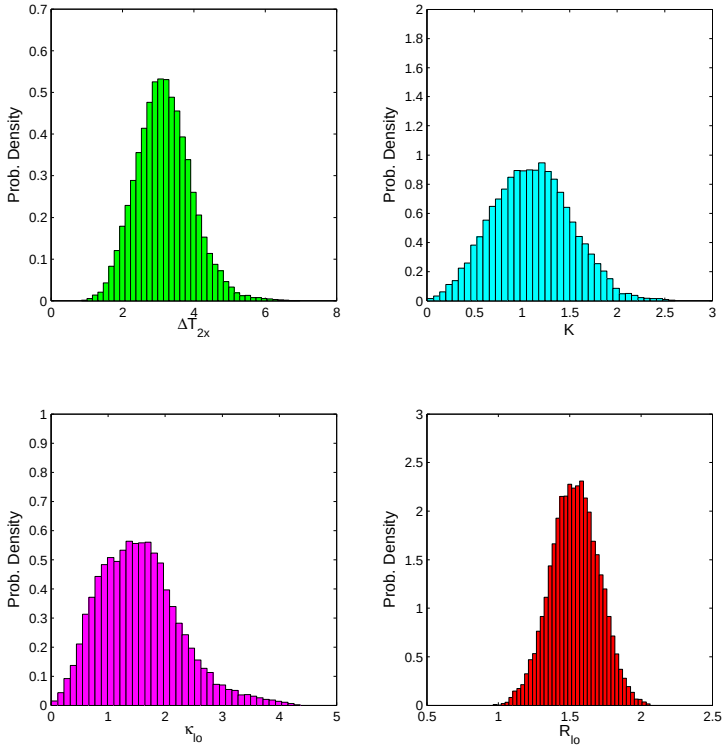

Figure 4.2: Parameter probability distributions associated with Table 4.9.

4.3.3 Correlation results

Another consideration is the correlations between the parameters (Tables 4.10 and 4.11). Examination of the posterior parameter sets reveals only small correlations between the different parameters, which indicates that estimates of the parameter values are not strongly related. There is some sensitivity to the number of iterations evident between the two tables. Joint frequency density plots for three combinations of parameter pairs are included for the larger correlations, climate sensitivity ΔT_{2x} and ocean diffusivity K (Figure 4.3(a)), ΔT_{2x} and the land ocean warming ratio R_{lo} (Figure 4.3(b)), R_{lo} and the land ocean heat exchange coefficient κ_{lo} (Figure 4.3(c)).

The correlation between ΔT_{2x} and K shows a positive value of 0.23 (for 25,000 iterations, Table 4.11), which is as expected, and is consistent with the pairs of results in Section 3.6.1 (it is also similar to the result found by *Forest et al.*, 2008; *Sokolov et al.*, 2010). A larger K means greater heat uptake by the ocean, which tends to reduce the surface temperature changes, and hence a larger climate sensitivity is required to compensate for this, so as to provide a good match to the observed temperature change. The posterior probability density function for these two parameters is shown as a grey–scale contour plot in Figure 4.3(a). The small positive correlation relationship is evident in that diagram, which has roughly elliptical contours associated with simple bi-variate normal distributions with correlations. The fact that the correlation coefficient is not larger may reflect the dominant role of ΔT_{2x}, as already seen in the relative uncertainty contributions in Section 4.2. The three sets of observational constraints were roughly equally weighted in the MCMH program, with the observational uncertainties scaled to achieve this balance. However it might be appropriate to consider a weighting that strengthens the constraint on K (this issue is taken up again in Chapter 6 in the context of the combined climate system and carbon cycle parameters).

Table 4.10: Correlations between MAGICC's climate parameters for 5,000 iteration run.

	ΔT_{2x}	K	κ_{lo}	R_{lo}
climate sensitivity ΔT_{2x}	1.00			
ocean vertical diffusivity K	0.16	1.00		
land ocean heat exchange κ_{lo}	0.06	0.10	1.00	
land/ocean warming ratio R_{lo}	−0.29	0.11	0.16	1.00

Table 4.11: Correlations between MAGICC's climate parameters for 25,000 iteration run.

	ΔT_{2x}	K	κ_{lo}	R_{lo}
climate sensitivity ΔT_{2x}	1.00			
ocean vertical diffusivity K	0.23	1.00		
land ocean heat exchange κ_{lo}	0.15	0.03	1.00	
land/ocean warming ratio R_{lo}	−0.12	0.02	−0.08	1.00

The joint density plot for ΔT_{2x} and R_{lo} (Figure 4.3(b)) indicates the small negative correlation between this pair of parameters, with elliptical contour lines. This is because slightly reduced

values for $R_{\rm lo}$ are required with increased $\Delta T_{2\rm x}$ in order to maintain the land ocean temperature contrast, since a larger $\Delta T_{2\rm x}$ creates a greater temperature increase for a given perturbation to the energy balance, which is then magnified over land relative to the ocean by $R_{\rm lo}$.

A third density plot is included for $\kappa_{\rm lo}$ and $R_{\rm lo}$. They have a small negative correlation coefficient r which is confirmed by the roughly circular density pattern seen in Figure 4.3(c).

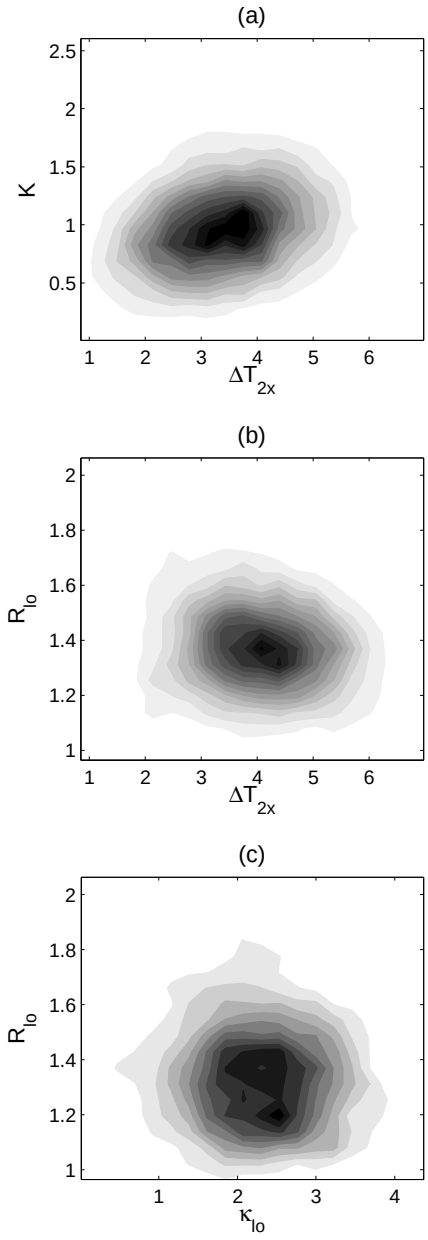

Figure 4.3: Joint climate parameter correlation plots for: (a) $\Delta T_{2\rm x}$ and K; (b) $\Delta T_{2\rm x}$ and $R_{\rm lo}$; (c) $\kappa_{\rm lo}$ and $R_{\rm lo}$; associated with Table 4.11 (25,000 iterations).

4.3.4 Information gained

The prior and posterior parameter distributions are related by a diagnostic likelihood function according to:

$$\mathbf{Prior}(x) \times \mathbf{LF}(x) \propto \mathbf{Post}(x) \tag{4.5}$$

where $\mathbf{Prior}(x)$ and $\mathbf{Post}(x)$ are the prior and posterior distributions of parameter x, and $\mathbf{LF}(x)$ is the likelihood function for that parameter.

Given that the priors are known and the posteriors are the outcome from the MCMH processing, the $\mathbf{LF}(x)$ can be calculated for each of the parameters. Then, if the $\mathbf{Prior}(x)$ was a uniform distribution, it, combined with the $\mathbf{LF}(x)$, would give the $\mathbf{Post}(x)$. Hence, the $\mathbf{LF}(x)$ can be viewed as the information gained from the MCMH and historical observations.

This is demonstrated here for the case with the four climate parameters used previously in Section 4.3.2 and Table 4.9 for 25,000 iterations. The $\mathbf{LF}(\Delta T_{2x})$ indicates that a uniform prior would be transformed into a largely normal distribution with a mean around 3.2°C and the broad prior range reduced, particularly at the lower end. The distributions have been restricted to a 5% to 95% interval and adjusted to avoid being distorted by the very small numbers at the tails, in effect creating boundaries similar to the limits for a uniform distribution.

The result for $\mathbf{LF}(K)$ shows a relatively flat distribution for values between about 1.0 and 1.5 cm^2s^{-1}, then tapering off either side, with a reduction in the likelihood for small values. Either the observations are not able to constrain the setting for K, or the model is not sufficiently sensitive to K for it to matter very much. The previous parameter sensitivity studies and testing of relative parameter uncertainty suggest that the latter is a factor. In addition, the large uncertainty associated with the ocean temperature change observations used with the MCMH–MAGICC program also provides only a weak constraint, unless a different weighting is applied. This topic is re-visited in Chapter 6, Section 6.2.

The likelihood function for the land ocean heat exchange parameter $\mathbf{LF}(\kappa_{\text{lo}})$ reveals that only quite small changes occur from the estimated prior, although there is a slight reduction in the incidence of values over 2.0. The comparison between the prior, indicated by the black curve, and the colour shaded posterior density histogram also shows this limited change.

For the $\mathbf{LF}(R_{\text{lo}})$, there is a reduction in the number of values over 1.6; the difference between the prior and posterior distributions is quite small.

This technique provides a useful tool for checking on the information gained from the historical observations that modifies the parameter prior distributions to arrive at the posterior distributions. Further analysis with the aerosol forcing parameter is introduced in Section 4.4 and continued again in Chapter 6.

4.3.5 Comparison to Chapter 3 results

A new table was constructed to compare the MCMH results discussed in this chapter as compared to the results of Chapter 3. This is Table 4.12, modified from Table 4.9, re-arranged and supplemented by adding the posterior mode column and the revised values from Chapter 3, Table 3.16.

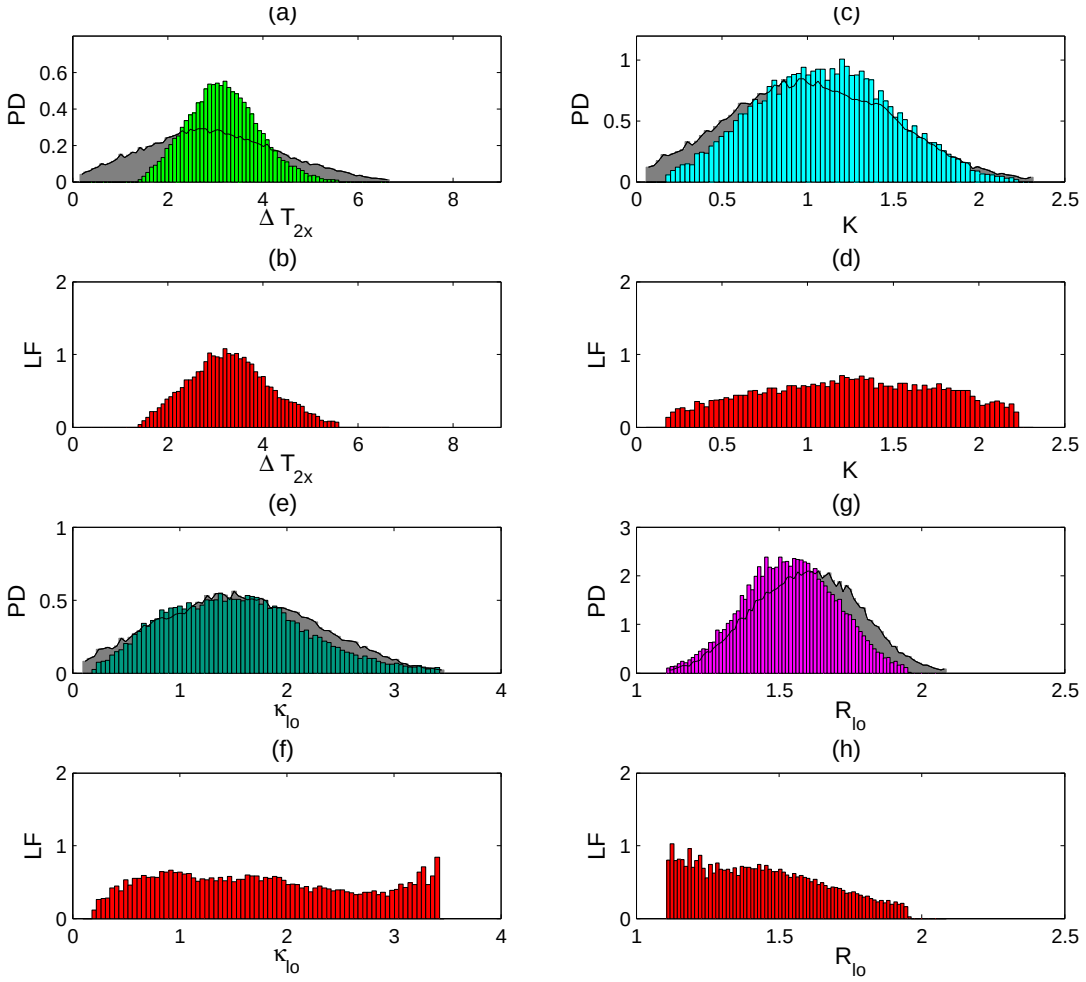

Figure 4.4: Likelihood functions obtained from the prior and posterior distribution for ΔT_{2x}, K, κ_{lo} and R_{lo} associated with Table 4.9 (PD = probability density, LF = Likelihood function). Grey shaded areas and black outline are the prior distribution.

The MCMH approach differs from that tested in Chapter 3, in which an attempt was made to isolate the primary climate system parameters using different sets of observational information gained from largely independent constrains and the requirement that MAGICC match the observed ocean temperature change and ocean heat content changes.

The ocean data pointed to a much lower value for the ocean diffusivity parameter K of about 0.6 cm^2s^{-1}, rather than 2.3 cm^2s^{-1} which was the default setting used for earlier versions of MAGICC. A lower K then leads to a reduced climate sensitivity ΔT_{2x} in order to best fit the observed 20th-century global–mean surface temperature changes.

The observed land ocean warming ratio, as well as the time series for the land-ocean temperature difference, strongly suggest that R_{lo} is around 1.5–1.6 for present day non-equilibrium conditions. The land−ocean temperature difference also indicated that the land ocean heat exchange parameter κ_{lo} appears to be around 2.0 $Wm^{-2}\,^{\circ}C^{-1}$, as compared to the previously standard setting of 1.0 $Wm^{-2}\,^{\circ}C^{-1}$.

However, the results from investigating these same four parameters with the MCMH–MAGICC program does not achieve the same revisions to ΔT_{2x} and K. On the one hand, the MCMH method

improves upon the approach used in Chapter 3 in that uncertainty in the observations and parameters is allowed for, but, in this case, the relatively large uncertainty associated with the ocean temperature change means that this observational constraint has little effect. Consequently K and $\Delta T_{2\mathrm{x}}$ hardly change (in either the mean or the mode), although there is a significant reduction in the spread of the posterior distribution for $\Delta T_{2\mathrm{x}}$.

In addition to reducing the standard distribution for $\Delta T_{2\mathrm{x}}$, the MCMH method also provides the posterior parameter sets which can be used to obtain probabilistic temperature change projections. Examples of this are included in Chapter 6, in the context of results for the combined climate system and carbon cycle parameters. The next section addresses the issue of aerosol forcing as another important uncertainty that has to be allowed for.

Table 4.12: Prior and posterior distributions for four MAGICC climate parameters (25,000 iterations), mode added.

parameter name	Chapter 3 value	prior mean	post mode	post mean	prior σ	post σ
climate sensitivity $\Delta T_{2\mathrm{x}}$	2.20	3.00	3.03	3.18	1.50	0.77
ocean vertical diffusivity K	0.60	1.00	0.94	1.11	0.50	0.41
land ocean heat exchange κ_{lo}	2.00	1.50	1.29	1.56	0.80	0.71
land/ocean warming ratio R_{lo}	1.60	1.60	1.55	1.54	0.20	0.17

4.4 MCMH and Aerosol Uncertainty

The importance of aerosol forcing as a source of uncertainty has been discussed previously (refer Sections 2.5.3 and 4.2.3). Here, aerosol forcing is added to the MCMH analysis to check whether or not is it possible to constrain its uncertainty. The method employed is similar to the previous uncertainty contribution analysis, in that only one parameter is used to represent all of the combined aerosol forcing parameters, the aerosol forcing parameter for the direct effect of fossil–fuel sulfate aerosols AF_{soxi}.

A prior distribution for AF_{soxi}, -0.5 ± 0.4 W m^{-2}, was used to represent the uncertainty for the total direct aerosol forcing in 2005 AF_{dir}, from which the total indirect forcing effect was scaled by a factor of 2.38 as before, to give the total aerosol forcing AF_{tot}. This was treated as a normal distribution but truncated to prevent positive values.

The set-up for the MCMH was modified to include additional observations. Combinations of Northern Hemisphere (NH), Southern Hemisphere (SH) and Northern minus Southern (N$-$S) decadal mean surface temperature changes were tested, although only the results for N$-$S are reported here. The differences between the results from these sets of observations were quite small. Using the N$-$S temperature data provides consistency with the L$-$O method and takes advantage of this derived time series as an extra set of independent observations. One reason for including the N$-$S data is that it might assist in constraining the aerosols forcing given the regional forcing distribution already provided with MAGICC (although there is then an assumption that this information is valid).

An initial test run of 12,000 iterations was conducted with the extra parameter AF_{soxi}, but with no additional observations (Table 4.13). These first results are similar to the previous results without AF_{soxi} (Section 4.3 and Table 4.9), with the main change being an increase in the standard deviations for the $\Delta T_{2\text{x}}$ posterior values. This is not surprising, given the relationship between climate sensitivity and aerosol forcing. What is perhaps a little unexpected is the significant reduction in the posterior mean and σ of AF_{soxi}.

Table 4.13: AF_{soxi} results without additional N−S observations (12,000 iterations).

parameter name	prior mean	prior σ	post mean	post σ
climate sensitivity $\Delta T_{2\text{x}}$	3.00	1.50	3.39	1.08
ocean vertical diffusivity K	1.00	0.50	1.12	0.47
land ocean heat exchange κ_{lo}	1.50	0.80	1.81	0.66
land/ocean warming ratio R_{lo}	1.60	0.20	1.59	0.16
aerosol forcing AF_{soxi}	-0.50	0.40	-0.28	0.10

The results reveal some differences with the addition of the N−S decadal mean observations (Table 4.14). The posterior σ for $\Delta T_{2\text{x}}$ and AF_{soxi} have reduced by similar proportions, although their means have hardly changed. The biggest change is to the mean for κ_{lo}, which suggests that the N−S observations have affected this parameter due to the different area fractions for land and ocean between the hemispheres. Accordingly this data set could be usefully applied as a constraint for the climate system parameters as well.

Table 4.14: AF_{soxi} results with additional N−S observations included.

parameter name	prior mean	prior σ	post mean	post σ
climate sensitivity $\Delta T_{2\text{x}}$	3.00	1.50	3.42	0.85
ocean vertical diffusivity K	1.00	0.50	1.09	0.40
land ocean heat exchange κ_{lo}	1.50	0.80	1.20	0.67
land/ocean warming ratio R_{lo}	1.60	0.20	1.67	0.15
aerosol forcing AF_{soxi}	-0.50	0.40	-0.29	0.08

The correlations structure, Table 4.15, as compared to the earlier table 4.11, has a very similar value between $\Delta T_{2\text{x}}$ and K, but much smaller values between $\Delta T_{2\text{x}}$, κ_{lo} and R_{lo}. This latter result suggests that the N−S observations are additional information that is being effective in helping to constrain κ_{lo} and R_{lo}.

There is a moderately strong negative correlation between $\Delta T_{2\text{x}}$ and AF_{soxi} of -0.35 (see also Figure 4.5). This is as expected, since the observed global–mean temperature change has to be maintained by the $\Delta T_{2\text{x}}$ and AF_{soxi} parameter combinations; an increase in climate sensitivity, which would increase the surface temperature change, is matched by an increase in aerosol forcing, that is, a more negative parameter value, to achieve a greater cooling effect. A similar relationship has been found by others (see, for example, *Meinshausen*, 2006).

Table 4.15: Correlations between MAGICC's climate parameters with AF_{soxi} and N−S added.

	$\Delta T_{2\text{x}}$	K	κ_{lo}	R_{lo}	AF_{soxi}
climate sensitivity $\Delta T_{2\text{x}}$	1.00				
ocean vertical diffusivity K	0.25	1.00			
land ocean heat exchange κ_{lo}	0.10	−0.21	1.00		
land/ocean warming ratio R_{lo}	−0.00	0.01	−0.13	1.00	
aerosol forcing AF_{soxi}	−0.35	−0.03	−0.07	−0.10	1.00

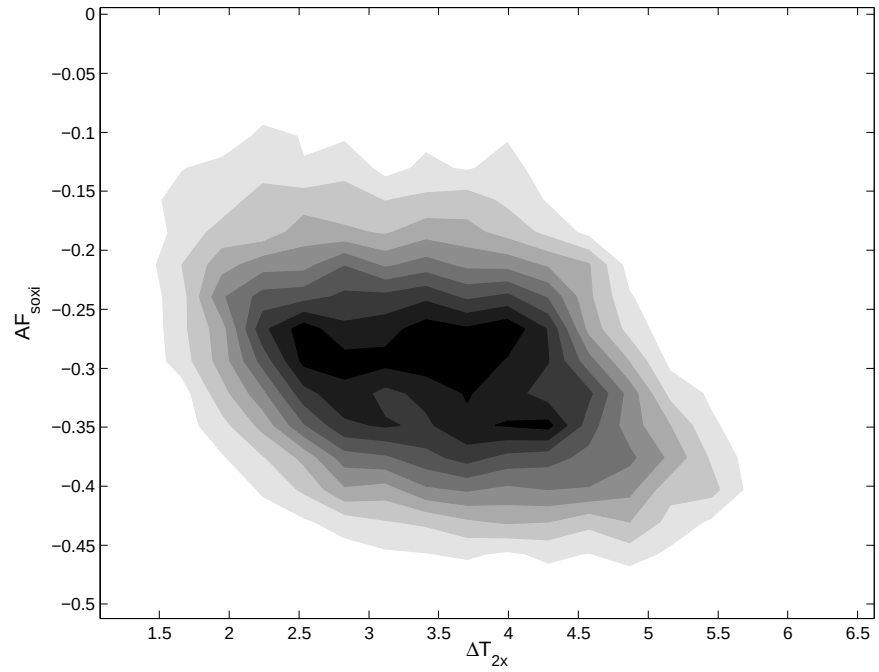

Figure 4.5: Posterior probability density function plot for joint distribution of $\Delta T_{2\text{x}}$ with AF_{soxi}, for Table 4.15 with N−S observations.

4.5 Chapter Summary

This chapter has taken a different approach to looking at the climate system parameters than that adopted in Chapter 3, applying an uncertainty analysis technique and a Bayesian statistical method to constraining the model parameters using observations.

The uncertainty analysis provided an alternative mathematically formulated approach to measuring the relative importance that changes to individual climate parameters make to MAGICC's temperature change results, as compared to the earlier parameter sensitivity testing approach. The two approaches are generally consistent in ranking the parameters. However, the uncertainty analysis has the advantage of reporting on the relative contributions to temperature change based on the variance of the model parameters, rather than an estimated range of feasible values. In either case, the climate sensitivity is by far the dominant parameter for the climate system, with ocean vertical diffusivity the second most significant; the remaining parameters contribute relatively little to the model's global–mean temperature change uncertainty.

This uncertainty analysis could also be applied to the land and ocean temperature change results, as well as the hemispheric temperature change results, if required, to check the relative importance of the parameters (as was done for the parameter sensitivity testing in Chapter 3).

Aerosol forcing is not a climate system parameter, but is an important contributor to the overall uncertainty. Accordingly, a parameter that represents the total aerosol forcing was introduced so that the relative importance of this uncertainty could be quantified. The results (Table 4.7) confirm that this source of uncertainty is significant, being noticeably larger than all of the climate system parameters except for climate sensitivity.

The Monte Carlo Metropolis–Hastings (MCMH) algorithm was introduced in this chapter as an alternative way of constraining MAGICC's climate system parameters using historical observations. It was successfully implemented and tested, and some results from the MCMH–MAGICC program have been presented. Overall, the MCMH program and the historical observations worked together to produce a useful outcome, with posterior distibutions that can be used for estimating future global–mean temperature changes. A comparison of parameters values derived from the different methods of estimating them is presented in Section 4.3.5. The main finding is that the combination of observations and independent constraints used in Chapter 3 led to somewhat different values for the primary climate system parameters than the best estimates derived from the MCMH method. These differences are largely due to the different weight given to the ocean temperature change profile. In Chapter 3 the ocean observations were first used to estimate the ocean parameters, and then estimates for the climate sensitivity were derived, whereas in Chapter 4 the MCMH treats all the observations equally while taking into account their uncertainty.

Other arrangements for the MCMH–MAGICC program are possible, with different parameter combinations, such as including α, w_{var} and κ_{ns}, as well as adding observations such as hemispheric temperature changes, the North$-$South temperature difference, separate temperature changes for the four boxes (NHL, NHO, SHL, SHO), and time series for ocean heat content changes at different ocean depths. Some of these observations are included in the investigations of Chapter 6. Further parameter combinations have not been investigated here, as the uncertainty

analysis indicated that they contribute little to the uncertainties in the projected global–mean temperature change.

The next chapter applies the uncertainty analysis technique and the MCMH algorithm to investigating MAGICC's carbon cycle parameters. The combined climate system and carbon cycle is then examined in Chapter 6.

Chapter 5

The Carbon Cycle

The carbon cycle model is an important feature of MAGICC that justifies regarding it as a simplified Earth System Model (ESM), or as a 'reduced complexity coupled carbon cycle–climate model' (*Meinshausen et al.*, 2009). It has essentially two parts; a terrestrial carbon cycle model, and an ocean carbon cycle model, which are described in Section 5.1.

MAGICC can use either historical emissions to calculate atmospheric carbon dioxide concentrations up to the present, or historical concentrations, after which future carbon dioxide concentrations are calculated according to a given set of emissions. The atmospheric carbon dioxide concentration is then converted to a radiative forcing that, in conjunction with all other forcings, provides the basis for calculating temperature changes.

Uncertainties in the exchanges of carbon between the atmosphere, land and ocean are an important part of the overall uncertainty associated with MAGICC's temperature change projections. One of the aims of this research is to assess these sources of uncertainty and how these can be represented. This chapter examines the uncertainties related to the carbon cycle arising from past observations and model limitations. Parameters are again a necessary part of the model; setting the values of the carbon cycle parameters is difficult owing to the relatively large number of parameters that need to be specified as compared to the limited observational data, particularly for estimating the temperature feedback terms.

The carbon cycle is not included as a component in many of the CMIP3 models, so that changes to atmospheric concentrations can only be provided as external additional CO_2, but then these complex models are missing the temperature feedback effects. On the other hand, some of the C4MIP models do not include non-CO_2 greenhouse–gases and aerosol effects. One of the advantages of MAGICC is that it does attempt to cover these different components, albeit as simplified large–scale radiative forcing factors. Section 5.2 reviews one previous approach to assessing the different contributions to increased temperatures that result from the carbon cycle parameters in the model, rather than the climate system parameters..

The carbon cycle parameters used in the model are introduced in Section 5.3. MAGICC version 6 has been calibrated against ten of the C4MIP carbon cycle models (*Friedlingstein et al.*, 2006), as detailed in *Meinshausen et al.* (2011a). MAGICC has the ability to emulate any one of these models. The sensitivity and uncertainty contribution of the 18 carbon cycle parameters is then investigated. Section 5.5 demonstrates that eight of the parameters account for nearly 99% of the overall uncertainty.

Examination of the available literature and a discussion with Malte Meinshausen found that calibration of MAGICC's carbon cycle against twentieth–century observations does not appear to have been previously attempted. This research program has successfully tackled this gap, as discussed in Section 5.5, using the MCMH algorithm introduced in Chapter 4. The release of observational data produced by the Global Carbon Project (GCP) for land and ocean fluxes was especially helpful in enabling this calibration. The outcome is a posterior parameter distribution for the carbon cycle parameters. The robustness and limitations of the result are discussed in the text.

The combined climate–carbon cycle is examined in Chapter 6, following on from the separate investigations of the climate system in Chapter 4 and the carbon cycle in this chapter.

5.1 Carbon Cycle Model

The carbon cycle in MAGICC is structured around two principal components, a terrestrial model and an ocean model. The terrestrial carbon cycle model is based on *Wigley* (1993), comprising four boxes: the atmosphere, plants, detritus and soil, illustrated schematically in Figure 5.1. Each box is effectively a carbon reservoir that evolves as carbon circulates through the system. The ocean component is represented by an impulse response function, that is, it is descibed as a mathematical relationship rather than the more physically based, but still idealised, terrestrial model.

The basic equation for calculating changes in atmospheric carbon dioxide can be expressed as the net result of fluxes between sources and sinks:

$$\frac{dM}{dt} = 2.123\frac{dC}{dt} = \sum(F_{\text{sources}}) - \sum(F_{\text{sinks}}) \tag{5.1}$$

M is carbon dioxide mass (GtC), C is concentration (ppmv), F_{sources} and F_{sinks} are the carbon fluxes. This is a simple carbon cycle model that allows for atmosphere–to–ocean fluxes and for the main terrestrial sources and sinks. It can be tuned to past concentration changes by inversion calculations (refer *Enting and Pearman*, 1987; *Seigenthaler and Oeschger*, 1987; *Wigley*, 1991b). Further details are also given in *Wigley et al.* (2000). Alternatively:

$$2.123\frac{dC}{dt} = 2.123\frac{\Delta C}{dt} = E(t) - F(t) \tag{5.2}$$

$\Delta C = C - C_0$, is the concentration change from an initial pre–industrial level C_0. $E(t)$ is the net total emissions and $F(t)$ the atmosphere–to–ocean flux, taken as changes relative to an assumed pre–industrial steady state. Emissions E are due to industrial activity I and changes in the terrestrial store, that is the net flux due to land–use changes D_{n} and changes associated with terrestrial feedbacks X:

$$E = I + D_n - X \tag{5.3}$$

Equation 5.2 becomes:

$$2.123\frac{\Delta C}{dt} = I + D_n - F - X \tag{5.4}$$

X represents the missing sink, effectively an amount used to balance the carbon budget when inverting the carbon cycle to match past concentration changes. In MAGICC this is interpreted as a CO_2 fertilisation effect. The CO_2 fertilisation factor β_s is then used to represent the enhancement to Net Primary Production (NPP) from increased atmospheric CO_2 concentrations. The latest version of MAGICC uses a linear combination of two methods, a logarithmic formula and the rectangular hyperbolic parameterisation of *Gifford* (1993) (for details, refer *Meinshausen et al.*, 2011a).

Wigley (1993) states that temperature feedbacks due to changes in temperature and atmospheric carbon dioxide concentration are included in MAGICC, although the early documentation did not provide a clear explanation of these feedbacks. The most recent work, *Meinshausen et al.* (2011a), clarifies this issue and explains that the increase in global–mean temperature is used as a proxy for the climate–related impacts on the carbon cycle due to changes in temperature and moisture. For the terrestrial model, there are four feedback factors, while the ocean has a single temperature feedback factor. Each of the temperature feedbacks is scaled assuming an exponential relationship.

The four terrestrial carbon cycle temperature dependent processes are related to temperature effects on respiration and decomposition. They are the temperature feedback factors for detritus σ_{Q}, NPP σ_{NPP}, respiration σ_{R} and soil σ_{U}.

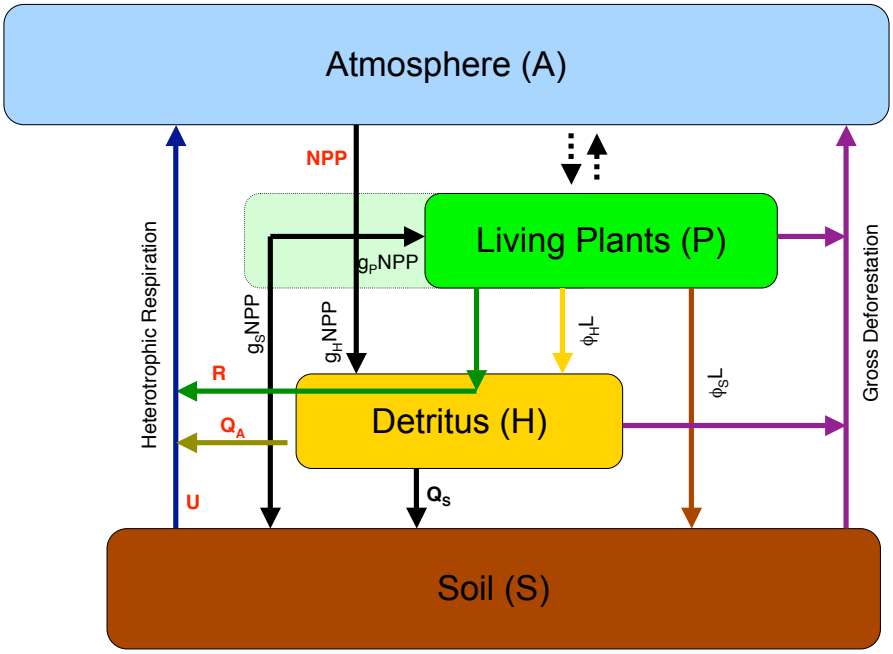

Figure 5.1: Schematic of MAGICC's terrestrial carbon cycle with the carbon pools and carbon fluxes (based on *Meinshausen et al.*, 2011a).

The ocean flux is represented as a convolution integral, following *Maier-Reimer and Hasselmann* (1987) (see also *Wigley*, 1991b; *Meinshausen et al.*, 2011a), which is used to account for all of the carbon taken up by the ocean, i.e, both organic and inorganic carbon, the 'biological

pump' and the 'chemical pump'. The net air–sea flux is proportional to the difference between the atmospheric concentration of carbon dioxide and the carbon dioxide partial pressure in the ocean:

$$F_{\mathrm{ocn}} = k(C_{\mathrm{atmos}} - pCO_2) \tag{5.5}$$

where k is the global average gas exchange coefficient (*Joos et al.*, 2001; *Meinshausen et al.*, 2011a)

The change in carbon $\Delta\Sigma\mathrm{CO}_2(t)$ at time t in the surface ocean is given by the convolution integral of the mixed layer impulse response function r_s and the net air–to–sea flux:

$$\Delta\Sigma\mathrm{CO}_2(t) = \frac{c}{hA}\{\int_{t_0}^{t} F_{\mathrm{ocn}}(t^{'})r_s(t-t^{'})\mathrm{d}t^{'}\} \tag{5.6}$$

The impulse response function for time $t <$one year is:

$$r_s(t) = 1.0 - 2.2617t + 14.002t^2 - 48.770t^3 + 82.986t^4 - 67.527t^5 + 21.037t^6$$

and for $t \geq 1$:

$$r_s(t) = \sum_{i=1}^{6} \gamma_i e^{-\tau_i t} \tag{5.7}$$

where γ_i and τ_i are the partitioning and relaxation coefficients respectively (detailed in *Meinshausen et al.*, 2011a).

The temperature sensitivity of the dissolved carbon, i.e., CO_2 solubility, is parameterised with an exponential expression so that the modelled $p\mathrm{CO}_2$ increases with sea–surface temperatures as given by:

$$pCO_2 = [pCO_2(t_0) + \Delta pCO_2(T_0)]e^{\alpha_T \Delta T} \tag{5.8}$$

where α_T is the temperature sensitivity factor (*Meinshausen et al.*, 2011a).

5.2 Carbon Cycle Parameters

The set of carbon cycle parameters required by MAGICC is listed in Table 5.1. Fifteen are for the terrestrial component and three for the oceanic component of the model. These parameters have been calibrated against ten of the C4MIP carbon cycle models; the calibration procedure is explained in *Meinshausen et al.* (2011a). The carbon cycle calibration was carried out for a total of 14 time series, seven with and seven without temperature feedbacks. Note that this calibration was done with default values of the climate system parameters, with ocean vertical diffusivity at 2.3 $\mathrm{cm}^2\mathrm{s}^{-1}$, ocean–to–land heat exchange enhancement at 1.4, ratio of land to ocean warming equal 1.3, except climate sensitivity $\Delta T_{2\mathrm{x}}$, which was calibrated to match the temperatures of the coupled runs for the model–specific CO_2 concentrations parameters.

The calibrated parameters are:

Table 5.1: MAGICC's carbon cycle parameters.

Parameter name	notation	units
temperature feedback factor, detritus	σ_{Q}	$^{\circ}\mathrm{C}^{-1}$
temperature feedback factor, NPP	σ_{NPP}	$^{\circ}\mathrm{C}^{-1}$
temperature feedback factor, respiration	σ_{R}	$^{\circ}\mathrm{C}^{-1}$
temperature feedback factor, soil	σ_{U}	$^{\circ}\mathrm{C}^{-1}$
CO_2 fertilisation factor	β_s	
CO_2 fertilisation method	β_m	
carbon flux partition, detritus to soil	Φ_{H}	
carbon flux partition, NPP to detritus	g_{H}	
carbon flux partition, NPP to plant	g_{P}	
carbon flux partition, plant to detritus	q_{H}	
initial NPP flux	N_0	GtC/yr
initial plant pool	P_0	GtC
initial respiration flux	$R_{(\mathrm{P},0)}$	GtC/yr
initial detritus pool	H_0	GtC
initial soil pool	S_0	GtC
ocean cc gas exchange scale factor	k	
ocean cc impulse response scale factor	O_{r}	
ocean cc temperature feedback	α_T	

- Four temperature sensitivities, σ_{NPP}, σ_{R}, σ_{Q}, σ_{U};
- Two fertilisation parameters, β_m and β_s;
- Four flux partition parameters, Φ_{H}, q_{S}, g_{P} and q_{H};
- Five fixed initial pool parameters, N_0, $R_{\mathrm{P},0}$, P_0, D_0, S_0;
- Three ocean parameters, k, O_{r} and α_T;
- A reference year for the initial pools, Y_{ref}.

The reference year and initial pool values were taken from each model setup, and then the remaining parameters calibrated so that MAGICC's carbon cycle aligns with each C4MIP model.

This is a total of 13 calibrated parameters plus six fixed parameters, giving a total of 19 parameters; the extra one is the Y_{ref}, a reference year for the start of the model. The 13 parameters were calibrated using the 14 time series according to an optimisation procedure (*Meinshausen et al.*, 2011a). The seven calibrated quantities were:

- Atmospheric CO_2 concentrations;
- Terrestrial carbon uptake;
- Oceanic carbon uptake;
- Net Primary Production;
- Terrestrial living carbon pool;

- Terrestrial dead carbon pool;
- Total respiration.

5.3 Parameter Sensitivity and Uncertainty

This part of the research program is concerned with assessing the relevant parameter sensitivities and uncertainty of the carbon cycle component.

Carbon cycle uncertainty is one of the main contributors to uncertainty in climate projections (*Denman et al.*, 2007), ranking as perhaps the third most important contributor to uncertainty for global–mean temperature change projections after emissions and climate sensitivity (*Wigley and Raper*, 2001). Although climate sensitivity is the dominant source of uncertainty, the carbon cycle uncertainty exceeds emissions–related uncertainties in the short term, to around 2040 (*Wigley*, 1994). Importantly, the interaction between the climate and carbon cycle is largely a positive feedback (*IPCC*, 2007b). Furthermore, these interactions are important for stabilisation scenarios (*Harvey*, 1989). Net emissions from past land use and the term used to balance the carbon budget (missing sink or fertilisation amount) appear to be the primary carbon cycle uncertainties (*Wigley*, 1994; 2000a). There is uncertainty in future oceanic uptake and terrestrial storage of carbon, together with a number of temperature–dependent feedback processes, such as soil respiration and ocean carbon uptake (*Plattner et al.*, 2001; *Jones et al.*, 2003). In addition, there is the potential for the oceanic and terrestrial sinks to reach saturation and cease to be net carbon sinks (*Le Quéré et al.*, 2007; *Canadell et al.*, 2007).

To illustrate the significance of the carbon cycle, Figure 5.2 shows a plot of the atmospheric CO_2 concentration and temperature change results from MAGICC for the A1FI scenario. By 2100, the difference between having the carbon cycle temperature feedbacks on or off is almost 100 ppm for CO_2 and nearly 0.3°C for the temperature change, using the model's standard settings.

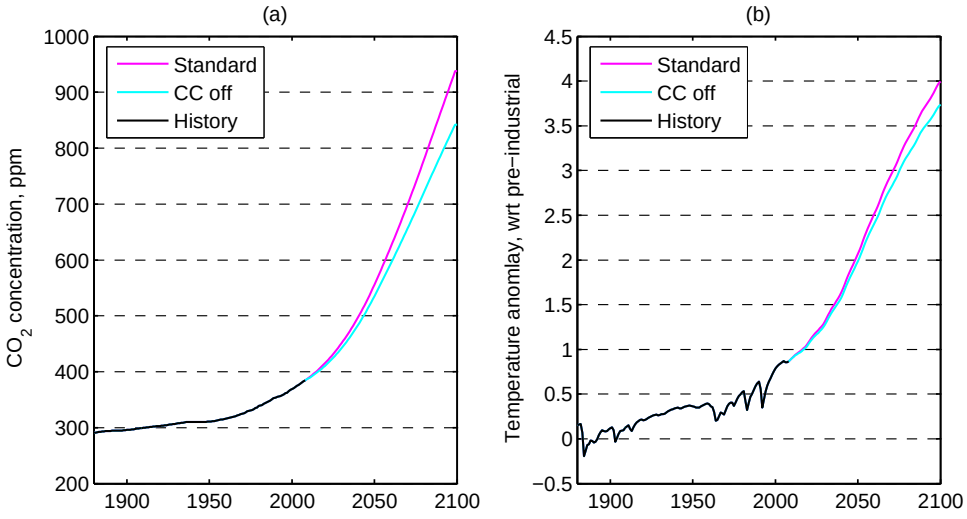

Figure 5.2: MAGICC A1FI projections with (magenta lines) and without (cyan lines) the carbon cycle feedback for: (a) CO_2 concentrations and, (b) temperature change.

The projected uncertainty in CO_2 by 2100 for the SRES A2 scenario from the C4MIP models was reported as a range between 732 and 1025 ppm (*Friedlingstein et al.*, 2006). It is possible to represent this range in MAGICC using a single parameter, the fertilisation factor β_s (although the values for β_s will be extreme), as illustrated in Figure 5.3. The temperature difference in 2100 between the low and high β_s settings is 0.81°C.

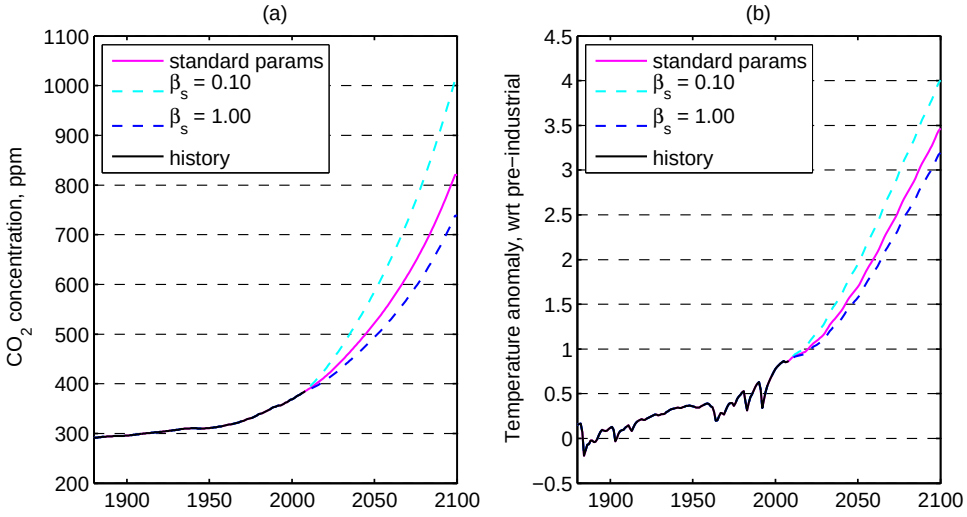

Figure 5.3: MAGICC A2 projections for: (a) CO_2 concentrations, and (b) temperature change, for high and low fertilisation factor parameter settings.

As an alternative guide to the importance of the carbon cycle parameters, a mean and standard deviation were calculated for each of the carbon cycle parameters based on the C4MIP calibrated values (*Meinshausen et al.*, 2011a). The seven most important parameters (determined from uncertainty testing as per the next section, Section 5.4) were all set to upper and lower bounds based on plus and minus two standard deviations. A normal distribution was assumed for all the parameters. The oceanic scale impulse response lower bound was cut off at 0.001 to avoid values of zero or less. The resulting temperature ranges (Figure 5.4) show a very wide temperature range, illustrated here for both the SRES A1FI scenario and a 450 ppm CO_2-equivalent stabilisation scenario. The very low temperature changes are due to the non-linear feedback response, especially for the ocean response which is very sensitive to small values of the impulse response scale factor, values which may not be supported by fitting to observations (addressed in Section 5.5).

The approach adopted for investigating carbon cycle uncertainty was to first test the relative contribution of each of the carbon cycle parameters to the uncertainty in projected temperature changes and CO_2 concentrations using the uncertainty analysis technique introduced in Chapter 4. This is addressed in the next section. Then, guided by these results, better estimates for a sub-set of these parameters were investigated using the Monte Carlo Markov Chain with Metropolis–Hastings (MCMH) algorithm, which brings in historical observations to assist in constraining the probable range of the parameter values.

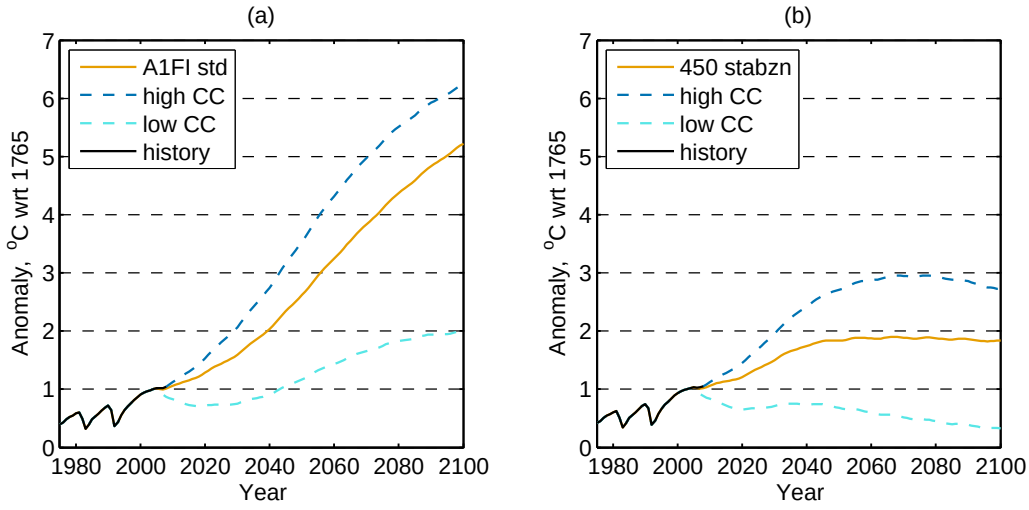

Figure 5.4: MAGICC carbon cycle results, with upper and lower limits set using two standard deviation ranges for seven of the carbon cycle parameters that most affect the temperature in 2100 for (a) A1FI emission scenario and, (b) 450 ppm CO_2-equivalent stabilisation scenario.

5.4 Uncertainty Testing

This section investigates the uncertainty in MAGICC's carbon cycle, using the same method as for the climate parameters (Chapter 4, Section 4.2). An initial range of values for each of the carbon cycle parameters, along with its mean and standard deviation, was determined from the C4MIP calibrated values (*Meinshausen et al.*, 2011a). The model was then executed in a similar way as before for the climate system parameters, varying each of the carbon cycle parameters in turn by 1% of its standard deviation so as to determine the effect that small alterations in the parameter values make to the resultant global–mean temperature change and CO_2 concentration in 2100.

The carbon cycle component of MAGICC is 'switched on' at a selected year; up to that point, the atmospheric greenhouse–gases are prescribed from historical concentrations. Thereafter, carbon dioxide concentrations evolve using pre–determined historical emissions data to the present and then according to some emissions scenario for the future. For the results presented next, historical concentrations up to 1960 were used, then historical emissions to 2010, followed by emissions based on the SRES A1FI scenario to 2100.

The results for uncertainty in temperature in 2100 are given in Table 5.2, with an overall uncertainty given by a standard deviation of 0.69°C. The top eight parameters collectively account for almost 99% of the uncertainty (98.93%). The four terrestrial temperature feedback factors feature prominently in these eight. The CO_2 fertilisation factor is the second most sensitive parameter after the respiration feedback factor. *Ricciuto et al.* (2011) also identified the CO_2 fertilisation factor and the respiration temperature sensitivity as the two key terrestrial carbon cycle parameters for their model (the University of Victoria Earth System Climate Model).

Similar results were obtained for the carbon dioxide concentration amount in 2100, as shown in Table 5.3, where the overall standard deviation is 240 ppm.

Table 5.2: Carbon cycle parameter uncertainty for temperature in 2100 with the A1FI emission scenario.

parameter name	σ	uncertainty contribution %
temperature feedback factor, respiration σ_{R}	0.12	27.02%
CO_2 fertilisation factor β_s	0.29	21.50%
temperature feedback factor, NPP σ_{NPP}	0.03	13.88%
ocean cc impulse response scale factor O_{r}	0.88	13.07%
carbon flux partition, NPP to plant g_{P}	0.24	9.61%
temperature feedback factor, detritus σ_{Q}	0.20	7.07%
temperature feedback factor, soil σ_{U}	0.07	6.39%
initial NPP flux N_0	6.62	0.38%
carbon flux partition, plant to detritus q_{H}	0.19	0.26%
initial plant pool P_0	200	0.26%
initial detritus pool H_0	21.6	0.25%
initial respiration flux $R_{(\mathrm{P},0)}$	1.22	0.22%
ocean cc temperature feedback α_T	0.01	0.05%
carbon flux partition, detritus to soil Φ_{H}	0.02	0.02%
initial soil pool S_0	392	0.01%
CO_2 fertilisation method β_m	0.44	0.01%
carbon flux partition, NPP to detritus g_{H}	0.21	0.00%
ocean cc gas exchange scale factor k	0.74	0.00%

Table 5.3: Carbon cycle parameter uncertainty for CO_2 in 2100 with the A1FI emission scenario.

Parameter name	σ	uncertainty contribution %
temperature feedback factor, respiration σ_{R}	0.12	28.25%
CO_2 fertilisation factor β_s	0.29	20.09%
temperature feedback factor, NPP σ_{NPP}	0.03	14.36%
ocean cc impulse response scale factor O_{r}	0.88	11.90%
carbon flux partition, NPP to plant g_{P}	0.24	10.35%
temperature feedback factor, detritus σ_{Q}	0.20	7.08%
temperature feedback factor, soil σ_{U}	0.07	6.54%
initial NPP flux N_0	6.62	0.32%
carbon flux partition, plant to detritus q_{H}	0.19	0.27%
initial plant pool P_0	200	0.25%
initial detritus pool H_0	21.6	0.24%
initial respiration flux $R_{(\mathrm{P},0)}$	1.22	0.20%
carbon flux partition, NPP to detritus g_{H}	0.21	0.07%
ocean cc temperature feedback α_T	0.01	0.03%
carbon flux partition, detritus to soil Φ_{H}	0.02	0.02%
initial soil pool S_0	392	0.01%
ocean cc gas exchange scale factor k	0.74	0.00%
CO_2 fertilisation method β_m	0.44	0.00%

5.5 Constraining the Carbon Cycle Parameters

The approach to constraining the carbon cycle parameters adopted here continues with the application of the MCMH program used in Chapter 4, re-configured to use selected prior carbon cycle parameter PDFs in conjunction with a set of historical observations.

Six of the carbon cycle parameters were selected; the top five in Tables 5.2 and 5.3 and the carbon flux partition, plant to detritus q_{H}. These represent about 85% of the overall carbon cycle uncertainty for temperature and CO_2 concentration changes in 2100.

The two temperature feedback factors for detritus σ_{Q} and soil σ_{U} were not included in order to limit the number of parameters being dealt with. None of the initial pools were included either at this stage because of the lack of observations with which to help constrain them. A choice of parameters has to be made for the experiments and time restricted the amount of testing that could be carried out.

The mean and standard distribution σ for each of the selected six parameters (Table 5.4) was determined from the C4MIP calibrated parameter settings provided with MAGICC (*Meinshausen et al.*, 2011a). The distributions were assumed to be normal, but some of the distributions have to be truncated to prevent invalid parameter values.

Table 5.4: Prior distributions for key MAGICC carbon cycle parameters — these six contribute to some 85% of the uncertainty in CO_2 and temperature changes (out of 18 parameters).

parameter	mean	σ	distribution %
temperature feedback factor, respiration σ_{R}	-0.01	0.12	normal
CO_2 fertilisation factor β_s	0.60	0.29	truncated normal
temperature feedback factor, NPP σ_{NPP}	-0.01	0.03	truncated normal
ocean cc impulse response scale factor O_{r}	1.42	0.88	normal
carbon flux partition, NPP to plant g_{P}	0.63	0.24	truncated normal
carbon flux partition, plant to detritus q_{H}	0.94	0.20	truncated normal

Historical observations used by the MCMH program for this carbon cycle only investigation were the global–mean temperature change (1850–2010, HadCRUT3), land and ocean carbon fluxes as estimated by the Global Carbon Project (1959–2009, GCP) (*Friedlingstein et al.*, 2010; *Le Quéré et al.*, 2009), and atmospheric CO_2 concentration changes from Mauna Loa (1959–2010) (Dr. Pieter Tans, NOAA/ESRL (www.esrl.noaa.gov/gmd/ccgg/trends/) and Dr. Ralph Keeling, Scripps Institution of Oceanography (scrippsco2.ucsd.edu/)). Decadal means were used to smooth out the natural inter–annual variability, which is not represented in MAGICC.

5.5.1 Initial results

The first set of results presented here is for a run of 120,000 iterations with priors based on Table 5.4, but with some small changes as per Table 5.5. The shape of these prior truncated normal distributions is shown in Figure 5.5. The MCMH program then produced posterior distributions, taking into account the historical observational data, with the results included in Table 5.5 and Figure 5.6.

The MCMH program has worked successfully. This is the first time that this method has been applied to constraining MAGICC's carbon cycle parameters (similar methods have been applied to other simple carbon cycle models, for example, *Ricciuto et al.*, 2008). The robustness of this result and its limitations are discussed in the next section.

Noteworthy features of the result achieved here are the significant reductions in the distributions for the CO_2 fertilisation factor β_s and the ocean carbon cycle impulse response scale factor O_r. The other parameters have only relatively small changes to their mean values and standard deviations.

Table 5.5: Priors and posterior distributions for key MAGICC carbon cycle parameters from MCMH program (120,000 iterations).

parameter	prior mean	post mean	prior σ	post σ
temperature feedback factor, respiration σ_R	-0.01	-0.05	0.15	0.12
CO_2 fertilisation factor β_s	0.50	0.70	0.50	0.22
temperature feedback factor, NPP σ_NPP	-0.01	-0.00	0.05	0.04
ocean cc impulse response scale factor O_r	1.50	0.97	1.00	0.24
carbon flux partition, NPP to plant g_P	0.50	0.54	0.25	0.21
carbon flux partition, plant to detritus q_H	0.80	0.74	0.20	0.15

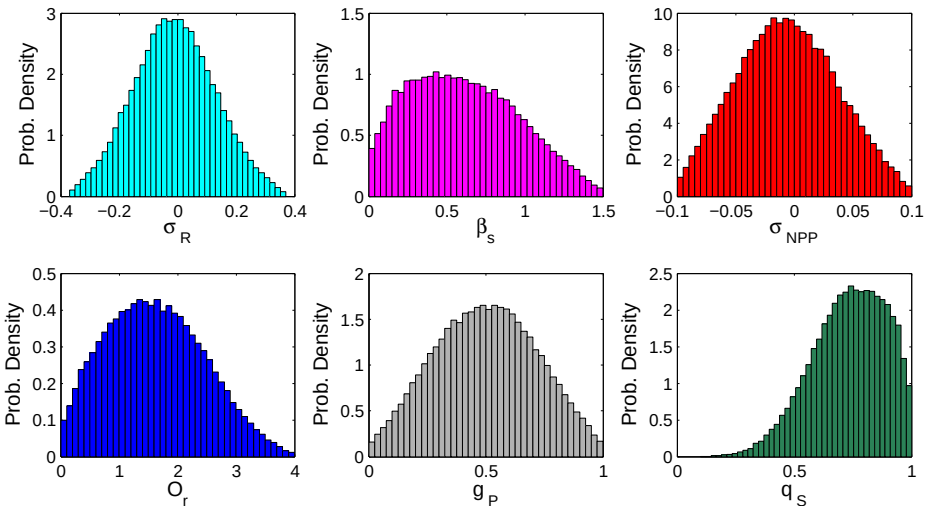

Figure 5.5: Carbon cycle prior distributions (120,000 iterations).

The decadal model distributions were verified against the observed decadal distributions to check for their overlap (refer Figure 5.8). Some adjustment of the observational uncertainties within the MCMH program was required to balance out the relative contributions of the different observational uncertainties to the overall uncertainty, and to ensure that the modelled distributions lie within the observational distributions. This is to both balance out the relative weights of the observational constraints (i.e., the individual components of the cost function), and to avoid the mismatch between the distributions that can otherwise occur. For example, the very small amount

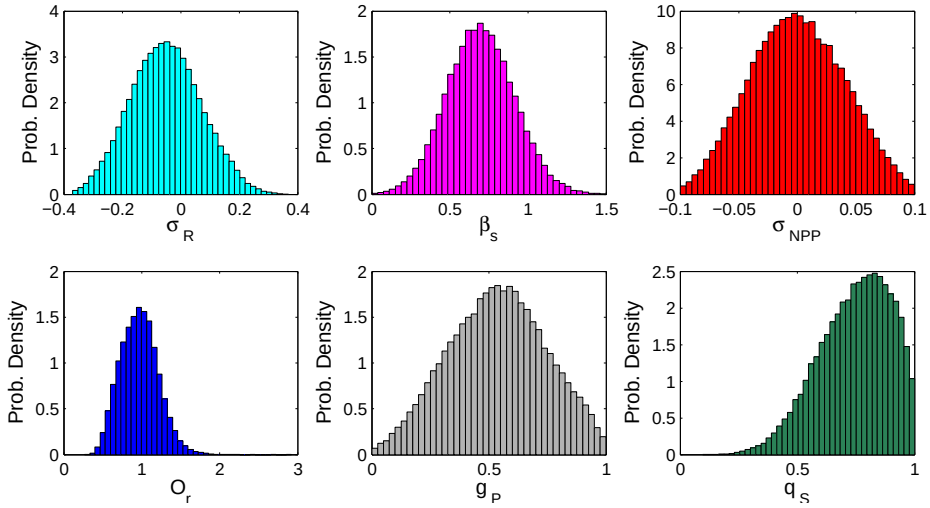

Figure 5.6: Carbon cycle posterior distributions (120,000 iterations).

of uncertainty associated with the observed CO_2 concentrations provides an impossibly tight envelope within which to fit the modelled CO_2 concentration. Another illustration from an early test run is included, Figure 5.7, which shows, in this case for the ocean flux, model results whose distributions fall outside the distributions for each of the five decadal observations.

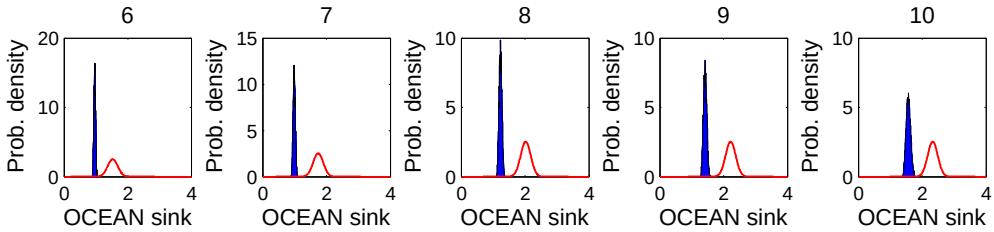

Figure 5.7: Illustrative carbon cycle decadal probability density distributions for modelled ocean carbon flux results and observations, showing the potential for a mismatch between the modelled results (the shaded blue histogram) and the observed distribution (the red curve).

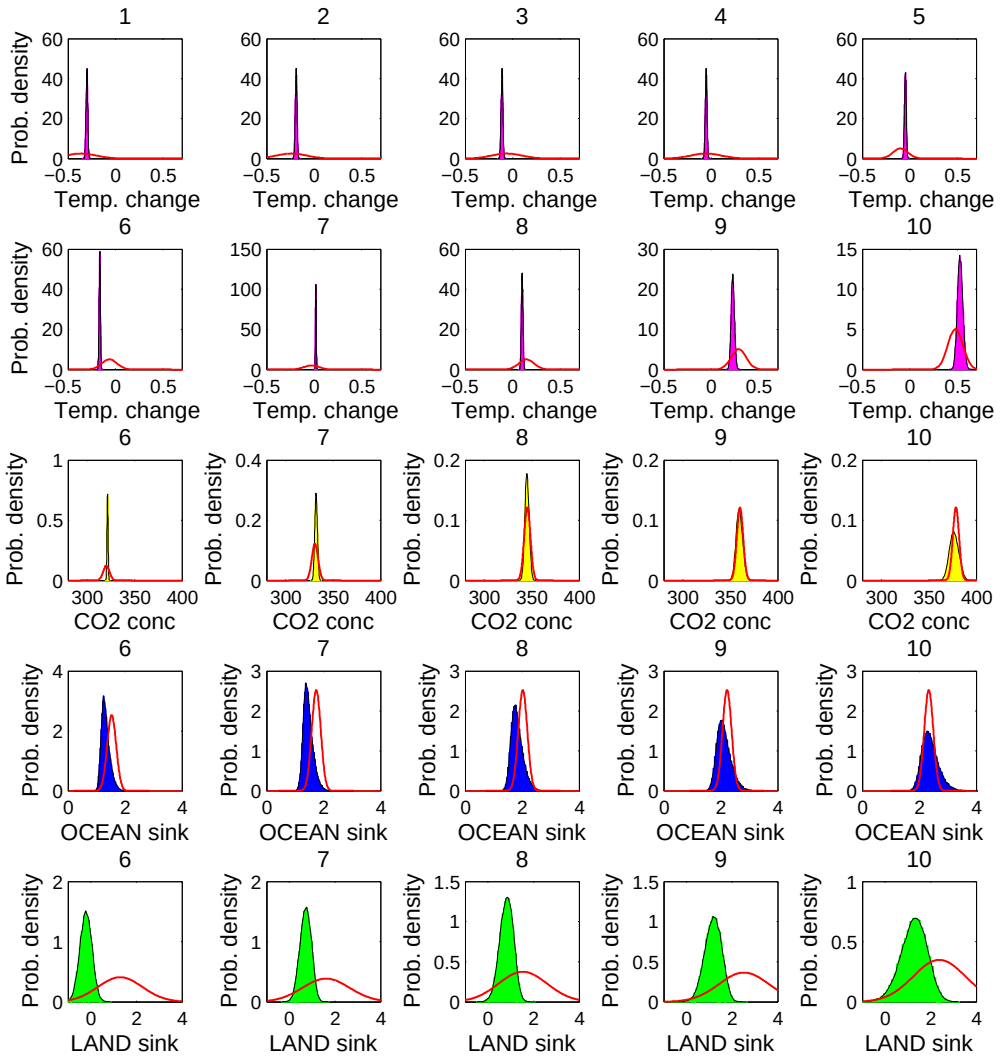

Figure 5.8: Carbon cycle decadal probability density distributions for modelled results (the shaded histograms) and observations (the red curve). The top two rows are for temperature change, then CO_2 concentrations, the ocean carbon flux and lastly the land carbon flux. The temperature change has 10 plots, one for each decade of observations, whereas the last three rows have only five.

The correlations between the posterior parameters were also tested for this inital set of carbon cycle MCMH results, as per Table 5.7. The correlations of the parameters before they were conditioned by the observations, that is, the prior parameter distributions, are included in Table 5.6. This confirms that they have no prior correlation, which is the expected result since the parameters were generated by a psuedo–random process. The MCMH program conditions these priors by running MAGICC and comparing the model results to the observations, the result of which is a set of accepted parameter sets which are the posterior distributions. The change in the correlation structure therefore provides some information about how successfully the observations have independently constrained the parameters. High correlations indicate that the observations have not been able to separately inform the parameter values, while low correlations suggest the observations have independently informed the parameters.

Table 5.6: Prior correlations between MAGICC carbon cycle parameters (120,000 iterations).

parameter	σ_{R}	β_s	σ_{NPP}	O_{r}	g_{P}	q_{H}
temperature feedback factor, respiration σ_{R}	1.00					
CO_2 fertilisation factor β_s	−0.01	1.00				
temperature feedback factor, NPP σ_{NPP}	0.02	0.01	1.00			
ocean cc impulse response scale factor O_{r}	0.04	0.01	−0.01	1.00		
carbon flux partition, NPP to plant g_{P}	0.03	0.02	0.01	−0.03	1.00	
carbon flux partition, plant to detritus q_{H}	−0.01	0.03	−0.01	0.01	−0.00	1.00

Table 5.7: Posterior correlations between MAGICC carbon cycle parameters for initial 120,000 iteration MCMH run.

parameter	σ_{R}	β_s	σ_{NPP}	O_{r}	g_{P}	q_{H}
temperature feedback factor, respiration σ_{R}	1.00					
CO_2 fertilisation factor β_s	0.40	1.00				
temperature feedback factor, NPP σ_{NPP}	0.30	−0.53	1.00			
ocean cc impulse response scale factor O_{r}	0.02	0.12	−0.03	1.00		
carbon flux partition, NPP to plant g_{P}	0.09	0.08	−0.22	−0.03	1.00	
carbon flux partition, plant to detritus q_{H}	0.03	0.11	−0.16	−0.02	0.09	1.00

The strongest correlations are a positive correlation of 0.403 between respiration feedback $\sigma_{\mathrm{R}}$and fertilisation factor β_s, and a negative correlation of -0.533 between β_s and temperature feedback factor for Net Primary Production σ_{NPP}. There are also small correlations between σ_{R} and σ_{NPP}, σ_{NPP} and g_{P}. The remaining correlations are very small.

The three strongest correlation relationships are included here as joint parameter density plots, Figure 5.9(a), (b) and (c).

To help understand these relationships, Figure 5.10 shows the effect that the high, mean and low parameter values for (a) CO_2 fertilisation factor β_s, (b) CO_2 respiration feedback factor σ_{R}, and (c) temperature feedback factor, NPP σ_{NPP}, have on temperature change projections, using the A1FI emission scenario. Note that larger values for β_s and σ_{NPP} result in reduced temperature changes, but σ_{R} operates in the reverse direction.

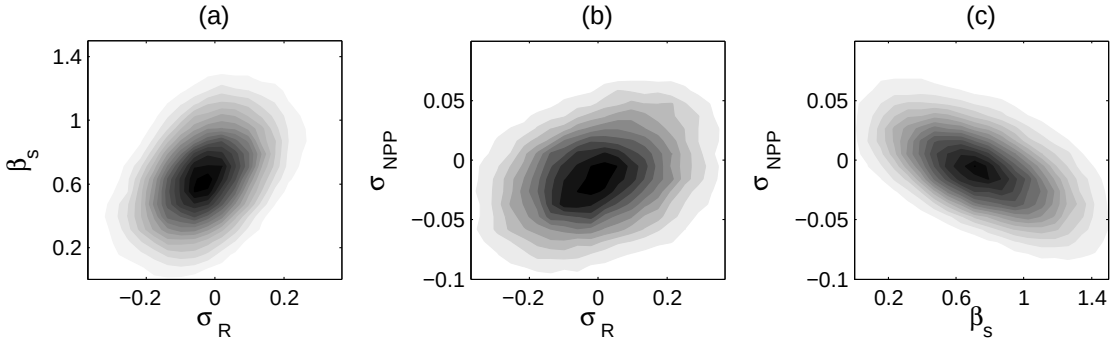

Figure 5.9: Carbon cycle parameter correlation plot, i.e., joint parameter density plot, for: (a) respiration temperature feedback σ_{R} and CO_2 fertilisation factor β_s; (b) σ_{R} and NPP temperature feedback σ_{NPP}; (c) β_s and σ_{NPP}.

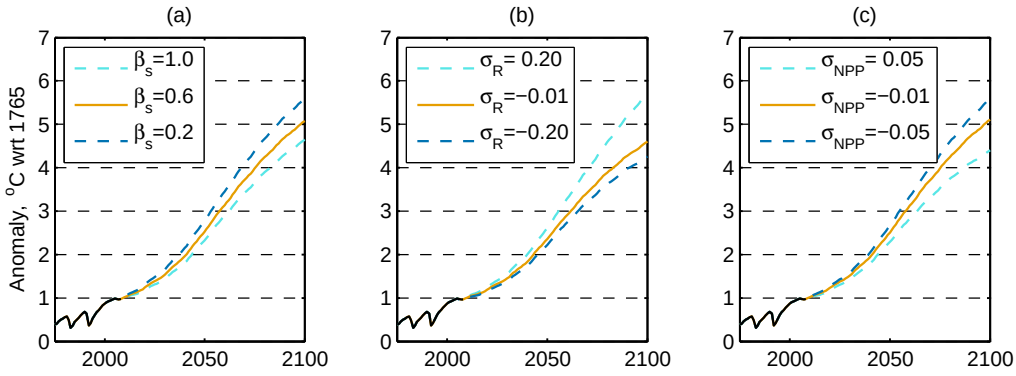

Figure 5.10: The influence of three carbon cycle parameter on temperature change: (a) CO_2 fertilisation factor β_s, (b) CO_2 respiration feedback factor σ_{R}, and (c) temperature feedback factor, NPP σ_{NPP} (A1FI emission scenario).

An increase in the CO_2 fertilisation factor β_s leads to a reduction in the amount of future warming (Figure 5.10(a)). A larger β_s means more plant production, therefore more CO_2 uptake, so that there is a reduction in the atmospheric CO_2 concentration and so less warming. However, more plant growth will also increase the amount of material available for respiration as it decays through the rapid turnover, detritus and soil boxes.

The plant decay processes are affected by temperature, parameterised in MAGICC by σ_{R}, σ_{H}, σ_{S}. These create a positive feedback effect, illustrated in Figure 5.10(b) for σ_{R}. Increases in these parameter values mean that more CO_2 is produced from heterotrophic respiration, increasing the atmospheric CO_2 concentration, which increases the amount of temperature change. The temperature feedback factor for respiration σ_{R} has the largest impact of the three because of a faster decay rate from the rapid turnover part of the living plant box.

At the same time as a bigger σ_{R} increases CO_2 emissions and hence greater concentrations, increases in atmospheric CO_2 encourage increases in living plant material, i.e., more NPP, which is modelled by the CO_2 fertilisation factor β_s, and hence these two parameters will covary. These effects are also coupled in MAGICC because the fertilisation factor is applied to the heterotrophic

respiration flux (*Meinshausen et al.*, 2011a). Hence, it is to be expected that these two parameters are positively correlated, as illustrated in Figure 5.9(a). The observational information supplied to the MCMH program is insufficient to fully separate these two parameters.

Larger, more positive values for $\sigma_{\rm NPP}$ mean an increase in NPP as temperature increases, so more CO_2 is taken up by living plants, reducing the atmospheric CO_2 concentration and reducing temperature changes, as shown in Figure 5.10(c). That plants are happier when warmer and tend to put on biomass is a gross global–scale generalisation that assumes no water or nutrient limitations. *del Grosso et al.* (2008) shows that temperature is less well correlated with NPP than precipitation, and that for non-tree dominated systems using NPP as a function of temperature increased model error in their case. These complexities can not be allowed for with MAGICC since it does not model precipitation or vegetation types. Instead, the temperature feedback parameters allow for the general uncertainty in how NPP will change in response to temperature changes at the global–scale.

The two temperature feedbacks $\sigma_{\rm NPP}$ and $\sigma_{\rm R}$ show a small positive correlation of 0.3 (illustrated by Figure 5.9(b)). They are connected to the amount of NPP or new plant material produced each year. If NPP is increased by a larger temperature feedback factor $\sigma_{\rm NPP}$ then the amount of CO_2 from decaying material will have to be increased to maintain the carbon budget (since more NPP means a reduction in atmospheric CO_2). A bigger value for $\sigma_{\rm R}$ will help to achieve this balance, and hence the correlation between these two.

The negative correlation of β_s with $\sigma_{\rm NPP}$ (Figure 5.9(c)) is also a consequence of maintaining the carbon budget. If β_s is larger, with more plant production, reducing atmospheric CO_2, then the temperature feedback $\sigma_{\rm NPP}$ change needed to offset this requires a smaller value.

The ocean carbon cycle impulse response scale factor $O_{\rm r}$ is largely isolated from the other parameters by the observations. The correlations are all very small, except for a small correlation with the CO_2 fertilisation factor β_s. This small interaction is unsurprising since β_s is associated with balancing the carbon budget, which is the balance of emissions with the land flux and ocean flux to achieve the atmospheric CO_2 concentrations.

Excluding the temperature sensitivity of the ocean to carbon uptake (the ocean carbon cycle temperature feedback α_T parameter) from the set of carbon cycle parameter has helped to reduce the complexity of these MCMH results. This was justified on the basis of the earlier uncertainty analysis, although it is known that the ocean temperature has an important influence on the solubility of CO_2.

5.5.2 Further carbon cycle MCMH testing

Some alternative strategies were investigated to further test the initial MCMH carbon cycle only results, looking at the affect of the time period for the observed CO_2 concentrations and CO_2 fluxes.

(i) Adding CO_2 observations from 1900. In this case, the carbon cycle was switched to using historical emissions in 1910 (rather than 1960), using both observed decadal global–mean temperatures and CO_2 concentrations as observational constraints, but without flux data until the 1960–69 decade.

This outcome reveals some differences as compared to the previous results, mainly in the means of the first two parameters, with surprisingly little change in the standard distributions, changes which may also be affected by the smaller number of iterations performed (12k rather than 120k). The changes in the two feedback terms, σ_{R} and σ_{NPP} are small, but significant for longer–term projections. The additional pre-1960 CO_2 concentrations and global–mean temperatures,[1] in the absence of additional flux data, are perhaps also influencing the results, despite the smaller changes in atmospheric concentrations and temperatures that occurred in the first half of the 20th–century.

Table 5.8: Prior and posterior distributions for key MAGICC carbon cycle parameters, with additional CO_2 concentration observations and using historical emissions from 1910 onwards (12,000 iterations).

parameter	prior mean	post mean	prior σ	post σ
temperature feedback factor, respiration σ_{R}	−0.01	0.00	0.15	0.13
CO_2 fertilisation factor β_s	0.50	1.16	0.50	0.26
temperature feedback factor, NPP σ_{NPP}	−0.01	−0.04	0.05	0.04
ocean cc impulse response scale factor O_{r}	1.50	0.76	1.00	0.21
carbon flux partition, NPP to plant g_{P}	0.50	0.54	0.25	0.19
carbon flux partition, plant to detritus q_{H}	0.80	0.75	0.20	0.14

(ii) The impact of dropping the last decade of observations (2000–2009), as compared to the initial results, was also tested, i.e., using four decades of observed fluxes and CO_2 concentrations, rather than five decades. These results (Table 5.9) also display noticeable changes in the posterior means for σ_{R}, β_s, σ_{NPP} and O_{r}, and in the standard deviations for σ_{R} and β_s.

These differences point to the value that additional observational information provides. Indeed, it is really only the relatively recent emergence of the Global Carbon Project data that has made it possible to use historical observations to constrain MAGICC's carbon cycle parameters. MAGICC does not have the capability of tracking carbon isotopes which would otherwise be another source of observations for helping to calibrate the carbon cycle parameters.

The carbon cycle parameters will be better constrained as more observations are accumulated. The value of additional observations could be further tested with a synthetic data experiment, whereby a forward model run is used to generate 'observations', which are then treated as a set of randomly distributed results and used as observational constraint to see how the posterior distributions change in response to the extra data.

An issue that has not been explored here is the role of the initial carbon pools. The uncertainty analysis indicated that the temperature change results are hardly affected by these values. However, this may be because the method used has the effect of dissipating the influence of the pool size by the time the carbon cycle is activated in 2005. This is a topic that perhaps warrants further investigation.

[1] CO_2 concentrations from NASA GISS 2002 GCM runs, as given on http://www.giss.nasa.gov/data/simodel/ghgases/GCM.html and included in MAGICC's history files; temperature data is HadCRUT3.

Table 5.9: Prior and posterior distributions for key MAGICC carbon cycle parameters, with four, rather than five, decades of land and ocean carbon fluxes (12,000 iterations).

parameter	prior mean	post mean	prior σ	post σ
temperature feedback factor, respiration σ_{R}	-0.01	-0.04	0.15	0.14
CO_2 fertilisation factor β_s	0.50	0.74	0.50	0.21
temperature feedback factor, NPP σ_{NPP}	-0.01	-0.00	0.05	0.04
ocean cc impulse response scale factor O_{r}	1.50	0.92	1.00	0.27
carbon flux partition, NPP to plant g_{P}	0.50	0.59	0.25	0.20
carbon flux partition, plant to detritus q_{H}	0.80	0.72	0.20	0.17

5.5.3 Alternative prior distributions

Another consideration is the extent to which the MCMH results are affected by the form of the prior distribution. The MCMH program was implemented using Gaussian priors, but these can approximate uniform distributions by having larger standard deviations, although it is also necessary to truncate the prior distributions to avoid physically impossible parameter values. As an example, distributions with standard deviations that are twice as large are shown in Figure 5.11 (except the carbon flux partition, plant to detritus q_{H} is unchanged).

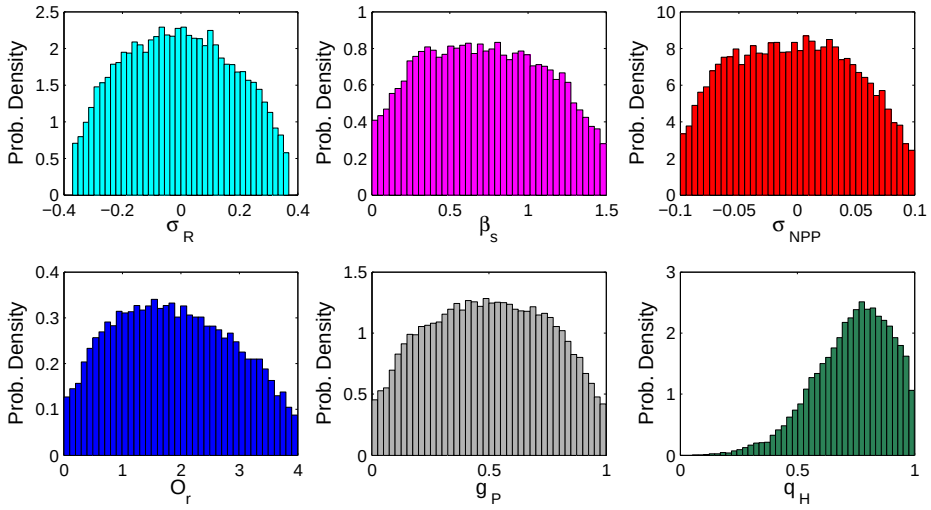

Figure 5.11: Modified carbon cycle parameter prior PDFs, with doubled standard deviations, except for q_{H}.

These modified priors can then be tested with the MCMH program. As it turns out, it is not possible to increase the standard deviations by very much before the number of acceptable results falls away substantially. This indicates that the prior distributions are then not very skillful. The MCMH algorithm, in its present configuration, has difficulty moving back into the likely parameter space when presented with an implausible parameter set that results in a large difference between the model results and the observational constraints. There are strategies to deal with this problem,

such as changing the parameter step lengths and monitoring the acceptance rate. However, this is not necessary when good priors are available.

One example using modified standard distributions is presented in Table 5.10. The first four prior standard deviation σ values have been increased by about 30%. Increasing the standard deviations beyond these values was found to result in very low acceptance rates for the parameter sets. The posterior results found here, as compared to the earlier initial results (Table 5.5), reveal some changes, noticeably for the posterior means and standard deviations in the first two parameters, σ_{R} and β_s. This result demonstrates that some of the posterior PDFs are sensitive to the prior PDFs.

Table 5.10: Prior and posterior distributions for carbon cycle parameters, with selectively increased standard deviations, except for g_{P} and q_{H} (12,000 iterations).

parameter	prior mean	post mean	prior σ	post σ
temperature feedback factor, respiration σ_{R}	-0.01	-0.07	0.20	0.14
CO_2 fertilisation factor β_s	0.50	0.65	0.65	0.26
temperature feedback factor, NPP σ_{NPP}	-0.01	0.01	0.07	0.04
ocean cc impulse response scale factor O_{r}	1.50	0.96	1.30	0.28
carbon flux partition, NPP to plant g_{P}	0.50	0.47	0.25	0.21
carbon flux partition, plant to detritus q_{H}	0.80	0.72	0.20	0.16

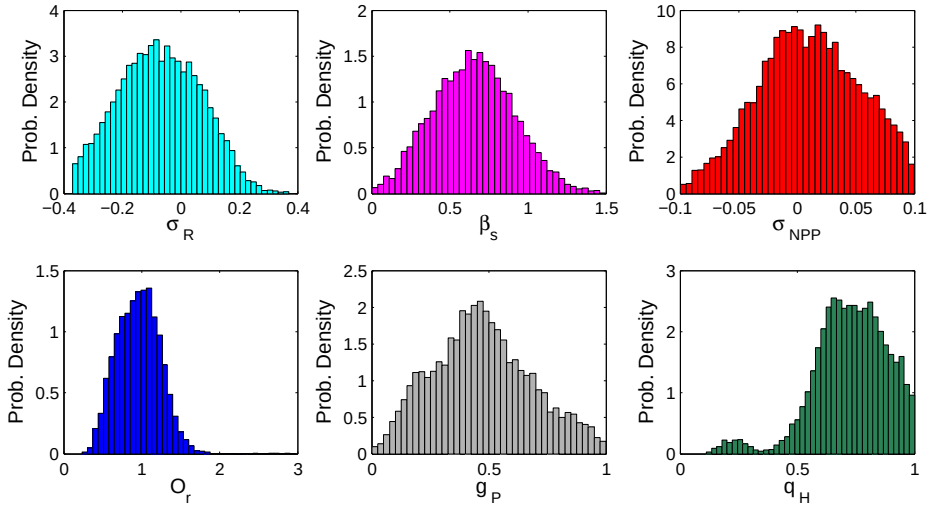

Figure 5.12: Carbon cycle parameter posterior histogram results for Table 5.10.

5.5.4 Information gained

Another perspective on the carbon cycle parameters' posterior distributions can be obtained by examining the change from the prior distributions using the diagnostic likelihood function $\mathbf{LF}(x)$, applying the same methodology as was used with the climate parameters (Section 4.3.4). This was done for the first set of distributions obtained above (Section 5.5.1), with the results shown in Figure 5.13. The first and third rows are the probability density histograms for each of the six parameters (i.e., the frequency histograms scaled by the number of observations), with the prior distribution indicated by the grey shaded region with black outline, and the coloured regions the posterior distribution. Then, under each parameter distribution, the likelihood functions are plotted as probability density histograms (the second and fourth rows). The shape of the likelihood functions is a measure of the information gained from the historical observations by the MCMH algorithm. The distribution results were restricted to a 5% to 95% interval to avoid issues caused by the very small numbers at the tails, effectively creating boundaries similar to the limits for a uniform distribution.

Studying the results in this way reveals some of the gains made, but also serves to highlight some issues.

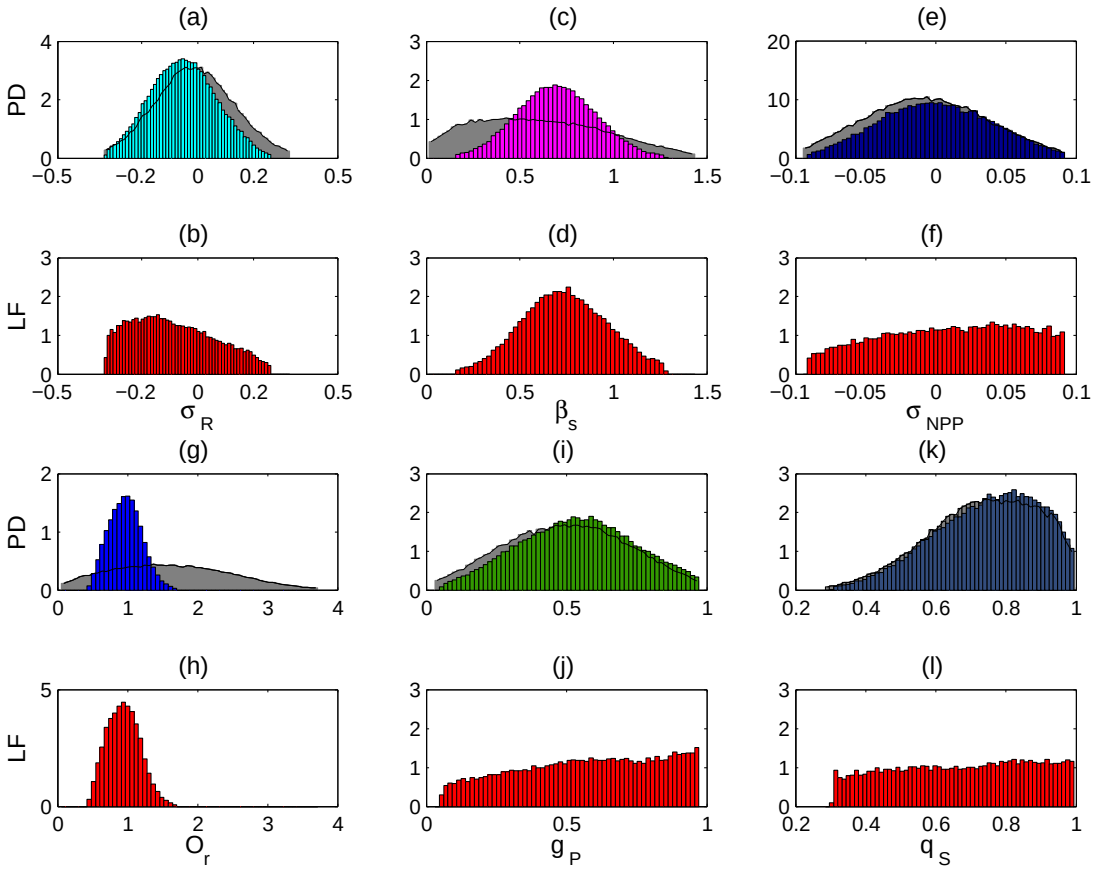

Figure 5.13: Carbon cycle likelihood functions for the 6 parameter prior and posterior distributions from the initial 120,000 iterations, Section 5.5.1 (PD = probability density, LF = likelihood function). The prior distribution is indicated by the grey shaded region with black outline.

The clearest result is for the single ocean parameter, the ocean carbon cycle impulse response scale factor O_{r}. If the prior had been assumed to be a uniform distribution, the posterior derived from this $\mathbf{LF}(O_{\mathrm{r}})$ would be an almost normal distribution. The relatively broad prior distribution, based initially on the range of C4MIP calibrated values, has been substantially reduced. This result can be partly attributed to having only one ocean parameter in the MCMH–MAGICC setup that lines up with the corresponding GCP ocean flux data, although the net fluxes are also constrained by the atmospheric CO_2 concentration data and the balance with historical emissions.

The results are more mixed for the five terrestrial carbon cycle parameters. The two flux partitions, carbon flux partition, NPP to plant g_{P}, and carbon flux partition, plant to detritus q_{H}, show little change in their distributions. Uniform priors for these would show little change brought about by the MCMH program. This is because the observations used do not relate directly to these two parameters. They are associated with the internal division of carbon between the carbon pools, whereas the observations relate to the flux into the terrestrial carbon cycle as a whole.

The terrestrial carbon cycle parameter that exhibits the most change is the CO_2 fertilisation factor β_s. It is perhaps the most 'exposed' of the five, and hence most affected by the land flux. It is also the parameter associated with the 'missing sink', the term needed to balance the carbon budget. A prior uniform distribution would be transformed into an approximately normal distribution with a mean of about 0.7, which is the same value given for the posterior mean in Table 5.5.

The two temperature feedback parameters for respiration σ_{R} and NPP σ_{NPP} are more problematic. They both have initial prior means of only -0.01. The C4MIP calibrated values span minimum to maximum ranges of -0.20 to 0.19 and -0.06 to 0.04 respectively, so both positive and negative values are possible. The MCMH transformations of these two parameters, as indicated by their likelihood functions, have different characteristics.

The $\mathbf{LF}$ for the respiration temperature feedback σ_{R} has a truncated and skewed profile. The original prior was restricted to an interval of -0.37 to 0.37, a little over twice the standard distribution, in order to limit the spread of accepted priors submitted for testing by MAGICC, effectively increasing the acceptance rate. However, the $\mathbf{LF}(\sigma_{\mathrm{R}})$, as compared to a uniform prior, suggests that the lower truncation point should have been extended a little further. The peak of the $\mathbf{LF}$ is around σ_{R} -0.18. Smaller, more negative, values of this parameter mean less CO_2 is produced from increased temperatures.

For the NPP temperature feedback σ_{NPP} , the $\mathbf{LF}(\sigma_{\mathrm{NPP}})$ is a modified uniform distribution, with some tapering off at the ends, although mainly at the lower or left hand end of the distribution. There is a slight shift upwards to more positive values for this parameter. This result suggests that σ_{NPP} cannot be resolved by the available data.

5.6 Chapter Summary

Calibrating MAGICC's carbon cycle parameters presents a number of challenges: there are more parameters to deal with than in the climate system, and there is limited data available to help calibrate those parameters, both in terms of the number of observations but also their temporal cover. This problem has been previously dealt with by making use of the results from more

complex carbon cycle models (*Meinshausen et al.*, 2011a). In this research work, a decision was made to investigate this calibration using observations, aided by the release of data compiled by the Global Carbon Project.

The uncertainty analysis technique introduced in Chapter 4 was first applied to assessing the significance of the carbon cycle parameters to the uncertainty in projected CO_2 concentrations and temperature changes. A subset of six carbon cycle parameters was selected for calibration based on the outcome of this analysis.

The MCMH method was then successfully applied to obtaining posterior probability distributions for these six carbon cycle parameters. As far as is known, this is the first time MAGICC's carbon cycle parameters have been constrained against historical observations, rather than against other models. This method is able to take into account uncertainty from the different observations and the response of the carbon cycle to changes in temperature and CO_2 concentrations. One of the things missing from this analysis is, however, the uncertainty in CO_2 fossil fuel and land use emissions, since these emissions data are processed as part of MAGICC, not as an external observation to constrain the model results. Historical emissions data are estimated to have an uncertainty of $\pm 6\%$ (GCP; http://www.globalcarbonproject.org/carbonbudget/09/hl-full.htm).

The robustness of the results was tested in a number of different ways, including examining the correlations, the number of iterations, amount of observations, and the influence of the prior distribution. These tests showed that the posterior results are somewhat affected by the MCMH set-up, particularly for the respiration feedback factor σ_{R} and CO_2 fertilisation factor β_s. Calibration of the two main temperature feedback factors σ_{R} and σ_{NPP} is particularly difficult, yet they are critical for future projections.

The limited number and time–span of historical observations make it difficult to better estimate MAGICC's carbon cycle parameters. However, there is potential for improvement, from new observational data, changes to the model design and perhaps using the available data in different ways. For example, observational data may be extended back in time as new analysis of ice core data can potentially provide estimates for land and ocean fluxes extending back over the last century or two. Furthermore, new data will become available as time proceeds, although important decisions concerning mitigation are needed sooner rather than later. It might also be possible to construct independent constraints, such as a land$-$ocean flux difference index to see if it provides additional information, similar to the land$-$ocean temperature constraint used with the climate system.

It might be feasible to modify MAGICC, adding the capability for tracking carbon isotopes, particularly if this will provide additional data on the carbon pools and help better estimate the temperature sensitivities. Some care needs to be exercised with this information so that double counting is avoided here. For example, the GCP land flux estimates are already informed by isotopic information. Another option might be to model separate ocean carbon cycles for the biological and chemical pumps, if the relevant observational data exists. Such data might also be divided hemispherically, so that there are Northern and Southern Hemisphere land and ocean fluxes, providing four carbon cycle regions similar to the four climate system regions. Again, this depends on the availability of the requisite data.

Further testing of the carbon cycle could also be carried out to investigate different parameter choices, including the addition of one or more parameters for the initial carbon pools, and possibly the ocean carbon cycle temperature feedback factor. However, changes to the model and alternative estimates of the carbon cycle parameters that have only a minor influence on projections may not be warranted. The relative importance of the carbon cycle needs to be considered in the context of its contribution to overall system. This is investigated in the next chapter.

Chapter 6

Combined Climate/Carbon Cycle Parameters

Previous chapters have introduced MAGICC and its basic principles (Chapter 2), investigated the climate system parameters (Chapters 3 and 4) and then the carbon cycle (Chapter 5), including consideration of the model's relative parameter sensitivity, uncertainty and some methods of constraining the parameter values using historical observations. This chapter now moves on to investigating the combined climate–carbon cycle system. Both systems interact with each other by virtue of CO_2 and temperature–dependent processes.

The combined uncertainty of the climate and carbon cycle parameters was first investigated, and then a method of including aerosol forcing uncertainty was added. The relative contribution of the different parameters to future temperature change provided a basis for selecting which parameters to include in the subsequent MCMH analysis. Most of the uncertainty is accounted for by just seven parameters, two for the climate system (climate sensitivity and ocean diffusivity), a composite aerosol forcing parameter, three terrestrial carbon cycle parameters (fertilisation factor, respiration and NPP temperature feedback factors), plus the ocean carbon cycle impulse response scale factor.

The MCMH–MAGICC program was applied, including some testing with different combinations of parameters, with prior values and observations as discussed in Section 6.2. From this, revised posterior parameter distributions were obtained. These distributions were then applied to obtain future temperature change distributions for a given emission scenario. In this chapter, the SRES A1FI and B1 scenarios are used to illustrate this process. The results are compared to the IPCC AR4 best estimate and likely range for temperature change in 2100. It was found that the observationally constrained MCMH results give a probability distribution with similar best estimates,[1] but with an increased lower bound and an overall narrowing for the likely range (67% confidence interval).

As well as being able to produce probabilistic temperature change projections, which was one of the goals of this research work, the posterior parameter distributions enable cumulative probability densities to be calculated, so that the risks of exceeding a specific temperature change amount can also be assessed. This is illustrated for the A1FI scenario, which shows a 50% chance

[1] Strictly speaking, a conditional probability for each set of emissions.

of exceeding 2°C global–mean temperature change by about 2045. Mention is also made of the land ocean temperature differences. Whilst it is perhaps an obvious point, mean land temperature changes are greater than mean sea–surface temperature changes. Consideration of global temperature targets associated with avoiding 'dangerous climate change', such as 2°C above pre-industrial, may overlook the fact that land surface temperatures will be in the order of 35% warmer. Accordingly, the results from looking at the risks of exceeding particular temperature change targets are assessed for both global–mean and land temperature changes.

More emission scenarios are investigated in the next chapter, Chapter 7, applying the posterior parameter distribution results from this chapter to examine temperature change distributions.

6.1 Combined Uncertainty

This section investigates uncertainty for the combined climate system and carbon cycle parameters using the same methodology that was used for the separate treatment of the climate system and carbon cycle in the previous two chapters (refer to the start of Section 4.2 and Section 5.4). Aerosol forcing uncertainty is also included as an additional parameter later in this section.

The standard deviations and normal or lognormal distributions were selected consistent with the previous arrangements. The results for temperature change uncertainty in 2100, listing all of the parameters, the variance components as standard deviations and their relative contribution to the total uncertainty, based on the A1FI emission scenario, are presented in Table 6.1. The overall standard deviation is 1.42°C, which gives a 5% to 95% confidence interval of plus or minus 2.32°C for the temperature in 2100 (assuming a normal distribution).

The top five parameters account for 91% of the overall uncertainty, headed by climate sensitivity ΔT_{2x} at almost 73% of the total, re-affirming the significance of this parameter. The next four are all carbon cycle parameters, ahead of any of the other climate system parameters.

For CO_2 concentration uncertainty in 2100 (Table 6.2), the carbon cycle parameters account for 96% of the overall uncertainty, while climate sensitivity ΔT_{2x} only plays a modest role. The overall standard deviation is 245 ppm, which gives a 5% to 95% confidence interval of plus or minus 402 ppm for CO_2 concentrations in 2100 (assuming a normal distribution). The CO_2 concentration lack of sensitivity to ΔT_{2x} is a little surprising, given the findings of previous studies (for example, *Friedlingstein et al.*, 2003; 2006). This uncertainty analysis may be influenced by the choice of the prior values; there is scope for further investigation of these results using the posterior parameter values derived from the MCMH algorithm (discussed in the next section) as well as a comparison of the carbon cycle gain and the land and ocean carbon sensitivity to atmospheric CO_2 and temperature change, along the lines of *Friedlingstein et al.* (2006) (see also *Gregory et al.*, 2009).

Table 6.1: Climate system and carbon cycle parameter uncertainty for temperature in 2100 with the A1FI emission scenario.

parameter name	σ	uncertainty contribution %
climate sensitivity $\Delta T_{2\mathrm{x}}$	1.21	72.55%
temperature feedback factor, respiration σ_{R}	0.37	6.67%
CO_2 fertilisation factor β_s	0.33	5.25%
temperature feedback factor, NPP σ_{NPP}	0.26	3.44%
ocean cc impulse response scale factor O_{r}	0.26	3.29%
carbon flux partition, NPP to plant g_{P}	0.22	2.42%
ocean vertical diffusivity K	0.20	2.07%
temperature feedback factor, detritus σ_{Q}	0.19	1.73%
temperature feedback factor, soil σ_{U}	0.18	1.58%
land ocean heat coefficient κ_{lo}	0.08	0.30%
land ocean warming ratio R_{lo}	0.05	0.13%
initial NPP flux N_0	0.04	0.10%
variable upwelling velocity fraction w_{var}	0.04	0.09%
north south heat coefficient κ_{ns}	0.04	0.07%
initial plant pool P_0	0.04	0.07%
carbon flux partition, plant to detritus q_{H}	0.04	0.06%
initial detritus pool H_0	0.04	0.06%
initial respiration flux $R_{(\mathrm{P},0)}$	0.03	0.06%
ocean cc temperature feedback α_T	0.02	0.02%
mixed–layer depth h	0.02	0.02%
polar sink water to mixed–layer temperature ratio β	0.02	0.01%
carbon flux partition, detritus to soil Φ_{H}	0.01	0.00%
initial upwelling velocity w_0	0.01	0.00%
CO_2 fertilisation method β_m	0.01	0.00%
initial soil pool S_0	0.01	0.00%
carbon flux partition, NPP to detritus g_{H}	0.01	0.00%
ocean cc gas exchange scale factor k	0.00	0.00%

Table 6.2: Climate system and carbon cycle parameter uncertainty for CO_2 concentrations in 2100 with the A1FI emission scenario.

parameter name	σ	uncertainty contribution %
temperature feedback factor, respiration σ_{R}	128.45	27.43%
CO_2 fertilisation factor β_s	108.16	19.45%
temperature feedback factor, NPP σ_{NPP}	92.19	14.13%
ocean cc impulse response scale factor O_{r}	85.19	12.06%
carbon flux partition, NPP to plant g_{P}	77.99	10.11%
temperature feedback factor, soil σ_{Q}	63.36	6.67%
temperature feedback factor, soil σ_{U}	61.32	6.25%
climate sensitivity $\Delta T_{2\mathrm{x}}$	37.09	2.29%
initial NPP flux N_0	14.35	0.34%
initial plant pool P_0	13.10	0.29%
carbon flux partition, plant to detritus q_{H}	12.37	0.25%
initial respiration flux $R_{(\mathrm{P},0)}$	11.90	0.24%
initial detritus pool H_0	11.53	0.22%
ocean vertical diffusivity K	7.69	0.10%
ocean cc temperature feedback α_T	6.36	0.07%
carbon flux partition, NPP to detritus g_{H}	5.62	0.05%
land ocean heat coefficient κ_{lo}	3.20	0.02%
carbon flux partition, detritus to soil Φ_{H}	2.93	0.01%
initial soil pool S_0	2.75	0.01%
land ocean warming ratio R_{lo}	1.74	0.01%
variable upwelling velocity fraction w_{var}	1.13	0.00%
ocean cc gas exchange scale factor k	0.67	0.00%
CO_2 fertilisation method β_m	0.54	0.00%
north south heat coefficient κ_{ns}	0.48	0.00%
initial upwelling velocity w_0	0.34	0.00%
mixed–layer depth h	0.16	0.00%
polar sink water to mixed–layer temperature ratio β	0.14	0.00%

6.1.1 With aerosol forcing uncertainty

Aerosol forcing uncertainty was added to the combined climate system and carbon cycle uncertainty for the temperature change in 2100 using similar methods as previously, with the total aerosol forcing uncertainty scaled from the direct sulfate forcing uncertainty (Section 4.2.3). The number of climate system and carbon cycle parameters was reduced to 5 climate and 8 carbon cycle parameters, selected on the basis of their relative significance and previous inclusion in the MCMH analyses.

Table 6.3: Climate system, carbon cycle and aerosol forcing uncertainty for temperature change in 2100 (with the A1FI emission scenario).

parameter name	σ	uncertainty contribution %
climate sensitivity ΔT_{2x}	1.14	55.44%
total aerosol forcing AF_{soxi}	0.74	23.78%
temperature feedback factor, respiration σ_{R}	0.34	4.90%
CO_2 fertilisation factor β_s	0.32	4.48%
ocean cc impulse response scale factor O_{r}	0.25	2.79%
temperature feedback factor, NPP σ_{NPP}	0.24	2.49%
ocean vertical diffusivity K	0.19	1.58%
carbon flux partition, NPP to plant g_{P}	0.19	1.51%
temperature feedback factor, detritus σ_{Q}	0.18	1.33%
temperature feedback factor, soil σ_{U}	0.16	1.12%
land ocean heat coefficient κ_{lo}	0.09	0.37%
land ocean warming ratio R_{lo}	0.05	0.13%
north south heat coefficient κ_{ns}	0.05	0.09%
carbon flux partition, plant to detritus q_{H}	0.02	0.01%

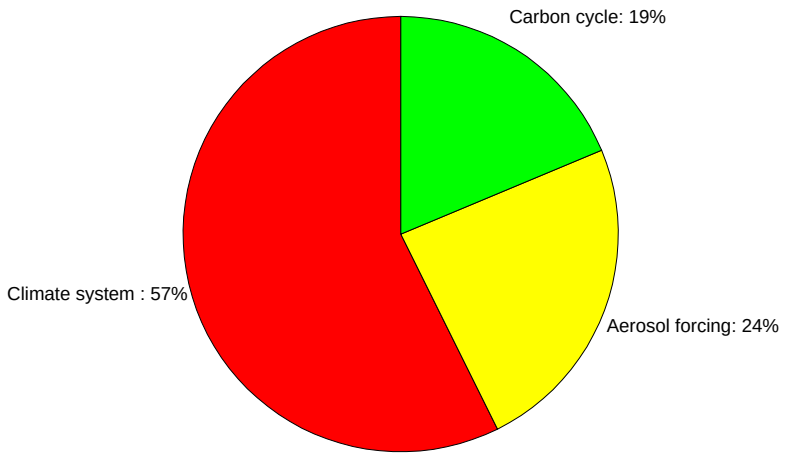

Figure 6.1: Proportional uncertainty contributions to temperature change for a given emission scenario (the A1FI emission scenario).

The results (Table 6.3) reveal an interesting shift in the uncertainty contributions for each of the selected parameters. Climate sensitivity now accounts for a little over half of the uncertainty. The contribution by parameter groups (Figure 6.1) show that the climate system parameters' contribution is 57%, total aerosol forcing is 24% and the carbon cycle parameters are 19% of the total (with rounding adjusted to total 100%).

6.1.2 Uncertainty Summary

The relative contributions of the individual parameters to the overall uncertainty for temperature change in 2100 (Table 6.3) indicates that the top seven parameters account for almost 96% of the uncertainty, or the top eight cover 97%. Of the eight parameters, climate sensitivity ΔT_{2x} and ocean vertical diffusivity K are the only two climate system parameters. The two land ocean parameters (land ocean heat coefficient $\kappa_{\rm lo}$ and land ocean warming ratio $R_{\rm lo}$) are, however, still important for setting the land ocean temperature contrast.

Apart from the aerosol forcing parameter, the carbon cycle parameters comprise the other key parameters, collectively accounting for almost 20% of the uncertainty of the temperature change in 2100. Note that these proportions are based on initial estimates for the standard deviations of each parameter, which will change when calibrated against observations. *Huntingford et al.* (2009) reported that the carbon cycle parameters contributed around 40% to the uncertainty in the C4MIP simulations, but the latter models did not account for aerosol uncertainties or consider non–CO_2 greenhouse–gases.

For MAGICC's parameters, the CO_2 respiration feedback factor $\sigma_{\rm R}$ and CO_2 fertilisation factor β_s are the main contributors to the uncertainty in projected temperature changes, followed by the ocean carbon cycle impulse response scale factor $O_{\rm r}$, the temperature feedback factor, NPP $\sigma_{\rm NPP}$ and the carbon flux partition, NPP to plant $g_{\rm P}$. The carbon flux partition, plant to detritus $q_{\rm H}$, makes a very small contribution.

This assessment then provides a basis for seeking to constrain a reduced set of parameters using observations and the MCMH algorithm, which is the subject of the next section.

6.2 MCMH for Combined Parameters

The application of the MCMH method was applied to the combined climate system and carbon cycle parameters by bringing together the prior distributions and observational data that were used for the results in the earlier cases. That is, the same four climate system parameters and six carbon cycle parameters, as listed in Table 6.4 (aerosol forcing is incorporated later on). This is a slightly larger set of parameters than suggested from the last section's summary; this larger set is used initially here for consistency with those used in Chapters 4 and 5. Similarly, the same sets of decadal observations were used, with up to eight historical observations against which to compare MAGICC's 20th–century results:

- Global–mean surface temperature changes (HadCRU);
- Land minus ocean surface temperature changes (HadCRU);
- North minus South hemispheric temperature changes (HadCRU);

- Ocean layer temperature changes (SW10);
- Ocean heat content changes (D08);
- Atmospheric CO_2 concentrations (Mauna Loa);
- Land carbon fluxes (GCP); and,
- Ocean carbon fluxes (GCP).

Different selections of parameters and observations were also tested, as discussed in subsequent parts of this chapter.

The initial results for the 10 combined parameters (Table 6.4) reveal notable changes to the means for respiration temperature feedback σ_{R} and the ocean carbon cycle impulse response scale factor O_{r}, as well as significant changes to the standard deviations for climate sensitivity $\Delta T_{2\mathrm{x}}$, the CO_2 fertilisation factor β_s, along with smaller changes for the land ocean heat exchange κ_{lo} and land/ocean warming ratio R_{lo} posterior standard deviations. Note, some care has to be exercised in assessing changes to the mean values, since many of the distributions are not Gaussian.

The change to the ocean carbon cycle impulse response scale factor O_{r} distribution is similar to that found for the carbon cycle alone (Chapter 5, Section 5.5.1 and Table 5.5), but with an increase in the standard deviation. The MCMH is able to constrain this parameter because of working with only one ocean parameter which aligns with the ocean carbon flux and CO_2 concentrations.

The correlation structure for these results (Table 6.5) has close similarities to those for the climate system parameters and the carbon cycle parameters as found previously for the separate systems (Chapters 4 and 5 respectively).

More detailed discussion of the distributions is held over until the end of this section where the information gained is assessed (see Section 6.2.4). Before that, aerosol forcing is incorporated into the investigation and alternative parameter arrangements tested.

Table 6.4: Prior and posterior distributions for key MAGICC climate system and carbon cycle parameters (15,000 iterations).

parameter	prior mean	post mean	prior σ	post σ
climate sensitivity $\Delta T_{2\mathrm{x}}$	3.00	3.04	1.50	0.74
ocean vertical diffusivity K	1.00	1.14	0.50	0.43
land ocean heat exchange κ_{lo}	1.50	1.56	0.80	0.62
land/ocean warming ratio R_{lo}	1.60	1.55	0.20	0.16
temperature feedback factor, respiration σ_{R}	−0.01	−0.07	0.15	0.13
CO_2 fertilisation factor β_s	0.50	0.65	0.50	0.18
temperature feedback factor, NPP σ_{NPP}	−0.01	0.00	0.05	0.04
ocean cc impulse response scale factor O_{r}	1.50	1.08	1.00	0.35
carbon flux partition, NPP to plant g_{P}	0.50	0.50	0.25	0.22
carbon flux partition, plant to detritus q_{H}	0.80	0.79	0.20	0.18

Table 6.5: Correlations between MAGICC's combined climate and carbon cycle parameters (15,000 iteration MCMH run).

parameter	ΔT_{2x}	K	κ_{lo}	R_{lo}	σ_R	β_s	σ_{NPP}	O_r	g_P	q_H
climate sensitivity ΔT_{2x}	1.00									
ocean vertical diffusivity K	0.17	1.00								
land ocean heat exchange κ_{lo}	0.10	0.15	1.00							
land/ocean warming ratio R_{lo}	−0.16	−0.05	0.08	1.00						
temperature feedback factor, respiration σ_R	0.03	0.10	0.04	0.10	1.00					
CO_2 fertilisation factor β_s	0.09	−0.07	0.03	0.01	0.35	1.00				
temperature feedback factor, NPP σ_{NPP}	0.07	0.15	−0.03	−0.00	0.43	−0.39	1.00			
ocean cc impulse response scale factor O_r	−0.14	0.01	−0.03	0.06	0.05	0.11	0.09	1.00		
carbon flux partition, NPP to plant g_P	0.05	0.19	0.02	0.13	0.08	0.05	−0.19	−0.04	1.00	
carbon flux partition, plant to detritus q_H	−0.05	0.00	0.10	−0.08	−0.06	−0.10	0.01	−0.04	0.10	1.00

6.2.1 With aerosol uncertainty included

The introduction of a composite aerosol forcing parameter provides a better representation of the uncertainties, but complicates the results (Table 6.6). The climate sensitivity $\Delta T_{2\mathrm{x}}$ shows an increase in its mean along with a lesser reduction in the standard deviation, yet the aerosol forcing has a relatively larger change to its mean and a very big reduction in its spread as compared to the prior mean and standard deviation. Adding the aerosol parameter also has some impact on the other parameters, including the carbon cycle components.

Table 6.6: Prior and posterior distributions for key combined climate, carbon cycle and aerosol forcing parameters (50,000 iterations).

parameter	prior mean	post mean	prior σ	post σ
climate sensitivity $\Delta T_{2\mathrm{x}}$	3.00	3.40	1.50	0.93
ocean vertical diffusivity K	1.00	1.09	0.50	0.43
land ocean heat exchange κ_{lo}	1.50	2.02	0.80	0.66
land/ocean warming ratio R_{lo}	1.60	1.61	0.20	0.15
total aerosol forcing AF_{soxi}	-0.50	-0.28	0.40	0.09
temperature feedback factor, respiration σ_{R}	-0.010	-0.045	0.15	0.13
CO_2 fertilisation factor β_s	0.50	0.81	0.50	0.28
temperature feedback factor, NPP σ_{NPP}	-0.010	0.006	0.05	0.04
ocean cc impulse response scale factor O_{r}	1.50	0.97	1.00	0.27
carbon flux partition, NPP to plant g_{P}	0.50	0.50	0.25	0.19
carbon flux partition, plant to detritus q_{H}	0.80	0.78	0.19	0.14

6.2.2 With OHC observations added

The ocean diffusivity K posterior shows only modest changes as compared to the prior mean and standard deviation in the combined MCMH runs. This is partly due to having a well-informed prior and the fact that the observational constraint provided by the ocean temperature change data has a large uncertainty. A prior mean of 1.0 $\mathrm{cm}^2\mathrm{s}^{-1}$ was used to see if the MCMH results show any tendency towards lower values, since previous analysis of the ocean temperature profile and ocean heat content (Chapter 3, Section 3.6.1) pointed towards a value of between 0.5 and 1.0 $\mathrm{cm}^2\mathrm{s}^{-1}$.

Additional observational data were introduced to further test this result. Three time series for ocean heat content (OHC) at 100m, 300 and 700m depths were added, arranged as 5 decadal means covering 1951 to 2000 and the prior mean for K changed to 0.70. The results (Table 6.7) yield a similar posterior mean value for K of 0.71 $\mathrm{cm}^2\mathrm{s}^{-1}$, along with a reduced standard distribution. It may be that the prior distribution is sufficiently consistent with the observations so that little change is required, or else the observational constraint, with the relatively large uncertainties for the OHC observations, is unable to affect the posterior distribution very much. This was not tested further.

Another point of interest is the change in climate sensitivity $\Delta T_{2\mathrm{x}}$, with the posterior mean changing back a little closer to 3.00. There is little change to the aerosol forcing numbers. The two temperature feedback factors for respiration σ_{R} and σ_{NPP} continue to move around, further

demonstrating their sensitivity to the MCMH setup. There is also some impact on the ocean carbon cycle impulse response scale factor $O_{\rm r}$, with an increase in its posterior standard deviation.

As part of testing the MCMH results, observations the Northern-Southern Hemisphere temperature difference observations were also added. However, this additional information was not found to be all that useful, with only marginal changes to the parameter values. It might be helpful for calibrating the North South heat exchange coefficient $\kappa_{\rm ns}$, but this was not included as one of the key parameters.

Table 6.7: Prior and posterior distributions for 11 combined climate, carbon cycle and aerosol forcing parameters with OHC observations added and revised prior for K (50,000 iterations).

parameter	prior mean	post mean	prior σ	post σ
climate sensitivity $\Delta T_{2{\rm x}}$	3.00	3.24	1.50	1.10
ocean vertical diffusivity K	0.70	0.71	0.50	0.35
land ocean heat exchange $\kappa_{\rm lo}$	1.50	1.75	0.80	0.64
land/ocean warming ratio $R_{\rm lo}$	1.60	1.62	0.20	0.17
total aerosol forcing $AF_{\rm soxi}$	-0.50	-0.31	0.40	0.09
temperature feedback factor, respiration $\sigma_{\rm R}$	-0.010	-0.023	0.15	0.13
CO_2 fertilisation factor β_s	0.50	0.77	0.50	0.26
temperature feedback factor, NPP $\sigma_{\rm NPP}$	-0.010	0.002	0.05	0.04
ocean cc impulse response scale factor $O_{\rm r}$	1.50	1.12	1.00	0.39
carbon flux partition, NPP to plant $g_{\rm P}$	0.50	0.51	0.25	0.20
carbon flux partition, plant to detritus $q_{\rm H}$	0.80	0.77	0.19	0.14

6.2.3 With alternate parameters

The MCMH runs discussed so far have involved 11 parameters for the combined climate–carbon cycle system and total aerosol forcing. It was noted in the uncertainty analysis (Section 6.1.2) that seven or eight parameters would be sufficient to cover 96 or 97% of the uncertainty in temperature change. Accordingly, the results for a reduced set of seven parameters were tested (Table 6.8). It was found that, in this case, the posterior parameter distributions for each of the seven parameters were quite similar to the 11 parameter results (Table 6.7).

Table 6.8: Prior and posterior distributions for seven combined climate, carbon cycle and aerosol forcing parameters, with OHC observations added (50,000 iterations).

parameter	prior mean	post mean	prior σ	post σ
climate sensitivity $\Delta T_{2{\rm x}}$	3.00	3.15	1.50	1.03
ocean vertical diffusivity K	0.70	0.66	0.50	0.36
total aerosol forcing $AF_{\rm soxi}$	-0.50	-0.30	0.40	0.09
temperature feedback factor, respiration $\sigma_{\rm R}$	-0.010	-0.026	0.15	0.14
CO_2 fertilisation factor β_s	0.50	0.75	0.50	0.24
temperature feedback factor, NPP $\sigma_{\rm NPP}$	-0.010	$-$ 0.002	0.05	0.04
ocean cc impulse response scale factor $O_{\rm r}$	1.50	1.11	1.00	0.37

The correlation structure for this seven parameter set of results is included in Table 6.9. The weak correlation between ΔT_{2x} and K is interesting; it demonstrates that the observations are independently constraining these two parameters, despite their close relationship. On the other hand, the moderately strong negative correlation between ΔT_{2x} and AF_{soxi} shows that the observations are not able to disentangle the climate sensitivity and aerosol forcing parameters.

Table 6.9: Correlations for the combined 7 parameter results in Table 6.8.

parameter	ΔT_{2x}	K	AF_{soxi}	σ_R	β_s	σ_{NPP}	O_r
climate sensitivity ΔT_{2x}	1.00						
ocean vertical diffusivity K	0.02	1.00					
total aerosol forcing AF_{soxi}	−0.47	−0.08	1.00				
temp. feedback factor, respiration σ_R	−0.01	−0.08	0.03	1.00			
CO_2 fertilisation factor β_s	0.09	−0.02	0.02	0.41	1.00		
temp. feedback factor, NPP σ_{NPP}	0.01	−0.10	0.03	0.32	−0.51	1.00	
ocean cc impulse response factor O_r	−0.07	0.00	−0.01	0.01	0.06	0.04	1.00

The positive correlation between β_s and σ_R and the negative correlation between β_s and σ_{NPP} are consistent with the results in Chapter 5 (Table 5.7), as is the weaker positive correlation between σ_R and σ_{NPP}. The remaining correlations are all very small.

6.2.4 Information gained

Additional insight into the MCMH parameter distributions can be gained from applying the diagnostic likelihood function $\mathbf{LF}(x)$, similar to the procedure applied previously to the climate system parameters (Section 4.3.4) and carbon cycle parameters (Section 5.5.4). Looking at the distributions in this way also avoids thinking just in terms of the mean and standard deviation, but also about the overall shape of the distribution (additional descriptors such as mode, median, skewness and kurtosis could also be considered). The $\mathbf{LF}(x)$ is also a diagnostic tool that shows up the lack of data to constrain some aspects of the parameter space.

The likelihood functions for the 7 combined parameter case, with the settings given in Table 6.8, are shown in Figure 6.2, and the 11 parameter case distributions for Table 6.7 settings are given in Figure 6.3. An extra table is included, Table 6.10, to make comparisons between the mean and and standard deviations of the 7 parameter and 11 parameter distributions easier. Note that the parameter values for each $\mathbf{LF}(x)$ were restricted to a 5% to 95% interval to avoid some of the problems with tiny numbers at the ends of the distributions that can result in very large values for the posterior to prior ratios.

The climate sensitivity ΔT_{2x} distribution is modified in both cases, with a reduction in the probability for both lower and higher values, while the distribution for K shows a shift towards lower values. The total aerosol forcing parameter exhibits a noticeable change from the prior to posterior distribution. The broad initial estimate for this distribution is considerably reduced. The two other parameters that display the most change are the CO_2 fertilisation factor β_s and the ocean carbon cycle impulse response scale factor O_r. The prior for β_s is constrained by the land flux data, while O_r is constrained by the ocean flux data, so that the overall observed carbon budget is maintained by the MAGICC results.

Table 6.10: Posterior means and standard deviations compared for the 7 parameter and 11 parameter combined climate, carbon cycle and aerosol forcing parameters from Table 6.8 and 6.7.

parameter	7p mean	11p mean	7p σ	11p σ
climate sensitivity $\Delta T_{2\mathrm{x}}$	3.15	3.24	1.03	1.10
ocean vertical diffusivity K	0.66	0.71	0.36	0.35
land ocean heat exchange κ_{lo}	-	1.75	-	0.64
land/ocean warming ratio R_{lo}	-	1.62	-	0.17
total aerosol forcing AF_{soxi}	-0.30	-0.31	0.09	0.09
temperature feedback factor, respiration σ_{R}	-0.026	-0.023	0.14	0.13
CO_2 fertilisation factor β_s	0.75	0.77	0.24	0.26
temperature feedback factor, NPP σ_{NPP}	-0.002	0.002	0.04	0.04
ocean cc impulse response scale factor O_{r}	1.11	1.12	0.37	0.39
carbon flux partition, NPP to plant g_{P}	-	0.51	-	0.20
carbon flux partition, plant to detritus q_{H}	-	0.77	-	0.14

The four additional parameters in the 11 parameter case exhibit only small changes from their prior to posterior distributions (Figure 6.3).

The 7 parameter and 11 parameter posterior distributions are plotted together in Figure 6.4 to help clarify the differences between the two. In fact, the differences are quite small, suggesting that the 7 parameter arrangement could be used for emission scenario projections.

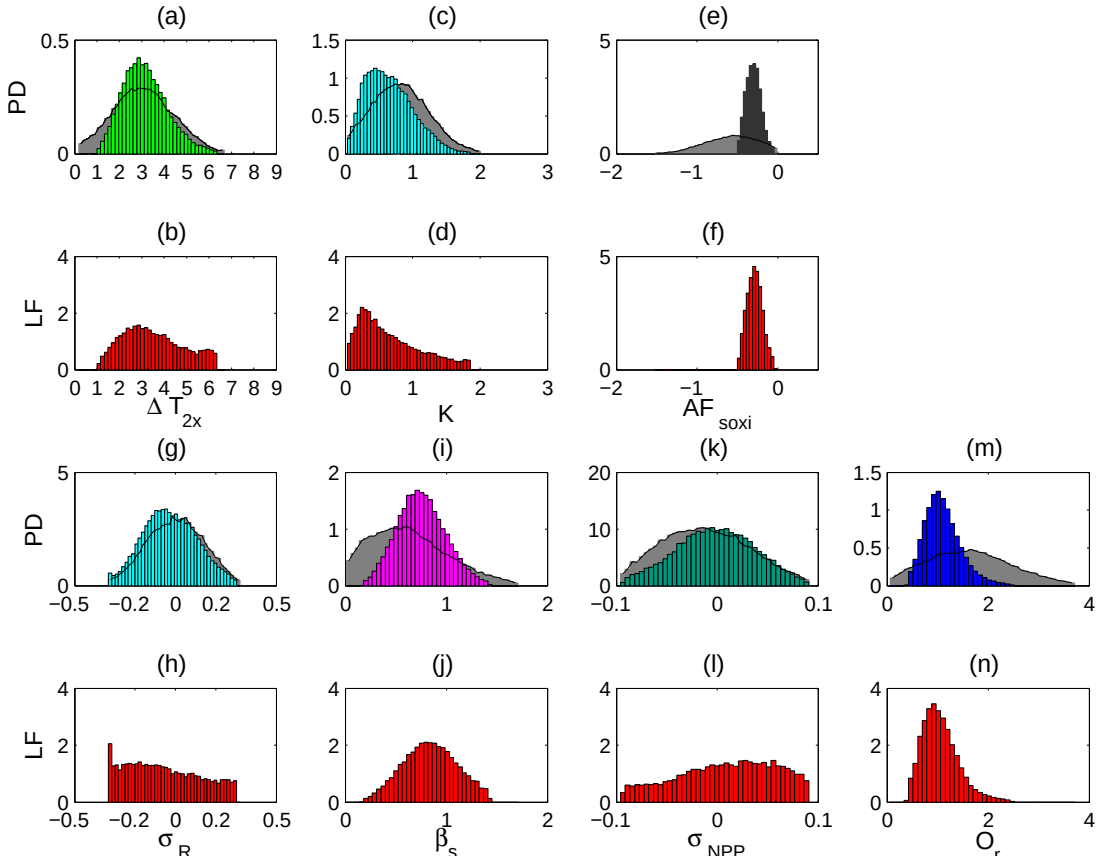

Figure 6.2: Combined 7 parameter likelihood function plots, comparing prior to posterior distributions (50k iterations, modified K prior) (PD = probability density). The prior distribution is indicated by the grey shaded region with black outline.

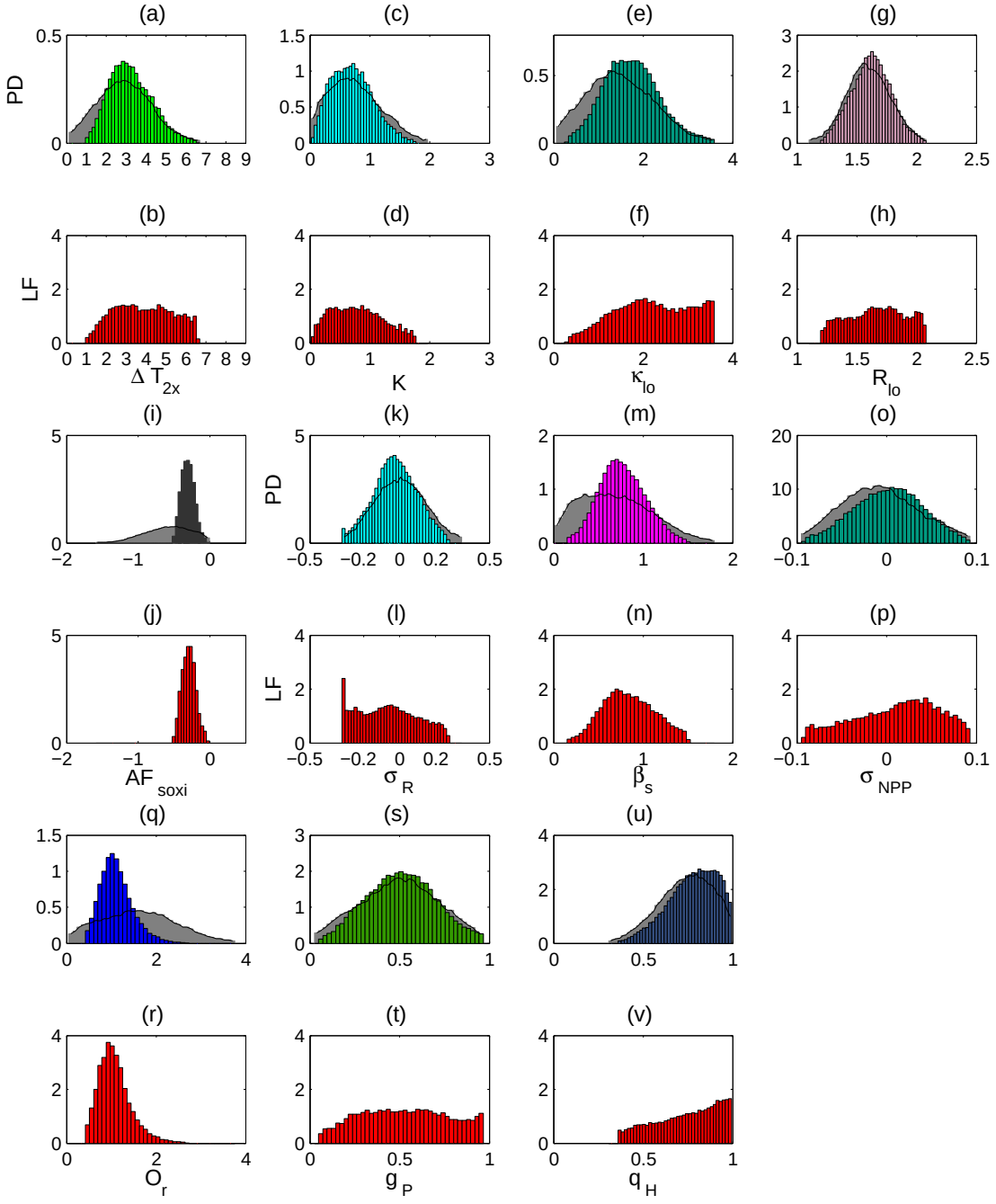

Figure 6.3: Combined 11 parameter likelihood function plots, comparing prior to posterior distributions (50k iterations, modified K prior). The prior distribution is indicated by the grey shaded region with black outline.

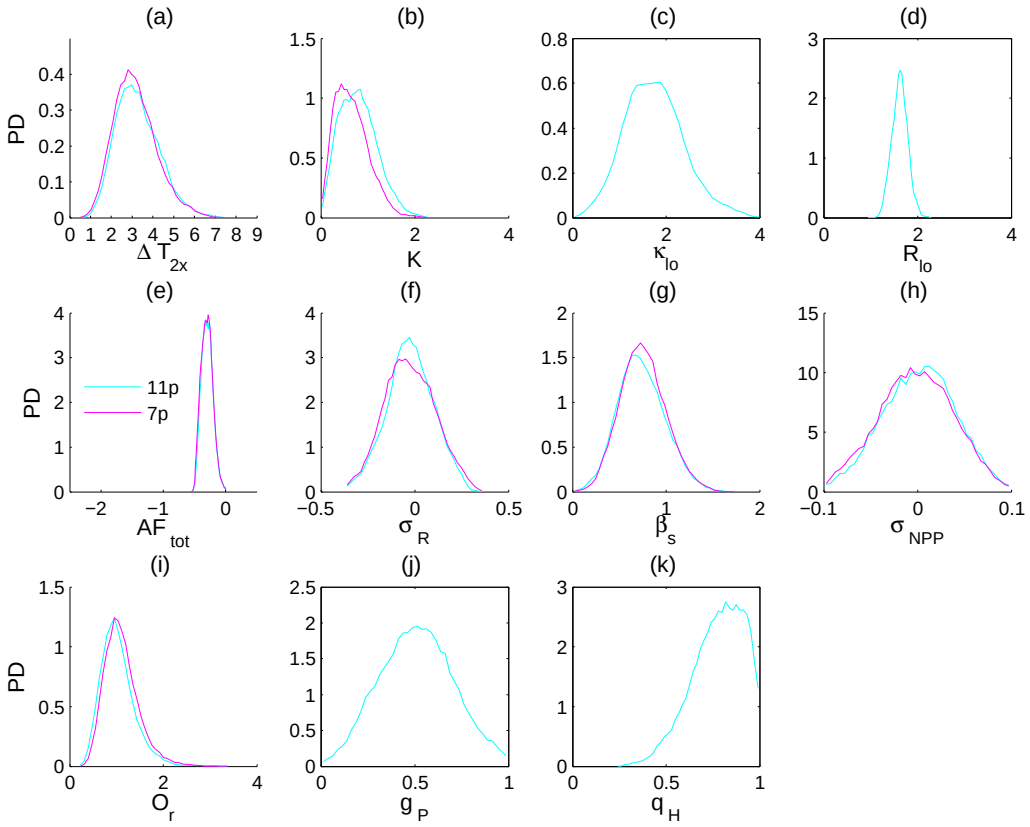

Figure 6.4: Overlay of posterior parameter distributions for the 7 parameter case (solid magenta lines) and 11 parameter case (solid cyan lines).

Another way of comparing the 7 parameter and 11 parameter posterior distributions is to examine what effect they have on future projections. To illustrate this, the temperature changes to the end of this century were calculated in conjunction with the A1FI emission scenario. The results for the 7 parameter case are plotted in Figure 6.5(a) and for the 11 parameter case in Figure 6.5(b). To help compare these two plots, Figure 6.6 shows the distributions for temperature change in 2100: (a) for the 7 parameter posteriors; (b) for the 11 parameter posteriors; and, (c) outlines for each histogram. The plots have been truncated at 12°C of temperature change, although there are still a tiny number of results for higher values. Some of the statistical attributes for these results are set out in Table 6.11.

The two sets of posterior parameter distributions yield very similar projected temperature change distributions, with only small variations and either of them could be used for temperature projections. Both encompass most of the uncertainties associated with the response of the combined climate–carbon cycle system to changes in radiative forcing brought about by changes in atmospheric greenhouse gases, with parameter distribution constrained by 20th-century observations, including uncertainty in those observations. The 11 parameter set has the advantage of including a constraint on the land ocean temperature difference. There are nevertheless still a number of limitations and assumptions that need to be kept in mind when considering projections derived from these distributions, which are discussed in the summary at the end of this chapter. The next section presents some applications of these distributions to obtaining probabilistic temperature projections.

Table 6.11: Temperature changes in 2100 compared for the 7 parameter results in Figure 6.5(a) and the 11 parameter results in Figure 6.5(b).

	7 parameters	11 parameters
mean	4.4°C	4.5°C
median	4.2°C	4.3°C
mode	4.2°C	4.1°C
likely range	3.0–5.6°C	3.1–5.8°C
σ	1.92	1.56

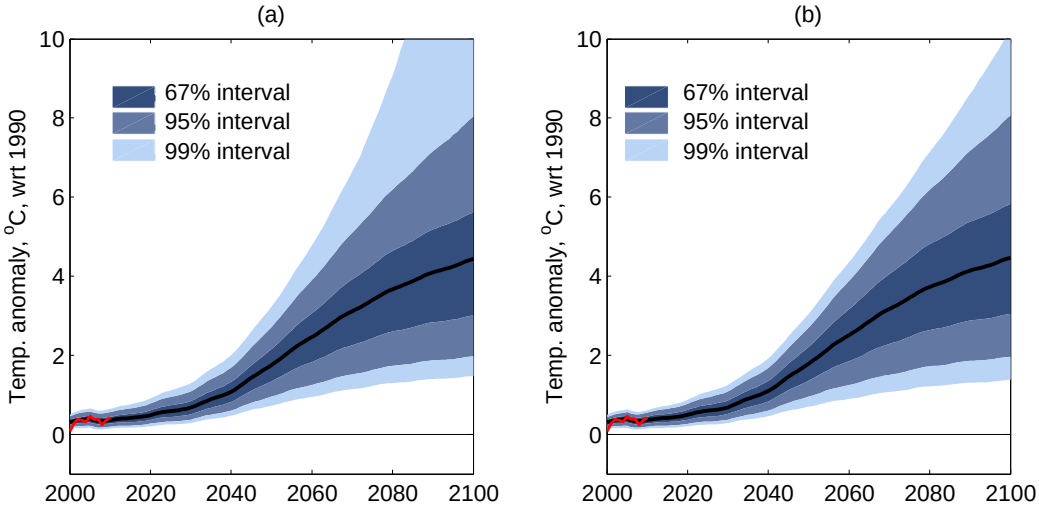

Figure 6.5: 21st-century temperature change projected for: (a) 7 parameter and, (b) 11 parameter posterior distributions applied to the A1FI emission scenario. Red line indicates historical temperatures (HadCRU) and solid black the mean temperature change.

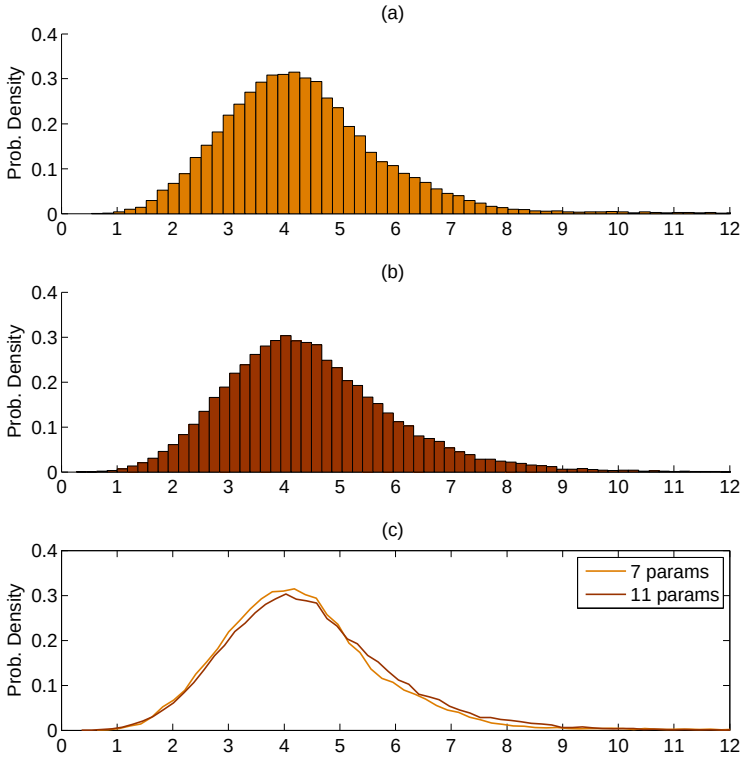

Figure 6.6: Comparison of distributions for temperature change in 2100 for the 7 parameter and 11 parameter posterior distributions.

6.3 Revised Projections

In this section, the posterior parameter distributions from Section 6.2.3 are applied to projecting temperature changes for two selected emission scenario, the SRES A1FI and B1 scenarios, to both demonstrate the method and compare the results to the IPCC AR4 estimates (*IPCC*, 2007b).

A set of posterior parameter distributions were used with the MCMH–MAGICC program to run the model forward, switching over from historical data until 2005, after which the emission scenario information is used. MAGICC was executed using 36,000 sets of parameter values, drawn from the posterior distribution. All of the resulting 36,000 annual mean surface temperature changes and CO_2 concentrations were saved for subsequent processing. The carbon cycle temperature feedbacks were left switched on unless noted otherwise. Parameters not included in the posterior distributions were left at their default settings. In the 7 parameter case, the land ocean heat exchange κ_{lo} was set to 2.0 $\text{W m}^{-2}\,^{\circ}\text{C}^{-1}$ and the land ocean warming ratio R_{lo} set to 1.6, while the two carbon cycle parameters were set to the BERNCC defaults: carbon flux partition, NPP to plant $g_{\text{P}} = 0.448$; carbon flux partition, plant to detritus $q_{\text{H}} = 0.999$.

6.3.1 SRES AIFI comparison

Before looking at the posterior projections, the results from the prior parameter distributions were also generated with the A1FI scenario, as shown in Figure 6.7(a) for temperature change and (b) for CO_2 concentrations. These results display a very wide spread for the projections, especially at the upper end of the distributions.

The prior distributions were created from the MCMH program by generating random sets of parameter values which were tested to check that they are members of the given initial parameter distribution (the first Metropolis decision rule). The values were not applied to MAGICC and tested for acceptability by the fit of the model results to observations.

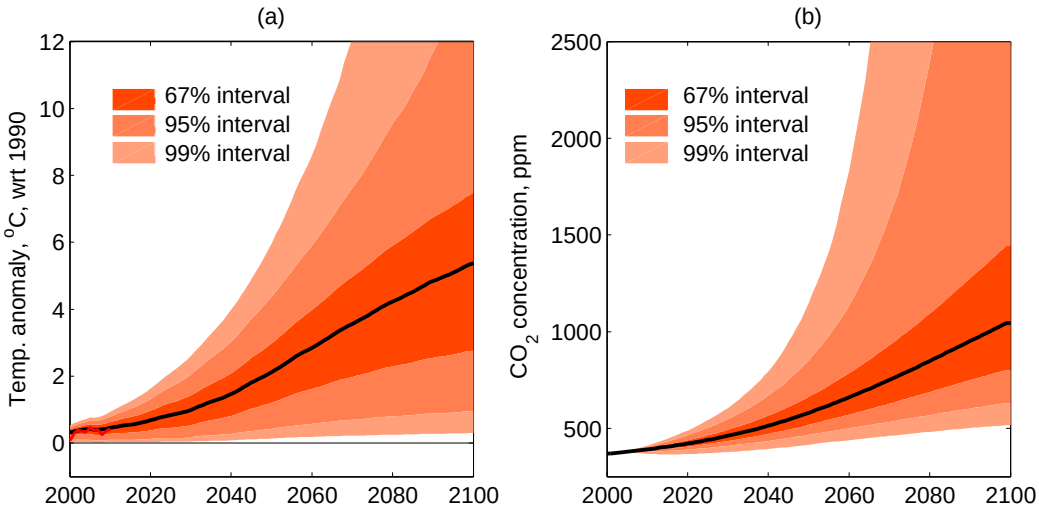

Figure 6.7: Projected priors for: (a) temperature change, and (b) CO_2 concentrations, for the A1FI emission scenario from the 11 parameter case prior parameter distribution (32,000 priors).

The posterior results are shown in Figures 6.8. Note that this distribution derives from the same 11 parameter, 50,000 iteration run referred to in Section 6.2.3, which generated just over 38,000 accepted parameter sets, of which 36,000 were used for the forward projections.

The resulting posterior projected temperature changes and CO_2 concentrations show reduced distribution ranges, as expected. These results were compared to the IPCC AR4 values (*IPCC*, 2007b), Table 6.12, which lists the best estimate and likely ranges for temperature change in 2100 (wrt 1990). A direct comparison is not possible as the IPCC best estimate is based on an ensemble mean from the CMIP3 models, with only informed estimates for the upper and lower bounds of the likely range. There was no probability distribution on which to base these numbers. Further, care is required in the interpretation of 'best estimate', which might easily be taken as the average or mean change. However, the distributions implied by the likely ranges, with their plus 60% and minus 40% would then be biased, with smaller probabilities for the worst outcomes (*Gay and Estrada*, 2010).

The mode and 67% confidence interval from the MAGICC probability distribution were used for comparison. The mode differs from the mean by 0.4°C because of the skewed distribution (in this example). The MAGICC prior has a best estimate (mode) of 4.9°C and likely (67% confidence interval) range of 2.8–7.5°C, which becomes 4.1°C (3.1–5.8°C) for the posterior temperature change in 2100. The prior has a much wider distribution, skewed towards larger temperature change values than for the posterior.

The posterior best estimate is a little more (0.1°C) than that for the IPCC A1FI projected temperature change, but with a narrower likely range. The increased lower bound indicates a greater risk of higher global–mean temperatures, which is an important result since it means that the chance of reaching 2°C global–mean temperature change (relative to 1990) is that much higher.

Table 6.12: A1FI temperature change projections for 2100 compared to MAGICC's results (wrt 1990).

A1FI	Prior mode (likely range)	Posterior mode (likely range)
IPCC AR4		4.0°C (2.4–6.4°C)
MCMH 11 params	4.9°C(2.8–7.5°C)	4.1°C (3.1–5.8°C)

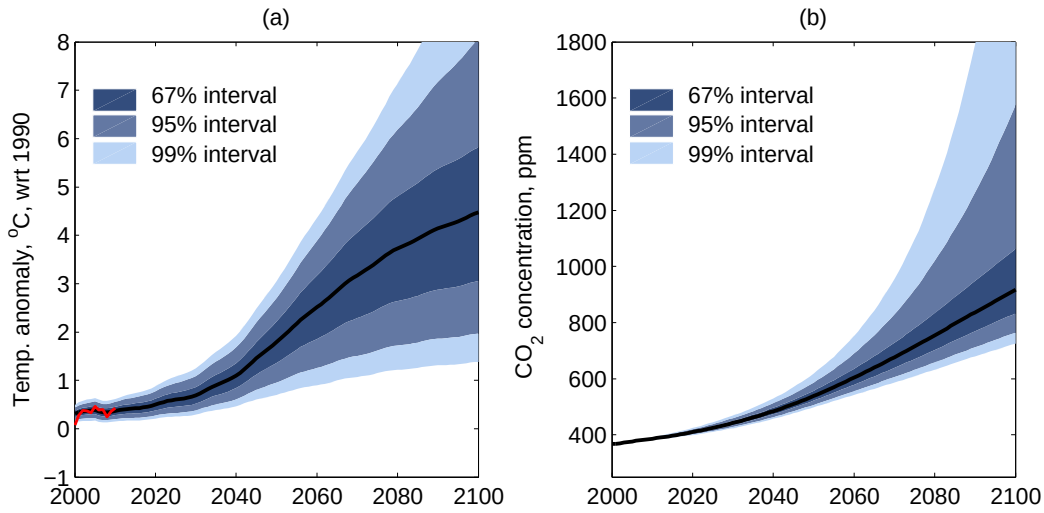

Figure 6.8: Projected posterior for: (a) temperature change, and (b) CO_2 concentrations, for the A1FI scenario from the 11 combined climate, carbon cycle and aerosol forcing posterior parameter distribution.

6.3.2 SRES B1 comparison

The prior and posterior temperature projections for the B1 scenario were also generated, in the same way as for A1FI. B1 is a low emissions scenario, with less temperature change. The MAGICC prior and posterior best estimates and likely ranges for temperature changes are tabled below (Table 6.13), with plots for 21st-century temperature change and CO_2 concentrations in Figures 6.9 and 6.10.

The posterior parameter distribution reduces the spread in the likely temperature change distribution as compared to the prior, although nearly all the change occurs at the warm end of the distribution. The mode for the posterior temperature change in 2100 was found to be 0.2°C less than the IPCC AR4 best estimate, the same at the lower end of the likely range and reduced at the upper end of the likely range. The cooler MAGICC mode may, in part, be due to the inclusion of aerosol forcing uncertainty.

Table 6.13: B1 temperature change projections for 2100 compared to MAGICC's results.

B1	Prior mode (likely range)	Posterior mode (likely range)
IPCC AR4		1.8°C (1.1–2.9°C)
MCMH 11 params	2.0°C(1.3–4.3°C)	1.6°C (1.1–2.5°C)

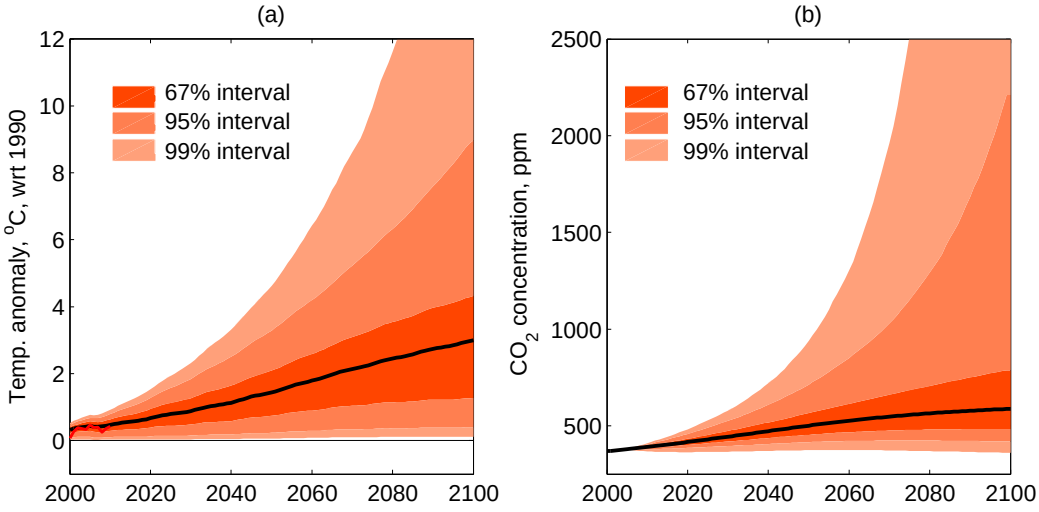

Figure 6.9: Projected prior for: (a) temperature change, and (b) CO_2 concentrations, for the B1 scenario from the 11 combined climate parameter, carbon cycle parameter and aerosol forcing posterior distributions.

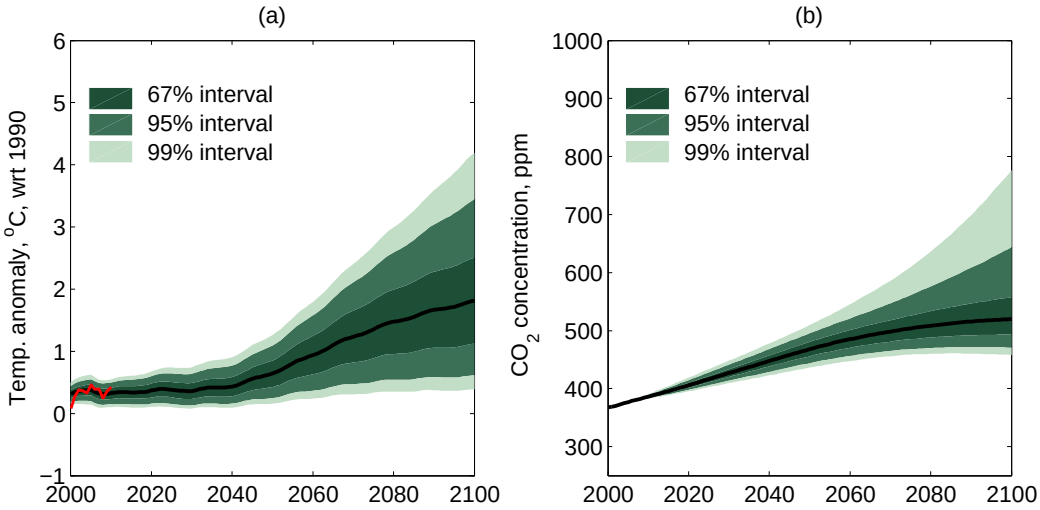

Figure 6.10: Projected posterior for: (a) temperature change, and (b) CO_2 concentrations, for the B1 scenario from the 11 combined climate parameter, carbon cycle parameter and aerosol forcing posterior distributions.

6.3.3 Role of the carbon cycle

Carbon cycle feedbacks on/off

Another perspective on the role of the carbon cycle and its influence on temperature change projections can be obtained by switching off the carbon cycle temperature feedbacks in MAGICC. This is readily achieved by using the appropriate configuration file setting, unlike the C4MIP models where this is much more difficult. The 11 parameter posterior distribution was used to test carbon cycle temperature feedbacks, with the results presented in Figure 6.11 for the A1FI scenario, for temperature with the carbon cycle feedbacks on (a) and switched off (b), and for CO_2 concentrations with the carbon cycle feedbacks on (c) and switched off (d).

The results for projected temperature change and CO_2 concentrations in 2100 are summarised in Table 6.14. The impact on the projected temperature change for the likely or 67% percentile confidence interval is from 3.1–5.8°C with the carbon cycle on, to 2.8–5.2°C with the carbon cycle feedbacks off. The effect is most noticeable on the temperature change for the mean, which is 4.5°C as compared to 4.0°C due to the more highly skewed distribution when the carbon cycle feedbacks are on. This is particularly evident in the CO_2 concentration plots (Figure 6.11 (c) and (d).

Reliable estimates for the temperature–dependent processes in the carbon cycle are clearly important. MAGICC represents these processes with four terrestrial components and one ocean component. The uncertainty analysis, which was used to guide the selection of the parameters for the MCMH calibration, identified two of these as being notable contributors, the temperature feedbacks for respiration σ_{R} and NPP σ_{NPP}. However, the observational data made little impact on improving their estimated values.

Table 6.14: Summary of A1FI projections for temperature change and CO_2 concentrations in 2100 with and without carbon cycle temperature feedbacks.

	Temp. change °C		CO_2 conc. ppm	
	On	Off	On	Off
mean	4.5	4.0	990	836
median	4.3	4.0	917	834
mode	4.1	4.0	880	830
likely	3.1–5.8	2.5–4.8	833–1063	758–910

C4MIP comparison

The carbon dioxide concentrations from MAGICC can also be compared to the C4MIP results (*Friedlingstein et al.*, 2006). This set of experiments was completed using the SRES A2 scenario with and without carbon cycle feedbacks. The results for the CO_2 concentrations in 2100 are listed in Table 6.15 for 10 of the 11 models for which data is available. A visual representation of the likely uncertainty ranges is given in Figure 6.12 for temperature change and CO_2 concentration in 2100.

The MAGICC CO_2 distributions, which are based on the MCMH calibration using observations, and not the C4MIP calibrated values of *Meinshausen et al.* (2011a), are not too dissimilar to the C4MIP values. The likely range with the carbon cycle feedbacks off are very close, with the C4MIP range 700–810 ppm as compared to the MAGICC likely range of 679–803 ppm. The ranges with the carbon cycle feedbacks on show a greater difference, 775–930 ppm for the C4MIP range as compared to 739–858 ppm for MAGICC, with the upper bounds having the greatest difference. The mean C4MIP difference in CO_2 concentrations in 2100 between the carbon cycle on and off is 83 ppm, whereas the difference is 61 ppm for MAGICC. This is due to model differences, but also in the treatment of the different climate system processes and radiative forcings.

The A2 scenario temperature change results shown in Figure 6.12(a) are a comparison between the IPCC AR4 (*IPCC*, 2007b) and the MAGICC results, which indicate a reduced range of uncertainty, with a much reduced upper bound.

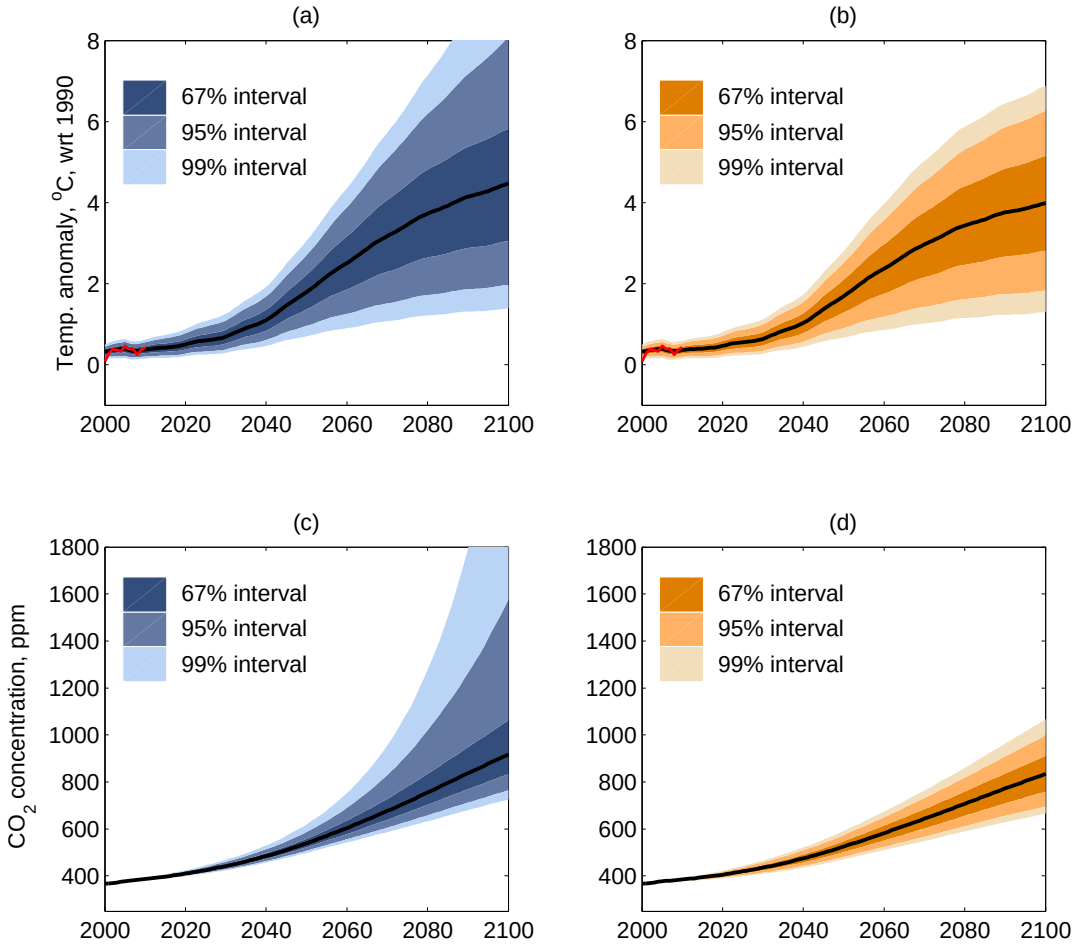

Figure 6.11: Projected temperature change and CO_2 concentrations distributions for the SRES A1FI emission scenario from 36,000 joint parameter sets with the 11 combined climate system, carbon cycle and aerosol forcing posterior parameter distribution with and without carbon cycle feedbacks: temperature change (a) with carbon cycle feedbacks on and, (b) off; CO_2 concentrations (c) with carbon cycle feedbacks on and, (d) off.

Table 6.15: Summary of C4MIP projections for CO_2 concentrations in 2100 with and without carbon cycle temperature feedbacks for the A2 scenario (*Friedlingstein et al.*, 2006).

	CO_2 conc. ppm	
C4MIP model	On	Off
BERN–CC	784	719
CSM–1	792	773
CLIMBER	870	812
FRCGC[a]	885	862
HadCM3LC	1025	801
IPSAL–CM2[b]	775	700
LLNL	732	681
MPI[b]	846	762
UMD2	967	869
UVic–2.7	930	801
C4MIP mean	861	778
MAGICC A2 mean	804	743
and likely range	739–858	679–803

[a] results extrapolated from 2098 end year.
[b] results extrapolated from 2099 end year.

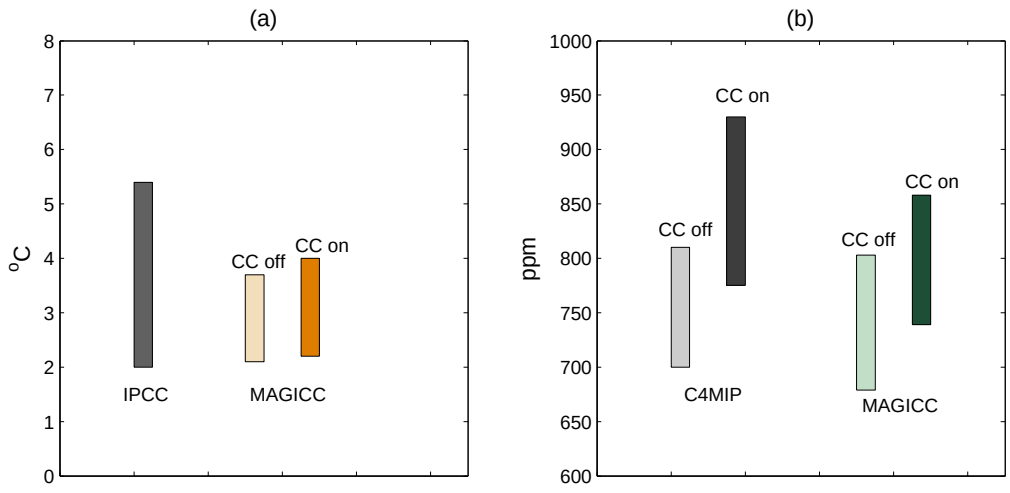

Figure 6.12: A2 scenario likely uncertainty ranges for: (a) temperature change in 2100 and, (b) CO_2 concentration, comparing IPCC AR4 temperature (*IPCC*, 2007a) and C4MIP CO_2 (*Friedlingstein et al.*, 2006) to MAGICC results.

6.3.4 Land–surface temperatures

In general, changes in global–mean near–surface air temperature anomalies (GSAT) are used as a primary metric of climate change. The GSAT provides a single metric that encapsulates a variety of associated changes, such as the melting of ice sheets and glaciers, impacts on precipitation and evaporation regimes, and changes to phenology. The recent upward trend in this metric has become a concern for many scientists across a broad range of disciplines as the evidence suggests that the magnitude of this change has not been seen at any time during the past 1,000 years or more (*Mann et al.*, 2008). This increase in temperature, if sustained, will most likely lead to large-scale alterations in the environmental conditions that plants and animals, including ourselves, have evolved to live in.

However, temperature changes around the globe are not evenly distributed, with warming above the global–mean expected in some areas, such as the polar regions. MAGICC does not have the capability of modelling these regional changes (a pattern scaling routine could be used for this purpose), but it is able to report separate land and ocean surface temperature changes. Indeed, the global–mean temperature is an area average derived from the land and ocean temperatures, according to the expression:

$$T_{\text{global}} = \frac{T_{\text{l}} \times f_{\text{l}} + T_{\text{o}} \times f_{\text{o}}}{(f_{\text{l}} + f_{\text{o}})} \tag{6.1}$$

with the land and ocean area fractions specified within MAGICC as f_{l} = 0.315 and f_{o} = 1 - f_{l} = 0.685. The ratio of land to ocean warming has a value of 1.6, based on recent observations (Chapter 3), so that:

$$T_{\text{l}} = 1.6 T_{\text{o}} \tag{6.2}$$

Then:

$$T_{\text{global}} = T_{\text{o}}(1.6 f_{\text{l}} + f_{\text{o}}) \tag{6.3}$$

hence:

$$T_{\text{o}} = 0.841 T_{\text{global}} \tag{6.4}$$

and:

$$T_{\text{l}} = 1.346 T_{\text{global}} \tag{6.5}$$

This shows that, as a reasonable approximation or ‘rule-of-thumb’, the land temperature change will be about 35% greater than the global–mean temperature change. Land–surface temperature changes are, in some ways, of more immediate importance, since we live on land, and many of the services we rely on are also land–based and affected by temperature, such as agriculture and fresh water. The land is also prone to greater heat extremes.

For a 2°C global–mean increase above pre-industrial, the land temperature increase will be around 2.7°C. In other words, it is not just a 2°C warming we have to be able to adapt to, if that

is the target for mitigation policy, but nearly 3°C over land. It is not clear that this issue is fully appreciated by policy–makers or the general public.

Another important consideration is understanding the degree of risk associated with particular targets. An emission pathway may be aimed toward avoiding, as an example, 2°C of global–mean warming above pre-industrial, but what is the chance that the target will be achieved, 90%, 50% or some other level? The posterior parameter distributions derived from the MCMH–MAGICC program allow an assessment of the risks, taking into account the range of uncertainty encompassed by these distributions, that is, allowing for the response of the combined climate–carbon cycle system as represented by MAGICC, uncertainty in aerosol forcing, and uncertainty in the observations. Not included are the risk of not following the assumed emission pathway, any additional non-linearities in the Earth's climate system, 'tipping point' events, and any other unforeseen processes (the 'unknown unknowns'),[2] as well as the limitations of using a simple climate model and its simplified representation of complex climate system processes.

The next section looks at one approach to representing risks, and then, in Chapter 7, the topic of future temperatures and emission pathways is examined further, applying the results from this chapter to some alternative scenarios.

6.3.5 Risks of exceedance

One way of considering the uncertainty around achieving a given global–mean warming target is to express it in terms of the risk of exceedance. The posterior parameter distributions from the MCMH evaluation can by applied to a future emission scenario or pathway (scenarios and pathways are discussed in Chapter 7), in the same way as the temperature change projections were produced in the A1FI example above (Section 6.3.1), but with annual temperature results sorted so as to enable cumulative distributions to be plotted.

An example is included here to illustrate this process, using the results from the A1FI and B1 scenarios, as shown in Figure 6.13(a) and (b). In addition to the global–mean temperature changes, land temperature changes have been considered for the reasons discussed in the previous section (Section 6.3.4).

These graphs show the risks of exceeding given temperature thresholds or targets, with curves provided for 2, 3 and 4°C. The figures can be interpreted in a number of different ways. For example, given a policy target of not exceeding 2°C of additional global–mean warming relative to pre-industrial temperatures, for the A1FI scenario in Figure 6.13(a), the black solid line indicates a 50% chance that 2°C will be reached by about 2042, and that it is almost certain that 2°C will be reached by the end of this century, with a 73% probability of reaching 4°C by 2100. A lower emission scenario, B1, Figure 6.13(b), shows the 50% probability of reaching 2°C moves out to around 2085.

[2]From a statement to the press made by Donald Rumsfeld, a former United States Secretary of Defense, in February 2002.

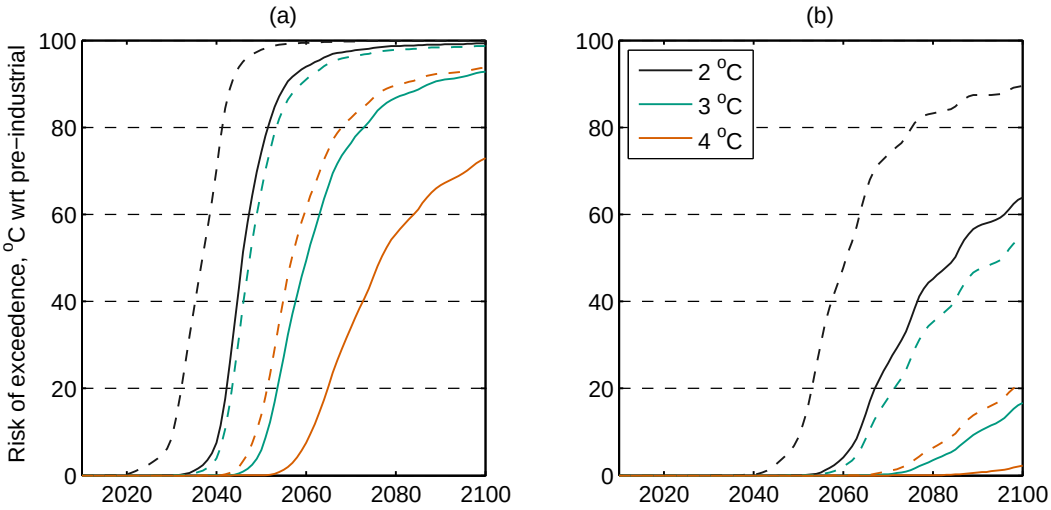

Figure 6.13: Risk of exceeding temperature change targets for: (a) the SRES A1FI and (b) B1 emission scenarios, from 36,000 joint parameter sets for the 11 combined climate parameter, carbon cycle parameter and aerosol forcing posterior distributions. Solid lines are for the global-mean, dashed lines for land temperature changes.

6.4 Uncertainty Components in Projections

6.4.1 From scientific uncertainty

An alternative way of evaluating the different components of the scientific uncertainty in projected temperature change in 2100 is to look at an emission scenario, such as the A1FI results, for the climate system only parameters, the carbon cycle only parameters, both with and without the carbon cycle temperature feedbacks. Three pairs of combinations were compared:

1. The combined 11 parameter posterior distributions for the overall uncertainty.
2. With only the four climate system parameters plus composite aerosol forcing parameter for the climate system uncertainty.
3. With only the six carbon cycle parameters for the carbon cycle uncertainty.

A summary of the results are set out in the accompanying Table 6.16 for temperature change and CO_2 concentrations in 2100, while the likely temperature change ranges are illustrated in Figure 6.14(a) and the likely CO_2 concentration ranges in Figure 6.14(b).

The likely temperature change uncertainty arising from the four climate plus total aerosol forcing parameters, shown by the central pair of bars in Figure 6.14(a), is actually slightly greater than that for the complete 11 parameters. The MCMH derived parameter sets mean that the carbon cycle parameters act together with the climate system to produce parameter combinations that produce acceptable fits to the observations, so that the upper end of the climate only uncertainty range is counteracted by carbon cycle parameter values that reduce the amount of temperature change.

Although the carbon cycle only temperature change uncertainty range is much narrower than that for the climate system, these parameters are essential to estimating the amount of warming that results from the carbon cycle temperature feedbacks, and in calibrating the model to match the historical observations. These results indicate the significance of the carbon cycle temperature feedbacks; these feedbacks add 0.5°C to the projected A1FI mean temperature change in 2100, but only 0.1°C to the mode (see also previous discussion in Section 6.3.3). The distributions for temperature change and CO_2 concentrations are very close to normal without the carbon cycle feedbacks, but become skewed to the right with the carbon cycle feedbacks turned on.

The role of the carbon cycle parameters is also seen in Figure 6.14(b), which shows a different pattern to the likely uncertainty ranges for CO_2 concentrations as compared to the temperature uncertainty bars in Figure 6.14(a). The climate system plus aerosol forcing parameters have almost no effect on CO_2 concentrations with the carbon cycle feedbacks switched off, and some impact with the carbon cycle on. This will be almost completely due to the climate sensitivity ΔT_{2x} and land ocean warming ratio R_{lo}. Most of the uncertainty range in the carbon cycle stems from the carbon cycle parameters themselves, including the carbon cycle temperature feedback parameters, but ΔT_{2x} and R_{lo} also contribute.

Table 6.16: Summary of A1FI projections for 2100 for alternate parameter arrangements.

Temperature change in 2100 (wrt 1990)									
	6 carbon			4 climate & AF			11 parameters		
	CC on	CC off	Δ	CC on	CC off	Δ	CC on	CC off	Δ
mean	4.3	4.0	0.3	4.6	4.1	0.5	4.5	4.0	0.5
median	4.3	4.0	0.3	4.5	4.0	0.5	4.3	4.0	0.3
mode	4.2	4.0	0.2	4.6	4.0	0.6	4.1	4.0	0.1
likely	4.0–4.7	3.7–4.3	0.3–0.4	3.2–6.0	2.9–5.2	0.3–0.5	3.1–5.8	2.8–5.2	0.3–0.6
CO_2 concentration in 2100, ppm									
	CC on	CC off	Δ	CC on	CC off	Δ	CC on	CC off	Δ
mean	939	834	105	981	846	121	990	836	154
median	908	831	77	978	846	844	917	834	83
mode	880	825	55	975	847	116	880	830	50
likely	831–1026	755–908	76–118	935–1026	841–851	94–175	833–1063	759–910	74–153

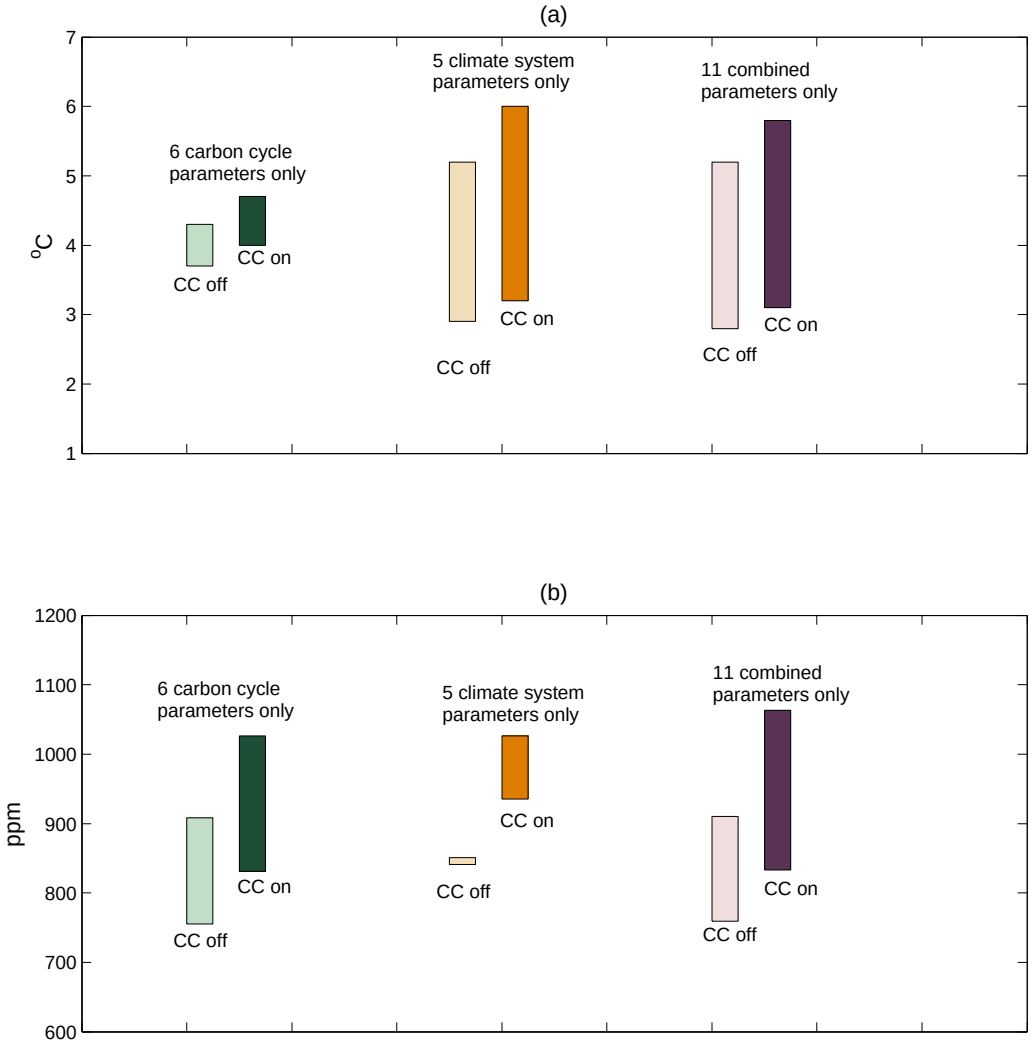

Figure 6.14: Comparison of A1FI likely temperature change CO_2 concentration intervals for different parameter sub-sets.

6.4.2 From emissions scenario

Uncertainty in future temperature changes also depends very much on the amounts of greenhouse–gases that are emitted, although it is difficult to capture this type of uncertainty since it is closely related to the range of emissions scenarios or pathways considered.

The A1FI and B1 scenarios examined in this chapter span the full range of emissions for the six SRES marker scenarios (discussed further in Chapter 7). Taking the likely range for each of these two scenarios (3.1–5.8°C and 1.1–2.5°C, from Tables 6.12 and 6.13), the combined likely range of projected temperature change is 1.1 to 5.8°C, with a central value for the A1FI/B1 likely range of 3.5°C (according to MAGICC and the 11 parameter posterior distributions). The A1FI likely interval span of 2.7°C has expanded to 4.7°C, an increase of 74% when the full range across the SRES emission scenarios is considered; the B1 interval span of 1.4°C has more than tripled. This range is illustrated in Figure 6.15.

It is difficult to characterise the contribution that future emissions make to the uncertainty in projected temperature changes, since the emission scenarios do not have probabilities associated with them. These two scenarios illustrate the lowest to highest range of emissions and resultant temperature changes for the SRES scenarios, and therefore provide a reasonable representation of the possible future temperature changes to the end of this century in the absence of effective mitigation. Taking the average of the A1FI and B1 modes for temperature change in 2100 (4.1°C and 1.6°C respectively) as the central best estimate for temperature change in 2100, that is 2.9°C, then, as a very rough guide, 50% of the uncertainty in the projected temperature change is due to uncertainty in the possible range of future emissions. Future emissions are discussed further in Chapter 7. The other 50% of the uncertainty arises from the scientific uncertainty associated with the response of the combined climate–carbon cycle system, for which climate sensitivity contributes about half, aerosol forcing about a quarter and the carbon cycle about a fifth of the scientific uncertainty, as determined by the uncertainty analysis in Chapter 6.

6.5 Review of Results

This chapter has examined the combined climate system and carbon cycle parameters, building on the methods developed in Chapters 4 and 5. The underlying theme of these three chapters has been understanding and quantifying the uncertainties associated with the climate system, and the relative contributions of the principal components to the overall uncertainty in global–mean temperature changes.

The scientific uncertainty in projected global–mean temperature change over this century is dominated by the temperature feedbacks in the climate system, collectively encapsulated by the climate sensitivity, which is represented in MAGICC by the climate sensitivity parameter $\Delta T_{2\mathrm{x}}$. The uncertainty analysis contained in this chapter found that around 50% of the scientific uncertainty of the temperature change in 2100 is accounted for by this one parameter. As a consequence, the estimated value of $\Delta T_{2\mathrm{x}}$ becomes critical to enabling MAGICC to produce reliable temperature change projections. There is also an issue concerning the interpretation of climate sensitivity, as either the equilibrium, effective or observed value, as well as was it being variable, that is, state–dependent, as discussed in Chapter 3, Section 3.1.1.

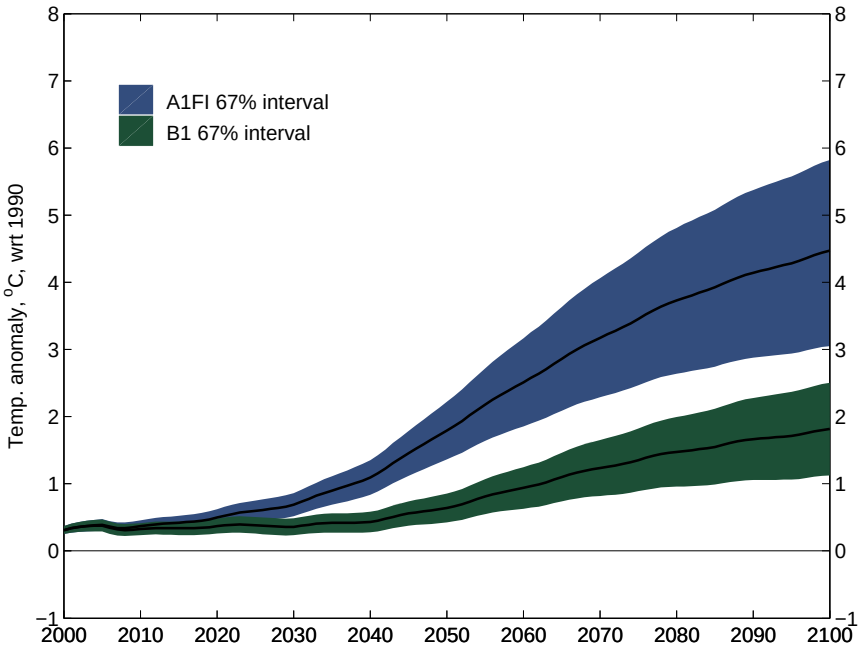

Figure 6.15: Comparison of A1FI and B1 likely temperature change intervals. Solid lines are for the mean of each distribution.

The results from the different attempts to assess the climate sensitivity parameter in MAGICC are summarised in Table 6.17. The standard or default setting for climate sensitivity is 3.0°C. Investigation of the climate system parameters in Chapter 3 proposed a lower value, based on a reduced ocean vertical diffusivity, which was estimated from historical ocean temperature and ocean heat content data. However, taking into account the uncertainty in total aerosol forcing and treating the model parameters equally with the MCMH method led to a higher estimate for climate sensitivity (Chapter 4). Including the carbon cycle and favouring a reduced ocean diffusivity setting changed this estimate again (Chapter 6).

The distribution of values for the climate sensitivity parameter ΔT_{2x} was found to be a skewed distribution with a mean of 3.24°C according to the MCMH results for the 11 combined climate, carbon-cycle and aerosol forcing parameters. The mode of this distribution is 2.85°C, with a likely (67% confidence interval) range of 2.17–4.33°C. This result can be compared to the AR4 best estimate of 3.0°C, likely range 2.00–4.50 °C (*IPCC*, 2007b).

The rate of heat uptake by the world ocean is also a contributor to this result, since a prior with a reduced value for the ocean diffusivity parameter K was selected. Although K was not found to be a big factor in the uncertainty analysis, it does play an important role in establishing the estimate for climate sensitivity ΔT_{2x}. Although ΔT_{2x} may only be be changed by a small amount as a result, small differences have a significant impact on temperature change projections.

Uncertainty in the climate sensitivity is also affected by the amount of aerosol forcing, which contributes to nearly 25% of the uncertainty for temperature change in 2100 according to the results obtained with MAGICC. Climate sensitivity and aerosol forcing are negatively correlated

and not easily separated. The total aerosol forcing comprises a variety of direct and indirect effects, all of which have their own associated uncertainties. For the purposes of this work, these uncertainties were grouped together into a single total aerosol forcing parameter AF_{soxi}. The MCMH algorithm was able to generate a parameter distribution for AF_{soxi} with a reduced spread as compared to the initial prior.

The role of the carbon cycle is also an important part of the overall uncertainty, although dispersed across the different parts of the terrestrial and oceanic biosphere. In addition, the temperature feedbacks for the carbon cycle are significant, although difficult to quantify. These carbon–cycle feedbacks are a positive feedback, increasing the amount of warming, and hence become more significant with greater warming, leading to acceleration of climate change (*Cox et al.*, 2000). The MCMH algorithm was successfully applied to estimating six of MAGICC's primary carbon cycle parameters using historical data as a constraint, something that has not been achieved previously. However, it is not clear how reliable the estimates for the two included temperature feedbacks are, especially for projecting into the future.

The parameter sets used with the MCMH algorithm did not include the ocean carbon cycle temperature feedback parameter α_T. The current structure of MAGICC is such that the ocean carbon cycle impulse response scale factor O_{r} is the predominant ocean carbon cycle parameter, according to the uncertainty analysis. However, this perhaps needs further investigation, since the solubility of carbon dioxide in the ocean is temperature dependent and expected to have an important role on the ability of the ocean to continue to act as a carbon sink.

The Monte Carlo Metropolis–Hastings algorithm has been demonstrated and found to be a valuable technique for estimating MAGICC's key model parameters. Historical observations of the climate and carbon cycle were used for this process. The resultant posterior parameter distributions provide a basis for projecting future temperature changes, and some examples are included within this chapter. A number of choices were made in the configuration of the MCMH–MAGICC program. Alternative arrangements could also be tested to verify the robustness of these results. For example, different observational data might be tried, such as NCDC and GISS surface temperature anomalies, and *Levitus et al.* (2009) ocean temperature and ocean heat content data. Other parameter combinations might also be investigated, such as the variable upwelling velocity fraction w_{var} or the initial NPP flux N.

This research has not investigated in any detail the issue of a variable/state–dependent climate sensitivity or the influence of the ocean temperature gradient on the ocean diffusivity K. The new version of MAGICC has provision for the relevant parameters. However, a state–dependent variable climate sensitivity can probably be only calibrated against data from complex AOGCMs. It might be possible to do something with a variable component to K, the dependence of vertical diffusivity on ocean warming gradient parameter Γ, using both the ocean vertical temperature change profile and time series of ocean heat content for multiple ocean depths. In addition to the whole ocean, it would also be interesting to investigate the hemispheric oceans to check MAGICC's Northern and Southern ocean vertical temperature profiles.

One of the other uncertainties not addressed here is that associated with the estimates for fossil fuel and land use emissions. The observations for these emissions are part of the carbon cycle after the switchover from using prescribed atmospheric greenhouse–gas concentrations, but

the uncertainty in the emissions is not captured. The annual uncertainty for fossil fuel emissions is estimated at $\pm 6\%$ (GCP), so that the effect of this source of uncertainty is quite small given the decadal averaging used for the MCMH observations.

Another set of observational uncertainties that have not been examined are related to the historical forcings for the Sun and volcanoes. Single data sets for these forcings are included as components for the 20th–century energy balance, but the uncertainty in these numbers is not allowed for in the MCMH processing. However, it is unlikely that these will have much of an impact. The radiative forcing change from the 11-year solar cycle is small, while volcanoes are short term events that have little long term influence. The uncertainties in these forcings could be explored by modifying the forcings by, say, $\pm$ 10% to see what affect this has on the temperature change results.

The posterior parameter distributions obtained from the MCMH processing encompass most of the scientific uncertainty related to the response of the climate system, as represented by MAGICC. In addition to the scientific uncertainty related to temperature change projections, future temperatures depend on the amount of greenhouse–gases that will be produced. This is a different type of uncertainty which depends on future choices about how energy is produced, how much fossil fuels continue to be burnt and the extent to which alternative energy sources play a larger role.

The MCMH posterior parameter distributions enhance MAGICC's results by enabling the production of probabilistic temperature change projections for a given emission scenario or pathway. The results for the SRES A1FI and B1 scenarios were produced in this chapter to demonstrate this capability, as well as for comparison with the results reported in the IPCC AR4 (*IPCC*, 2007a, Table SPM.3). The projections were found to have narrower likely temperature change ranges but similar best estimates as compared to the results reported in the IPCC AR4. One reason the IPCC has wider estimates is that the ranges were based on a number of different models rather than a single model. In addition, carbon cycle feedbacks were not directly taken into account, but were included as an extra estimate. The IPCC Table SPM.3 likely range values have a lower value 40% less than the best estimate and an upper value +60% greater than the best estimate, to allow for both carbon cycle and climate system uncertainties. This result was largely informed by using the high and low carbon cycle feedback settings with AR4 version of MAGICC, and is not a probability distribution (*IPCC*, 2007b, p804).

Further examples of emission scenarios are examined in the next chapter, which considers the nature of temperature changes in the 21st–century, the extent to which some increase in temperatures are inevitable from past greenhouse–gas emissions, and the range of future temperature changes that follow on from different emission pathways.

Table 6.17: Review of MAGICC parameter results. Values tabled for Chapter 4 onward are means from the MCMH results.

Param.	Name	Std.[a]	Ch3[b]	Ch4[c]	Ch5[d]	prior[e]	post[e]
ΔT_{2x}	Climate sensitivity	3.00	2.20	3.42	-	3.00	3.24
K	Ocean effective vertical diffusivity	2.30	0.60	1.09	-	0.70	0.71
R_{lo}	Land-ocean warming ratio	1.30	1.60	1.67	-	1.60	1.62
κ_{lo}	Heat exchange coefficient land-ocean	1.00	2.00	1.20	-	1.50	1.75
w_{var}	Variable upwelling fraction	0.70	0.20	-	-	-	
AF_{soxi}	Aerosol forcing (direct sulfate)	-	-	-0.31	-	-0.50	-0.31
σ_R	Temp. feedback factor, respiration	0.011	-	-	-0.05	-0.01	-0.02
σ_{NPP}	Temp. feedback factor, NPP	0.068	-	-	0.00	-0.01	-0.00
β_s	CO_2 fertilisation factor	0.649	-	-	0.70	0.50	0.77
g_P	Carbon flux partition, NPP to plant	0.448	-	-	0.54	0.50	0.51
q_H	Carbon flux partition, plant to detritus	0.999	-	-	0.74	0.80	0.77
O_r	Ocean cc impulse response scale factor	0.949	-	-	0.97	1.50	1.12

Notes:
[a] Standard values for climate from AR4 settings and carbon cycle from BERNCC.
[b] Based on Table 3.16.
[c] Table 4.14.
[d] Table 5.5.
[e] Priors and posts from Chapter 6, Table 6.7 (11 parameter case).

Chapter 7

Future Temperatures and Emissions Pathways

This chapter explores some aspects of future temperature projections, in particular applying the posterior parameter distributions developed in Chapter 6 to produce probabilistic results for selected emission scenarios and pathways. This technique provides a way of quantifying the scientific uncertainty associated with the projections, one of the goals of this research.

The methods used in this research differ from recent studies using MAGICC (such as, *Meinshausen et al.*, 2009; *Rogelj et al.*, 2010; *Meinshausen et al.*, 2011a;b;c) in that the model's primary climate system and carbon cycle parameters have all been calibrated using historical observations and not some combination of CMIP3 and C4MIP model results. In addition, two semi-independent observational indices for land−ocean and Northern−Southern hemisphere temperature differences were used to help reduce the cross-correlation between the surface temperature observations used previously. Furthermore, more extensive ocean observations have been incorporated into the calibration, with both multiple sub–surface ocean temperature changes and ocean heat content changes, to improve estimates for the climate system parameters.

The uncertainty in future temperature changes depends partly on the temperature response of the Earth's climate to a change in radiative forcing brought about by changes in atmospheric greenhouse–gas concentrations. This is the scientific uncertainty examined in the previous chapters. Future global–mean near-surface air temperature (GSAT) changes will also be influenced by natural variability on inter–annual to decadal time scales by modes of variability such as the El Niño Southern Oscillation and the Pacific Decadal Oscillation, as well as the influence of short term solar cycles and stochastic volcanic events.

Future temperature changes will also depend on the amount of continued greenhouse–gas emissions. These emissions in turn depend on a range of different factors which have been captured in the process of developing various emission scenarios, such as population, new energy generating technologies and economic growth. Such scenarios provide one way to explore alternate possible futures. The range of emissions envisaged by these scenarios is also a significant contributor to the spread in projected temperature changes given in the IPCC AR4. Having quantified the relative sources of scientific uncertainty to temperature change in 2100 for two particualr emission scenarios, the SRES A1FI and B1 scenarios in Chapter 6, this chapter considers a wider range of emission scenarios and pathways.

The current warming trend due to the enhanced greenhouse effect is expected to continue in the near term as a result of the existing greenhouse–gas concentrations and the heat already introduced into the climate system as a consequence of fossil fuel burning and land clearing over the past few decades. This 'committed' warming is the topic of the first section in this chapter.

The next part examines some of the major emission scenarios that have been used to investigate potential future temperature changes, with a focus on the six SRES marker scenarios and the new Representative Concentration Pathways (RCPs). Instead of the scenario approach, these concentration pathways have associated information about future emission levels but do not have the same 'storyline' aspect to them. In other words, these concentration pathways lack the same sort of rationale as scenarios — the pathways were not built up from considerations of factors such as population growth, energy intensity, GDP per capita in the way that scenarios are. Emission pathways are useful for testing the emissions consistent with a particular goal, such as achieving certain greenhouse–gas concentration levels or temperature targets. The question is then left as to how to achieve that level of emissions.

The third section considers the issue of stabilising the climate in the context of the United Nations Framework Convention on Climate Change (UNFCCC) Article 2. Two examples of stabilisation scenarios are examined in some detail, with the conclusion that drastic reductions in greenhouse–gas emissions are required to stabilise atmospheric concentrations and limit the amount of global–mean temperature change. The discussion turns to the question of 'dangerous climate change' and the associated 2°C global warming target agreed at the UNFCCC 2009 Conference of the Parties in Copenhagen. Although this target has questionable scientific validity, it has come to be a widely accepted benchmark. It is in the light of this that the combined global emissions efforts are examined, based on the recent Copenhagen pledges. There is a considerable gap between the emission reductions required to have a less than 25% chance of exceeding 2°C global–mean warming above pre-industrial and those currently planned.

7.1 Climate Commitment

7.1.1 Climate commitment introduced

'Climate commitment' considers the climate changes that are likely to occur from anthropogenic greenhouse–gas emissions up to the present day. The aim is to convey a measure of what has already been set in train and point out that further increases in global–mean surface temperatures (GSAT) will result even if anthropogenic greenhouse–gas emissions could be stopped immediately due to the sudden cessation of negative aerosol forcing, as discussed later in Section 7.1.2.

Climate commitment can be looked at in a number of different ways, with a range of authors having used various definitions. *Wetherald et al.* (2001) discussed warming commitment as the difference between realised warming at a specific time and equilibrium warming for a given GHG concentration. *Hare and Meinshausen* (2006) considered four forms of climate commitment:

1. Constant–emissions commitment. This is the warming that would result from maintaining present emissions. At current levels, this would lead to increasing GHG concentrations and hence further warming.

2. A constant–forcing commitment, or constant–composition commitment, with fixed GHG and aerosol concentrations. The warming commitment is due to the slow adjustment of the climate system to changes in radiative forcing. Warming would also continue until a new equilibrium temperature was reached.

3. Abrupt cessation of emissions, or geophysical commitment. The resulting temperatures are a function of the biogeophysical aspects of the climate system adjusting to the GHGs and aerosols in the atmosphere and uptake of GHGs into the biosphere and the ocean.

4. Feasible emissions scenario commitment, where warming is determined from a plausible emissions profile, taking into account current trends and feasible technological, economic and policy changes.

Wigley (2005) examined constant–composition commitments and constant–emissions commitments, pointing out that warming estimates are very dependent on climate sensitivity and aerosol forcing. *Teng et al.* (2006) noted that there is a commitment to additional warming and sea level rise even if atmospheric GHG and aerosol concentrations could be stabilised right now. Stabilising GHG and aerosol concentrations at 2000 levels, their results showed that the globally averaged temperature from an average of 16 AOGCM models will be nearly $0.5°C \pm 0.2°C$ warmer by the late 21st–century as compared to the 20th–century. *Meehl et al.* (2006) included consideration of climate commitment in their study, with GHGs and aerosols fixed at year 2000 levels. A number of model experiments were run with the CCSM3 coupled climate model with results that indicated a 0.4°C committed warming for the constant–composition case, additional to the 0.6°C rise over the 20th–century.

However, constant–composition commitment should not be regarded as the unavoidable warming that will eventuate from past greenhouse–gas emissions. *Matthews and Weaver* (2010) argue that zero–emissions commitment is the more appropriate perspective. Constant–composition commitment requires continued GHG emissions otherwise carbon sinks will gradually reduce the atmospheric concentration of CO_2, and hence gradually declining GSAT.

Climate commitment lends itself to investigation with a simplified climate model such as MAGICC, since the different types of commitment can be readily modelled over long time periods. The constant–composition case is effectively one in which radiative forcing is held constant. GSAT then adjusts over time to a new equilibrium temperature. This was tested, as shown in Figure 7.1, in which the global–mean temperature change by 2100 is 1.2°C, slowly rising to 1.3°C by 2300 (very similar to that obtained by *Matthews and Weaver*, 2010).

For their zero–emissions results, *Matthews and Weaver* (2010) do not appear to have taken into account the loss of aerosols that would accompany zero CO_2 emissions since there is no rise in temperature following the changeover point.

The most recent IPCC report discusses many of these issues in Chapter 7 of WG1, including the work of *Brasseur and Roeckner* (2005) (*IPCC*, 2007b, Figure 7.24), which considers the hypothetical removal of anthropogenic sulfate aerosol particles. Their results suggest that this would result in an immediate increase in the global average temperature of about 0.8°C and precipitation by 3%. This climate commitment case corresponds to constant GHG concentrations but

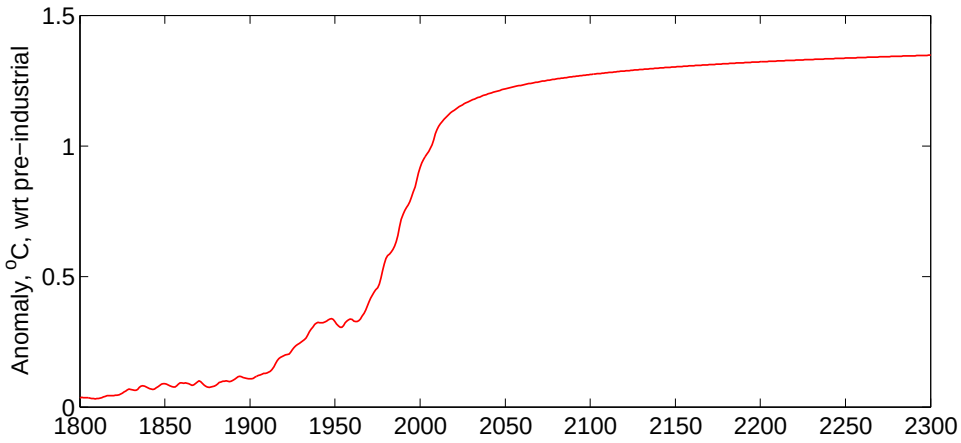

Figure 7.1: Constant–composition commitment temperature change, based on a changeover in 2010 to constant radiative forcing.

no aerosols, related to the long atmospheric lifetimes of GHGs (decades to centuries), whereas aerosols have very short lifetimes (a few days only).

A recent paper by *Ramanathan and Feng* (2008) noted that the 2005 GHG concentration of about 455ppm CO_2-equivalent corresponds to an estimated equilibrium temperature of 2.4°C (1.4–4.3°C), which is into the range of 'dangerous anthropogenic interference with the climate system'. The planet has not yet experienced this increase because it is masked by the cooling effect of aerosols and the delay in ocean heat transfer, i.e., the equilibrium temperature will not be reached until some time in the future (centuries rather than decades). Ocean expansion, and hence sea–level rise, will continue for many years to come. Note that the *Ramanathan and Feng* (2008) temperature change was based on different estimates for direct and indirect aerosol forcing as compared to those of the IPCC AR4.

CO_2-equivalent concentration is used as a measure of the combined effect of the long–lived greenhouse–gases, but it has been used in different ways according to what components are included. For atmospheric concentrations, CO_2-equivalent concentration can refer to the concentration of carbon dioxide that has the same warming effect as the combined effect of all of the greenhouse–gases, but without the cooling effect of aerosols (for example, *Stern*, 2007). Alternatively, CO_2-equivalent concentration is the net forcing of all anthropogenic radiative forcing agents including greenhouse–gases, tropospheric ozone, and aerosols but not natural forcings (for example, *Meinshausen et al.*, 2006). In this thesis, all the CO_2-equivalent concentration results are for the long–lived greenhouse-gases only (Kyoto protocol), and hence do not include aerosols or tropospheric ozone.[1] MAGICC version 6 provides reports for both CO_2-equivalent concentrations with all anthropogenic forcings included and for the long–lived greenhouse–gases only.

The zero–emissions commitment and fixed–emissions commitment cases are investigated next using MAGICC.

[1]The usage here is also not the measurement based on emissions, in which emissions of various greenhouse–gases are converted using their global warming potential (GWP).

7.1.2 Fixed emissions and MAGICC

Although climate commitment from constant GHG concentrations can be assessed, in practice it is really human actions that currently influence the level of GHG emissions. To gauge climate commitment from this perspective, two hypothetical situations were examined, a zero–emissions commitment scenario, in which it is assumed that all GHG emissions are switched off, and a fixed–emissions commitment scenario which sets future emissions at a constant level. A third intermediate scenario is included for comparison, an emissions pathway designed to achieve stabilisation of atmospheric GHG concentrations.

If all emissions stopped in 2010, as indicated by the solid green line in Figure 7.2(a), then the temperature change would initially spike upwards, due to the loss of aerosols, and then gradually decline to about 0.7°C (likely range 0.5–1.4°C) in 2100 relative to pre-industrial temperatures (Figure 7.2(b)) using the posterior parameter distributions (11 parameter case) from Chapter 6 rather than relying on a single set of parameters.

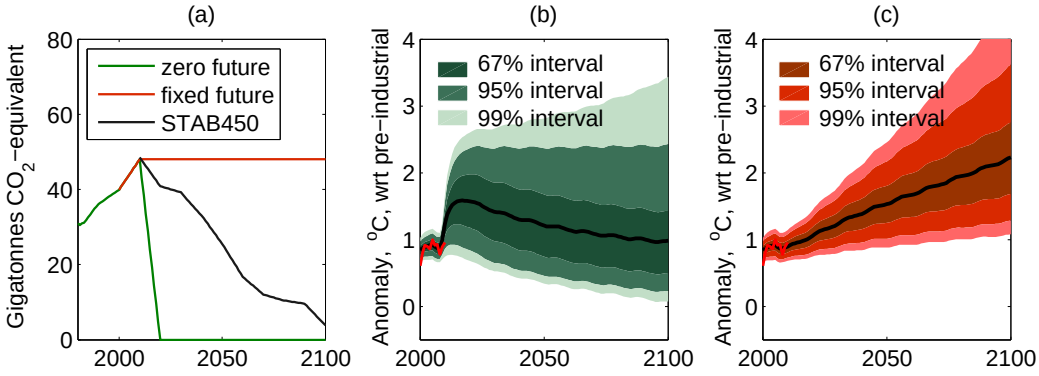

Figure 7.2: Temperature distributions for the hypothetical emissions climate commitment experiments: (a) emissions, $GtCO_2$-equivalent, (b) temperature change from zero future emissions after 2010 and, (c) temperature change after fixing emissions at 2010 levels.

Alternatively, if emissions could be fixed and held at 2010 levels, then GSAT would continue to increase, reaching a best estimate (mode) of 2.1°C of warming by the end of this century with a likely range of 1.7–2.7°C (wrt pre-industrial), Figure 7.2(c).

An intermediary level of emissions is also shown by the green line in Figure 7.2(a). These are the emissions for a stabilisation scenario designed to achieve a 450ppm CO_2 equivalent concentration and keep warming below 2°C. This type of scenario is discussed further in Section 7.3.

The zero–emissions overnight scenario is clearly unrealistic, while the fixed–emissions scenario is a kind of optimistic business–as–usual scenario. The current trend in emissions (Figure 7.3) is one of accelerating growth, with the growth rate shifting from 1.1% per year for 1990–1999 to over 3% for 2000-2004 (*Raupach et al.*, 2007). The recent global financial crisis put a dent in this growth rate (*Friedlingstein et al.*, 2010) but the outlook is for sustained emissions growth in the absence of effective measures to curtail this trend (*Sheehan*, 2008). One estimate is that global emissions from fossil–fuels will double between 2005 and 2030 under business–as–usual conditions, i.e., in the absence of mitigation policies (*Garnaut*, 2011).

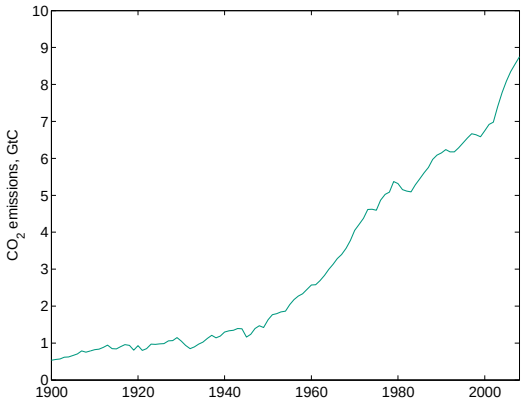

Figure 7.3: Global CO_2 emissions 1900–2008 from fossil–fuel burning, cement manufacture and Gas Flaring (*Boden et al.*, 2010).

In order to assess the amount and likelihood of further global warming with a climate model, some assessment of future greenhouse–gas emissions has to be made. A number of emissions scenarios have been constructed for that purpose; these are investigated next.

7.2 Future Temperatures and Emission Scenarios

The total temperature increase over the past 150 years, 1850 to 2005, was 0.76°C (0.57–0.95°C), with a linear warming trend of 0.13°C (0.10–0.16°C) per decade for the last 50 years (*IPCC*, 2007a). This rate of warming is currently increasing, such that over the past 25 years the rate has moved up to 0.19°C per decade (*Allison et al.*, 2009). The temperature increase by 2100 will be approaching 2.5–3°C if this rate is maintained. Rather than simply extrapolating from past trends, climate models seek to represent the underlying physical processes so that future temperature projections can be made that take into account the different contributing causes. These will include factors such as variations in insolation and changes to the composition of the atmosphere that affect the radiative balance at the top of the atmosphere.

Emission scenarios have been utilised as one way of providing the inputs to calculate the change in atmospheric greenhouse–gases, as previously described. They are intended to be plausible, internally consistent stories that describe future releases of greenhouse–gases and aerosols. Assumptions are made about patterns of economic growth, demography and technology development. An emission scenario can only be one among many possible futures, and so multiple scenarios are used to provide alternative perspectives.

A variety of scenarios have been developed and analysed over the past two or three decades for this purpose, although the SRES scenarios (*Nakicenovic and Swart*, 2000) have come to dominate most of the recent literature. There were previous scenarios associated with the earlier IPCC assessment reports, the five SA90 scenarios (*IPCC*, 1990) and the six IS92 scenarios (*IPCC*, 1992). The SRES scenarios are discussed next, including probabilistic temperature changes and concentration results using the MCMH derived posterior parameter distributions developed in Chapter 6.

The SRES scenarios

There are a total of 40 SRES scenarios, with six illustrative marker scenarios (A1FI, A1B, A1T, A2, B1, B2). Details of the emissions and related storylines are provided in *Nakicenovic and Swart* (2000) and the IPCC TAR (*IPCC*, 2001). The six marker scenarios are examined here, both for comparison to the IPCC AR4 results but also to consider the contribution this mix of scenarios makes to the spread in temperature change projections.

The SRES scenarios have received a number of critical reviews, for example, *Tol et al.* (2005); *Nakicenovic et al.* (2006); *Girod et al.* (2009). The latter analysis suggests that these scenarios benefit from improvements in methodology, including more credible storylines, but suffer from the larger number of scenarios and lack of meaningful titles. Of greater concern are some of the assumptions built into the SRES scenarios, such as population growth, technological change and energy intensity (*Pielke Jr et al.*, 2008) and the increasing gap between actual emissions and many of the scenarios. Present–day emissions are tracking higher than most of the SRES scenarios, including the high emissions A1FI scenario (*Raupach and Canadell*, 2010; *Reichstein*, 2010). *Manning et al.* (2010) try to argue that such statements are mistaken, since there are some higher emission scenarios, including the A1B. However, A1B is only initially a high growth scenario which decelerates and then declines after 2050. A1FI appears the closest of the SRES marker

scenarios to present trends in the absence of effective mitigation policies. The A1B scenario represents the type of pathway needed to avoid large temperature changes. It still envisages a world of very rapid economic growth but with lower population growth and a speedy introduction of new and more efficient energy technologies. Included in this storyline are themes of economic and cultural convergence and capacity building, with a substantial reduction in regional differences in per capita income (*Nakicenovic and Swart*, 2000). People pursue personal wealth rather than environmental quality, which is a theme of the B1 scenario (a summary of the storylines is included in the IPCC AR4 Summary for Policy Makers, *IPCC*, 2007a).

All of the SRES scenarios are meant to be regarded as equally plausible (which is not the same as equally likely), and none of them are mitigation scenarios. This framing is understandable in the context in which the scenarios were developed, and that only subjective probabilities could be applied (refer, for example, to *Schneider*, 2001). With the passage of time, some of the lower emissions scenarios seem unlikely to eventuate in the absence of strong mitigation policies. The lack of probabilities for the scenarios does, however, adversely impinge on decision–making and risk assessments which depend very much on how uncertainty is managed (*Gay and Estrada*, 2010).

A comparison of the SRES marker scenario results using MAGICC and the 11 parameter case posterior distributions is presented in Table 7.1 for CO_2 concentration, CO_2-equivalent concentration, radiative forcing and temperature change in 2100, with corresponding plots in Figure 7.4. Note that the CO_2- equivalent concentration is for the Kyoto protocol greenhouse–gases (carbon dioxide, methane, nitrous oxide, sulphur hexafluoride and two groups of hydrofluorocarbons and perfluorocarbons), while the total radiative forcing includes the net negative forcing from the aerosol components.

The MAGICC projections agree quite well with the IPCC results except for the A1T and A2 scenarios. The disparities seem to stem mainly from the aerosol forcing uncertainty effect, but perhaps also carbon cycle feedback effects; these are not adequately allowed for in the IPCC results. For example, the IPCC A1T and B2 best estimates and likely ranges are the same, yet their emission scenarios are very different; the A1T CO_2 emissions peak and then decline, whereas they continue to grow in the B2 scenario with, for example, in 2100, emissions of fossil fuel CO_2 of 4.3 GtC and 13.8 GtC respectively, but then sulfate emissions for A1T are 20.3 MtS compared to B2's 47.9 MtS; the net radiative forcing for each scenario is determined by the cumulative greenhouse–gas concentrations offset by short–lived aerosol cooling. The MAGICC results produce a larger net radiative forcing for A1T than B2, and hence the higher temperature changes.

The combined SRES likely range presented here spans 1.1–5.8°C, as compared to the AR4 range of 1.1–6.4°C which was introduced in Chapter 1 as one of the motivations for this research, that is, to understand the reasons for this wide range. It is clear that a significant proportion of this uncertainty is due to the estimates for future greenhouse–gas emissions. Individual scenarios have their own temperature change uncertainty range. Lower emission scenarios, such as B1, have a narrower uncertainty range than higher emissions scenarios, such as AIFI.

Table 7.1: Summary of SRES projections for 2100.

CO_2 concentration in 2100, ppm						
Name	A1B	A1FI	A1T	A2	B1	B2
mean	730	990	671	804	529	627
median	686	917	580	789	520	598
mode	665	880	575	775	510	580
likely	632–784	833–1063	525–696	739–858	493–558	557–671
CO_2-equivalent concentration in 2100, ppm						
Name	A1B	A1FI	A1T	A2	B1	B2
mean	888	1362	816	1123	617	804
median	837	1263	710	1103	608	769
mode	830	1260	680	1090	600	750
likely	772–952	1150–1459	644–845	1034–1196	577–651	717–858
Total radiative forcing in 2100, $W\,m^{-2}$						
Name	A1B	A1FI	A1T	A2	B1	B2
mean	5.77	7.51	5.72	5.94	3.76	5.13
median	5.6 1	7.33	5.43	5.89	3.69	5.01
mode	5.55	7.25	5.30	5.79	3.63	4.95
likely	5.16–6.25	6.78–8.05	4.90–6.32	5.46–6.38	3.41–4.05	4.57–5.57
Temperature change in 2100, °C (wrt 1990)						
Name	A1B	A1FI	A1T	A2	B1	B2
mean	3.3	4.5	3.6	3.1	1.8	2.9
median	3.2	4.3	3.3	3.1	1.7	2.7
mode	2.9	4.1	3.2	3.0	1.6	2.6
likely	2.2–3.9	3.1–5.8	2.2–4.9	2.2–4.0	1.1–2.5	1.9–3.8
IPCC[a]						
best	2.8	4.0	2.4	3.4	1.8	2.4
likely	1.7–4.4	2.4–6.4	1.4–3.8	2.0–5.4	1.1–2.9	1.4–3.8

[a] Best estimate and likely range (*IPCC*, 2007a).

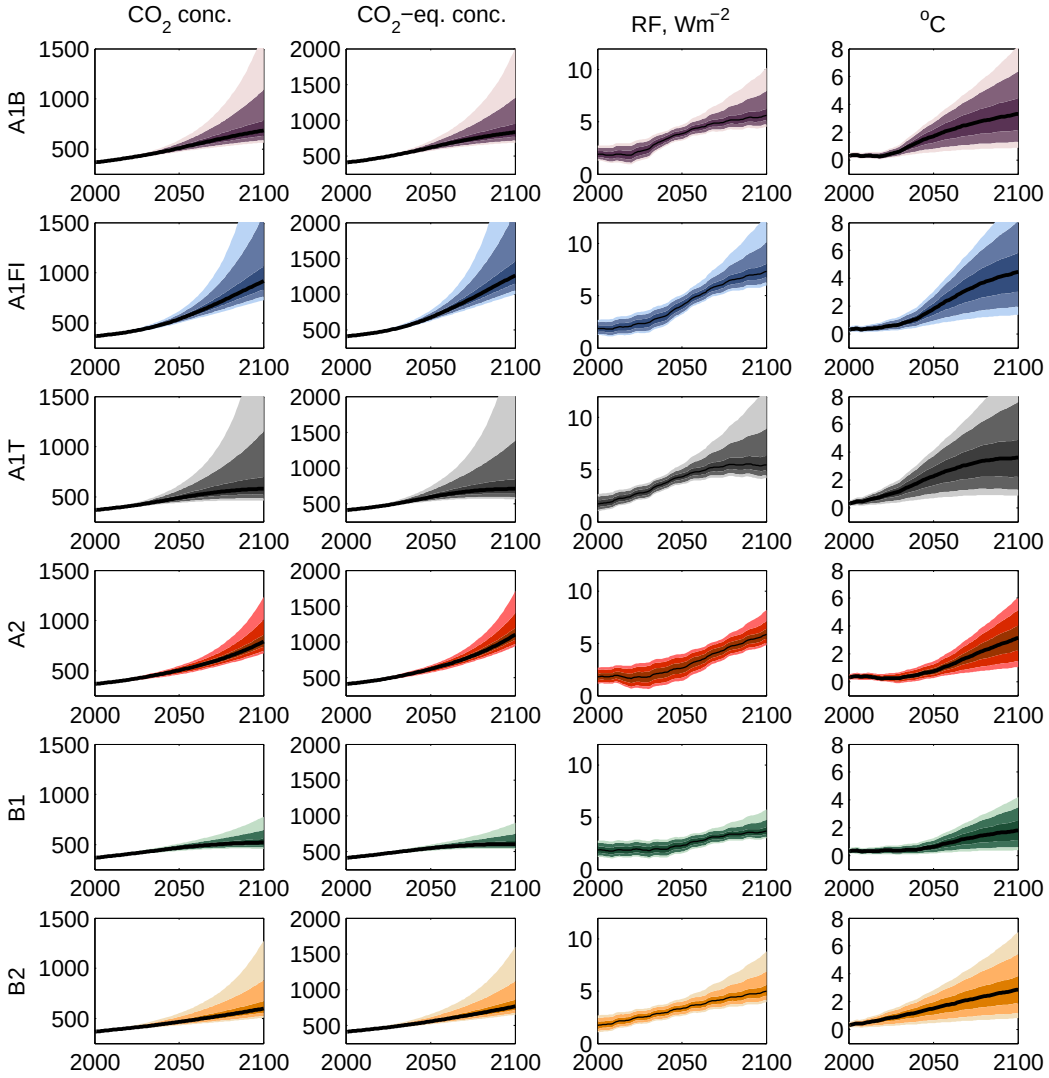

Figure 7.4: SRES plots for CO_2 concentration, CO_2 equivalent concentration, radiative forcing, and temperature change wrt 1990 for 6 marker scenarios, 2000–2100: A1B, A1FI, A1T, A2, B1, and B2. Shaded areas are 67%, 95% and 99% confidence intervals.

The RCP scenarios

The latest IPCC scenarios are called Representative Concentration Pathways (RCPs) and explained by *Moss et al.* (2010), which provides a useful historical overview of climate scenarios and an introduction to the RCPs. Unlike the SRES scenarios, the new RCPs are not grounded with any storyline, or built up from consideration of population, energy intensity, per capita GDP etc. The claim that 'this new generation of scenarios will improve society's understanding of plausible climate and socio–economic futures' (*Moss et al.*, 2010) seems unlikely without additional information. They appear, not unreasonably, to be designed for the needs of climate modelling groups, and reflect the importance of a consistent set of emissions and concentrations for model inter–comparison experiments. The RCPs avoid the messy complexities of the real world. One discussion proposes that the socio–economic conditions that would result in the given GHG concentrations have to be worked out in reverse (*Hibbard et al.*, 2007), which seems to be a strange and artificial view of the causal connections between anthropogenic actions and changes in surface temperature. The idea is, apparently, to make things more open and flexible, with allowance for mitigation and adaptation options (*Inman*, 2011). This promotes a change from looking at how temperatures might evolve for a set of socio–economic assumptions to considering what choices will lead to a particular pathway. If a small temperature change outcome is the aim, then decisions and policies have to be made that will achieve that outcome, although there are multiple emissions pathways that can deliver the same end result.

There are four RCP scenarios based on future radiative forcing levels, summarised in Table 7.2. MAGICC has played an important role in the development of the RCPs, including the greenhouse–gas concentrations and emissions commensurate with them (*Meinshausen et al.*, 2011b;c). It is perhaps an interesting question as to the relationship between emissions and each of the RCPs, since the emissions for the RCPs have been worked out by different modelling groups for each of the nominal radiative forcing levels in 2100 (that is, 8.5 $\mathrm{W\,m^{-2}}$, 6.0 $\mathrm{W\,m^{-2}}$, 4.5 $\mathrm{W\,m^{-2}}$ and 3.0 $\mathrm{W\,m^{-2}}$ peak and decline to 2.6 $\mathrm{W\,m^{-2}}$), which means that the emissions and RCPs are dependent on model parameter values.

Table 7.2: Summary of Representative Concentration Pathways (RCPs).

Name	Radiative forcing	Concentration, CO_2 equivalent, ppm
RCP8.5	Increasing radiative forcing to 8.5 $\mathrm{W\,m^{-2}}$ in 2100	over 1,370 in 2100
RCP6	Radiative forcing stabilising at 6.0 $\mathrm{W\,m^{-2}}$ after 2100 (without overshoot)	$\approx$ 850 at stabilisation
RCP4.5	Radiative forcing stabilising at 4.5 $\mathrm{W\,m^{-2}}$ after 2100 (without overshoot)	$\approx$ 650 at stabilisation
RCP3PD	Radiative forcing peaks at approx. 3.0 $\mathrm{W\,m^{-2}}$ before 2100 and then declines	$\approx$ peak at 490

Table 7.3: Summary of RCP projections for 2100.

Temperature change in 2100, °C (wrt 1990)				
Name	RCP3PD	RCP45	RCP6	RCP85
mean	1.2	2.5	3.2	4.9
median	1.0	2.3	3.1	4.6
mode	0.8	2.1	2.9	4.5
likely	0.5–1.8	1.4–3.4	2.1–4.4	3.3–6.3
CO_2 concentration in 2100, ppm				
Name	RCP3PD	RCP45	RCP6	RCP85
mean	426	561	689	989
median	414	525	650	892
mode	405	510	630	860
likely	394–447	488–596	601–739	807–1047
CO_2-equiv. concentration in 2100, ppm				
Name	RCP3PD	RCP45	RCP6	RCP85
mean	480	653	819	1372
median	466	612	774	1245
mode	460	600	760	1180
likely	445–503	570–693	717–876	1192–1451
Total radiative forcing in 2100, W m^{-2}				
Name	RCP3PD	RCP45	RCP6	RCP85
mean	2.54	4.38	5.67	8.23
median	2.43	4.19	5.50	8.0 0
mode	2.35	4.05	5.45	7.90
likely	2.18–2.81	3.81–4.81	5.08–6.13	7.47–8.78

The posterior parameter distributions were applied to the four RCP scenarios. A summary of the results for CO_2 concentration, CO_2 equivalent concentration, radiative forcing, and temperature change in 2100 (wrt 1990) is given in Table 7.3, and plotted for the period 2000–2100 in Figure 7.5 .

RCP85 has a high level of greenhouse–gas emissions that results in more than triple the pre-industrial CO_2 concentration by 2100. It has similar total CO_2 emissions to the A1FI scenario, which is its nearest equivalent. However, is has higher CH_4 emissions and much lower sulfate, CO, NMVOC and NO_x emissions, with a net higher radiative forcing that produces more warming by the end of the 21st-century.

A comparison of the main greenhouse–gas and sulfate emissions is shown in Figure 7.6. This example was constructed using a single set of model parameters. The two scenarios exhibit very similar radiative forcing and temperature change over the 21st-century. It is also interesting to compare the temperature changes using the MCMH posterior parameter distributions (refer Figure 7.7, as well as Tables 7.1 and 7.3). The likely temperature change ranges for the A1FI and RCP85 scenarios are dissimilar as a result of the way the uncertainties propagate through the model results.

RCP3PD is an overshoot scenario, which has emissions peaking in 2020 and declining thereafter, with CO_2 fossil fuel emissions going negative from 2080 and land use CO_2 reaching zero emissions by 2125. Methane emissions are also substantially reduced. Greenhouse–gas emissions and net radiative forcing are less than those for the B1 scenario, being more comparable to a stabilisation scenario such as the STAB450 scenario discussed later (Section 7.3). Whilst it is possible to construct an emissions pathway with negative CO_2 fossil fuel emissions there is no existing technology that can deliver this result.

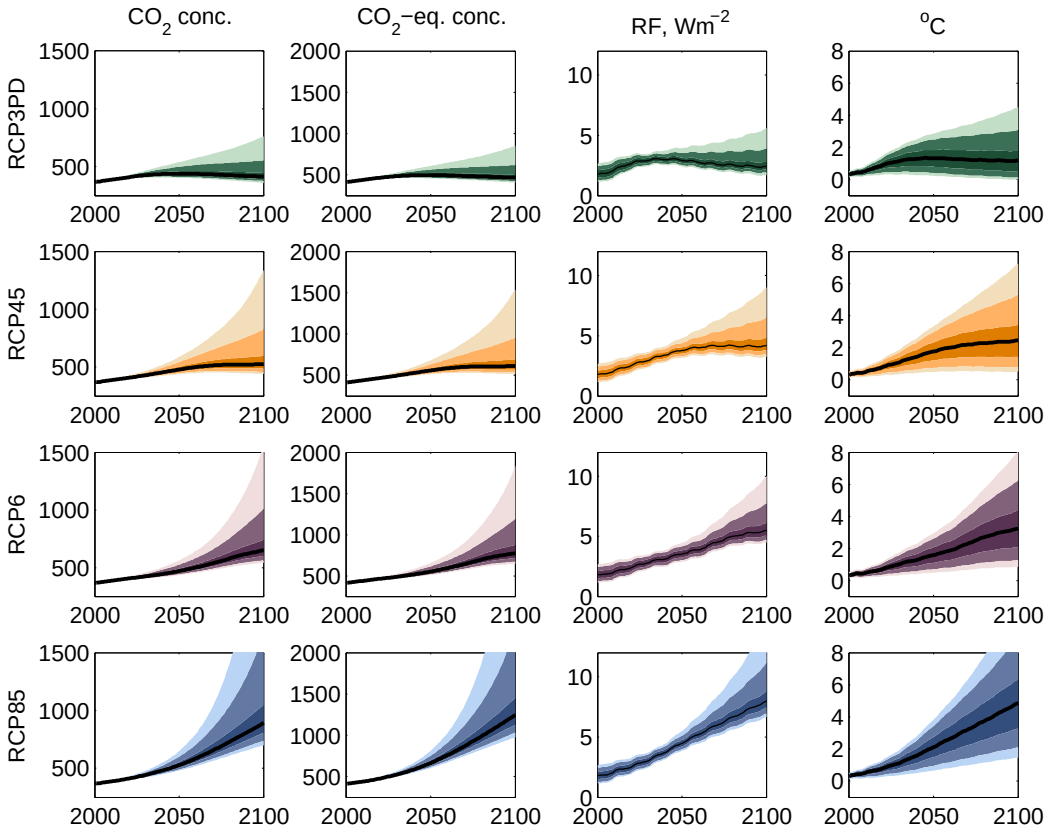

Figure 7.5: RCP plots for CO_2 concentration, CO_2 equivalent concentration, radiative forcing, and temperature change wrt 1990 for the four scenarios, 2000–2100: RCP3PD, RCP45, RCP6 and RCP85. Shaded areas are 67%, 95% and 99% confidence intervals.

RCP45 lies between the B1 and B2 scenarios in terms of radiative forcing and temperature change, although close to B1 for CO_2-equivalent concentrations (see Figures 7.8 and 7.9). The RCP45 greenhouse–gas emissions are similar to B1 but the difference in the sulfate emissions combines with the aerosol forcing uncertainty to create some disparity in the resultant temperature change distributions.

RCP6 is comparable to the A1B scenario, with similar CO_2 emissions, although with different pathways for methane and sulfate emissions, as shown in Figure 7.10. The net results are almost the same for radiative forcing and temperature change in 2100.

This survey of the Representative Concentration Pathways suggests that these new emission pathways, as constituted in the cases used here, are comparable to some of the older SRES marker

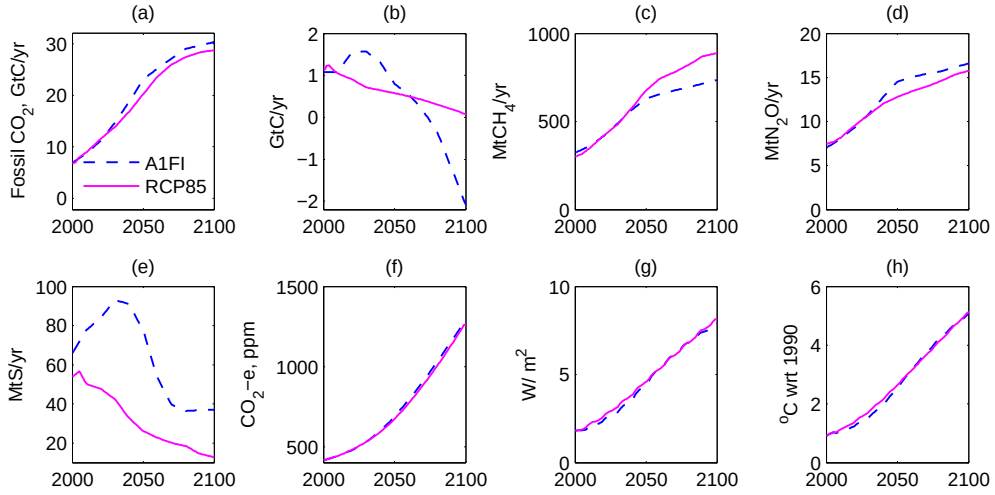

Figure 7.6: A1FI and RCP85 compared, with emissions for: (a) fossil fuel CO_2, (b) land use CO_2, (c) Methane, (d) Nitrous oxide, (e) Sulphate, with (f) the CO_2 equivalent concentration, (g) radiative forcing, and (h) temperature change wrt 1990 for A1FI (dashed blue line) and RCP85 (solid magenta line), with a single set of model parameters.

scenarios. However, differences in the emission components can produce varied outcomes when the uncertainties encapsulated by the MCMH parameter distributions are applied to the alternate emissions pathways. Differences in CO_2 emissions will be affected by the carbon cycle parameters, and the sulfate emissions by the aerosol forcing parameters. There are also differences in some of the other emission components, such as CO, VOC, NO_x and halocarbons.

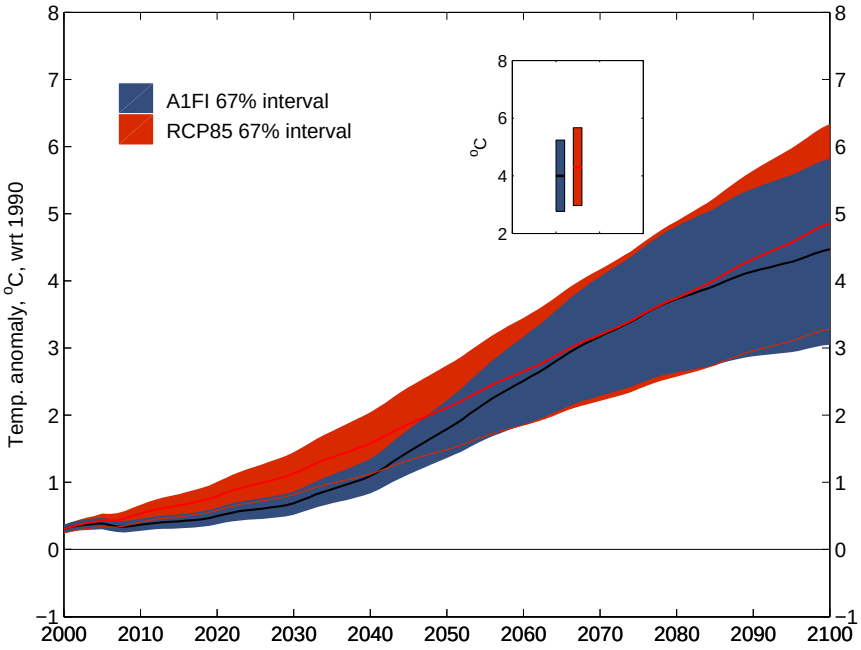

Figure 7.7: A1FI (blue) and RCP85 (red) likely temperature change 2000-2100 compared, with inset for likely ranges in 2100. Heavy solid lines are mean temperature changes.

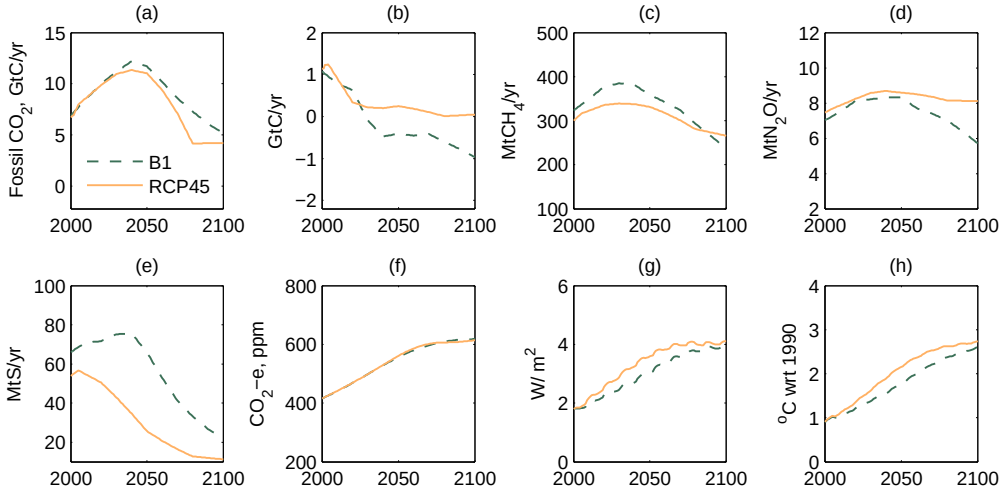

Figure 7.8: B1 and RCP45 compared, with emissions for: (a) fossil fuel CO_2, (b) land use CO_2, (c) Methane, (d) Nitrous oxide, (e) Sulphate, with (f) the CO_2 equivalent concentration, (g) radiative forcing, and (h) temperature change wrt 1990 for B1 (dashed green line) and RCP45 (solid yellow line), with a single set of model parameters.

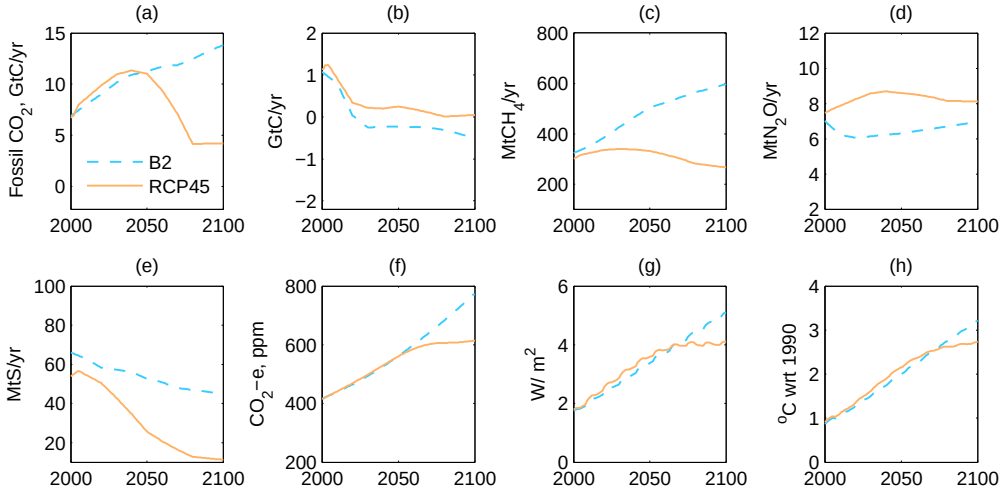

Figure 7.9: B2 and RCP45 compared, with emissions for: (a) fossil fuel CO_2, (b) land use CO_2, (c) Methane, (d) Nitrous oxide, (e) Sulphate, with (f) the CO_2 equivalent concentration, (g) radiative forcing, and (h) temperature change wrt 1990 for B2 (dashed blue line) and RCP45 (solid yellow line), with a single set of model parameters.

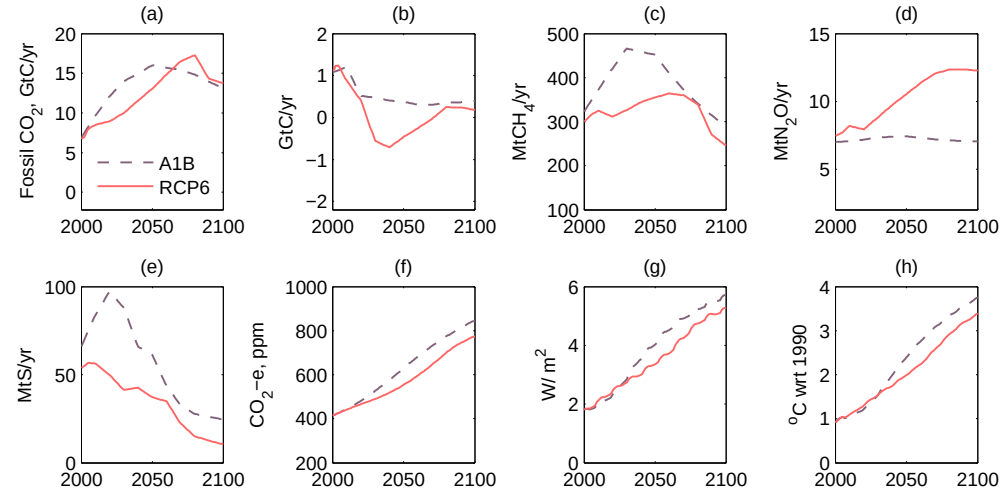

Figure 7.10: A1B and RCP6 compared, with emissions for: (a) fossil fuel CO_2, (b) land use CO_2, (c) Methane, (d) Nitrous oxide, (e) Sulphate, with (f) the CO_2 equivalent concentration, (g) radiative forcing, and (h) temperature change wrt 1990 for A1B (dashed purple line) and RCP6 (solid orange line), with a single set of model parameters.

Other emission scenarios

Neither the SRES or RCP scenarios provide a complete basis for estimating future temperature changes. The SRES scenarios are now over 10 years old and the assumptions that were used for their storylines need updating to reflect revised trends in population, economic growth and energy intensity. The RCPs do not start out with an associated storyline in the same sense as the SRES scenarios (*Inman*, 2011). Instead the changes in GHG emissions provide a spread in radiative forcings for model inter-comparison purposes. It has been proposed that compatible storylines will be worked out in a parallel process (*Hibbard et al.*, 2011; *Moss et al.*, 2010).

Many other scenarios have been developed for various purposes, such as those used by the IEA (*International Energy Agency*, 2010), U.S. Climate Change Science Program, (*Clarke et al.*, 2007), the UK Climate Projections report (*Murphy et al.*, 2009) and the Garnaut Review in Australia (*Garnaut et al.*, 2008; *Garnaut*, 2011). However, the variety of scenarios and differing assumptions make it difficult to select which ones provide a good basis for projecting future temperature changes.

Another guide to future emission trends are the international agreements that stem from the United Nations Framework Convention on Climate Change (UNFCCC), the Kyoto Protocol and the subsequent negotiations and national pledges. These are discussed further in Section 7.4.

There are also scenarios aimed specifically at stabilisation of the climate and 'avoiding dangerous climate change'; the next section continues the investigation of emission scenarios and pathways with an examination of these.

7.3 Stabilising the Climate

This section examines future temperature changes from a different angle, where the concern is to avoid, or at least minimise, further change to global–mean surface temperatures. The SRES and RCP scenarios lead to a range of temperature change projections, as discussed in the previous section, in which the outcome follows from the associated GHG emissions and subsequent concentrations. The issue is now reversed, so that rather than estimating future temperature changes for a given set of emissions or radiative forcing, the question is what emission pathways are compatible with a particular goal, such as a concentration level or temperature change target. One of the benefits gained by this reversal is that it circumvents the probability question of which scenario is most likely. Emission scenarios nevertheless remain relevant to the question of what is the likely temperature change over the 21st-century, which is important for impacts and adaptation assessments.

Stabilisation scenarios were developed in conjunction with the work of the IPCC, with a series of CO_2 concentration profiles for atmospheric concentrations of 350, 450, 550, 650 and 750 ppm (S350–S750) (*Enting et al.*, 1994). Corresponding estimates for global–mean temperature change and sea–level rise were estimated by, for example, *Wigley* (1995) and *Schlesinger and Malyshev* (2001). An alternate set of profiles, the WRE profiles (WRE350–WRE750) with modified emission pathways, were constructed by *Wigley et al.* (1996). Both sets are discussed in detail in *IPCC* (1997) and *Wigley* (2000a).

These stabilisation cases also emerged in the context of the United Nations Framework Convention on Climate Change (UNFCCC) Article 2, which states that the aim of the Convention is the stabilisation of atmospheric greenhouse–gas concentrations at a level that would 'prevent dangerous anthropogenic interference with the climate system'. In addition, Article 3 includes the wording 'protect the climate system for the benefit of present and future generations of humankind', and Article 4 has 'with the aim of returning individually or jointly to their 1990 levels these anthropogenic emissions of carbon dioxide and other greenhouse gases' (quoting selectively from the full text).

An informative background to these principles, the evolution of the UNFCCC and the Kyoto protocol, is provided by *Oppenheimer and Petsonk* (2005). Two threads are apparent in this development, one which centers on emissions and concentrations, and another where rates and amounts of warming are the focus. These two, while closely related, may be the reason why stabilisation scenarios and 'avoiding dangerous climate change' can appear to be separate topics. During the mid-1990s, consideration of emission trajectories that would deliver long–term stabilisation led to a view that two degrees total warming and a concentration of 450ppm CO_2-equivalent were appropriate targets. Concerns over feasibility and economic consequences of GHG emission reductions also emerged.

Since the Kyoto Protocol was adopted in 1997, further attempts have been made to interpret the meaning of 'dangerous anthropogenic interference', some of which are reviewed by *Oppenheimer and Petsonk* (2005), who point out a range of difficulties in establishing what constitutes 'dangerous' and the variety of temporal, spatial, social, cultural and ethical issues that impinge on this subject. Also outlined are some options for translating the objectives of Article 2 into emissions pathways that could be adopted as mitigation policy. Methods include a *tolerable window* approach, with population–based and sustainability versions, which involve the application of a number of criteria together that have the effect of limiting the number of feasible emissions pathways. An alternative method is the *benefit–cost framework* which uses monetary costs to optimally determine emissions and concentrations pathways. These methods place different emphasis on environmental limits and economic growth.

As an illustration of the environmental approach, *Keller et al.* (2005) examined the climate policies needed to reduce the risk of coral reef bleaching and the disintegration of the West Antarctic Ice Sheet. Estimates of the respective temperature change limits were set at 1.5°C to prevent extensive and sustained coral bleaching, and 2.5°C to prevent triggering disintegration of the West Antarctic Ice Sheet. The authors concluded that substantial reductions in anthropogenic GHGs are required, although the costs may be high, depending on the discount rate used in the economic model.

A single, simple definition of 'dangerous climate change' is not easy to arrive at, with a variety of attempts having been made. For an overview of this issue see, for example, *Schneider and Lane* (2006) and also *Ramanathan and Feng* (2008), *Smith et al.* (2009) and *Hare et al.* (2011). The development of ideas to address this concept included 'reasons for concern' (*IPCC*, 2001) and greater consideration of impacts and vulnerabilities, with a growing worry that smaller increases in GSAT will lead to significant consequences (*Smith et al.*, 2009). Given this, *Mann* (2009) argued that 'dangerous anthropogenic interference' with the climate is in the range 1–2°C of warming,

and that stabilisation of GHG concentrations at more than 450 ppm CO_2-equivalent would be a 'terribly risky prospect'. *Hansen* (2005) has argued strongly that 2°C is not a responsible target, and such a warming limit is less than any of the SRES scenarios (note that the results in Table 7.1 require an extra 0.5°C added to make them relative to pre-industrial). More recently, *Hansen et al.* (2008) makes a case for reducing atmospheric CO_2 concentration back to 350 ppm on the basis that equilibrium climate sensitivity is nearer to 6°C based on paleoclimate data, as opposed to the conventional 3°C climate sensitivity which only allows for fast feedback processes.

Despite these well–founded misgivings, a 2°C climate target has become an established benchmark, perhaps for pragmatic reasons, since 1°C is pretty much foregone and limiting warming to 2°C is an extremely challenging target in the face of the minimal efforts to reduce GHG emissions so far and the meagerness of international agreements to date.

The history of this target is surveyed in *Randalls* (2010), from its emergence as the proposed policy target for the European Union in 1996 to the temperature target of the 2009 Copenhagen accord, despite its problematic status. Indeed, *Tol* (2007) has previously argued that this target has no real foundation. Yet, whilst it may be a little arbitrary, a maximum warming of 2°C appears to be a useful target if it serves the purpose of actually bringing about changes to GHG emissions and thereby avoiding significant adverse consequences to the environment. It provides a reference for assessing mitigation policies. In addition, the target, whether it is 1.5 or 2°C cannot be given precisely when the parametric uncertainty means the target can't be translated back into an emissions pathway with any certainty anyway. Further discussion is reminiscent of the expression 'fiddling while Rome burns', since urgent action is required if current warming trends are to be reduced; the precise target is not the real issue. As well, delaying action leaves open the potential for more rapid warming with a subsequent demand for faster reductions in emissions to achieve the same level of stabilisation. Increased overshoot, that is with higher temperature change peaks before settling back to the stabilisation temperature, runs a greater risk for reaching threshold events (*O'Neill and Oppenheimer*, 2004).

Despite the ambiguities attached to the term 'dangerous climate change', there has been an emerging acceptance of its usefulness for framing the challenge of human–induced climate change. It is in this context that investigations of stabilisation scenarios have moved away from a focus on CO_2 emissions alone to multi–gas emission pathways, for example, *Meinshausen* (2006); *van Vuuren et al.* (2006); *den Elzen et al.* (2007). More recently, the concept of a greenhouse–gas emissions budget has gained traction amongst the research community, for example, *Meinshausen et al.* (2009) and *Allen et al.* (2009) and government interest (see, for example, *WBGU*, 2009).

To illustrate the challenge posed by stabilisation scenarios, two examples are included here, based on the Garnaut review 450 and 550 ppm stabilisation scenarios (*Garnaut*, 2008), designated STAB450 and STAB550 here, where the numbers indicate the target CO_2 equivalent concentrations.[2] The STAB450 scenario is illustrated in Figure 7.11, which shows emissions for the principal greenhouse–gases along with the resulting CO_2 concentrations, CO_2-equivalent concentrations, total radiative forcing and temperature change over the 21st-century, using the 11 parameter posterior distributions to obtain the uncertainty ranges shown. Similarly, the STAB550 scenario

[2]The STAB450 and STAB550 emissions may not be exactly the same as the final numbers used in the Garnaut review but will be very similar.

is illustrated in Figure 7.11. Values for CO_2, CO_2-equivalent, radiative forcing and temperature change in 2100 are summarised in Table 7.4.

The STAB450 scenario can achieve the goal of keeping under 2°C warming according to the best estimate or mode result of 1.5°C temperature change in 2100, adding 0.5°C to Table 7.4 to make the temperatures relative to pre-industrial. The STAB450 results can be contrasted with a present day CO_2 concentration of 390 ppm,[3] and the CO_2-equivalent concentration of 470ppm in 2010.[4] In other words, the conditions for the STAB450 scenario have already been reached, so that limiting temperature change to avoid 'dangerous climate change' will be all but impossible in the absence of drastic reductions in greenhouse–gas emissions. The STAB450 emissions required to achieve this outcome have a sharp reduction, with fossil fuels emissions reduced to less than 95% of present day levels, and land use has negative emissions, that is the land has to take up more CO_2 through large–scale re-afforestation. CH_4 and N_2O have significant reductions, which implies major changes to agricultural practices. The feasibility and means to accomplish these emission reductions are not explored here.

Table 7.4: Summary of STAB450 and STAB550 projections for 2100. Radiative forcing (RF) and temperature change (ΔT) are relative to 1990.

STAB450				
	CO_2 conc.	CO_2-e conc.	RF	ΔT
mean	431	491	2.9 8	1.4
median	416	474	2.87	1.2
mode	411	465	2.85	1.1
likely	395–456	450–518	2.56–3.30	0.7–2.0
STAB550				
	CO_2 conc.	CO_2-e conc.	RF	ΔT
mean	466	544	3.68	1.8
median	455	532	3.61	1.7
mode	448	525	3.57	1.6
likely	431–493	505–576	3.31–4.00	1.1–2.5

The risk of exceeding 2°C of global–mean temperature change during this century (relative to pre-industrial) is plotted in Figure 7.13 for the STAB450 and STAB550 scenarios. This indicates that, for the STAB450 scenario, there is an approximately 40% chance of exceeding 2°C of warming during the second half of the century according to MAGICC, with the posterior parameter distributions derived as discussed previously (if the emissions on which the scenario is based are achieved). The STAB550 scenario shows a 50% probability of exceeding 2°C by 2080. These examples demonstrate how MAGICC, in conjunction with the MCMH based posterior parameter distributions provides a tool that can evaluate scenarios and obtain results expressed in terms of probabilities.

[3] August 2011 measurement at Mauna Loa; http://www.esrl.noaa.gov/gmd/ccgg/trends/

[4] Based on a greenhouse–gas radiative forcing balance of 2.81 $\mathrm{W\,m^{-2}}$ relative to 1750; NOAA–ESRL, http://www.esrl.noaa.gov/gmd/aggi/, accessed 24/11/2011.

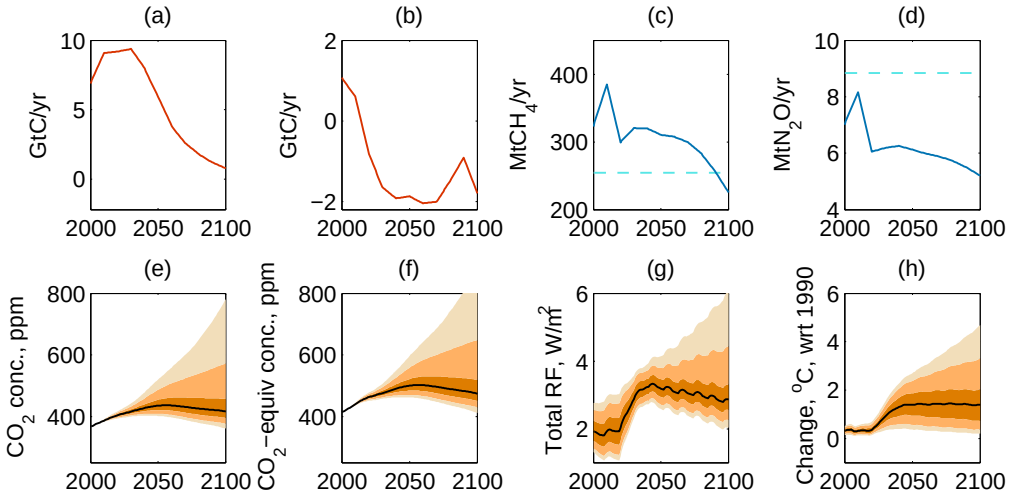

Figure 7.11: The STAB450 stabilisation scenario: (a) CO_2 fossil fuel emissions, (b) CO_2 land use emissions, (c) CH_4 emissions, with solid line for anthropogenic sources and dashed for natural sources, (d) N_2O emissions, with solid line for anthropogenic sources and dashed for natural sources, (e) CO_2 concentrations, (f) CO_2 equivalent concentrations, (g) total radiative forcing, and (h) temperature change wrt 1990. Shaded areas are 67%, 95% and 99% confidence intervals.

Accepting that 2°C maximum global–mean surface temperature change above pre-industrial is a worthwhile aspirational target, the next section investigates present trends and mitigation efforts aimed towards minimising the risk of exceeding this target.

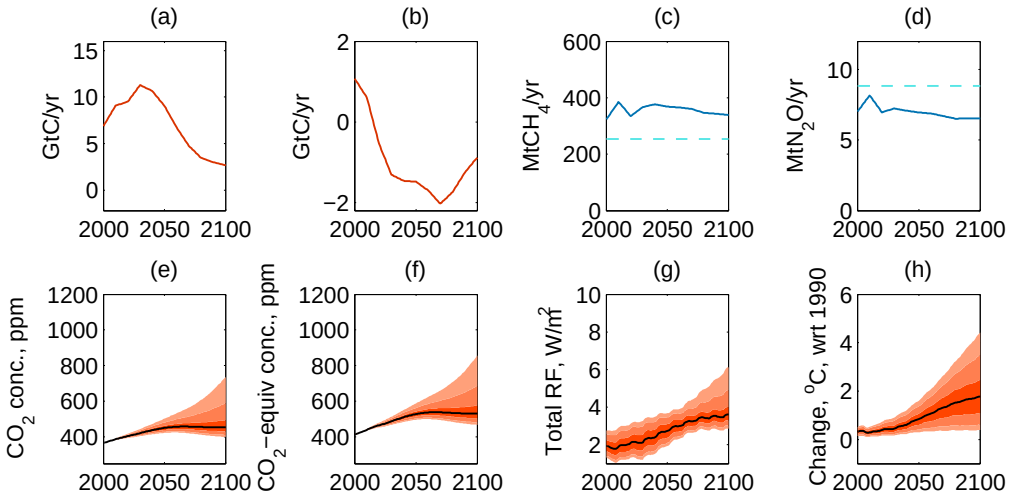

Figure 7.12: (a) CO_2 fossil fuel emissions, (b) CO_2 land use emissions, (c) CH_4 emissions, with solid line for anthropogenic sources and dashed for natural sources, (d) N_2O emissions, with solid line for anthropogenic sources and dashed for natural sources, (e) CO_2 concentrations, ((f) CO_2 equivalent concentrations, (g) total radiative forcing, and (h) temperature change wrt 1990 for the STAB550 stabilisation scenario. Shaded areas are 67%, 95% and 99% confidence intervals.

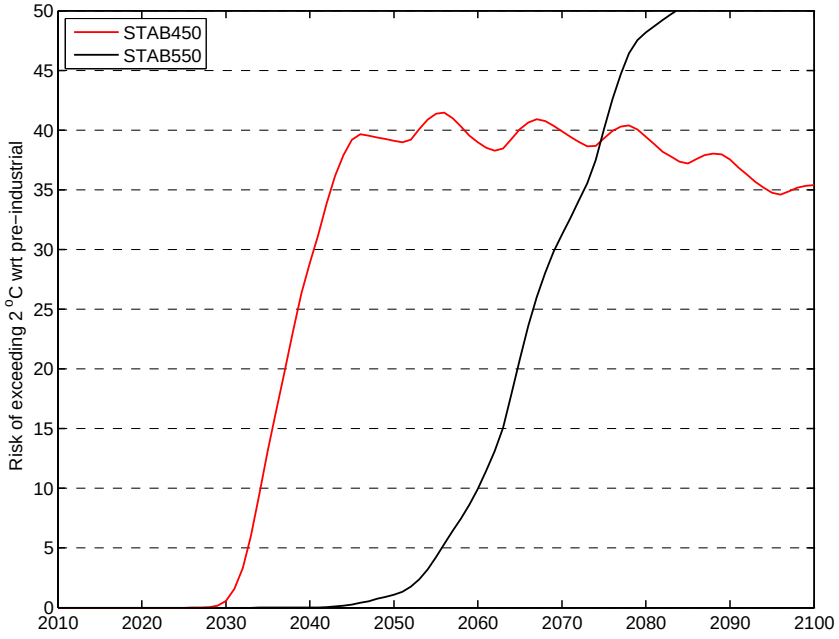

Figure 7.13: (Risk of exceeding 2°C global–mean temperature change (relative to pre-industrial) for the STAB450 and STAB550 stabilisation scenarios.

7.4 Emissions for Two Degrees

The previous section introduced stabilisation scenarios in the context of the UNFCCC mandate to limit human–induced temperature change. Under the auspices of the UNFCCC, and following on from the Kyoto protocol, developed and developing countries have been negotiating and, to a greater or lesser extent, engaging in efforts to reduce their greenhouse–gas emissions. The 'business–as–usual' scenarios, of which the SRES A1FI is an exemplar, exhibit continued emissions growth. However, such a trend will not be followed if nations implement and achieve the levels of mitigation they are pledged to.

A recent study, *Rogelj et al.* (2010), assessed the national emissions–reduction pledges agreed to at the Copenhagen Accord meeting in December 2009. They compiled emission estimates based on national pledges, or, if no such pledges have been made, used previous announcements or otherwise business–as–usual growth. A new reference case or 'baseline' scenario was developed, using historical emissions data to 2009 and then future emissions estimated based on the SRES A1B pathway (full details, *PIK*, 2009). This baseline itself appears somewhat optimistic, since it requires the current upward growth in emissions to be curtailed despite the sustained demand for fossil fuels that is now evident. The A1B scenario was based on a low population growth path which peaked at 8.7 billion people in 2050 and reduced to 7.1 billion by 2100, whereas a recent UN estimate projects the population to reach 10.1 billion by the end of this century.[5] Furthermore, the A1B scenario relies on the introduction of new and more efficient energy technologies and reduced energy intensity, including a reduction in the share of coal in primary energy (*Nakicenovic and Swart*, 2000). Whilst the latter might eventuate, more effective action is required in the face of current trends.

A 'pessimistic' emissions scenario was created assuming nations achieve their lowest stated emission goals, and an alternative 'pessimistic plus long–term target' scenario was also developed which allows for substantial emissions reductions from 2020 onwards in order to achieve the 2°C warming target.

A comparison of the CO_2 equivalent emissions from the Copenhagen scenarios with the A1FI, B1 and RCP3PD scenarios is shown in Figure 7.14. The A1FI emissions exhibits continued growth that is completely incompatible with the 2°C target, while the remaining scenarios have emissions that peak and then decline to different levels. Projections for the A1FI, B1 and RCP3PD scenarios have been covered earlier in this chapter, while details for the three Copenhagen scenarios are shown in Figures 7.15, 7.16 and 7.17 for greenhouse–gas emissions, resulting concentrations, radiative forcing and temperature change (relative to 1990), along with a summary for 2100 set out in Table 7.5.

The risks of exceeding 2°C are plotted in Figure 7.18 for the three Copenhagen scenarios, both for the global–mean temperature change and for the land surface temperature change (relative to pre-industrial). This plot shows that only the 'pessimistic plus' scenario provides a reasonable chance of achieving the 2°C global–mean temperature change target. However, the reduction in emissions to accomplish this are drastic, as indicated by the top row of Figure 7.17. The proposed emissions may indeed be unattainable, since this scenario has, by 2080, zero fossil fuel emissions and minimal amounts for land use change, methane and nitrous oxide, which would imply a total

[5] UN News Service, 3 May 2011.

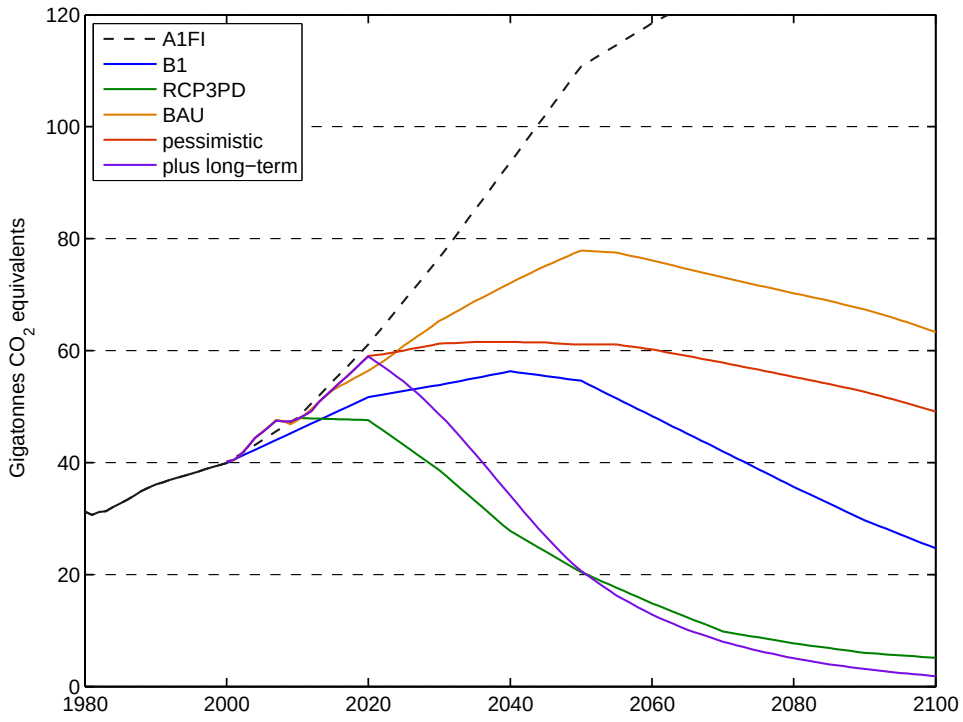

Figure 7.14: Global emissions, $GtCO_2$-equivalent, for six different emission scenarios and pathways.

revolution in energy production and agriculture during the course of this century. Compared to the STAB450 stabilisation scenario considered previously (Section 7.3), the CO_2 emissions are a little less demanding in that negative emissions from land use are not required,

The Copenhagen 'pessimistic plus' scenario involves a peak in temperature around mid-century, which, for the mean, reaches 1.9°C above pre-industrial, while the upper bound of the likely range hovers close to 2.4°C between about 2045 and 2070 (relative to pre-industrial; refer additional plot in Figure 7.19). There is very little leeway if a reasonable chance of limiting global–mean temperature change to 2°C above the pre-industrial global–mean temperature is to be achieved. Any errors in this assessment, such as missing climate processes, rapid or additional changes in the climate system from reaching a tipping point like permafrost melting, would mean that this temperature target will not be achievable. In addition, the greater increase in temperature over land relative to the global–mean, as discussed previously in Section 6.3.4, means that the risk of exceeding 2°C over land reaches 80% around 2045 (Figure 7.18).

Table 7.5: Summary of Copenhagen scenarios for 2100. Radiative forcing (RF) and temperature change (ΔT) are relative to 1990.

Baseline				
	CO_2 conc.	CO_2-e conc.	RF	ΔT
mean	703	890	5.67	3.1
median	667	848	5.53	3.0
mode	645	820	5.50	2.8
likely	617–754	785–954	5.10–6.12	2.1–4.2
Pessimistic				
	CO_2 conc.	CO_2-e conc.	RF	ΔT
mean	637	776	5.04	2.8
median	606	740	4.89	2.6
mode	585	725	4.8 0	2.4
likely	563–682	689–829	4.5–5.5	1.7–3.7
Pessimistic plus long–term target				
	CO_2 conc.	CO_2-e conc.	RF	ΔT
mean	436	464	2.25	0.9
median	425	452	2.15	0.8
mode	423	444	2.07	0.6
likely	404–456	431–485	1.90–2.51	0.3–1.5

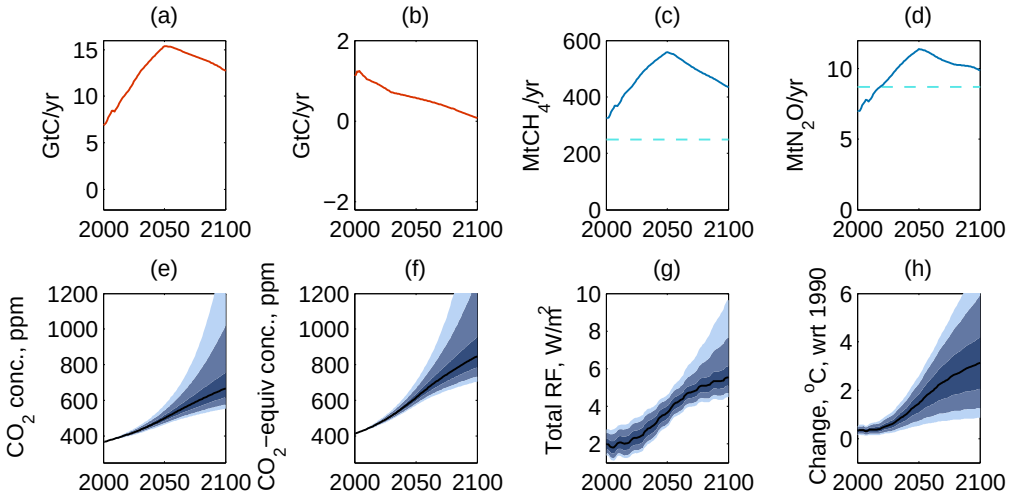

Figure 7.15: Copenhagen baseline: (a) CO_2 fossil fuel emissions, (b) CO_2 land use emissions, (c) CH_4 emissions, with solid line for anthropogenic sources and dashed for natural sources, (d) N_2O emissions, with solid line for anthropogenic sources and dashed for natural sources, (e) CO_2 concentrations, (f) CO_2 equivalent concentrations, (g) total radiative forcing, and (h) temperature change wrt 1990 for the Copenhagen baseline stabilisation scenario. Shaded areas are 67%, 95% and 95% confidence intervals.

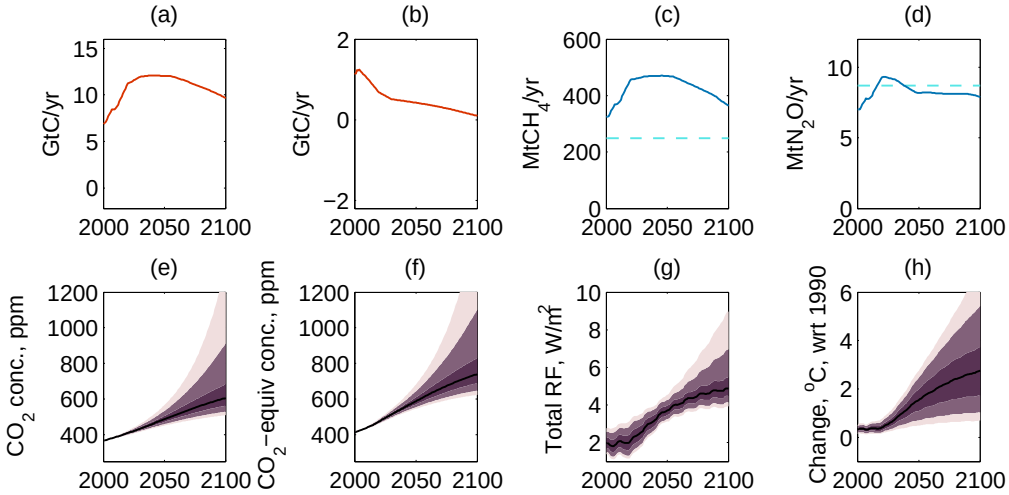

Figure 7.16: Copenhagen minimum pledges (pessimistic): (a) CO_2 fossil fuel emissions, (b) CO_2 land use emissions, (c) CH_4 emissions, with solid line for anthropogenic sources and dashed for natural sources, (d) N_2O emissions, with solid line for anthropogenic sources and dashed for natural sources, (e) CO_2 concentrations, (f) CO_2 equivalent concentrations, (g) total radiative forcing, and (h) temperature change wrt 1990 for the Copenhagen minimum pledges (pessimistic) stabilisation scenario. Shaded areas are 67%, 95% and 99% confidence intervals.

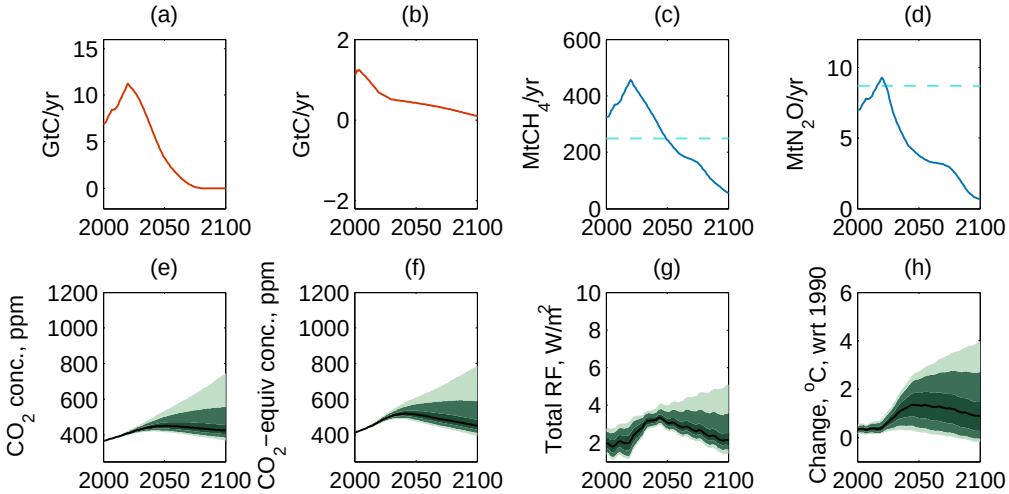

Figure 7.17: Copenhagen modified pledges (pessimistic plus long–term target): (a) CO_2 fossil fuel emissions, (b) CO_2 land use emissions, (c) CH_4 emissions, with solid line for anthropogenic sources and dashed for natural sources, (d) N_2O emissions, with solid line for anthropogenic sources and dashed for natural sources, (e) CO_2 concentrations, (f) CO_2 equivalent concentrations, (g) total radiative forcing, and (h) temperature change wrt 1990 for the Copenhagen modified pledges (pessimistic plus long–term target) stabilisation scenario. Shaded areas are 67%, 95% and 99% confidence intervals.

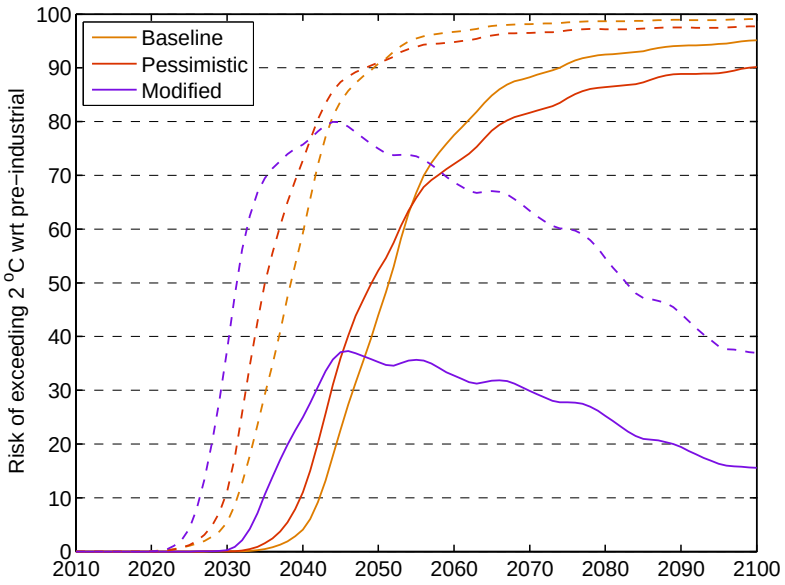

Figure 7.18: Copenhagen scenarios exceedance plot for risk of exceeding 2°C global–mean temperature change (solid lines) and land surface temperature change (dashed lines), relative to pre-industrial.

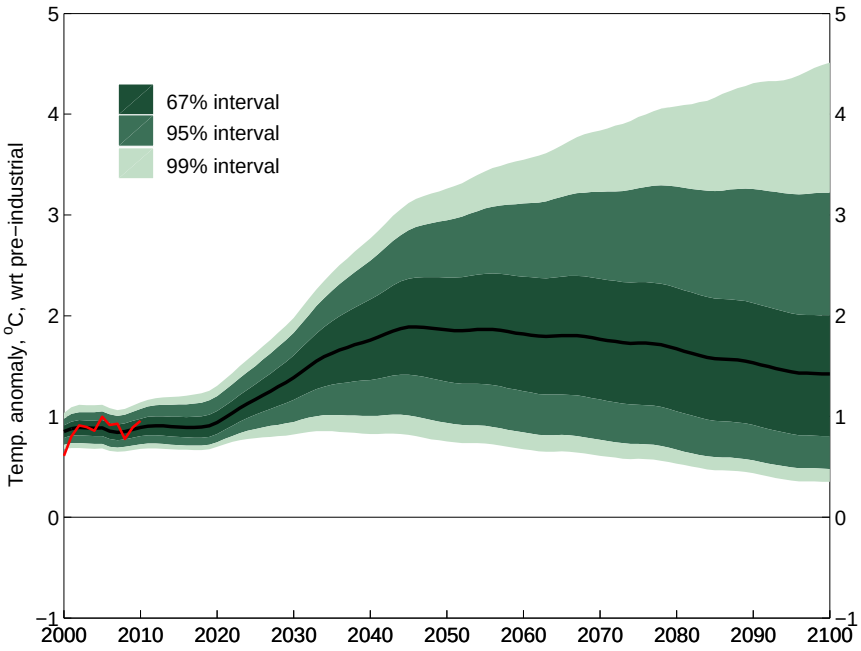

Figure 7.19: Temperature change plot for the Copenhagen modified pledges (pessimistic plus long–term target) stabilisation scenario (wrt pre-industrial). Shaded areas are 67%, 95% and 99% confidence intervals.

7.5 Discussion

Model projections

The utility of MAGICC and the MCMH derived posterior parameter distributions is made evident by the relative ease with which different emission scenarios and pathways have been modelled and results obtained for analysis in this chapter. 17 cases have been presented here (2 climate commitment cases, 6 SRES scenarios, 4 RCPs, 2 stabilisation pathways and 3 Copenhagen scenarios). As well, to re-iterate a point made earlier, MAGICC's parameters, including the key carbon cycle parameters have, for the first time, been constrained using historical observations to arrive at this posterior parameter distribution. Testing parametric uncertainties with an AOGCM across this number of scenarios would be completely infeasible, yet it can be completed with MAGICC in 2 to 3 weeks on a desktop computer. There are trade–offs here: a more complex model with better physics might be used instead, although without the ability to constrain it or produce enough realisations to give a probability for the results, or we can use a simple model with its primary parameters constrained probabilistically as demonstrated in this thesis.

For each set of emissions, MAGICC was executed 36,000 times to create a range of results that can be interpreted as probabilities, something that cannot be readily accomplished with a complex model. This parameter distribution, as discussed in Chapter 6, is based on an evaluation of the model results as compared to historical observations. The ability of this distribution to reproduce the 20th-century global–mean surface temperature is illustrated in Figure 7.20. This process–based model fit is then taken to be a reasonable basis for projecting temperature change into the future (*Enting*, 2008, discusses some of the relative merits and problems of process modelling versus curve fitting, together with related issues concerning uncertainty).

The MCMH posterior parameter distributions were used to generate probabilistic temperature change projections contained in this chapter, within the accompanying table and diagrams. This provides a means of capturing most of the uncertainty connected with a scenario as well as a basis for evaluating and comparing different scenarios.

Investigation of the existing climate commitment was accomplished with two hypothetical emissions cases, a zero–emissions case and a continuing fixed–emissions scenario. The zero-emissions scenario, although impossible to achieve in the short–term, provides a 'best–case' outcome for future warming, in which atmospheric greenhouse–gas concentrations gradually decline and the present–day temperature change of around 1°C, after initially spiking up due to the loss of the aerosol cooling effect, steadily drops to about 0.7°C (0.4–1.4°C) by the end of this century (relative to pre-industrial). Alternatively, if greenhouse–gas emissions could be held at their current 2010 levels, temperatures would continue to steadily rise, reaching approximately 2.1°C by 2100 (1.7–2.7°C).

More generally, future temperature change depends on the amount of greenhouse–gas emissions that society continues to produce, which depends on a range of factors, ranging across population growth, energy intensity, efficiency and new technologies, to mitigation policies. Different emissions scenarios and pathways have been constructed in order to capture these factors. The SRES scenarios (*Nakicenovic and Swart*, 2000) have tended to dominate this area since their inception, although they are now somewhat dated. The six marker scenarios were modelled here to

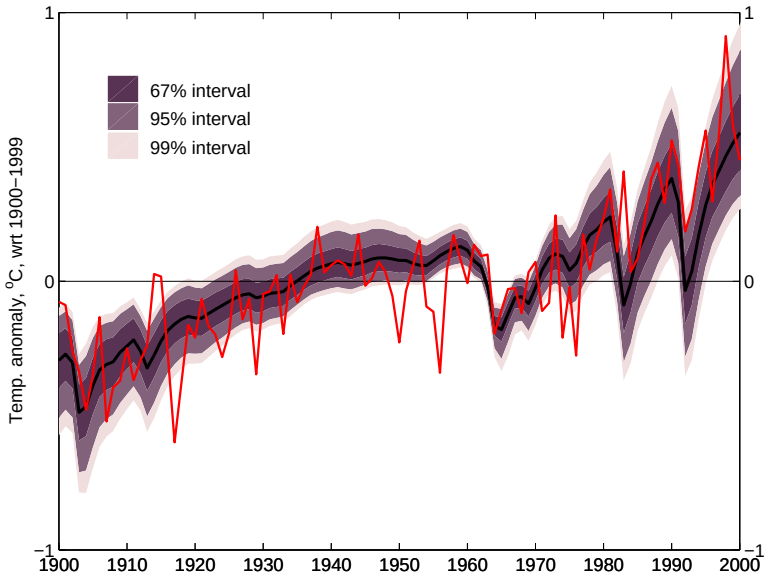

Figure 7.20: 20th-century observed temperature change (solid red line; HadCRUT3) plotted with MAGICC's fit using MCMH posterior parameter distributions (set with respect to the 20th-century).

demonstrate the MAGICC–MCMH results and provide a basis of comparison to the IPCC AR4 projections. The model distributions were found to have narrower likely ranges ranges as compared to the IPCC results, with, in most cases, increased lower bounds and reduced upper bounds. The results are not directly comparable, since the IPCC numbers were not probability distributions. Their best estimates are ensemble means derived from 23 AOGCMs, with upper and lower bounds for the likely range estimated from other, less complex, models in order to account for further uncertainties. It is unclear, however, how and which other uncertainties were included, such as radiative forcings for carbon cycle feedbacks, different aerosol components, tropospheric and atmospheric ozone and so forth.

It is expected that the new Representative Concentration Pathways (RCPs) will achieve greater consistency in the next round of AOGCM modelling for CMIP5, which will lead in to the IPCC's Fifth Assessment Report. Some characteristics of the RCPs have been presented here, along with results for the four main RCPs and a comparison to the SRES scenarios. RCP85 was found to be similar to A1FI, RCP45 to B1, and RCP6 to A1B, but RCP3PD is a stabilisation pathway with overshoot rather than a non-mitigation scenario.

The idea of stabilising the climate arises from concerns that recent emission trends will lead to temperature changes sufficient to cause significant adverse impacts on our environment. It is in this context that the UNFCCC goal of avoiding 'dangerous climate change' is discussed and two examples of stabilisation scenarios based on 450 ppm and 550 ppm CO_2-equivalent concentrations are assessed. It is evident that avoiding a 25% risk of exceeding 2°C global–mean temperature (relative to pre-industrial) requires drastic cuts in greenhouse–gas emissions. The temperature change probability distribution provided by the MAGICC–MCMH program enables the risk of

exceedance to be calculated. The conclusion reached is that, to avoid 2°C of warming around 80 to 100% of our energy production will need to come from non-CO_2 producing sources, as others have found (see, for example, *Caldeira et al.*, 2003; *Matthews and Caldeira*, 2008).

The emissions required to avoid two degrees warming above pre-industrial were discussed in relation to the Copenhagen pledges. The national commitments made so far fall well short of the emission cuts needed to avoid 'dangerous climate change'. Past performance in achieving emission targets is also not very encouraging; while some individual countries are making substantial efforts, for example, England and Germany, others have failed to meet previous targets (e.g., Canada), and the efforts of others have been fairly minimal so far (e.g., the USA and Australia). Unless these pledges are significantly increased and achieved by around 2020 the likelihood of limiting warming to less than 2°C is very small. Delaying emissions reductions increases the risk of exceeding 2°C global–mean surface temperature change (relative to pre-industrial) and demands a higher reduction rate, potentially beyond what is technically feasible (see also, for example, discussion in *den Elzen et al.*, 2010).

The present international emission reduction pledges are inadequate to the task, as illustrated by the Copenhagen pessimistic scenario. If the A1FI scenario is regarded as a reasonable business–as–usual scenario, then we are facing the prospect of a 60% chance of exceeding 4°C by the end of this century. The Copenhagen baseline scenario is a rather more positive case, that, similar to the A1B scenario, expects emissions to flatten out and decline after the current period of high growth.

Model limitations

Although probabilistic temperature projections can be produced using the MCMH derived posterior parameter distributions to represent uncertainty in future temperature change, as demonstrated in this chapter, the results remain contingent on a number of factors.

The results presented here stem from a consistent methodology, and can be successfully compared to other results, such as the IPCC projections(*IPCC*, 2007b) and those tabled in *Meinshausen et al.* (2011b). Differences appear to stem from methods used, and the processes and parameters included in the uncertainties. Confidence in the MAGICC–MCMH posterior parameter distributions is arrived at based on the systematic assessment of the model parameters, the use of historical observations in constraining all of the key model parameters in the MCMH calibration, and the ability of the model to reproduce the 20th-century global–mean temperature change, as shown in Figure 7.20. Then, since MAGICC is a process–based model rather than a curve–fitting model, it is anticipated that MAGICC is able to reliably project temperature changes in to the future for a given set of greenhouse–gas emissions. Additional confidence in this ability is gained from the fact that MAGICC's projections compare well with projections from more complex models when it is calibrated to emulate those models (MAGICC's 'skill' is detailed in *Meinshausen et al.*, 2011a;b).

However, the uncertainty given by the temperature distributions for a given set of emissions still has its limitations. The method applied here did not include all of the climate system and carbon cycle parameters, on the basis of the uncertainty analysis. This implies that not all of the parameter uncertainty was addressed, leaving some scope for some additional uncertainty, although that is expected to be very small. In addition, certain assumptions have been made in accepting the existing settings for all the remaining model parameters involved in the gas-cycle

equations, radiative forcing values and distributions, and so forth, that are required for MAGICC to operate. There are limitations imposed by the representation of the aerosol forcing uncertainty with just one parameter and the temperature dependence of the ocean vertical diffusivity parameter K needs further investigation, as does the state–dependent nature of the climate sensitivity parameter. In addition, the climate model may be missing one or more key processes. MAGICC is inherently a simplified model that lacks the detailed physics of more complex models such as EMICs or three-dimensional ESMs. The hemispheric means from this model cannot address some of the issues associated with spatio–temporal patterns, such as the efficacy of volcanic forcings and the impact of ocean basin circulations on energy transfer. Nevertheless, it can capture a wider range of uncertainty as compared to AOGCMs because MAGICC can explicitly allow for a range of aerosol forcing and carbon cycle components, something that is difficult to address in AOGCMs without perturbed physics ensembles and the integration of carbon–cycle feedbacks.

The response of the climate system and the carbon cycle may behave differently outside the range of calibration. That is, at higher levels of radiative and temperature change, one or more of the simple gas–model relationships (Appendix C) or radiative forcing equations (Appendix B) may no longer apply. In addition, non-linear or threshold changes might occur. Indeed, *Broecker* (1987) suggested awhile ago that we are conducting a dangerous experiment 'We play Russian roulette with climate, hoping that the future will hold no unpleasant surprises', and that the Earth's climate system responds in sharp jumps rather than in a smooth and gradual way. Examples of these possible changes include the collapse of the Atlantic thermohaline circulation, dieback of the Amazon rainforest, rapid collapse of ice sheets and ice shelves, and the release of substantial amounts of greenhouse–gases currently locked away in permafrost and methane clathrates. The loss of Arctic summer sea–ice and the Greenland ice sheet may well occur with temperature changes that are reasonably likely to eventuate during this century, 0.5–2°C, and the Atlantic thermohaline circulation, persistent El Niño conditions, loss of the Indian summer monsoon and Amazon forest loss with 3–5°C of warming, which is quite possible with unmitigated business–as–usual emissions (thresholds are based on estimates from *Lenton et al.*, 2008). Other potential tipping elements are the West Antarctic ice sheet and changes to the Bodélé Depression dust source in Chad (*Schellnhuber*, 2009). Furthermore, it is possible that there may be unexpected consequences of changing global–mean temperatures that impact at a regional scale, such as the recent dramatic emergence of an ozone hole in the Arctic (*Manney et al.*, 2011).

Despite these limitations and potential improvements, MAGICC combined with observationally constrained posterior parameter distributions obtained with the MCMH algorithm is a valuable tool for projecting future global–mean temperature changes. It is able to provide insights as to how the climate system responds to anthropogenic greenhouse–gas emissions, allowing for a wide range of radiative forcing components that affect the Earth's energy balance, including carbon cycle feedbacks. A simple Earth system model such as MAGICC is of course limited in the range of climate variables it deals with as compared to more complex models.

Chapter 8

Conclusion

This chapter presents a summary of the main findings of this research work and the response to the research questions posed in Chapter 1.

8.1 Summary of Contributions

This research has investigated the reasons behind the wide range of temperature change projections given in the IPCC Fourth Assessment Report. In large part this is due to the emissions scenarios used to make the projections, together with the scientific uncertainty associated with each scenario. The latter is the uncertainty arising from the temperature response of the Earth's biogeophysical climate system, the main contributors to which are climate sensitivity, aerosol forcing and the carbon–cycle.

The highlights of this research can be summarised as having:

- Investigated and demonstrated the successful application of some observationally based independent constraints, notably the land−ocean temperature difference and the SST to OHC ratio, which help to better estimate some of the key climate system parameters. The application of these largely independent constraints is a feature of this research;

- Quantified the contribution different model parameters make to the overall uncertainty in the model results as a basis for prioritising which parameters to constrain. This indicated that most of the uncertainty in the response of the climate system to a perturbation in radiative forcing arises from the climate sensitivity parameter, along with a contribution from the ocean vertical diffusivity parameter, while the remaining climate system parameters have little influence on the global–mean temperature results. Aerosol forcing uncertainty, limited in this investigation to a single parameter, is also an important contributor to the uncertainty in temperature change. The importance of the carbon cycle was also confirmed, but it was found that more carbon cycle parameters needed to be included to represent the role of the carbon cycle in the model results. Note that this evaluation applies to the prior estimates of the parameters' standard distributions, not the posterior results;

- Investigated and revised the model's ocean parameters to improve the modelled ocean temperature profile and ocean heat content changes as compared to observations. This included

correcting a model error and significant changes to the previous standard settings for the ocean vertical diffusivity and variable upwelling fraction parameters. There remains a mismatch between the observed upper ocean warming and the model, which is also evident in complex models, that needs further investigation;

- Implemented a Monte Carlo Metropolis–Hastings (MCMH) algorithm that works in conjunction with MAGICC. Of particular interest is the inclusion of observations to estimate the carbon cycle parameters, something that has not been previously accomplished with MAGICC. A reduction in the distribution for the CO_2 fertilisation factor and the ocean carbon cycle impulse response scale factor where achieved as a result, although little improvement was obtained for the carbon cycle temperature feedback parameters for NPP and respiration.

- Combined the MCMH algorithm with 20th-century observations to estimate the joint climate system and carbon cycle parameter space so as to arrive at a set of posterior parameter distributions that can then be used for forward projections. This allows probabilistic projections to be produced and the risks of exceeding a given temperature change amount to be estimated. The results obtained in this way represent most of the uncertainty in the response of the climate system for a given emissions scenario, not just a multi-model ensemble mean with additional uncertainties 'tacked on', as was the case for the IPCC AR4 results (*IPCC*, 2007b);

- Applied the cumulative distributions used to estimate the risks of exceeding a global–mean temperature change to the mean land temperature change, showing the higher probability of exceeding 2°C on land, based on the observationally constrained estimates for the land ocean warming ratio R_{lo} and land ocean heat coefficient κ_{lo};

- Applied the MCMH derived posterior parameter distributions to the SRES emission scenarios in order to compare the results to those reported in the IPCC AR4 (*IPCC*, 2007b). It was found that, for most of the six marker scenarios analysed, the best estimates were similar, but with increased lower bounds for the likely temperature change (67% confidence interval), which increases the risk of greater warming;

- Confirmed previous investigations that found avoiding 'dangerous climate change' requires massive reductions in emissions of greenhouse–gases, and that the time remaining in which to achieve such reductions is rapidly running out.

8.1.1 Uncertainty in temperature projections

This research has investigated uncertainties in the Earth's climate system response to increasing anthropogenic greenhouse–gases, with a focus on global–scale temperature changes using a simplified Earth system model as the research tool. The principal outcome was the development of methods to constrain the model parameters with historical climate observations so that probabilistic temperature change projections that take into account different sources of scientific uncertainty could be produced.

Parameter sensitivity and uncertainty analysis, along with testing of twentieth–century model results against historical observations, were used to identify the primary model parameters as a basis for prioritising which parameters to constrain. Some alternative constraints were developed based on data sets derived from historical observations that provide additional independent information that has only weak correlations to global–mean temperature data. These constraints are the land−ocean and hemispheric temperature differences, and the SST/OHC ratio. The use of these temperature differences is an alternative approach to constraining the parameters in a simple climate model that does not appear to have been applied in this way before. The land−ocean temperature difference was found to be helpful in setting the parameters associated with the land ocean temperature contrast.

The SST/OHC used in this research is similar to the effective heat capacity or OHC to global–surface temperature ratio used by *Frame et al.* (2005) and *Andrews and Allen* (2008), but MAGICC reports separate land–surface and sea–surface temperatures, which enables this different ratio to be used. The two different approaches to estimating K, that is using the ocean temperature change profile and the SST/OHC ratio, point towards a substantially lower value than that used as the default setting in the versions of MAGICC used for the IPCC Third and Fourth Assessment Reports.

A Monte Carlo Markov Chain with Metropolis–Hastings algorithm (MCMH) was also used to investigate parameter distributions for the climate system and the carbon cycle parameters separately and then combined. Twentieth–century observations were used to help constrain these model parameters. This method provides a way of quantifying uncertainty and allows probabilistic temperature change projections to be made. A number of examples of projected future temperature changes that employ MCMH results have been included in Chapters 6 and 7.

The results led to a reduction in the likely range of projected temperatures as compared to the IPCC AR4 values, with generally similar best estimates but increased lower bounds. The interaction of the carbon cycle and the climate system due to the CO_2 and temperature dependent processes leads to greater risk of warming than that indicated by the IPCC. This result has important implications for international agreements on mitigation policies, since this increased risk of greater temperature change means that even more significant reductions in greenhouse gas emissions will be required if a target such as limiting warming above pre-industrial global–mean temperatures to 2°C, the threshold generally accepted for avoiding ‘dangerous climate change’.

8.1.2 Ocean heating

The ocean plays an important role in the climate system, soaking up heat and setting the transient response of the system. The most recent observations indicate that there is a noticeable increase in the world ocean’s temperature change in the upper part of the ocean, particularly in the top 200m, an increase that is not reproduced by the CMIP3 models. This issue was investigated using MAGICC in order to consider its significance for future global–mean temperature change projections. It was determined that the model’s ocean temperature change parameters needed revising. In addition, a re-formulation of the ocean heat calculation was required to correct a program error.

The fit between MAGICC’s representation of the ocean temperature change and the observed change was found to be improved by reducing the variable component of the upwelling diffusion

equation (w_{var}) and substantially reducing the standard value for the ocean vertical diffusivity K. However, the exponential form of ocean heat diffusion equation does not lend itself to representing the sharp change in temperature in the upper ocean. This more surface–trapped temperature change is associated with wind–driven subduction and ocean current, complex processes that perhaps need modelling in some other way. The addition of a new parameter that allows K to change with the ocean thermal gradient, introduced into the new version of MAGICC may help with this problem, however time did not permit further investigation of this topic.

Observations of ocean temperature change and ocean heat content were used to constrain MAGICC's ocean parameter settings. The ocean parameters have to be prioritised because these parameters set the model's transient climate response. The surface temperature results are all derived from the mixed–layer temperature changes, which in turn is affected by the rate at which heat is moved downwards into the deeper ocean layers. If heat is transfered too quickly away from the mixed layer then lower surface temperatures will be reported.

However, the ocean diffusivity is closely tied to the climate sensitivity, so that to match the observed 20th-century global-mean temperature changes, a lower ocean vertical diffusivity also leads to a reduction in climate sensitivity. On the other hand, uncertainty in aerosol forcing has to be considered as well. The MCMH approach allows these different parameters to be assessed simultaneously on the basis of fitting to a suite of 20th-century historical observations.

8.1.3 Carbon cycle uncertainties

Uncertainty in the carbon cycle feedback/response to increasing atmospheric CO_2 due to the fertilisation effect and temperature changes is an important part of the uncertainty in projected global-mean temperature changes. The uncertainties in modelling the carbon cycle arise for a number of reasons including the lack of relevant observations with sufficient temporal and spatial coverage and model limitations. MAGICC lacks the capability to track carbon isotopes and hence is unable to make use of this additional resource.

MAGICC has only previously been calibrated against the complex carbon cycle models of the Coupled Carbon Cycle Climate Model Intercomparison Project (C4MIP; *Friedlingstein et al.*, 2006). In this research, the model's carbon cycle parameters were successfully calibrated using observations. However, only a reduced set of parameters were calibrated in this way due to limited global–scale observational data, but also on the basis of the uncertainty contributions of the individual parameters that shows a small number of them account for most of the uncertainty. The uncertainty analysis also found that, whilst the carbon cycle parameters have the most impact on CO_2 concentrations, climate sensitivity also plays a role.

The analysis presented in this thesis determined that the CO_2 fertilisation factor β_s and ocean carbon cycle impulse response scale factor O_{r} could be estimated from the observations, while the temperature feedback terms for respiration σ_{R} and NPP σ_{NPP} remain difficult to constrain. The lack of long term observations and the uncertain response of terrestrial vegetation and the ocean biosphere to conditions significantly different to those over the past few thousand years make it very difficult to assess how the system will respond in the future.

Carbon–cycle uncertainty is estimated to contribute around 20% of the overall uncertainty in projected temperature change for a given emission scenario.

8.1.4 Stabilising emissions

In addition to issues concerning scientific uncertainty discussed in the preceding sections of this chapter, future temperature changes also depend on the choices that influence the amounts of greenhouse–gases produced in the years ahead. Some alternative ways of considering temperature changes were addressed in Chapter 7, beginning with the concept of 'climate commitment' as a thought experiment that provides some insight into the nature of the mitigation challenge. The zero–emissions and fixed emissions at 2010 levels examples indicate the extent of the challenge for limiting further increases in global–mean temperatures. The extreme case of zero further emissions is still not able to bring temperatures back to pre-industrial by the end of this century, while maintaining current emissions would see a temperature increase of around 2°C above pre-industrial by 2100.

The posterior parameter distributions from the MCMH analysis were used to investigate a number of different emission scenarios to demonstrate the application of this method and for comparing the resulting global–mean temperature changes to the results from other models, in particular the values reported in the IPCC AR4. For this reason the six SRES (Special Report on Emissions Scenarios, (*Nakicenovic and Swart*, 2000)) marker scenarios were examined. In addition, the RCPs (Representative Concentration Pathways) were also investigated as these will provide a basis of comparison to the new results that will come out of the CMIP5 experiments leading up to the next IPCC report.

Stabilisation pathways were also analysed in the context of dangerous climate change, the emission reductions required to keep atmospheric concentrations below a target such as 450 ppm CO_2 equivalent or a temperature increase of 2°C above pre-industrial temperatures by 2050. With current greenhouse gas (GHG) concentrations already around 470ppm CO_2-equivalent, massive cuts in emissions are required to reverse the present trend and prevent additional temperature increases. Examination of the STAB450 and RCP3PD emissions shows that near zero greenhouse–gas emissions are needed to keep the risk of exceeding 2°C below 25%, with, for example, net CO_2 emissions reducing to less than 1 GtC from 2070 onwards. These emission pathways are overshoot scenarios that demonstrate the difficulty of this task, with the temperature changes only decreasing very gradually despite drastic emission cuts. International mitigation agreements are, so far, inadequate to the challenge.

A number of potential non-linear changes and threshold events or tipping points were noted at the end Chapter of 7 (see also *Raupach et al.*, 2011, for additional discussion of vulnerabilities). Whilst it has not been possible to assess the risks associated with the these possibilities here, the precautionary principle suggests that such events must be avoided, otherwise they will tend to accelerate further changes, for example from the reduced ice albedo due to the loss of ice sheets and sea ice, and from increases in greenhouse–gases as a consequence of permafrost melting.

8.2 Future Directions

During the course of this research work a number of topics were noted as candidates for further investigation.

The uncertainty analysis technique that was applied to assessing the relative contributions that individual parameters make to the overall uncertainty could be tested in more depth to confirm the generality or otherwise of the results. Different fractions of the standard deviations and alternate scenarios could be tested to check the linearity assumption, as well as using the posterior standard deviations from the MCMH work to see how the relative contributions change.

The ocean temperature and ocean heat content changes are of central importance to the workings of MAGICC. Accordingly, further analysis of the discrepancies between observations and the model results is needed. Possible avenues for further exploration include having a state–dependent ocean vertical diffusivity, and examination of the hemispheric ocean temperatures and heat content in addition to the world ocean values.

The ocean carbon cycle is currently modelled in MAGICC with a single response function. This could potentially be changed to a different method so as to represent the chemical and biological pumps, which might help with investigating the effects of increased atmospheric CO_2 concentrations and global–mean temperature changes in terms of ocean acidification, the changing magnitude of the ocean carbon sink and the temperature dependence of CO_2 solubility.

In connection with the MCMH program, there is scope for further work to test, verify and potentially improve the results achieved here. Areas for further investigation include:

- Increasing the number of iterations used to derive the posterior distributions from 50,000 to, for example, 100,000 and 250,000 to determine the effect this has on the parameter values;

- Testing alternate sets of observational data, such as NASA GISS and NCDC surface temperatures and different ocean temperature and ocean heat content change data;

- Examining different parameter combinations, using, for example, one or two of the carbon initial pool sizes, the variable upwelling fraction and including the ocean vertical diffusivity gradient variable;

- Testing land minus ocean carbon flux as a potentially independent constraint for the carbon cycle, similar to the L−O temperature difference;

- Considering options for the aerosol forcing components, with perhaps two parameters for direct and indirect effects rather than a single combined total aerosol forcing parameter. In addition, to research alternative methods which can assist with these settings.

The ability to estimate sea–level rise has been dropped from the current version of MAGICC, although it was one of the reasons MAGICC was developed originally. It would undoubtably be a very useful capability if this feature could be re-instated.

Another interesting application for MAGICC is that of estimating the carbon budget for a given temperature change target. Whilst this type of analysis has been performed by others (examples include *Allen et al.*, 2009; *Zickfeld et al.*, 2009; *Meinshausen et al.*, 2009), this work could be re-visited in light of the new posterior parameter distributions obtained here, particularly in view of the carbon cycle parameters having been constrained by historical observations.

8.3 Closing Remarks

MAGICC provides a valuable tool for assessing the risks of human–induced climate change. It is a relatively simple climate model as compared to fully coupled three–dimensional AOGCMs, yet it has a comparable ability to reproduce the observed 20th-century global–mean temperature record, although limited on short time scales because it lacks modes of natural variability. This is supported by MAGICC's ability to emulate the complex models both for the last century as well as for projections to the end of this century. That such a simplified energy–balance model works so well provides confidence that, at least for the global–scale, the principal mechanisms behind the recent global temperature trend are correctly understood.

Calibration of the model's climate system and carbon cycle parameters against historical observations using the MCMH algorithm reduces the reliance on complex models as well as enabling probabilistic temperature change projections to be made. This allows the uncertainty in temperature changes for a given scenario to be quantified and risks to be assessed. This research work will help to maintain and improve the reliability of MAGICC for this purpose.

Appendix A

MAGICC Energy Balance Equations

A.1 Four energy balance equations

For ease of reference, this appendix sets out the upwelling–diffusion equations used in MAGICC, following *Meinshausen et al.* (2011a) (with similar, but not identical, notation).

There are four transient energy balance equations for the four model regions:

$$f_{\mathrm{no}}(\zeta_{\mathrm{o}}\frac{d\Delta T_{\mathrm{no},1}}{dt} - \Delta Q_{\mathrm{no}} + \lambda_{\mathrm{o}}\alpha T_{\mathrm{no},1} + F_{\mathrm{n}}) = \kappa_{\mathrm{lo}}(\Delta T_{\mathrm{nl}} - \mu\alpha\Delta T_{\mathrm{no},1}) + \kappa_{\mathrm{ns}}\alpha(\Delta T_{\mathrm{so},1} - \Delta T_{\mathrm{no},1}) \tag{A.1}$$

$$f_{\mathrm{nl}}(\zeta_{\mathrm{l}}\frac{d\Delta T_{\mathrm{nl}}}{dt} - \Delta Q_{\mathrm{nl}} + \lambda_{\mathrm{l}}\Delta T_{\mathrm{nl}}) = \kappa_{\mathrm{lo}}(\mu\alpha\Delta T_{\mathrm{no},1} - \Delta T_{\mathrm{nl}}) \tag{A.2}$$

$$f_{\mathrm{so}}(\zeta_{\mathrm{o}}\frac{d\Delta T_{\mathrm{so},1}}{dt} - \Delta Q_{\mathrm{so}} + \lambda_{\mathrm{o}}\alpha T_{\mathrm{so},1} + F_{\mathrm{s}}) = \kappa_{\mathrm{lo}}(\Delta T_{\mathrm{nl}} - \mu\alpha\Delta T_{\mathrm{so},1}) + \kappa_{\mathrm{ns}}\alpha(\Delta T_{\mathrm{so},1} - \Delta T_{\mathrm{so},1}) \tag{A.3}$$

$$f_{\mathrm{nl}}(\zeta_{\mathrm{l}}\frac{d\Delta T_{\mathrm{nl}}}{dt} - \Delta Q_{\mathrm{nl}} + \lambda_{\mathrm{l}}\Delta T_{\mathrm{nl}}) = \kappa_{\mathrm{lo}}(\mu\alpha\Delta T_{\mathrm{so},1} - \Delta T_{\mathrm{nl}}) \tag{A.4}$$

The subscripts correspond to the Northern Hemisphere (n), Southern Hemisphere (s), land (l) and ocean (o). Area fractions are designated by f with the appropriate subscript. The additional numbered subscript, such as $\Delta T_{\mathrm{no},1}$, refers to the ocean layer number, with the mixed layer designated as 1. The additional layers, that is layer 2 onwards, are 100m deep, with the number of layers set by a model parameter (default 50).

ΔQ_x is the radiative forcing perturbation for region x (nl, no, nl, so). F_{n} and F_{s} are the net heat fluxes at the bottom of the Northern Hemisphere and Southern Hemisphere mixed layers respectively.

The heat capacity for land ζ_{l} is assumed to be zero, while the ocean bulk heat capacity ζ_{o} for each hemisphere is:

$$f_{\mathrm{no}}\zeta_{\mathrm{o}} = f_{\mathrm{no}}\rho ch$$
$$f_{\mathrm{so}}\zeta_{\mathrm{o}} = f_{\mathrm{so}}\rho ch$$

where ρ is the density of seawater, c is the specific heat capacity and h is the depth of the mixed layer. λ_{l} and λ_{o} are the climate feedbacks for land and ocean, derived from the climate sensitivity parameter $\Delta T_{2\mathrm{x}}$ and land ocean warming ratio R_{lo}, as explained in the next section, Appendix A.2.

α is the scaling factor used to convert the mixed layer temperatures ($\Delta T_{\mathrm{no},1}$ and $\Delta T_{\mathrm{so},1}$) to the ocean near surface air temperatures (ΔT_{no} and ΔT_{so}) (discussed in Section 3.1.3).

μ is a new parameter introduced in to MAGICC version 6 to provided for asymmetric land ocean heat exchange, although its default setting is 1. It allows additional control over the relative temperature changes for the land and ocean. In this research work R_{lo} alone was used in the MCMH calibration of the primary MAGICC parameters. It would be possible to leave R_{lo} at a fixed value, that is, leaving it at an equilibrium setting, and then allowing μ to vary (refer *Meinshausen et al.*, 2011a, for additional explanation).

Looking just at the Northern hemisphere equations and re-arranging Equation A.2:

$$\Delta T_{\mathrm{nl}} = \frac{f_{\mathrm{nl}}\Delta Q_{\mathrm{nl}} + \kappa_{\mathrm{lo}}\mu\alpha\Delta T_{\mathrm{no},1}}{f_{\mathrm{nl}}\lambda_{\mathrm{l}} + \kappa_{\mathrm{lo}}} \tag{A.5}$$

Then, substituting ΔT_{nl} in to equation A.1:

$$\begin{aligned} f_{\mathrm{no}}(\zeta_{\mathrm{o}}\frac{d\Delta T_{\mathrm{no},1}}{dt} - \Delta Q_{\mathrm{no}} + \lambda_{\mathrm{o}}\alpha T_{\mathrm{no},1} + F_{\mathrm{n}}) = \\ \frac{\kappa_{\mathrm{lo}}}{\frac{\kappa_{\mathrm{lo}}}{f_{\mathrm{nl}}} + \lambda_{\mathrm{l}}}(\Delta Q_{\mathrm{nl}} - \lambda_{\mathrm{l}}\mu\alpha\Delta T_{\mathrm{no},1}) \\ +\kappa_{\mathrm{ns}}\alpha(\Delta T_{\mathrm{so},1} - \Delta T_{\mathrm{no},1}) \end{aligned} \tag{A.6}$$

The next step is to determine F_{n}, since that leads to $d\Delta T_{\mathrm{no},1}/dt$, the mixed layer temperature change, which, along with $d\Delta T_{\mathrm{so},1}/dt$, are MAGICC's prognostic temperature variables. F_{n} is the net heat flux at the bottom of the mixed layer which depends on the downward heat transfer from vertical diffusivity K and the upwelling and down-welling components, both of which act on the temperature change ΔT from the initial ocean temperature profile. Hence:

$$
\begin{aligned}
F_{\mathrm{n}} = \frac{K}{0.5h_d}\rho c(\Delta T_{\mathrm{no},1} - \Delta T_{\mathrm{no},2}) \\
-w\rho c(\Delta T_{\mathrm{no},2} - \beta\Delta T_{\mathrm{no},1}) \\
-\Delta w\rho c(T^0_{\mathrm{no},2} - T^0_{\mathrm{no,sink}})
\end{aligned} \tag{A.7}
$$

$T^0_{\mathrm{no},2}$ is the initial temperature for water in layer z, or in the down-welling pipe, in which case z = "sink". w is the upwelling rate, which varies over time from its initial state w_0, with the change in upwelling velocity Δw^t=(w_t - w_0) at time t.

The top layer is assumed to be well–mixed, so that the gradient of the temperature changes is calculated by the difference of the changes divided by half the thickness of the second layer. Substituting F_{n} from A.7 into equation A.6, together with using discreet time steps gives:

$$
\begin{aligned}
\frac{d\Delta T_{\mathrm{no},1}}{dt} \approx \frac{\Delta T^{t+1}_{\mathrm{no},1} - \Delta T^t_{\mathrm{no},1}}{\Delta t} = & \\
\frac{1}{\zeta_{\mathrm{o}}}\Delta Q^t_{\mathrm{no}} & \text{: forcing} \\
-\frac{\lambda_{\mathrm{o}}\alpha}{\zeta_{\mathrm{o}}}\Delta T^{t+1}_{\mathrm{no},1} & \text{: feedback} \\
-\frac{K}{0.5h_d h}(\Delta T^{t+1}_{\mathrm{no},1} - \Delta T^{t+1}_{\mathrm{no},2}) & \text{: diffusion} \\
+\frac{w^t}{h}(\Delta T^{t+1}_{\mathrm{no},2} - \beta\Delta T^{t+1}_{\mathrm{no},1}) & \text{: upwelling} \\
+\frac{\Delta w^t}{h}(T^0_{\mathrm{no},2} - T^0_{\mathrm{no,sink}}) & \text{: variable upwelling} \\
+\frac{\kappa_{\mathrm{lo}}(\Delta Q^t_{\mathrm{nl}} - \lambda_{\mathrm{l}}\mu\alpha\Delta T^{t+1}_{\mathrm{no},1})}{\zeta_{\mathrm{o}} f_{\mathrm{no}}(\frac{\kappa_{\mathrm{lo}}}{f_{\mathrm{nl}}} + \lambda_{\mathrm{l}})} & \text{: land forcing} \\
+\frac{\kappa_{\mathrm{ns}}\alpha}{\zeta_{\mathrm{o}} f_{\mathrm{no}}}(\Delta T^t_{\mathrm{so},1} - \Delta T^t_{\mathrm{no},1} & \text{: inter-hemispheric exchange}
\end{aligned} \tag{A.8}
$$

The temperature change for the layers under the mixed layer depends on the diffusion and upwelling terms:

$$
\begin{aligned}
\frac{\Delta T^{t+1}_{\mathrm{no},z} - \Delta T^t_{\mathrm{no},z}}{\Delta t} = \frac{K}{0.5(h + h'_d)h_d}(\Delta T^{t+1}_{\mathrm{no},z-1} - \Delta T^{t+1}_{\mathrm{no},z}) \\
-\frac{K}{h_d^2}(\Delta T^{t+1}_{\mathrm{no},z+1} - \Delta T^{t+1}_{\mathrm{no},z+1}) \\
+\frac{w^t}{h_d}(\Delta T^{t+1}_{\mathrm{no},z+1} - \Delta T^{t+1}_{\mathrm{no},z}) \\
+\frac{\Delta w^t}{h_d}(T^0_{\mathrm{no},z+1} - T^0_{\mathrm{no},z})
\end{aligned} \tag{A.9}
$$

where h'_d is zero for the layer below the mixed layer (z=2) and h_d otherwise.

For the bottom layer (z=n), the down-welling term has to be included in the calculation:

$$\begin{aligned}\frac{\Delta T_{\mathrm{no},n}^{t+1} - \Delta T_{\mathrm{no},n}^{t}}{\Delta t} &= \frac{K}{h_d^2}(\Delta T_{\mathrm{no},n-1}^{t+1} - \Delta T_{\mathrm{no},n}^{t+1}) \\ &+ \frac{w^t}{h_d}(\beta \Delta T_{\mathrm{no},1}^{t} - \Delta T_{\mathrm{no},n}^{t+1}) \\ &+ \frac{\Delta w^t}{h_d}(T_{\mathrm{no,sink}}^{0} - T_{\mathrm{no},n}^{0}) \end{aligned} \tag{A.10}$$

Similar equations apply to the Southern Hemisphere.

These equations apply to the constant–depth area profile case. However, MAGICC provides for a depth–dependent ocean with entrainment, whereby the area cross–section of the ocean decreases with depth. This is discussed further in Section A.3

A.2 Partitioning of feedbacks

Different feedback parameters are used over land and ocean, based on an adjustable equilibrium land to ocean warming ratio, R_{lo}. As noted in Section 3.1.2, since the ocean heat uptake is zero when the Earth's radiative energy balance is zero, the global energy balance equation can be arranged into land and ocean components:

$$\Delta Q = \lambda \Delta T = f_{\mathrm{l}} \lambda_{\mathrm{l}} \Delta T_{\mathrm{l}} + f_{\mathrm{o}} \lambda_{\mathrm{o}} \Delta T_{\mathrm{o}} \tag{A.11}$$

where ΔQ, λ and ΔT are the global–mean forcing, climate feedback and global–mean temperature change respectively. The right–hand terms use the land and ocean area fractions, f_{l} and f_{o}, the separate land and ocean feedbacks, λ_{l} and λ_{o}, together with the matching mean surface temperature changes for the land $\Delta \mathrm{T_l}$ and for the ocean $\Delta \mathrm{T_o}$. λ_{l} and λ_{o} are calculated from a set of non-linear equations for a given land ocean warming ratio R_{lo} (= $\Delta \mathrm{T_l}/\Delta \mathrm{T_o}$).

The atmosphere is assumed to be in equilibrium with the ocean mixed layer, so that the energy balance for the Northern Hemisphere is given by:

$$\begin{aligned} f_{\mathrm{no}} \lambda_{\mathrm{o}} \Delta T_{\mathrm{no}} = \quad & \text{: outgoing long wave radiation flux} \\ f_{\mathrm{no}} \Delta Q_{\mathrm{no}} \quad & \text{: forcing} \\ +\kappa_{\mathrm{lo}}(\Delta T_{\mathrm{nl}} - \mu \Delta T_{\mathrm{no}}) \quad & \text{: land ocean heat exchange} \\ +\kappa_{\mathrm{ns}} \alpha (\Delta T_{\mathrm{so}} - \Delta T_{\mathrm{no}}) \quad & \text{: hemispheric heat exchange} \end{aligned} \tag{A.12}$$

where Δ $\mathrm{T_{no}}$ is the surface temperature change over the Northern Hemisphere ocean, Δ $\mathrm{Q_{no}}$ is the corresponding radiative forcing, with the area fraction f_{no} as before. κ_{lo} and κ_{ns} are heat exchange coefficients for land ocean and hemispheric exchanges. An additional parameter is provided for asymmetric land ocean heat exchange, μ (for full details see *Meinshausen et al.*, 2011a, Section A4.2).

The equilibrium energy balance equations for the other three regions are:

$$
\begin{aligned}
f_{\mathrm{nl}}\lambda_{\mathrm{l}}\Delta T_{\mathrm{nl}} =& f_{\mathrm{nl}}\Delta Q_{\mathrm{nl}} \\
&+ \kappa_{\mathrm{lo}}(\mu\Delta T_{\mathrm{no}} - \Delta T_{\mathrm{nl}}) && \text{(A.13)} \\
f_{\mathrm{so}}\lambda_{\mathrm{o}}\Delta T_{\mathrm{so}} =& f_{\mathrm{so}}\Delta Q_{\mathrm{so}} \\
&+ \kappa_{\mathrm{lo}}(\Delta T_{\mathrm{sl}} - \mu\Delta T_{\mathrm{so}}) \\
&+ \kappa_{\mathrm{ns}}\alpha(\Delta T_{\mathrm{no}} - \Delta T_{\mathrm{so}}) && \text{(A.14)} \\
f_{\mathrm{sl}}\lambda_{\mathrm{l}}\Delta T_{\mathrm{sl}} =& f_{\mathrm{sl}}\Delta Q_{\mathrm{sl}} \\
&+ \kappa_{\mathrm{lo}}(\mu\Delta T_{\mathrm{so}} - \Delta T_{\mathrm{sl}}) && \text{(A.15)}
\end{aligned}
$$

This set of four equations, A.12–A.15, is solved iteratively for the solution where λ_{l} is closest to λ.

A.3 The upwelling–diffusion–entrainment equations

MAGICC allows for the option of a depth–dependent ocean area profile plus entrainment from the polar sinking water, which requires some modification to the energy–balance equations in Section A.1 (refer *Meinshausen et al.*, 2011a, for additional details). This section sets out the modified equations as they are implemented in MAGICC version 6.

The entrainment is modelled so that the upwelling velocity in the main column is the same in each layer, and mass conservation is maintained by entrainment from the narrow down–welling pipe. As the ocean area decreases with depth, the upwelling mass flux would also have to decrease with depth. To offset this, the amount of entrainment into layer z is assumed to be proportional to the decrease in area from the top to the bottom of each layer.

Three area correction factors are used:

$$
\begin{aligned}
\theta_z^{\mathrm{top}} &= \frac{A_z}{(A_{z+1} + A_z)/2} \\
\theta_z^{\mathrm{b}} &= \frac{A_{z+1}}{(A_{z+1} + A_z)/2} \\
\theta_z^{\mathrm{dif}} &= \frac{A_{z+1} - A_z}{(A_{z+1} + A_z)/2} && \text{(A.16)}
\end{aligned}
$$

where A_z is the area at the top of the layer z or bottom of layer $z-1$ and the denominator is an approximation for the mean area of each ocean layer.

For the mixed layer, all the terms in Equation A.9 that include $\Delta T_{\mathrm{no},1}^{t+1}$ are collected on the left hand side in variable $A(1)$, and all terms involving $\Delta T_{\mathrm{no},2}^{t+1}$ are collected in variable $B(1)$ on the left hand side. All the remaining terms are placed in variable $D(1)$ on the right hand side, so that the equation becomes:

$$
\Delta T_{\mathrm{no},1}^{t+1} = -\frac{B(1)}{A(1)}\Delta T_{\mathrm{no},2}^{t+1} + \frac{D(1)}{A(1)} \qquad \text{(A.17)}
$$

with:

$$\begin{aligned} A(1) = 1.0 &+ \theta_1^{\text{top}} \Delta t \frac{\lambda_{\text{o}} \alpha}{\zeta_{\text{o}}} && \text{: feedback over ocean} \\ &+ \theta_1^{\text{b}} \Delta t \frac{K}{0.5 h h_d} && \text{: diffusion to layer 2} \\ &+ \theta_1^{\text{b}} \Delta t \frac{w^t \beta}{h} && \text{: down–welling} \\ &+ \theta_1^{\text{top}} \Delta t \frac{\kappa_{\text{lo}} \lambda_{\text{l}} \mu \alpha}{\zeta_{\text{o}} f_{\text{no}} (\frac{\kappa_{\text{lo}}}{f_{\text{nl}}} + \lambda_{\text{l}})} && \text{: feedback over land} \end{aligned} \tag{A.18}$$

$$\begin{aligned} B(1) = &- \theta_1^{\text{b}} \Delta t \frac{K}{0.5 h h_d} && \text{: diffusion to layer 2} \\ &+ \theta_1^{\text{b}} \Delta t \frac{w^t}{h} && \text{:upwelling from layer 2} \end{aligned} \tag{A.19}$$

$$\begin{aligned} D(1) = \Delta T_{\text{no},1}^t & && \text{: previous temperature} \\ &+ \theta_1^{\text{top}} \Delta t \frac{1}{\zeta_{\text{o}}} \Delta Q_{\text{no}} && \text{:ocean forcing} \\ &\theta_1^{\text{top}} \Delta t \frac{\kappa_{\text{ns}} \alpha}{\zeta_{\text{o}} f_{\text{no}}} (\Delta T_{\text{so},1}^t - \Delta T_{\text{no},1}^t) && \text{: hemispheric heat exchange} \\ &+ \theta_1^{\text{top}} \Delta t \frac{\kappa_{\text{lo}} \Delta Q_{\text{nl}}}{\zeta_{\text{o}} f_{\text{no}} (\frac{\kappa_{\text{lo}}}{f_{\text{nl}}} + \lambda_{\text{l}})} && \text{: land forcing} \\ &+ \theta_1^{\text{top}} \Delta t \frac{\Delta w^t}{h} (T_{\text{no},2}^0 - T_{\text{no,sink}}^0) && \text{: variable upwelling} \end{aligned} \tag{A.20}$$

For the layers in between the mixed and bottom layers, the terms are re-ordered so that $A(z)$ comprises the terms for $\Delta T_{\text{no},z-1}^{t+1}$, $B(z)$ the terms for $\Delta T_{\text{no},z}^{t+1}$, $C(z)$ the terms for $\Delta T_{\text{no},z+1}^{t+1}$ and $D(z)$ the remaining terms, so that:

$$\Delta T_{\text{no},z-1}^{t+1} = -\frac{B(z)}{A(z)} \Delta T_{\text{no},z}^{t+1} - \frac{C(z)}{A(z)} \Delta T_{\text{no},z+1}^{t+1} + \frac{D(z)}{A(z)} \tag{A.21}$$

with:

$$A(z) = -\theta_z^{\text{top}} \Delta t \frac{K}{0.5 (h_d + h'_d) h_d} \quad \text{: diffusion from layer above} \tag{A.22}$$

$$\begin{aligned} B(z) = 1.0 &+ \theta_z^{\text{b}} \Delta t \frac{K}{h_d^2} && \text{: diffusion to layer below} \\ &+ \theta_z^{\text{top}} \Delta t \frac{K}{0.5 (h_d + h'_d) h_d} && \text{: diffusion to layer above} \\ &+ \theta_z^{\text{top}} \Delta t \frac{w^t}{h_d} && \text{: upwelling to layer above} \end{aligned} \tag{A.23}$$

$$\begin{aligned} C(z) = &- \theta_z^{\mathrm{b}} \Delta t \frac{K}{h_d^2} && \text{: diffusion from layer below} \\ &- \theta_z^{\mathrm{top}} \Delta t \frac{w^t}{h_d} && \text{:upwelling from layer below} \end{aligned} \tag{A.24}$$

$$\begin{aligned} D(z) = \Delta T_{\mathrm{no,z}}^t & && \text{: previous temperature} \\ &+ \Delta t \frac{\Delta w^t}{h_d} (\theta_z^{\mathrm{b}} T_{\mathrm{no},z+1}^0 - \theta_z^{\mathrm{top}} T_{\mathrm{no,z}}^0) && \text{: variable upwelling} \\ &+ \theta_z^{\mathrm{dif}} \Delta t \frac{w^t}{h_d} \beta \Delta T_{\mathrm{no,1}}^{t-1} && \text{: entrainment} \\ &+ \theta_z^{\mathrm{dif}} \Delta t \frac{\Delta w^t}{h_d} T_{\mathrm{no,sink}}^0) && \text{: variable entrainment} \end{aligned} \tag{A.25}$$

where h'_d is zero for the layer below the mixed layer and h_d otherwise.

For the bottom layer, the respective $A(n)$ for $\Delta T_{\mathrm{no},n-1}^{t+1}$, $B(n)$ for $\Delta T_{\mathrm{no},n}^{t+1}$, and $D(n)$ terms are:

$$\Delta T_{\mathrm{no},n-1}^{t+1} = -\frac{B(n)}{A(n)} \Delta T_{\mathrm{no},n}^{t+1} - \frac{D(n)}{A(n)} \tag{A.26}$$

$$A(n) = -\theta_n^{\mathrm{top}} \Delta t \frac{K}{h_d^2} \qquad \text{: diffusion from layer } n-1 \tag{A.27}$$

$$\begin{aligned} B(n) = 1.0 + \theta_n^{\mathrm{top}} \Delta t \frac{K}{h_d^2} & && \text{: diffusion to layer } n-1 \\ &+ \theta_z^{\mathrm{top}} \Delta t \frac{w^t}{h_d} && \text{: upwelling to layer } n-1 \end{aligned} \tag{A.28}$$

$$\begin{aligned} D(n) = \Delta T_{\mathrm{no,n}}^t & && \text{: previous temperature} \\ &+ \theta_n^{\mathrm{top}} \Delta t \frac{w^t}{h_d} \beta \Delta T_{\mathrm{no,1}}^{t-1} && \text{:down–welling from top layer} \\ &- \theta_z^{\mathrm{top}} \Delta t \frac{\Delta w^t}{h_d} T_{\mathrm{no,n}}^0 && \text{: variable upwelling} \\ &+ \theta_z^{\mathrm{top}} \Delta t \frac{\Delta w^t}{h_d} T_{\mathrm{no,sink}}^0 && \text{: variable down–welling} \end{aligned} \tag{A.29}$$

and similarly for the Southern Hemisphere.

The Equations A.17 to A.29 can be solved consecutively from the bottom to the top layer at each time step.

Appendix B

MAGICC Equations for Calculating Radiative Forcing

This appendix presents the main parameterised expressions used within MAGICC to estimate the radiative forcing due to changes in greenhouse–gases, tropospheric ozone and aerosols, following *Meinshausen et al.* (2011a). Forcing efficacies were not investigated as part of this research and, accordingly, are not included here, although there is provision to apply different efficacies in MAGICC (refer *Meinshausen et al.*, 2011a, and discussions in *Hansen et al.*, 2005 and *Meehl et al.*, 2007b).

B.1 Carbon dioxide

A simplified expression for calculating CO_2 radiative forcing is used, as introduced in Chapter 2, Section 2.2.1:

$$\Delta Q_{\mathrm{CO_2}} = \alpha_{\mathrm{CO_2}} \ln(\mathrm{C}/\mathrm{C}_0) \tag{B.1}$$

where $\alpha_{\mathrm{CO_2}}$ has a value of 5.35 Wm $^{-2}$ (based on *Myhre et al.*, 1998), $\Delta Q_{\mathrm{CO_2}}$ is the adjusted forcing due to the CO_2 concentration C (ppm) above the pre-industrial concentration C_0 (278 ppm). The logarithm allows for the 'saturation' effect which means that increases in CO_2 concentrations have a reduced amount of forcing as less radiation is absorbed by the atmospheric CO_2.

B.2 Methane and nitrous oxide

Concentrations of methane and nitrous oxide influence each other since they have overlapping absorption bands. The expressions for methane and nitrous oxide forcing allow for this as follows (see also *Myhre et al.*, 1998; *Ramaswamy et al.*, 2001):

$$\Delta Q_{\mathrm{CH_4}} = \alpha_{\mathrm{CH_4}}(\sqrt{C_{\mathrm{CH_4}}} - \sqrt{\mathrm{C}^0_{\mathrm{CH_4}}}) - f(\mathrm{C}_{\mathrm{CH_4}}, \mathrm{C}^0_{\mathrm{N_2O}}) - f(\mathrm{C}^0_{\mathrm{CH_4}}, \mathrm{C}^0_{\mathrm{N_2O}}) \tag{B.2}$$

$$\Delta Q_{\mathrm{N_2O}} = \alpha_{\mathrm{N_2O}}(\sqrt{C_{\mathrm{N_2O}}} - \sqrt{\mathrm{C}^0_{\mathrm{N_2O}}}) - f(\mathrm{C}_{\mathrm{CH_4}}, \mathrm{C}^0_{\mathrm{N_2O}}) - f(\mathrm{C}^0_{\mathrm{CH_4}}, \mathrm{C}^0_{\mathrm{N_2O}}) \tag{B.3}$$

where the overlap is given by the function:

$$f(\mathrm{M},\mathrm{N}) = 0.47\ln(1+0.6356(\frac{\mathrm{MN}}{10^6})^{0.75}+0.007\frac{\mathrm{M}}{10^3}(\frac{\mathrm{MN}}{10^6})^{1.52}) \tag{B.4}$$

where M and N are the CH_4 and N_2O concentrations (ppb), and $\Delta Q_{\mathrm{CH_4}}$, $\Delta Q_{\mathrm{N_2O}}$ the respective forcings. The α terms are the gas scaling parameters.

Methane has an additional forcing factor that arises from the methane–induced enhancement of stratospheric water vapour. This is assumed to be proportional to the 'straight' methane radiative forcing before the subtraction of the N_2O overlap, and is given by the formula:

$$\Delta Q_{\mathrm{CH_4}}^{\mathrm{stratoH2O}} = \nu\alpha_{\mathrm{CH_4}}(\sqrt{C_{\mathrm{CH_4}}}-\sqrt{\mathrm{C}^0_{\mathrm{CH_4}}}) \tag{B.5}$$

where ν is the proportionality factor (default 15%).

B.3 Tropospheric ozone

The change in tropospheric ozone concentrations (in DU) is given by (*Ehhalt et al.*, 2001):

$$\Delta(\mathrm{tropO_3}) = \mathrm{S}^{\mathrm{O_3}}_{\mathrm{CH_4}}\Delta\ln(\mathrm{CH_4})+\mathrm{S}^{\mathrm{O_3}}_{\mathrm{NO_x}}E_{\mathrm{NO_x}}+S^{\mathrm{O_3}}_{\mathrm{CO}}E_{\mathrm{CO}}+S^{\mathrm{O_3}}_{\mathrm{VOC}}E_{\mathrm{VOC}} \tag{B.6}$$

where $S^{\mathrm{O_3}}_{\mathrm{x}}$ are the respective sensitivity coefficients of tropospheric ozone to methane and the precursor emissions NO_x, CO and VOC. The radiative forcing is then obtained from a linear approximation:

$$\Delta Q_{\mathrm{tropO_3}} = \alpha_{\mathrm{tropO_3}}\Delta(\mathrm{tropO_3}) \tag{B.7}$$

where $\alpha_{\mathrm{tropO_3}}$ is the radiative efficiency factor (default 0.042).

B.4 Stratospheric ozone

Depletion of stratospheric ozone produces a negative global–mean radiative forcing according to the formula:

$$\Delta Q_t = \eta_1(\eta_2\times\Delta\mathrm{EESC_t})^{\eta_3} \tag{B.8}$$

where the radiative forcing is assumed to be proportional to the equivalent effective stratospheric chlorine (EESC), with η_1 as the sensitivity scaling factor, $\Delta\mathrm{EESC}_t$ is the EESC concentrations above 1980 levels (ppb), the factor η_2 is $\frac{1}{100}$ (ppb^{-1}) and η_3 is the sensitivity exponent (refer *Meinshausen et al.*, 2011a; *Daniel et al.*, 1999, for further details).

B.5 Halogenated gases

Simple relationships are employed to derive the global–mean radiative forcing $\Delta Q_{t,i}$ of halogenated gases based on their atmospheric concentrations:

$$\Delta Q_{t,i} = \rho_i (C_{t,i} - C_{0,i}) \tag{B.9}$$

where ρ_i is the radiative efficiency for gas i, with concentration C in year t above its initial concentration C_0 (refer *Meinshausen et al.*, 2011a; *Ehhalt et al.*, 2001, for further details).

B.6 Tropospheric aerosols

The radiative forcing of direct aerosols are approximated by linear abundance relationships for sulphate, nitrate, black carbon and organic carbon. These abundances are estimated from their hemispheric emissions. The ratio of direct forcing over land and ocean areas in each hemisphere is based on *Hansen et al.* (2005).

The indirect radiative forcing is estimated from the time series of sulphate, nitrate, black carbon and organic carbon optical thickness according to:

$$\Delta Q_{\mathrm{Alb},i} = r \times \mathrm{P}_{\mathrm{Alb},i} \times \log\left(\frac{\sum_g w_g \mathrm{N}_{\mathrm{g},i}}{\sum_g w_g \mathrm{N}_{\mathrm{g},i}}\right) \tag{B.10}$$

where $\Delta Q_{\mathrm{Alb},i}$ is the first indirect aerosol forcing in the four model regions i (land and ocean in each hemisphere). $\mathrm{P}_{\mathrm{Alb},i}$ is the four region pattern of aerosol indirect effects related to cloud albedo (*Twomey*, 1977) in a reference year. The second indirect effect on cloud cover (*Albrecht*, 1989) is modelled similarly using a reference year pattern $\mathrm{P}_{\mathrm{Cvr},i}$. The respective patterns are based on *Hansen et al.* (2005).

The scaling factor r allows a global–mean first or second indirect forcing to be specified for a specific reference year. The number concentrations of soluble aerosols $\mathrm{N}_{\mathrm{g},i}$ in year t are normalised relative to their pre-industrial level $\mathrm{N}^0_{\mathrm{g},i}$ in that reference year individually for each of the sulphate, nitrate, black carbon and organic carbon aerosols.

The default contribution shares w_{g} for each aerosol type to the indirect aerosol effect are assigned to reflect the preliminary results of *Hansen et al.* (2005) (refer also *Meinshausen et al.*, 2011a, for further details concerning the relative contributions and limitations).

The number concentrations $\mathrm{N}_{\mathrm{g},i}$ are estimated from historical optical thickness estimates and extrapolated into the future by scaling with hemispheric emissions. The general logarithmic relationship between number concentrations $\mathrm{N}_{\mathrm{g},i}$ and forcing $\Delta Q_{\mathrm{Alb},i}$ is based on *Wigley* (1991a); *Wigley and Raper* (1992); *Gultepe and Issac* (1999) and *Hansen et al.* (2005).

Appendix C

MAGICC Non–CO_2 Concentrations

For ease of reference, this appendix provides details concerning the conversion of emissions to concentrations, following *Meinshausen et al.* (2011a). CO_2 emissions to concentrations is dealt with in Chapter 5, and the radiative forcing formulas are covered in Appendix B.

C.1 Methane

Natural emissions of methane are inferred from balancing the budget for a given historical period, such as from 1980–1990, so that:

$$E^n_\phi = \theta(\Delta C_\phi - C_{\phi'}/\tau_{\mathrm{tot}}) - E^f_\phi - E^b_\phi \tag{C.1}$$

where E^n_ϕ, E^f_ϕ and E^b_ϕ are the average natural, fossil and land–use related emissions respectively. θ is the conversion factor between atmospheric concentrations and mass loadings. $C_{\phi'}$ is the average concentration and ΔC_ϕ the annual change in concentrations.

The net atmospheric lifetime τ_{tot} is the sum of the tropospheric chemical lifetime, the characteristic soil lifetime and other components (such as stratospheric):

$$\frac{1}{\tau_{\mathrm{tot}}} = \frac{1}{\tau_{\mathrm{tropos}}} + \frac{1}{\tau_{\mathrm{soil}}} + \frac{1}{\tau_{\mathrm{other}}} \tag{C.2}$$

The feedback of methane on tropospheric OH (the hydroxyl radical) and its own lifetime is parameterised from complex three–dimensional atmospheric chemistry models (*Ehhalt et al.*, 2001). The default relationship assumes tropospheric OH decreases by 0.32% for every 1% increase in CH_4. The change in tropospheric OH abundances is modelled as:

$$\Delta \ln(\mathrm{tropOH}) = \mathrm{S}^{\mathrm{OH}}_{\mathrm{CH_4}} \Delta \ln(\mathrm{CH_4}) + \mathrm{S}^{\mathrm{OH}}_{\mathrm{NO_x}} \mathrm{E}_{\mathrm{NO_x}} + \mathrm{S}^{\mathrm{OH}}_{\mathrm{CO}} \mathrm{E}_{\mathrm{CO}} + \mathrm{S}^{\mathrm{OH}}_{\mathrm{VOC}} \mathrm{E}_{\mathrm{VOC}} \tag{C.3}$$

where S^{OH}_x is the sensitivity of tropospheric OH towards CH_4, NO_x, CO and VOC. Increases in tropospheric OH abundances decrease the lifetime τ' of methane which is approximated by the exponential relationship:

$$\tau'_{\mathrm{CH_4,tropos}} = \tau^0_{\mathrm{CH_4,tropos}} \exp^{\Delta \ln(\mathrm{tropOH})} \tag{C.4}$$

There is also a temperature sensitivity on the net effect of tropospheric chemical reaction rates to allow for, which adjusts the tropospheric lifetime of CH_4:

$$\tau_{\mathrm{CH_4,tropos}} = \frac{\tau^0_{\mathrm{CH_4,tropos}}}{\frac{\tau^0_{\mathrm{CH_4,tropos}}}{\tau'_{\mathrm{CH_4,tropos}}} + S_{\tau_{\mathrm{CH_4}}}\Delta T} \tag{C.5}$$

where $S_{\tau_{\mathrm{CH_4}}}$ is the temperature sensitivity coefficient and ΔT is the temperature change above a user-defined year, e.g., 1990.

C.2 Nitrous oxide

Nitrous oxide emissions are estimated from a budget similar to methane. However, for N_2O the average concentrations $C_{\phi'} = C_{\phi-3}$ are taken for a period shifted by three years to adjust for the delay in transport of tropospheric N_2O to the main stratospheric sink. The feedback between the atmospheric burden C_{N_2O} and its own lifetime is approximated by:

$$\tau_{\mathrm{N_2O}} = \tau^0_{\mathrm{N_2O}}\left(\frac{\mathrm{C_{N_2O}}}{\mathrm{C^0_{N_2O}}}\right)^{S_{\tau_{\mathrm{N_2O}}}} \tag{C.6}$$

where $S_{\tau_{\mathrm{N_2O}}}$ is the sensitivity coefficient and the superscript '0' indicates a pre-industrial reference state.

C.3 Tropospheric aerosols

Changes in hemispheric aerosol abundances are estimated from changes in their hemispheric emissions. Where emissions of particular species are missing from an emissions scenario, such as black carbon (BC) and organic carbon (OC) in the case of the SRES scenarios, proxy emissions are estimated by scaling from other emissions, such as CO as a proxy emission for BC and OC.

C.4 Halogenated gases

Concentrations of halogenated gases assumes time–variable lifetimes. The net atmospheric lifetime τ_i for each halogenated gas i is calculated by summing the inverse lifetimes related to stratospheric, OH–related and other sinks. Stratospheric lifetimes are assumed to decrease by 15% per degree of global–mean surface temperature warming, due to an increased Brewer–Dobson circulation. Losses due to Tropospheric OH are scaled by parameterised changes in OH abundances, matching the respective lifetime of methane. The concentration $C_{t,i}$ for the beginning of each year t is updated using a central differencing formula:

$$C_{t+1,i} = \tau_i E_{t,i}\frac{\rho_{\mathrm{atm}}}{m_{\mathrm{atm}}\mu_i}(1 - e^{\frac{-1}{\tau_i}}) + C_{t,i}(1 - e^{\frac{-1}{\tau_i}}) \tag{C.7}$$

where $E_{t,i}$ is the average emissions of gas i through year t, $C_{t,i}$ the atmospheric concentration of gas i in year t, ρ_{atm} the average density of air, m_{atm} the total mass of the atmosphere, and μ_i is the mass per mol of gas i.

For hydrogenated halocarbons, the tropospheric OH related lifetimes are assumed to vary in proportion to the changes in methane lifetime.

References

Albrecht, B. A. (1989), Aerosols, cloud microphysics, and fractional cloudiness, *Science*, *245*, 1227–1230.

Allen, M. R., P. A. Stott, J. F. B. Mitchell, R. Schnur, and T. Delworth (2000), Quantifying the uncertainty in forecasts of anthropogenic climate change, *Nature*, *407*, 617–620.

Allen, M. R., D. J. Frame, C. Huntingford, C. D. Jones, J. A. Lowe, M. Meinshausen, and N. Meinshausen (2009), Warming caused by cumulative carbon emissions towards the trillionth tonne, *Nature*, *458*, 1163–1166.

Allison, I., N. L. Bindoff, R. A. Bindschadler, P. M. Cox, N. de Noblet, M. H. England, et al. (2009), *The Copenhagen Diagnosis: Updating the World on the Latest Science*, The University of New South Wales Climate Change Research Centre.

Ammann, C. M., G. A. Meehl, and W. M. Washington (2003), A monthly and latitudinally varying volcanic forcing dataset in simulations of 20th century climate, *Geophysical Research Letters*, *30*(12), 1657.

Andrews, D. G., and M. R. Allen (2008), Diagnosis of climate models in terms of transient climate response and feedback response time, *Atmospheric Science Letters*, *9*, 7–12.

Andronova, N., and M. E. Schlesinger (2001), Objective estimation of the probability density function for climate sensitivity, *Journal of Geophysical Research*, *106*, 22,605–22,611.

Andronova, N., M. E. Schlesinger, S. Dessai, M. Hulme, and B. Li (2007), The concept of climate sensitivity: history and development, in *Human–induced Climate Change: An Interdisciplinary Assessment*, edited by M. E. Schlesinger, H. S. Kheshgi, J. Smith, F. de la Chesnaye, J. M. Reilly, T. Wilson, and C. Kolstad, pp. 5–17, Cambridge University Press, Cambridge.

Barker, P. M., J. R. Dunn, C. M. Domingues, and S. E. Wijffels (2011), Pressure sensor drift in Argo and their impacts, *Journal of Atmospheric and Oceanic Techmology*, *(in press)*.

Bellouin, N., O. Boucher, J. Haywood, and M. Shekar Reddy (2005), Global estimate of aerosol direct radiative forcing from satellite measurements, *Nature*, *438*, 1138–1141.

Boden, T., G. Marland, and R. Andres (2010), *Global, Regional, and National Fossil-Fuel CO_2 Emissions*, Carbon Dioxide Information Analysis Center, Oak Ridge National Laboratory, U.S. Department of Energy.

Boer, G. J., K. Hamiltion, and W. Zhu (2005), Climate sensitivity and climate change under strong forcing, *Climate Dynamics*, *24*, 685–700.

Brasseur, G. P., and E. Roeckner (2005), Impact of improved air quality on the future evolution of climate, *Geophysical Research Letters*, *32*, doi:L23704.

Broecker, W. S. (1987), Unpleasant surprises in the greenhouse?, *Nature*, *328*, 123–126.

Brohan, P., J. J. Kennedy, I. Harris, S. F. B. Tett, and P. D. Jones (2006), Uncertainty estimates in regional and global observed temperature changes: A new data set from 1850, *Journal of Geophysical Research*, *111*, doi:10.1029/2005JD006548, (http://www.cru.uea.ac.uk/cru/data/temperature/).

Cai, W., and P. H. Whetton (2001), Modes of sst variability and the fluctuation of global mean temperature, *Climate Dynamics*, *17*, 889–901.

Caldeira, K., A. K. Jain, and M. I. Hoffert (2003), Climate sensitivity uncertainty and the need for energy without CO_2 emission, *Science*, *299*(5615), 2052–2054.

Canadell, J., D. E. Pataki, R. M. Gifford, R. A. Houghton, Y. Luo, M. R. Raupach, P. Smith, and W. Steffen (2007), Saturation of the terrestral carbon sink, in *Terrestrial ecosystems in a changing world*, edited by J. G. Canadell, D. E. Pataki, and L. Pitelka, The IGBP Series, pp. 59–78, Pringer-Verlag, Berlin.

Clarke, L. E., J. A. Edmonds, H. D. Jacoby, H. M. Pitcher, J. M. Reilly, and R. Richels (2007), *Scenarios of greenhouse gas emissions and atmospheric concentrations*, U.S. Climate Change Science Program, Department of Energy, Washington, DC.

Claussen, M. (2005), Table of EMICS, http://www.pik-potsdam.de/emics.

Claussen, M., et al. (2002), Earth system models of intermediate complexity: closing the gap in the spectrum of climate system models, *Climate Dynamics*, *18*, 579–586.

Colman, R., and B. McAvaney (2009), Climate feedbacks under a very broad range of forcing, *Geophysical Research Letters*, *36*, doi:10.1029/2008GL036268.

Cox, P. M., R. A. Betts, C. D. Jones, S. A. Spall, and Totterdell (2000), Acceleration of global warming due to carbon–cycle feedbacks in a coupled climate model, *Nature*, *408*, 184–187.

Craig, H. (1969), Abyssal carbon and radiocarbon in the Pacific, *Journal of Geophysical Research*, *74*(23), 5491–5506.

Cubasch, U., and R. D. Cess (1990), Processes and modelling, in *Climate Change: The IPCC Scientific Assessment*, edited by J. T. Houghton, G. Jenkins, and J. J. Ephraums, pp. 69–91, Cambridge University Press, Cambridge.

Cubasch, U., and G. Meehl (2001), Projections of future climate changes, in *Climate Change 2001: The Scentific Basis*, edited by J. T. Houghton, Y. Ding, D. Griggs, M. Noguer, P. J. v. d. Linden, and D. Xiaosu, pp. 525–582, Cambridge University Press, Cambridge, UK.

Daniel, J. S., S. Solomon, and R. W. Portmann (1999), Stratospheric ozone destruction: The importance of bromine relative to chlorine, *Journal of Geophysical Research*, *104*(D19), 23,871–23,880.

del Grosso, S., W. Parton, T. Stohlgren, D. Zheng, D. Bachelet, S. Prince, K. Hibbard, and R. Olson (2008), Global potential net primary production produced from vegetation class, precipitation, and temperature, *Ecology*, *89*(8), 2117–2126.

den Elzen, M. G. J., M. Meinshausen, and D. Van Vuuren (2007), Multi-gas emission envelopes to meet greenhouse gas concentration targets: Costs versus certainty of limiting temperature increase, *Global Environmental Change*, *17*, 260–280.

den Elzen, M. G. J., D. P. van Vuuren, and J. van Vliet (2010), Postponing emission reductions from 2020 to 2030 increases climate risks and long–term costs, *Climatic Change*, *99*, 313–320.

Denman, K., G. P. Brasseur, A. Chidthaisong, P. Ciais, P. M. Cox, R. E. Dickinson, D. Hauglustaine, C. Heinze, and E. Holland (2007), Couplings between changes in the climate system and biogeochemistry, in *Climate Change 2007: The Physical Science Basis. Contribution of Working Group I of the Fourth Assessment Report*, edited by S. Solomon, D. Qin, M. Manning, Z. Chen, M. Marquis, K. B. Averyt, M. Tignor, and H. L. Miller, IPCC.

Dessai, S., and M. Hulme (2003), *Does climate policy need probabilities? Working Paper 34*, Tyndall Centre for Climate Change Research.

Domingues, C. M., J. A. Church, N. J. White, P. J. Gleckler, S. E. Wijffels, P. M. Barker, and J. R. Dunn (2008), Improved estimates of upper–ocean warming and multi–decadal sea–level rise, *Nature*, *453*, 1090–1093.

Drost, F., D. Karoly, and K. Braganza (2011), Communicating global climate change using simple indices: an update, *Climate Dynamics*, doi:10.1007/s00382-011-1227-6.

Ehhalt, D., et al. (2001), Atmospheric chemistry and greenhouse gases, in *Climate Change 2001: The Scentific Basis*, edited by J. T. Houghton, Y. Ding, D. Griggs, M. Noguer, P. van der Linden, X. Dai, K. Maskell, and C. Johnson, Cambridge University Press.

Enting, I. G. (2008), Assessing the information content in environmental modelling: A carbon cycle perspective, *Entropy*, *10*, 556–575.

Enting, I. G. (2011), Seeking carbon-consistency in the climate-science-to-policy interface, *Biogeochemistry*, *104*, 59–67.

Enting, I. G., and G. I. Pearman (1987), Description of a one-dimensional carbon cycle model calibrated using techniques of constrained inversion, *Tellus*, *39B*, 459–476.

Enting, I. G., T. M. L. Wigley, and M. Heimann (1994), *Future emissions and concentrations of carbon dioxide: key ocean/atmosphere/land analyses*, Division of Atmospheric ResearchTechnical Paper No. 31, CSIRO.

Fawcett, R. (2007), Has the world cooled since 1998?, *Bulletin of the Australian Meteorological and Oceanographic Society*, *20*, 141–148.

Feulner, G., and S. Rahmstorf (2010), On the effect of a new grand minimum of solar activity on the future climate on earth, *Geophysical Research Letters*, *37*, doi:10.1029/2010GL042710.

Folland, C. K., et al. (2001), Global temperature change and its uncertainties since 1861, *Geophysical Research Letters*, *28*(13), 2621–2624.

Forest, C., P. Stone, A. P. Sokolov, M. R. Allen, and M. Webster (2002), Quantifying uncertainties in climate system properties with the use of recent climate observations, *Science*, *295*(5552), 113–118.

Forest, C., M. Webster, and J. M. Reilly (2004), Narrowing uncertainty in global climate change, *The Industrial Physicist*, *Aug/Sep*, 20–23.

Forest, C. E., P. H. Stone, and A. P. Sokolov (2008), Constraining climate model parameters from observed 20th century changes, *Tellus*, *60A*, 911–920.

Forster, P. M., and J. M. Gregory (2006), The climate sensitivity and its components diagnosed from Earth radiation budget data, *Journal of Climate*, *19*, 39–52.

Frame, D. J., B. B. B. Booth, J. A. Kettleborough, D. A. Stainforth, J. M. Gregory, M. Collins, and M. R. Allen (2005), Constraining climate forecasts: the role of prior assumptions, *Geophysical Research Letters*, *32*, doi:10.1029/2004GL022241.

Friedlingstein, P., J.-L. Dufresne, P. M. Cox, and P. Rayner (2003), How positive is the feedback between climate and the carbon cycle?, *Tellus*, *55B*, 692–700.

Friedlingstein, P., et al. (2006), Climate–carbon cycle feedback analysis: results from the C4MIP model intercomparison, *Journal of Climate*, *19*, 3337–3353.

Friedlingstein, P., et al. (2010), Update on CO_2 emissions, *Nature Geoscience*, published online: 21 November 2010.

Garnaut, R. (2008), *The Garnaut Climate Change Review*, Cambridge University Press, Melbourne.

Garnaut, R. (2011), *The Garnaut Review 2011: Australia in the global response to climate change*, Cambridge University Press.

Garnaut, R., S. Howes, F. Jotzo, and P. Sheehan (2008), Emissions in the platinum age: The implications of rapid development for climate change mitigation, *Oxford Review of Economic Policy*, *24*(2), 377–401.

Garrett, C. (1979), Mixing in the ocean interior, *Dynamics of Atmospheres and Oceans*, *3*(2–4), 239–265.

Gay, C., and F. Estrada (2010), Objective probabilities about future climate are a matter of opinion, *Climatic Change*, *99*, 27–46.

Gifford, R. M. (1993), Implications of CO_2 effects on vegetation for the global carbon budget, in *The Global Carbon Cycle*, *Proceedings of the NATO Advanced Study Institute*, vol. 15, edited by M. Heimann, Springer-Verlag, Berlin.

Girod, B., A. Wiek, H. Mieg, and M. Hulme (2009), The evolution of the IPCC's emissions scenarios, *Environmental Science and Policy*, *2*, 103–118.

Gouretski, V., and K. P. Koltermann (2007), How much is the ocean really warming?, *Geophysical Research Letters*, *34*, doi:10.1029/2006GL027834.

Gregory, J., and M. Webb (2008), Tropospheric adjustment induces a cloud component in CO_2 forcing, *Journal of Climate*, *21*, 58–71.

Gregory, J. M., R. J. Stouffer, S. C. B. Raper, P. A. Stott, and N. A. Rayner (2002), An observationally based estimate of the climate sensitivity, *Journal of Climate*, *15*(22), 3117–3121.

Gregory, J. M., C. D. Jones, P. Cadule, and P. Friedlingstein (2009), Quantifying carbon cycle feedbacks, *Journal of Climate*, *22*, 5232–5250.

Grubler, A., and N. Nakicenovic (2001), Identifying dangers in an uncertain climate, *Nature*, *412*, 15.

Gultepe, I., and G. A. Issac (1999), Scale effects on averaging cloud droplet and aerosol number concentrations, *Journal of Climate*, *12*, 1268–1279.

Hansen, J., et al. (2008), Target atmospheric CO_2: where should humanity aim?, *The Open Atmospheric Science Journal*, *2*, 217–231.

Hansen, J. E. (2005), A slippery slope: How much global warming constitutes "dangerous anthropogenic interference", *Climatic Change*, *68*, 269–279.

Hansen, J. E., A. A. Lacis, R. Ruedy, M. Sato, and H. Wilson (1993), How sensitive is the World's climate?, *Research and Exploration*, *9*(2), 143–158.

Hansen, J. E., et al. (2002), Climate forcings in Goddard Institute for Space Studies SI2000 simulations, *Journal of Geophysical Research*, *107*, 4347.

Hansen, J. E., et al. (2005), Efficacy of climate forcings, *Journal of Geophysical Research*, *110*, 45, doi:D18104.

Hansen, J. E., M. Sato, P. Kharecha, G. Russell, D. W. Lea, and M. Siddall (2007), Climate change and trace gases, *Philosophical Transactions of the Royal Society*, *365*, 1925–1954.

Hansen, J. E., R. Ruedy, and K. Lo (2010), Global surface temperature change, *Reviews of Geophysics*, *48*, (http://data.giss.nasa.gov/gistemp/).

Hare, B., and M. Meinshausen (2006), How much warming are we committed to and how much can be avoided?, *Climate Change*, *75*, 111–149.

Hare, W. L., W. Cramer, M. Schaeffer, A. Battaglini, and C. C. Jaeger (2011), Climate hotspots: key vulnerable regions, climate change and limits to warming, *Regional Environmental Change*, *11*, S1–S13.

Harman, I. N., M. Ford, G. Jakeman, S. J. Phipps, M. Brede, J. J. Finnigan, D. Gunasekera, and H. Ahammad (2008), Assessement of future global scenarios for the Garnaut Climate Change Review: An application of the GIAM framework, *Tech. rep.*, CSIRO.

Harvey, L. D. D. (1989), Effect of model structure on the response of terrestrial biosphere models to CO_2 and temperature increases, *Global Biogeochemical Cycles*, *3*, 137–153.

Harvey, L. D. D., and R. K. Kaufmann (2002), Simultaneously constraining climate sensitivity and aerosol radiative forcing, *Journal of Climate*, *15*(20), 2837–2861.

Harvey, L. D. D., and M. E. Schneider (1985a), Transient climate response to external forcing on 10–10,000 year time scales. Part 1: Experiments with globally averaged, coupled, atmosphere and ocean energy balance models, *Journal of Geophysical Research*, *90*, 2191–2205.

Harvey, L. D. D., and M. E. Schneider (1985b), Transient climate response to external forcing on 10–10,000 year time scales. Part 2: Sensitivity experiments with a seasonal, hemispherically averaged, coupled atmosphere, land, and ocean energy–balance model, *Journal of Geophysical Research*, *90*, 2207–2222.

Harvey, L. D. D., J. M. Gregory, M. I. Hoffert, A. K. Jain, M. Lai, R. Leemans, S. C. B. Raper, T. M. L. Wigley, and J. de Wolde (1997), *An Introduction to Simple Climate Models used in the IPCC Second Assessment Report*, IPCC Technical Paper II, IPCC.

Hibbard, K. A., G. A. Meehl, P. M. Cox, and P. Friedlingstein (2007), A strategy for climate change stabilisation experiments, *EOS*, *88*(20), 217–219.

Hibbard, K. A., D. P. van Vuuren, and J. Edmonds (2011), A primer on theRepresentative Concentration Pathways (RCPs) and the coordination btwen the climate and integrated assessment modeling communities, *CLIVAR Exchanges*, *16*(56), 12–15.

Hoffert, M. I., A. J. Callegari, and C.-T. Hseih (1980), The role of deep sea heat storage in the secular response to climate forcing, *Journal of Geophysical Research*, *85*, 6667–6679.

Hulme, M., S. C. B. Raper, and T. M. L. Wigley (1995), An integrated framework to address climate change (ESCAPE) and further developments of the global and regional climate modules (MAGICC), *Energy Policy*, *23*, 347–355.

Huntingford, C., J. A. Lowe, B. B. B. Booth, C. D. Jones, G. R. Harris, L. K. Gohar, and P. Meir (2009), Contributions of carbon cycle uncertainty to future climate projection spread, *Tellus*, *61B*(2), 355–360.

Inman, M. (2011), Opening the future, *Nature Climate Change*, *1*, 7–9.

International Energy Agency (2010), *World Energy Outlook 2010*, International Energy Agency.

IPCC (1990), *Climate Change: The IPCC Scientific Assessment*, Cambridge University Press, Cambridge, UK.

IPCC (1992), *Climate Change 1992: The Supplementary Report to the IPCC Scientific Assessment*.

IPCC (1996), *Climate Change 1995: The Science of Climate Change*, Cambridge University Press, Cambridge.

IPCC (1997), An introduction to simple climate models used in the IPCC Second Assessment Report: IPCC Technical Paper II.

IPCC (1997), *Stabilization of Atmospheric Greenhouse Gases: Physical, Biological and Socio-economic Implications*.

IPCC (2001), *Climate Change 2001: The Scientific Basis. Contribution of Working Group I of the Third Assessment Report*, Cambridge, UK.

IPCC (2007a), *Climate Change 2007: The Physical Science Basis. Working Group I Contribution to the Fourth Assessment Report. Summary for Policymakers, Technical Summary and Frequently Asked Questions.*, Cambridge University Press, Cambridge, UK.

IPCC (2007b), *Climate Change 2007: The Physical Science Basis. Contribution of Working Group I of the Fourth Assessment Report*, Cambridge University Press, Cambridge, UK.

Jain, A. K., H. S. Kheshgi, M. I. Hoffert, and D. J. Wuebbles (1995), Distribution of radiocarbon as a test of global carbon cycle models, *Global Biogeochemical Cycles*, *9*, 153–166.

Jones, C. D., P. Cox, and C. Huntingford (2003), Uncertainty in climate–carbon–cycle projections associated with the sensitivity of soil respiration to temperature, *Tellus*, *55B*, 642–648.

Jones, C. D., P. M. Cox, and C. Huntingford (2006), Climate–carbon cycle feedbacks under stabilization: uncertainty and observational constraints, *Tellus*, *58B*, 603–613.

Jones, P. D. (1994), Recent warming in global temperature series, *Geophysical Research Letters*, *21*(12), 1149–1152, doi:10.1029/94GL01042.

Jones, R. N. (2000), Managing uncertainty in climate change projections — issues for impact assessment, *Climatic Change*, *45*, 403–419.

Joos, F., C. Prentice, S. Sitch, R. Meyer, G. Hooss, G.-K. Plattner, S. Gerber, and K. Hasselmann (2001), Global warming feedbacks on terrestrial carbon uptake under the intergovernmental panel on climate change (IPCC) emission scenarios, *Global Biogeochemical Cycles*, *15*(4), 891–907.

Joshi, M., K. P. Shine, M. Ponater, N. Stuber, R. Sausen, and L. Li (2003), A comparison of climate response to different radiative forcings in three general ciculation models: towards an improved metric of climate change, *Climate Dynamics*, *20*, 843–854.

Karoly, D. J., and K. Braganza (2001), Identifying global climate change using simple indices, *Geophysical Research Letters*, *28*, 2205–2208.

Keller, K., M. Hall, S.-R. Kim, D. F. Bradford, and M. Oppenheimer (2005), Avoiding dangerous antropogenic interference with the climate system, *Climatic Change*, *73*, 227–238.

Knorr, W., and J. Kattge (2005), Inversion of terrestrial ecosystem model parameter values against eddy covariance measurements by Monte Carlo sampling, *Global Change Biology*, *11*, 1333–1351.

Knutti, R., et al. (2008), A review of uncertainties in global temperature projections over the twenty-first century, *Journal of Climate*, *21*, 2651–2662.

Kopp, G., and J. Lean (2011), A new, lower value of total solar irradiance: Evidence and climate significance, *Geophysical Research Letters*, *38*, doi:10.1029/2010GL045777.

Lacis, A. A., J. E. Hansen, and M. Sato (1992), Climate forcings by stratospheric aerosols, *Geophysical Research Letters*, *19*, 1607–1610.

Lambert, F. H., M. J. Webb, and M. M. Joshi (2011), The relationship between land–ocean surface temeprature contrast and radiative forcing, *Journal of Climate*, *24*, 3239–3256.

Le Quéré, C., et al. (2007), Saturation of the Southern Ocean CO_2 sink due to recent climate change, *Science*, *316*, 1735–1738.

Le Quéré, C., M. R. Raupach, J. G. Cansdell, G. Marland, R. A. Houghton, P. Ciais, and P. Friedlingstein (2009), Trends in the sources and sinks of carbon dioxide, *Nature Geoscience*, *22*, 831–836.

Lean, J. L., and D. H. Rind (2008), How natural and anthropogenic influences alter global and regional surface temperatures: 1889 to 2006, *Geophysical Research Letters*, *35*, doi: 10.1029/2008GL034864.

Lenton, T. M., H. Held, E. Kriegler, J. W. Hall, W. Lucht, S. Rahmstorf, and H. J. Schellnhuber (2008), Tipping elements in the Earth's climate system, *Proceedings of the National Academy of Sciences*, *105*(6), 1786–1793.

Levitus, S., J. I. Antonov, and T. P. Boyer (2005), Warming of the world ocean, 1955-2003, *Geophysical Research Letters*, *32*, doi:L02604.

Levitus, S., J. I. Antonov, T. P. Boyer, R. A. Locarnini, H. E. Garcia, and A. V. Mishonov (2009), Global ocean heat content 1955–2008 in light of recently revealed instrumentation problems, *Geophys. Res. Lett.*, *36*, doi:10.1029/2008GL037155.

Leyendekkers, J. V. (1976), *Thermodynamics of Seawater Part I*, Dekker, New York.

Libardoni, A. G., and C. E. Forest (2011), Sensitivity of distributions of climate system properties to the surface temperature dataset, *Geophysical Research Letters*, *38*, doi: 10.1029/2011GL049431.

Luyten, J. R., J. Pedlosky, and H. Stommel (1983), The ventilated thermocline, *Journal of Physical Oceanography*, *13*, 292–309.

Maier-Reimer, E., and K. Hasselmann (1987), Transport and storage in the ocean — an inorganic ocean–circulation carbon cycle model, *Climate Dynamics*, *2*, 63–90.

Manabe, S., and R. J. Stouffer (1980), Sensitivity of a global climate model to an increase of CO_2 concentration in the atmosphere, *Journal of Geophysical Research*, *85*(C10), 5529–5554.

Mann, M. E. (2009), Defining dangerous anthropogenic interference, *Proceedings of the National Academy of Sciences*, *106*(11), 4065–4066.

Mann, M. E., Z. Zhang, M. K. Hughes, R. S. Bradley, S. K. Miller, S. Rutherford, and F. Ni (2008), Proxy–based reconstructions of hemisperic and global surface temperature variations over the past two millenia, *Proceedings of the National Academy of Sciences*, *105*(36), 13,252–13,257.

Manney, G. L., et al. (2011), Unprecedented Arctic ozone loss in 2011, *Nature*, *online*, doi: 10.1038/nature10556.

Manning, M., J. A. Edmonds, S. Emori, A. Grubler, K. Hibbard, F. Joos, et al. (2010), Misrepresentation of the IPCC CO_2 emission scenarios, *Nature Geoscience*, *3*, 376–377.

Matthews, H. D., and K. Caldeira (2008), Stabilizing climate requires near–zero emissions, *Geophysical Research Letters*, *35*, doi:L04705.

Matthews, H. D., and A. J. Weaver (2010), Committed climate warming, *Nature Geoscience*, *3*, 142–143.

McGuffie, K., and A. Henderson-Sellers (2001), Forty years of numerical climate modelling, *International Journal of Climatology*, *21*, 1067–1109.

McGuffie, K., and A. Henderson-Sellers (2005), *A Climate Modelling Primer*, 3rd ed., John Wiley and Sons Ltd., Chichester, England.

Meehl, G., et al. (2006), Climate change projections for the twenty-first century and climate change commitment in the CCSM3, *Journal of Climate*, *19*, 2597–2616.

Meehl, G., C. Covey, T. Delworth, M. Latif, B. McAvaney, J. Mitchell, R. J. Stouffer, and K. E. Taylor (2007a), The WCRP CMIP3 multi-model dataset: A new era in climate change research, *Bull. Am. Meteorol. Soc.*, *88*, 1383–1394.

Meehl, G. A., G. J. Boer, C. Covey, M. Latif, and R. J. Stouffer (2000), The Coupled Model Intercomparison Project (CMIP), *Bull. Am. Meteorol. Soc.*, *81*, 313–318.

Meehl, G. A., et al. (2007b), Global climate projections, in *Climate Change 2007: The Physical Science Basis. Contribution of Working Group I to the Fourth Assessment Report of the Intergovernmental Panel on Climate Change*, edited by S. Solomon, D. Qin, M. Manning, Z. Chen, M. Marquis, K. B. Averyt, M. Tignor, and H. L. Miller, Cambridge University Press.

Meinshausen, M. (2005), SiMCaP's EQW-PATHFINDER.

Meinshausen, M. (2006), What does a 2°C target mean for greenhouse gas concentrations?, in *Avoiding Dangerous Climate Change*, edited by H. J. Schellnhuber, W. Cramer, N. Nakicenovic, T. M. L. Wigley, and G. Yohe, chap. 28, Cambridge University Press, Cambridge, UK.

Meinshausen, M., B. Hare, T. M. L. Wigley, D. van Vuuren, M. G. J. den Elzen, and R. Swart (2006), Multi-gas emissions pathways to meet climate targets, *Climatic Change*, *75*, 151–194.

Meinshausen, M., S. C. B. Raper, and T. M. L. Wigley (2008), Emulating IPCC AR4 atmosphere-ocean and carbon cycle models for projecting global-mean, hemispheric and land/ocean temperatures: MAGICC 6.0, *Atmos. Chem. Phys. Discussions*, *8*, 6153–6272.

Meinshausen, M., N. Meinshausen, W. Hare, S. C. B. Raper, K. Frieler, R. Knutti, D. J. Frame, and M. R. Allen (2009), Greenhouse–gas emission targets for limiting global warming to 2°C, *Nature*, *458*, 1158–1162.

Meinshausen, M., S. C. B. Raper, and T. M. L. Wigley (2011a), Emulating coupled atmosphere-ocean and carbon cycle models with a simpler model, MAGICC6 – Part 1: Model description and calibration, *Atmospheric Chemistry and Physics*, *11*, 1417–1456.

Meinshausen, M., T. M. L. Wigley, and S. C. B. Raper (2011b), Emulating coupled atmosphere-ocean and carbon cycle models with a simpler model, MAGICC6 – Part 2: Applications, *Atmospheric Chemistry and Physics*, *11*, 1457–1471.

Meinshausen, M., et al. (2011c), The RCP greenhouse gas concentrations and their extensions from 1765 to 2300, *Climatic Change*, *submitted*.

Mitchell, T. D. (2003), Pattern scaling: An examination of the accuracy of the technique for describing future climate change, *Climatic Change*, *60*, 217–242.

Morantine, M., and R. G. Watts (1990), Upwelling diffusion climate models: analytical solutions for radiative and upwelling forcing, *Journal of Geophysical Research*, *95*, 7563–7571.

Mosegaard, K., and M. Sambridge (2002), Monte Carlo analysis of inverse problems, *Inverse Problems*, *18*, R29–R54.

Mosegaard, K., and A. Tarantola (1995), Monte Carlo sampling of solutions to inverse problems, *Journal of Geophysical Research*, *100*(B7), 12,431–12,447.

Moss, R. H., J. A. Edmonds, K. Hibbard, M. Manning, S. K. Rose, D. van Vuuren, et al. (2010), The next generation of scenarios for climate change research and assessment, *Nature*, *463*, 747–756.

Murphy, J. M. (1995), Transient response of the Hadley Centre coupled ocean-atmosphere model to increasing carbon dioxide. Part III: Analysis of global–mean response using simple models, *Journal of Climate*, *8*, 496–514.

Murphy, J. M., et al. (2009), *UK Climate projections report: Climate change projections*, Exeter.

Myhre, G., E. J. Highwood, K. P. Shine, and F. Stordal (1998), New estimates of radiative forcing due to well mixed greenhouse gases, *Geophysical Research Letters*, *25*(14), 2715–2718.

Nakicenovic, N., and R. Swart (2000), *IPCC Special Report on Emissions Scenarios*, Cambridge University Press, Cambridge, UK.

Nakicenovic, N., P. Kolp, K. Riahi, M. Kainuma, and T. Hanaoka (2006), Assessment of emissions scenarios revisited, *Environmental Economics and Policy Studies*, *7*, 137–173.

New, M., and M. Hulme (2000), Representing uncertainty in climate change scenarios: a Monte-Carlo approach, *Integrated Assessment*, *1*, 200–213.

O'Neill, B. C., and N. B. Melnikov (2008), Learning about parameter and structural uncertainty in carbon cycle models, *Climatic Change*, *89*, 23–44.

O'Neill, B. C., and M. Oppenheimer (2004), Climate change impacts are sensitive to the concentration stabilization path, *Proceedings of the National Academy of Sciences*, *101*(47), 16,411–16,416.

O'Neill, B. C., and W. Sanderson (2008), Population, uncertainty, and learning in climate change decision analysis, *Climatic Change*, *89*, 87–123.

Oppenheimer, M., and A. Petsonk (2005), Article 2 of the UNFCCC: Historical origins, recent interpretations, *Climatic Change*, *73*, 195–226.

Osborn, T. J., and T. M. L. Wigley (1994), A simple model for estimating methane concentration and lifetime variations, *Climate Dynamics*, *9*, 181–193.

Osborn, T. J., S. C. B. Raper, and K. R. Briffa (2006), Simulated climate change during the last 1,000 years: comparing the ECHO-G general circulation model with the MAGICC simple climate model, *Climate Dynamics*, *27*(2/3), 185–197.

Pielke Jr, R., T. M. L. Wigley, and C. Green (2008), Dangerous assumptions, *Nature*, *3*, 531–532.

PIK (2009), PRIMAP IV baseline reference, https://sites.google.com/a/primap.org/www/the-primap-model/documentation/baselines/primap4.

Pittock, A. B., R. N. Jones, and C. D. Mitchell (2001), Probabilities will help us plan for climate change, *Nature*, *413*, 249.

Plattner, G.-K., F. Joos, T. F. Stocker, and O. Marchal (2001), Feedback mechanisms and sensitivities of ocean carbon uptake under global warming, *Tellus*, *53B*, 564–592.

Pollack, H. N. (2005), *Uncertain Science ... Uncertain World*, Cambridge University Press, Cambridge.

Prather, M. (1996), Time scales in atmospheric chemistry: Theory, GWPs for CH_4 and CO, and runaway growth, *Geophysical Research Letters*, *23*, 2597–2600.

Privalsky, V. E., and D. T. Jensen (1995), Assessment of the influence of ENSO on annual global air temperatures, *Dynamics of Atmospheres and Oceans*, *22*, 161–178.

Ramanathan, V., and Y. Feng (2008), On avoiding dangerous anthropogenic interference with the climate system: Formidable challenges ahead, *Proceedings of the National Academy of Sciences*, *105*(38), 14,245–14,250.

Ramaswamy, V., O. Boucher, J. Haigh, D. Hauglustaine, J. Haywood, G. Myhre, T. Nakajiama, G. Shi, and S. Solomon (2001), Radiative forcing of climate change, in *Climate Change 2001: The Scentific Basis*, edited by J. T. Houghton, Y. Ding, D. Griggs, M. Noguer, P. van der Linden, X. Dai, K. Maskell, and C. Johnson, Cambridge University Press.

Randalls, S. (2010), History of the 2°C climate target, *WIREs Climate Change*, *1*, 598–605.

Raper, S. C. B., and U. Cubasch (1996), Emulation of the results from a coupled general circulation model using a simple climate model, *Geophysical Research Letters*, *23*, 1107–1110.

Raper, S. C. B., T. M. L. Wigley, and R. A. Warrick (1996), Global sea level rise: past and future, in *Sea-level rise and coastal subsidence: causes, consequences and strategies*, edited by J. D. Milliman and B. U. Haq, pp. 11–45, Kluwer Academic Publishers, Dordrecht.

Raper, S. C. B., J. M. Gregory, and T. J. Osborn (2001), Use of an upwelling–diffusion energy balance climate model to simulate and diagnose A/OGCM results, *Climate Dynamics*, *17*, 601–613.

Raupach, M. R., and J. Canadell (2010), Carbon and the anthropocene, *Current Opinion in Environmental Sustainability*, *2*(4), 210–218.

Raupach, M. R., G. Marland, P. Ciais, C. Le Quere, J. Canadell, G. Klepper, and C. B. Field (2007), Global and regional drivers of accelerating CO_2 emissions, *Proceedings of the National Academy of Sciences*, *104*, 10,288–10,993.

Raupach, M. R., J. G. Canadell, P. Ciais, P. Friedlingstein, P. J. Rayner, and C. M. Trudinger (2011), The relatonship between peak warming and cumulative CO_2 emissions and its use to quantify vulnerabilities in the carbon-climate-human system, *Tellus*, *63B*, 145–164.

Rayner, N. A., P. Brohan, D. E. Parker, C. K. Folland, J. J. Kennedy, M. Vanicek, T. Ansell, and S. F. B. Tett (2006), Improved analyses of changes and uncertainties in marine temperature measured in situ since the mid-nineteenth century: the HadSST2 dataset, *Journal of Climate*, *19*, 446–469, (http:www.cru.uea.ac.uk/cru/data/temperature/).

Rayner, P. J., E. Koffi, M. Scholze, T. Kaminski, and J.-L. Dufresne (2011), Constraining predictions of the carbon cycle using data, *Philosophical Transactions of the Royal Society*, *369*, 1955–1966.

Reichstein, M. (2010), Journal club, *Nature*, *464*, 145.

Ricciuto, D. M., K. J. Davis, and K. Keller (2008), A Bayesian calibration of a simple carbon cycle model: The role of observations in estimating and reducing uncertainty, *Global Biogeochemical Cycles*, *22*, doi:10.1029/2006GB002908.

Ricciuto, D. M., R. Tonkonojenkov, N. M. Urban, R. D. Wilkinson, D. Matthews, K. J. David, and K. Keller (2011), Assimilation of global carbon cycle observations into an Earth system model to estimate uncertain terrestrial carbon cycle parameters, *Global Biogeochemical Cycles*, *in revision*.

Robock, A., and M. P. Free (1996), The volcanic record in ice cores for the past 2000 years, in *Climatic Variations and Forcing Mechanisms of the Last 2000 Years*, edited by P. D. Jones, R. S. Bradley, and J. Jouzel, Springer-Verlag, Berlin.

Roe, G. H., and M. B. Baker (2007), Why is climate sensitivity so unpredictable, *Science*, *318*, 629–632.

Rogelj, J., J. Nabel, C. Chen, W. Hare, K. Markmann, and M. Meinshausen (2010), Copenhagen Accord pledges are paltry, *Nature*, *464*, 1126—1128.

Sansó, B., and C. Forest (2009), Statistical calibration of climate system properties, *Applied Statistics*, *58*(4), 485–503.

Santer, B., T. Wigley, M. Schlesinger, and J. Mitchell (1990), Developing climate scenarios from equilibrium GCM results, *Tech. rep.*, Max Planck Institute for Meeorology.

Sato, M., J. E. Hansen, M. P. McCormick, and J. B. Pollack (1993a), Stratospheric aerosol optical depths, 1850-1990, *Journal of Geophysical Research*, *98*(D12), 22,987–22,994.

Sato, M., J. E. Hansen, K. McGuffie, and J. B. Pollack (1993b), Stratospheric aerosol optical depth (data updated 2002), *Journal of Geophysical Research*, *98*, 22,987–22,994.

Schaeffer, M., and E. Stehfets (2010), The climate subsystem in IMAGE updated to MAGICC 6.0, *Netherlands Environmental Assessment Agency (PBL)*.

Schellnhuber, H. J. (2009), Tipping elements in the Earth system, *Proceedings of the National Academy of Sciences*, *106*(49), 20,561–20,563.

Schlesinger, M. E., and S. Malyshev (2001), Changes in near–surface temperature and sea level for the Post-SRES CO_2–stabilisation scenarios, *Integrated Assessment*, *2*, 95–110.

Schlesinger, M. E., and L. J. Williams (1997), *COSMIC — Country specific model for intertemporal climate*, Electric Power Research Institute.

Schneider, S. H. (2001), What is 'dangerous' climate change?, *Nature*, *411*, 17–19.

Schneider, S. H., and J. Lane (2006), An overview of 'dangerous' climate change, in *Avoiding Dangerous Climate Change*, edited by H. J. Schellnhuber, W. Cramer, N. Nakicenovic, T. M. L. Wigley, and G. Yohe, chap. 2, Cambridge University Press.

Seigenthaler, U., and H. Oeschger (1987), Biospheric CO_2 emissions during the past 200 years reconstructed by deconvolution of ice core data, *Tellus*, *39B*, 140–154.

Senior, C. A., and J. Mitchell (2000), The time–dependence of climate sensitivity, *Geophysical Research Letters*, *27*(17), 2685–2688.

Sheehan, P. (2008), The new global growth path: implications for climate change analysis and policy, *Climatic Change*, *91*, 211–231.

Shine, K. P., R. G. Derwent, D. J. Wuebbles, and J.-J. Morcrette (1990), Radiative forcing on climate, in *Climate Change: The IPCC Scientific Assessment*, edited by J. T. Houghton, G. Jenkins, and J. J. Ephraums, pp. 41–68, Cambridge University Press, Cambridge, UK.

Siegenthaler, U., and F. Joos (1992), Use of a simple climate model for studying oceanic tracer distributions and the global carbon cycle., *Tellus*, *44B*, 186–207.

Smith, J. B., S. H. Schneider, M. Oppenheimer, G. W. Yohe, W. Hare, M. D. Mastrandrea, A. Patwardhan, I. Burton, et al. (2009), Assessing dangerous climate change through an update of the Intergovernmental Panel on Climate Change (IPCC) "reasons for concern", *Proceedings of the National Academy of Sciences*, *106*(11), 4133–4137.

Smith, S. J., and T. M. L. Wigley (2006), Multi-gas forcing stabilization with Minicam, *The Energy Journal*, pp. 373–391.

Smith, T. M., R. W. Reynolds, T. C. Peterson, and J. Lawrimore (2008), Improvements to NOAA's historical merged land–ocean surface temperature analysis (1880–2006), *Journal of Climate*, *21*, 2283–2293, (http:www.ncdc.noaa.gov/cmb-faq/anomalies.html).

Sokolov, A. P., C. E. Forest, and P. H. Stone (2010), Sensitivity of climate change projections to uncertainties in the estimates of observed changes in deep-ocean heat content, *Climate Dynamics*, *34*, 735–745.

Stern, N. (2007), *The Economics of Climate Change - The Stern Review*, Cambridge University Press, Cambridge.

Stocker, T. F., and R. Knutti (2003), Do simplified climate models have any useful skill?, *CLIVAR Exchanges*, *8/1*(1), 7–10.

Stott, P. A., S. F. B. Tett, G. S. Jones, M. R. Allen, W. J. Ingram, and J. Mitchell (2001), Attribution of twentieth century temperature change to natural and anthropogenic causes, *Climate Dynamics*, *17*, 1–21.

Sutton, R. W., B. Dong, and J. M. Gregory (2007), Land/sea warming ratio in response to climate change: IPCC AR4 model results and comparison with observations, *Geophysical Research Letters*, *34*, doi:10.1029/2006GL028164.

Teng, H., L. E. Buja, and G. Meehl (2006), Twenty-first-century climate change commitment from a multi-model ensemble, *Geophysical Research Letters*, *33*(L07706).

Thompson, D. W. J., J. M. Wallace, P. D. Jones, and J. J. Kennedy (2009), Identifying signatures of natural climate variability in time series of global–mean surface temperatures: Methodology and insights, *Journal of Climate*, *22*, 6120–6141.

Tol, R. S. J. (2007), Europe's long–term climate target: a critical evaluation, *Energy Policy*, *35*, 424–432.

Tol, R. S. J., B. O'Neill, and D. van Vuuren (2005), A critical assessement of the IPCC SRES scenarios.

Tomassini, L., P. Reichert, R. Knutti, T. F. Stocker, and M. E. Borsuk (2007), Robust Bayesian uncertainty analysis of climate system properties using Markov Chain Monte Carlo methods, *Journal of Climate*, *20*, 1239–1254.

Twomey, S. (1977), The influence of pollution on the shortwave albedo of clouds, *Journal of Atmospheric Sciences*, *34*, 1149–1152.

Urban, N. M., and K. Keller (2010), Probabilistic hindcasts and projections of the coupled cliamte, carbon cycle and Atlantic meridional overturning circulation system: A Bayesian fusion of century–scale observations with a simple model, *Tellus A*, *62*(5), 737–750, doi:10.1111/j.1600-0870.2010.00471.x.

van Vuuren, D., B. Eickhout, P. L. Lucas, and M. G. J. den Elzen (2006), Long-term multi-gas scenarios to stabilise radiative forcing – exploring costs and benefits within an integrated assessment framework, *The Energy Journal*, pp. 201–233.

van Vuuren, D., J. Lowe, E. Stehfest, L. Gohar, A. F. Hof, C. Hope, R. Warren, M. Meinshausen, and G.-K. Plattner (2011), How well do integrated assessment models simulate climate change?, *Climatic Change*, *104*, 255–285.

Veronis, G. (1975), The role of models in tracer studies, in *Numerical models of ocean circulation*, pp. 133–146, National Academy of Sciences, Washington, D.C.

WBGU (2009), *Solving the climate dilemma: The budget approach*, WBGU (German Advisory Council on Global Change).

Webster, M., M. Babiker, M. Mayer, J. M. Reilly, J. Harnisch, R. Hyman, M. Sarofim, and C. Wang (2002), Uncertainty in emissions projections for climate models, *Atmospheric Environment*, *36*, 3659–3670.

Webster, M., et al. (2003), Uncertainty analysis of climate change and policy response, *Climatic Change*, *61*, 295–320.

Wetherald, R. T., R. J. Stouffer, and K. W. Dixon (2001), Committed warming and its implications for climate change, *Geophysical Research Letters*, *28*(8), 1535–1538.

Wigley, T. M. L. (1991a), Could reducing fossil–fuel emissions cause global warming?, *Nature*, *349*, 503–506.

Wigley, T. M. L. (1991b), A simple inverse carbon cycle model, *Global Biogeochemical Cycles*, *5*(4), 373–382.

Wigley, T. M. L. (1993), Balancing the carbon budget. Implications for projections of future carbon dioxide concentration changes., *Tellus*, *45B*, 409–425.

Wigley, T. M. L. (1994), How important are carbon cycle uncertainties, in *Climate change and the agenda for research*, edited by T. Hanisch, Westview Press, Boulder.

Wigley, T. M. L. (1995), Global–mean temperature and sea level consequences of greenhouse gas concentration stabilization, *Geophysical Research Letters*, *22*, 45–48.

Wigley, T. M. L. (1997), The observed global warming record: What does it tell us?, *Proceedings of the National Academy of Sciences*, *94*, 8314–8320.

Wigley, T. M. L. (2000a), Stabilization of CO_2 concentration levels, in *The Carbon Cycle*, edited by T. Wigley and D. Schimel, pp. 258–276, Cambridge University Press, Cambridge.

Wigley, T. M. L. (2000b), ENSO, volcanoes and record-breaking temperatures, *Geophys. Res. Lett.*, *27*(24), 4101–4104.

Wigley, T. M. L. (2004), MAGICC/SCENGEN 4.1: Technical manual.

Wigley, T. M. L. (2005), The climate change commitment, *Science*, *307*, 1766–1769.

Wigley, T. M. L. (2008), *MAGICC/SCENGEN 5.3: User Manual*, NCAR, Boulder, CO.

Wigley, T. M. L., and S. C. B. Raper (1987), Thermal expansion of sea level associated with global warming, *Nature*, *330*, 127–131.

Wigley, T. M. L., and S. C. B. Raper (1990), Natural variability of the climate system and detection of the greenhouse effect, *Nature*, *344*, 324–327.

Wigley, T. M. L., and S. C. B. Raper (1991), Detection of the enhanced greenhouse effect on climate, in *Climate Change: Science, Impacts and Policy*, edited by J. Jager and H. L. Ferguson, pp. 231–242, Cambridge University Press, Cambridge, UK.

Wigley, T. M. L., and S. C. B. Raper (1992), Implications for climate and sea level of revised IPCC emissions scenarios, *Nature*, *357*, 293–300.

Wigley, T. M. L., and S. C. B. Raper (1993), Future changes in global–mean temperature and sea level, in *Climate and sea level changes: Observations, projections, and implications*, edited by R. A. Warrick, E. M. Barrow, and T. M. L. Wigley, pp. 111–133, Cambridge University press, Cambridge, UK.

Wigley, T. M. L., and S. C. B. Raper (2001), Interpretation of high projections for global–mean warming, *Science*, *293*, 451–454.

Wigley, T. M. L., and S. C. B. Raper (2002), Reasons for larger warming projections in the IPCC Third Assessment Report, *J. Clim.*, *15*, 2945–2952.

Wigley, T. M. L., and M. E. Schlesinger (1985), Analytical solution for the effect of increasing CO_2 on global mean temperature, *Nature*, *315*, 649–652.

Wigley, T. M. L., R. Richels, and J. A. Edmonds (1996), Economic and environmental choices in the stabilization of atmospheric CO_2 concentrations, *Nature*, *379*, 240–243.

Wigley, T. M. L., S. C. B. Raper, M. Hulme, and S. J. Smith (2000), The MAGICC/SCENGEN climate scenario generator version 2.4: Technical manual.

Wigley, T. M. L., C. M. Ammann, B. Santer, and S. C. B. Raper (2005), Effect of climate sensitivity on the response to volcanic forcing, *Journal of Geophysical Research*, *110*, doi: 10.1029/2004JD005557.

Wigley, T. M. L., R. Richels, and J. A. Edmonds (2007), Overshoot pathways to CO_2 stabilization in a multi–gas context, in *Human–induced climate change: an interdisciplinary assessment*, edited by M. E. Schlesinger, H. S. Kheshgi, J. Smith, F. C. de la Chesnaye, J. M. Reilly, T. Wilson, and C. Kolstad, pp. 84–92, Cambridge University Press.

Wijffels, S. E. (2009), New estimates of ocean warming rates and how well they are simulated by AR4, Greenhouse 2009, Perth, Australia.

Wijffels, S. E., J. Willis, C. M. Domingues, P. Barker, N. J. White, A. Gronell, R. K, and C. J. A. (2008), Changing expendable bathythemograph fall rates and their impact on estimates of thermosteric sea level rise, *Journal of Climate*, *21*, 5657–5672.

Williams, K. D., W. J. Ingram, and J. M. Gregory (2008), Time variation of effective climate sensitivity in GCMs, *Journal of Climate*, *21*, doi:10.1175/2008JCLI2371.1.

Yu, H., et al. (2006), A review of measurement–based assessments of the aerosol direct radiative effect and forcing, *Atmospheric Chemistry and Physics*, *6*, 613–666.

Zickfeld, K., M. Eby, H. D. Matthews, and A. J. Weaver (2009), Setting cumulative emissions targets to reduce the risk of dangerous climate change, *Proceedings of the National Academy of Sciences*, *106*(38), 16,129–16,134.

Author/s:
Bodman, Roger William

Title:
Estimating uncertainties in future global warming using a simple climate model

Date:
2011

Citation:
Bodman, R. W. (2011). Estimating uncertainties in future global warming using a simple climate model. PhD thesis, School of Earth Sciences, The University of Melbourne.

Persistent Link:
http://hdl.handle.net/11343/37057